UNICA

UNIVERSITÀ
DEGLI STUDI
DI CAGLIARI

Ph.D. DEGREE IN
PHYSICS

Cycle XXXV

TITLE OF THE Ph.D. THESIS

Experimental characterization and computational modeling

of N-doped Carbon Dots for future optoelectronic applications

Scientific Disciplinary Sector

FIS/01

Ph.D. Student: Chiara Olla

Supervisor Prof. Carlo Maria Carbonaro

Final exam. Academic Year 2021/2022
Thesis defence: March 2023 Session

A nonno Gigi

Abstract

Over the past few years, significant efforts have been made to replace semiconductor quantum dots and rare-earth-based materials currently adopted in optoelectronics and photonics with more environmental-friendly and cost-effective fluorophores. A promising solution is the class of fluorescent carbon-based nanoparticles known as Carbon Dots (CDs). CDs generally present a high quantum yield (QY) in the blue-green wavelength region, which can be comparable to their inorganic counterparts, with limitations in the red range that can be partially overcome through proper functionalization of the surface or *ad-hoc* doping. CDs' main feature is their almost ubiquitous excitation-dependent photoluminescence, the emission properties being of which can be easily modified through chemical functionalization and surface passivation. These optical properties, along with high chemical inertness, resistance to photobleaching, and biocompatibility, make CDs highly desirable for many technological purposes. Despite these advantages, CDs present some critical issues to address in order to develop CD-based technology. The main challenge is the lack of deep knowledge about their structure, which is strongly linked to the origin of their photoluminescence. At present, their emission properties are not exclusively ascribed to a single mechanism: quantum confinement, due to their hypothesized nanosized sp^2 carbon core, and molecular states or surface states, due to fluorophores formation and surface traps, respectively, are both considered. Also, the synergistic interplay between the proposed models further complicates the scenario. This thesis work aims to provide a comprehensive experimental characterization and computational framework for this new material, with a focus on its optical properties and in particular on the role of nitrogen for future optoelectronic applications. In **Chapter 1**, an introduction to CD nanoparticles is presented, including an overview of their classifications, optical features and associated mechanisms, design strategies, and possible characterizations and applications.

The following **Chapter 2** introduces the importance of combining computational methods with experimental ones, reporting a review of a variety of theoretical CD works that employed density functional theory methods for the calculation of optical properties in doped and functionalized models.

Chapter 3, on the other hand, reports our multi-technical investigation of CD-silica hybrids, emphasizing the role of the matrix in tuning the luminescent properties, not only as a tool for increasing the relative contribution of molecular N-species during the synthesis, but also as a suitable environment for studying the less intense surface-state emissive centers.

With the aim of targeting the role of nitrogen in CD formation, **Chapter 4** illustrates our detailed analysis of the differences between N-doped CDs and pristine ones obtained from citric acid, with a particular focus on the distinct nature of the emitting centers under examination.

Continuing on the same topic, **Chapter 5** describes our innovative methodology for studying the reaction pathway of the formation of N-doped CDs from citric acid and urea, combining optical spectroscopy with nuclear magnetic resonance (NMR) techniques to give insight into the different molecular and core/surface centers produced.

Chapter 6 thoroughly discusses the pioneering formation of CDs from hydrazine precursors in order to investigate the N–N bond and its related optical features. **Chapter 7**, in turn, gives an overview of our ongoing research on the implementation of other nitrogen sources for the production of more efficient CDs.

Finally, **Chapter 8** summarizes the main purposes of this thesis and the results obtained in the above research works. Each chapter that focuses on experimental results is accompanied by a supplementary section in the appendix.

Table of contents

List of Figures

List of Tables

Chapter 1

Introduction

1.1 Carbon Dots: definition and classification

Nanomaterials have emerged as an incredible investigation field due to their distinctive physical and chemical properties compared to their bulk counterparts, such as higher surface area, different thermal and electrical conductivity, and excellent mechanical properties, as well as the occurrence of quantum and magnetic effects.[1–5] All materials with at least one size lower than 100 nm belong to this class, and their classification is based on the number of dimensions not confined in this nanoscale range.[6]

Zero-dimensional nanomaterials have all dimensions limited to this extent, and the most common representation of them are nanoparticles. A type of nanoparticle that has received considerable attention is semiconductor quantum dots (QDs), whose dimensions fall in the 1-10 nm range. In this nanoscale range, the optical properties are strongly linked to quantum mechanical phenomena because the conduction electrons are trapped in a bowl-like potential with discrete electronic states, which makes them an artificial atom structure. Since a photogenerated electron-hole pair has an exciton diameter in the same dimension range, tuning the size and shape of the QDs influences its absorption and emission features.[7,8]

These luminescent properties, combined with enhanced photostability and high quantum yield (QY), make QDs a particularly promising material for optical applications. However, the tedious and expensive synthetic procedures, along with their toxicity to human health and the environment, represent major drawbacks

not only in their use for biomedical purposes,[9] but also for the growing demand for more environmental-friendly and cost-effective fluorophores in optoelectronics and photonics. A promising green and low-cost alternative is represented by a wide class of fluorescent carbon-based nanoparticles named Carbon Dots (CDs).

CDs were accidentally discovered as a side product during the purification of carbon nanotubes by Xu and coworkers in 2004,[10] which marked the start of a brand-new line of research that provides thousands of papers on the topic each year.[11] Despite the similar name derived from their semiconductor counterparts, CD nanoparticles share only a few features with QDs, such as nanoscale size and efficient lighting performance in the visible region. Nevertheless, in most cases, nanoparticles belonging to this class have very different structural and optical properties. CD is an extensive term used to describe a diverse set of nanoscale carbon systems.[12] A general classification has been provided to distinguish particles according to their inner structure (**Figure 1.1.1**):

- Graphene Quantum Dots (GQDs) present the highest ordered structure among the CD family. They are constituted of a single or a few graphene layers with lateral dimensions not larger than 100 nm. In this anisotropic and layered structure, carbon atoms are arranged in rings of six, with each atom covalently bonded to three others, resulting in delocalized electrons in the π orbitals. This honeycomb crystal lattice of carbon atoms provides sp^2 hybridized characteristics, which are mainly responsible for their electrical and optical properties. In particular, the size and shape of these systems greatly affect the size of their band gap and, consequently, their emissive properties.[13,14]
- Carbon Nano Dots (CNDs) are defined as small carbon nanoparticles with a typical size of less than 10 nm in all three dimensions. Their general representation is built on the “core-shell” model: a spherical-like carbon core consisting of multiple layers of stacked graphene fragments with varying degrees of sp^2/sp^3 hybridization and a surface rich in functional groups and molecular moieties.[15] The ratio between the disordered and ordered contributions is highly dependent on the synthesis and environmental conditions, resulting in surface passivation and elemental doping that influence the optical properties.[16] When CNDs have a high degree of crystallinity, they are sometimes referred to as Carbon Quantum Dots (CQDs).
- Carbonized Polymer Dots (CPDs) are polymer-based nanoparticles that are smaller than 100 nm in all dimensions, arranged as polymeric aggregates or cross-linked structures and produced from linear polymers or monomers.[12] Unlike most polymeric structures, CPDs possess a π-electronic system, which

furnishes a semiconductor-like band gap, leading to efficient absorption and emission features that can be tuned by altering the molecular arrangement of the polymer.[17] According to some authors, CPDs are believed to be produced as an intermediate product in CND synthesis, as polymerization and graphitization are considered two subsequent processes.[18]

Despite the structural differences, all carbon nanosystems share highly appealing optical features such as high QY, especially in the blue-green wavelength region, and a peculiar excitation-dependent emission that is the observed emission is redshifted when the excitation energy decreases. The proposed mechanisms for the luminescence differ depending on the type of CD under examination. Nevertheless, these emissive properties, combined with low toxicity and biocompatibility, high chemical inertness, resistance to photobleaching, and water solubility/dispersibility, make CD an incredible material suitable for a wide variety of technological applications.[19]

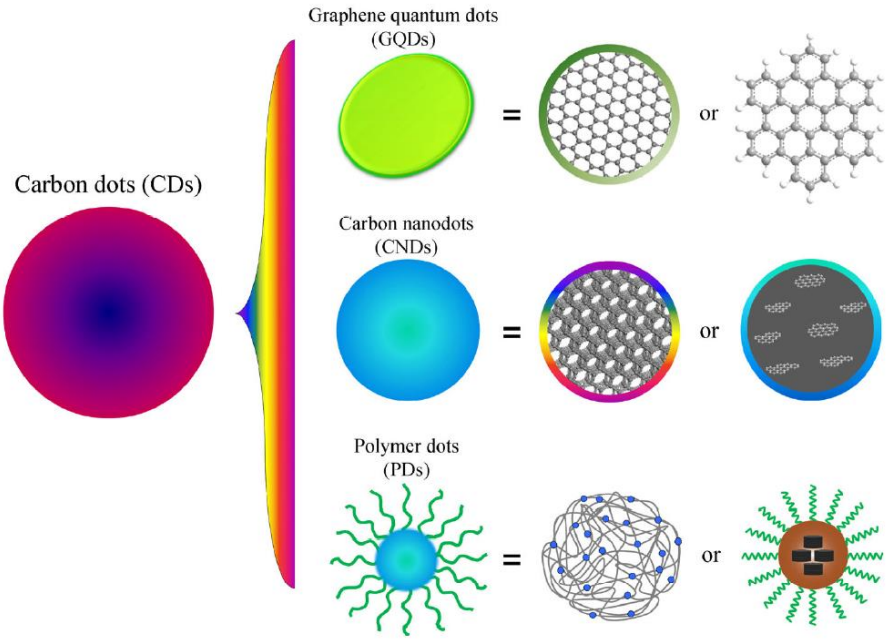

Figure 1.1.1. Three types of fluorescent CDs: graphene quantum dots (GQDs), carbon nanodots (CNDs), and carbon polymer dots (CPDs).[12]

1.2 Optical properties and photoluminescence mechanisms

All CD nanoparticles present similar absorption and emission features. In terms of optical absorption, CDs generally present two absorption contributions in the near and far UV regions, with a tail extending into the visible region. The far UV peak is typically ascribed to the π–π* transition of the π-conjugated electrons in the sp^2 network due to aromatic C=C bonds, whilst the near UV one is assigned to the n–π* transition caused by heteroatom-containing surface functional groups or molecular moieties. The assignment of the tail in the visible region is more debated, likely due to lower-energy surface centers related to the functionalization of CDs.[19,20] Potential modifications in the ratio of these contributions can indicate alterations in the composition, arrangement, or hybridization degree.[12]

The related photoluminescence (PL) properties are an essential feature for the development of new technology based on this material. The CD emission peak is typically broad and a large Stokes shift, which can reach up to 100 nm, is often recorded. The most efficient emission bands are observed in the blue-green region when excited at near-UV and visible wavelengths, with the QY dependent on the synthesis conditions.[16] Fluorescence is the most commonly observed phenomenon, with an average lifetime in the nanosecond range (4-15 nm) that is often calculated via non-single exponential PL decays, indicating multiple contributions to the overall spectrum and the presence of non-radiating channels.[19]

The excitation-dependent behavior is the main distinctive property of CDs, even though excitation-wavelength independent emissions have also been reported.[21,22] The explanation of this phenomenon is challenging and strictly related to the nature of the CDs under examination, possibly due to a broad size distribution of the dots, different surface emissive traps, or the co-presence of various molecular entities. Currently, four main PL mechanisms have been proposed (**Figure 1.2.1**):

- The *Quantum Confinement Effect* (QCE) mainly occurs in GQD nanoparticles due to their highly ordered structure, resulting in optical features that depend on their size and shape, similar to inorganic QDs. When GQDs and mostly crystalline CNDs have dimensions smaller than their exciton Bohr radius, continuous valence and conduction energy bands turn into discrete electronic levels, like in atomic structures. The presence of conjugated π-domains is responsible for QCE in CD and is considered the origin of fluorescence from carbon-core states.[23,24] Indeed, as the size of π-domains increases, the band gap

value decreases, resulting in a redshift of the emission peak, which typically falls in the UV-visible region.[20]

- *Surface defect states* are the most popular explanation for accounting for the emissive properties of various types of CDs with a certain degree of disordered structure. The boundary region, composed of the hybridized sp^2/sp^3 carbon backbone, functional groups attached to the surface, and dangling bonds, is distinct from the core and is responsible for different emission centers. The complexity of this boundary region can elucidate the peculiarities of CD fluorescence properties. Just like in the semiconductor field, surface states can be classified as intrinsic and extrinsic. Intrinsic centers, due to the termination of the particle lattice interacting with the environment, can explain the presence of emissive traps, while extrinsic ones, representing surface lattice defect such as adsorbed or bonded chemical species, can describe the excitation-wavelength dependence of the emission.[12,16,19,20]
- The *molecular state* model supports the presence of fluorescent molecules, both at the surface and incorporated in the core, as building blocks of the CD system. CDs produced using small organic molecules and with low carbonization temperatures usually exhibit molecular fluorescence that decreases as the temperature increases, as the fluorophore is consumed to form the crystalline core. Molecular fluorescence generally shows strong emission with a higher QY compared to the QCE and surface states PL, but the latter has higher photostability.[12,20] This model does not take into account the excitation-dependence of CD fluorescence because molecular emission is not dependent on the excitation wavelength. A possible justification is the presence of a set of different emitting molecules or a collection of polycyclic aromatic hydrocarbons (PAH) whose different band gaps can provide different excitation/emission centers.[19,25]
- *Crosslink Enhanced Emission (CEE)* was observed in CPD nanoparticles due to their unique polymeric structure.[18] As the name implies, the crosslinked structure leads to an enhancement of the luminescence by affecting it from two fronts: immobilization and generation of new energy levels.[26] Immobilization of the polymeric chains reduces the causes of non-radiative transitions, such as vibrations and rotations. This confinement has little effect on energy levels, leading to an increase in fluorescence without changing the emission peak.[27] On the other hand, crosslinking impacts energy levels by reducing the distance between functional groups, causing the electron clouds to overlap and couple, or leading to the formation of chemical bonds. In the

first case, through-space interaction splits intrinsic energy levels, and in the latter, they generate new ones.

This overview of the proposed PL mechanisms is useful in understanding the strong correlation between optical properties and structure. As the structure of CD is very complex, it can be assumed that fluorescence is related to the synergistic interplay of the emitting core, surface states, and molecules in different ratios, depending on the synthetic procedure. Thus, implementing controlled synthesis is essential for obtaining a better comprehension of the CD structure and PL mechanism for proposed applications.

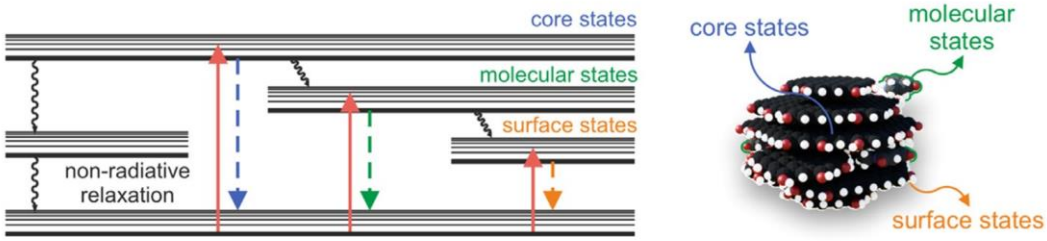

Figure 1.2.1. Schematic representation of three of the main PL mechanism in CD. The red arrows indicate electronic transitions related to absorption, which can relax non-radiatively as represented by the black wavy arrows, or radiatively, as shown by the colored dashed arrows. Adapted figure from our work.[28]

1.3 Design of CDs: synthesis, doping, and functionalization

The basic requirement for synthesizing CDs is the use of a compound with a carbon skeleton. However, different morphologies are closely linked to various synthetic procedures and precursors. Given these premises, two approaches to synthesize CDs as a nanomaterial are commonly used: the top-down and bottom-up methods (**Figure 1.3.1**).

- The *top-down* approach involves the production of CDs through the chemical or physical cutting of carbon sources, including both bulk and nanomaterial sources such as carbon soot, carbon fiber, graphene, graphitic carbon nitride, and fullerenes.[11] This methodology was the first to be adopted as it provided the very first CDs obtained as residues of single-wall carbon nanotubes

produced via the arc-discharge procedure.[10] Since then, arc discharge and laser ablation have been implemented for the production of high-ordered CDs such as GQDs and crystalline CNDs.[29–31] However, the use of specific instrumentation and the need for post-synthesis treatments to achieve competitive QY makes the whole procedure expensive and disadvantageous. Oxidative cleavage is a more popular method in this category, involving the breaking of carbon bonds using a strong oxidant compound. In the case of chemical oxidation, the reaction temperature and oxidant concentration determine the shape and size of the CD.[32] The electrochemical procedure, instead, regulates the nature of CD according to the applied voltage and solution pH.[33]

- Bottom-up methods generate CDs through a combustion or thermal process of small molecules or polymeric precursors, such as citric acid, phloroglucinol, phenylenediamine, and various types of biomasses. A general easy and low-cost synthetic process is provided through direct pyrolysis, microwave-assisted pyrolysis, and hydrothermal/solvothermal treatment.[10,34] These thermal treatments may have different target temperatures, working pressures, and synthesis times, resulting in carbon structures with a higher degree of disorder compared to top-down nanoparticles and are consequently classified as CNDs and CPDs. In the bottom-up approach, optical properties are largely determined by the dominant presence of surface state and/or fluorescent molecules.[35] Among the bottom-up approaches, the hydrothermal method provides an efficient and scalable route to synthesizing carbon particles under milder conditions from organic acids, amines, saccharides, and their derivatives.[36,37] The proposed mechanism of CD formation in this case is related to the polymerization, aromatization, nucleation, and growth of precursors in the water medium.[37–41] Microwave-assisted and direct pyrolysis of small organic precursors are assumed to follow a similar pattern, producing molecular fluorophores in the first part of the reaction that act as seeds for CD nucleation, resulting in the formation of nanosized graphitic domains.[42–44]

Nowadays, bottom-up methods are the most popular, as they combine simple thermal treatments with a virtually infinite set of molecular precursors. Pristine CDs, whose structure includes only carbon and oxygen atoms, generally emit blue fluorescence with low QY. To improve photoluminescent properties, surface modification/functionalization and doping are commonly used. In the first case, the introduction of functional groups and heteroatoms alters the surface state, adding/modifying surface traps and changing the interactions of carbon atoms on

the edges with their neighbors. Doping is achieved by incorporating heteroatoms into the carbon network. Both phenomena can create/suppress energy levels and enhance the QY compared to pristine CDs, effectively tuning the optical properties, and contributing to a better understanding of the related PL mechanisms. Despite the ubiquitous presence of oxygen, the amount and the type of functional group provided during the synthetical treatment highly affect the optical performances of the obtained nanoparticles. In particular, oxygen in the form of carboxyl, carbonyl, hydroxyl, and epoxy groups not only affect the CD optical properties but also the solubility and biocompatibility.[45] Nitrogen is another commonly studied dopant. The radius of nitrogen atoms is similar to that of carbon atoms, allowing them to be easily incorporated into the carbon network as graphitic, pyrrolic, and pyridinic nitrogen. The presence of amino and cyano groups is also under investigation. These different forms of nitrogen are supposed to influence the band gap size of the material in different ways, sometimes causing blue or redshift. Other typical dopants are sulfur, boron, and phosphorous, along with nitrogen and other elements as co-dopant. Understanding the role of these different heteroatoms as dopants and surface groups is challenging from a purely experimental approach, due to the highly complex structure of these systems. For this reason, more and more research papers are employing a combined experimental and computational approach which can help a better understanding of these fascinating material properties. In **Chapter 2,** further information about the relationship between doping and functionalization with PL properties will be provided from a computational perspective.

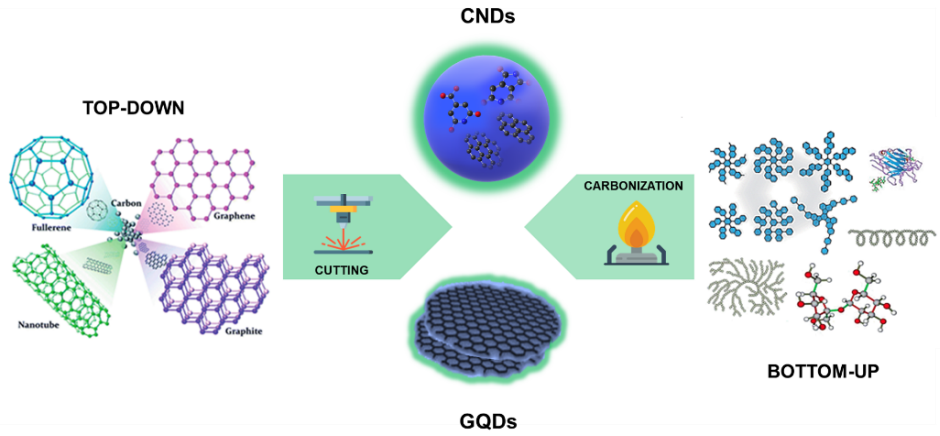

Figure 1.3.1. Representation of the possible synthesis methods to prepare GQDs and CNDs. Adapted figure from our work.[28]

1.4 Characterization methods and optoelectronic applications: the CANDL² project

The characterization of CDs involves a multi-technical approach to obtain the structural, spectroscopic, dynamic, and functional properties. The most relevant techniques include optical and vibrational spectroscopies as well as electron microscopy. Firstly, the interpretation of optical absorption and PL results is crucial for understanding the characteristics of CDs in the context of all PL mechanisms previously discussed (**Section 1.2**). Other optical spectroscopies employed are time-resolved photoluminescence and transient absorption spectroscopy. Time-resolved photoluminescence (TR-PL) is an excellent technique for identifying any energy and/or charge transfer mechanisms related to functional groups and interacting molecules. However, this process becomes complicated if the systems under investigation are CDs because of their complex nature, in which inner states strongly interact with surface states and show emission wavelength-dependent lifetime. Uncovering charge/energy transfer through the study of fluorescence decay in such systems would help in understanding the quenching process, the origin of the spectral components, and the structural relaxation.[46] Transient optical absorption spectroscopy (TAS) is another powerful tool that allows the recording of absorbance variations as a function of wavelength and time. TAS has been used in the CD research field to identify surface states and observe the kinetics of radical formation on the surface.[47–49] The main limitation of these highly sensitive and effective techniques is the regulation of excitation power, which can potentially induce photochanges in the CD structure due to high-density power light beams.[50]

In addition to optical spectroscopy techniques, vibrational spectroscopies are effectively used to study the nature of functional groups and bonds in CDs. For instance, Fourier transform infrared spectroscopy (FTIR) can be employed to investigate the formation of the carbonaceous core, the presence of heteroatoms, and the surface functionalities of CDs.[51] However, there is a limitation of possible overlap of product signals with those of by-products and precursors. Another effective vibrational technique is Raman spectroscopy, which is commonly employed to study graphitic systems, addressing sp^2 and sp^3 hybridization, number of layers, and eventual defects.[52,53] A common challenge in using Raman spectroscopy for CD studies is the excitation wavelength in the visible range, which induces fluorescence and masks lower Raman signals. A potential solution is the use of Surface Enhanced Raman Scattering (SERS) which has higher

sensitivity compared to classic Raman and allows for clearer spectra recording. X-ray photoelectron spectroscopy (XPS) also helps link structural and optical properties and provides crucial information on the elemental composition of CDs. Finally, microscopy techniques are employed to analyze the size, shape, and crystallinity of CDs. Transmission electron microscopy (TEM) is commonly utilized to investigate CD morphology, often in conjunction with selected area electron diffraction (SAED) or high-resolution TEM (HRTEM). However, similar to optical spectroscopy, the probe energy density must be regulated to avoid carbonization of the samples, and the poor contrast of carbon-based nanoparticles presents a challenge for CD imaging. In addition to these widely used techniques, nuclear magnetic resonance (NMR) has been recently employed to gain insight into the complex structure of CDs, yielding impressive results in the study of CD doping and the discovery of new molecular species produced during synthesis.[22,54]

All of these characterization techniques aim to reveal the remarkable luminescence and structural properties of CDs, with the goal of developing new technologies based on this material that are suitable for various applications such as drug delivery,[55] sensors,[56] detectors,[57] photocatalysis,[58] biosensing, cell labeling, imaging,[59] thermoelectrics[60] and optoelectronic devices such as LEDs and lasers (**Figure 1.4.1**).[61,62] The latter is of particular interest for replacing rare-earth and semiconductor-based materials currently used in these fields. Indeed, the broad emission spectrum of CDs is well-suited for the fabrication of white LEDs, which have been viewed as the next-generation lighting devices due to their energy-saving, long-lifetime, and compact size features.[61] A different challenge involves developing CD-based lasers with high brightness and high monochromaticity for which only a few studies have shown good results.[63]

Several critical issues must be addressed in order to use CDs for these specific application fields. Firstly, the strong relationship between structure and photoluminescence must be understood in order to tune emissions according to the structure. Additionally, since the most efficient performance of CDs is in the blue-green range, the QY in the red range must be improved, with the goal of achieving an overall QY that is competitive with other fluorescent materials such as quantum dots and organic dyes. Finally, the interaction between CDs and a solid-state matrix must be understood in order to design CD-based lighting and lasing technology.

These purposes gathered four Italian universities and research centers (University of Sassari, University of Cagliari, University of Palermo, Consiglio Nazionale delle Ricerche di Bari) that join the "*CArbon NanoDots for Light-*

emitting materials and Lasing applications" abbreviated *CANDL*^{2}, a project funded by MIUR within PRIN call.

Our group at the University of Cagliari is involved in two complementary fields. The first involves developing a theoretical study of CDs to predict their optical properties and validate experiments, while the second focuses on the full characterization of CDs produced through different methods and in different matrices. In terms of theoretical modeling, we aim to understand the correlation between structure and optical properties, with a specific focus on the role of nitrogen doping. In the experimental characterization, our goal is to identify the best precursors for synthesis and to gain a deeper understanding of their interaction with host matrices. This thesis was developed with the objectives of the CANDL^2 project in mind and it is hoped that it will contribute to these exciting challenges.

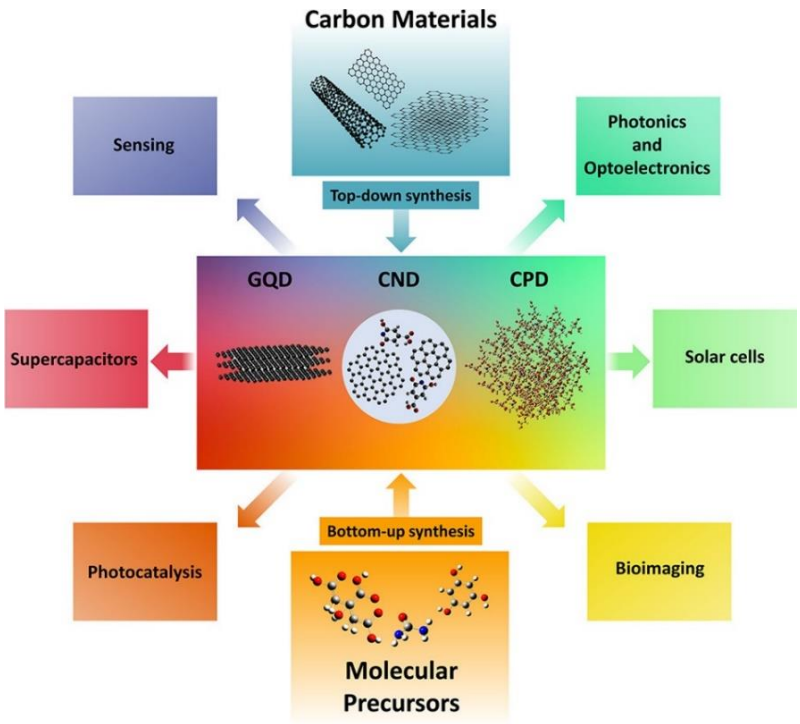

Figure 1.4.1. Synthetic approaches for the different forms of carbon dots (CND, carbon nanodot; GQD, graphene quantum dot; CPD, carbonized polymer dot) and main areas of application. Original figure from our work.[50]

Chapter 2

Modeling optical properties of doped/functionalized CDs

Mocci, F.; de Villiers Engelbrecht, L.; **Olla, C.**; Cappai, A.; Casula, M. F.; Melis, C.; Stagi, L.; Laaksonen, A.; Carbonaro, C. M. **Carbon Nanodots from an *In Silico* Perspective.** *Chemical Reviews* **2022**, *122* (16), 13709–13799. https://doi.org/10.1021/acs.chemrev.1c00864.

Carbonaro, C.M.; de Villiers Engelbrecht, L.; **Olla, C.**; Cappai, A.; Casula, M. F.; Melis, C.; Stagi, L.; Laaksonen, A.; Mocci, F. **Graphene Quantum Dots and Carbon Nanodots: modelling of zero-dimensional carbon nanomaterials.** Chapter of the book "Zero-Dimensional Carbon Nanomaterials", edited by *Elsevier* (in printing)

2.1 Introduction

The complexity of CD nature requires the combination of different experimental techniques to gain information on both its structure and optical properties for use in technological fields. However, as mentioned in **Section 1.4**, experimental methods have some limitations that may hinder a full understanding of its luminescent mechanisms. Computational methods are powerful tools in revealing these processes, investigating the levels of electrons in atoms,

molecules, and nanostructures at different scales through modern molecular modeling and providing microscopic information that cannot be obtained through experimental techniques or exceeds their capabilities.

A variety of computational methods, ranging from quantum mechanical (QM) to classical molecular mechanics (MM) simulations, have been employed at different levels of theory to understand the properties and interactions of CDs with other chemical entities. The choice of the computational method depends on various parameters such as computational cost, system size, the accuracy of the method, and theoretical and computational complexity of the property (**Figure 2.1.1**). For instance, classical modeling techniques represent a compromise between computational cost and the model size and complexity when simulating the interactions of CDs with small organic molecules and large biomolecules, as well as with the solvating environment. In contrast, QM methods are widely employed for the investigations of optical properties of smaller molecules such as pyrene, coronene, perylene, or graphene-like layers due to their generally high computational cost.

To assist both experimental and computational researchers in choosing the most appropriate and accurate method for simulating a selected CD system, and to help navigate the vast collection of literature on this topic, these two works have been undertaken. The aim is to promote the investigation of CDs and to apply virtual chemistry to gain further insights necessary for customization of these amazing systems for novel applications. This chapter will focus on the modeling of optical properties and provide a review of studies on the simulations of doped and functionalized CDs.

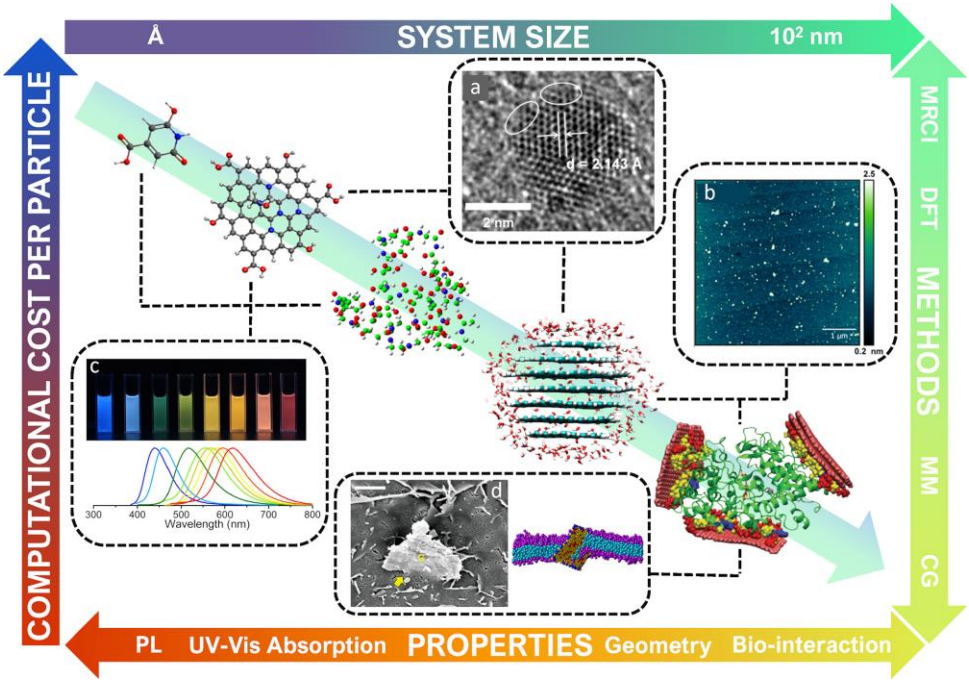

Figure 2.1.1. Examples of computational models of CDs of increasing complexity, from single molecule to molecular complex structures, and related experimental features, used to create a "road map" to find a compromised solution to perform computational studies. Original figure from our work.[50]

2.2 Computational methods for modeling optical properties of CDs: DFT and TD-DFT

QM studies are particularly relevant for their role in the investigation of the origin of CD optical features. The increasing number of works intends to reveal the peculiar mechanism of CD excitation-dependent emission, linking it to their structural and morphological properties, where both ordered and amorphous carbon structures were observed and foreseen to play a role. In those cases where the optical properties are the focus of the investigations, it is necessary to model the electronic structure and energy levels and how they are affected by the environment, and the calculations should be performed using a QM method to solve the Schrödinger equation. The choice of a particular QM method, or combination of QM methods, depends on many factors: the size of the system to be modeled, its degree of conformational freedom, the type of information to be

obtained, available computational power, the presence of benchmark calculations for similar systems, and more.

Among the quantum mechanical methods applied to the study of the optical properties of CDs, Density Functional Theory (DFT) methods are by far the most used. Compared to other QM methods, DFT methods have a greater capability of coupling reasonable accuracy with relatively low computational cost. DFT methods derive from the 1964 Hohenberg and Kohn theorems,[64] stating that all the ground-state properties of an N-electron system are uniquely determined by the total electron density (ρ). In the later Kohn–Sham DFT formulation, the total energy of the ground state is expressed as a sum of exact terms, and an important (although small) contribution to the energy is given by the exchange-correlation (XC) term E_{XC}:

$$E[\rho] = T[\rho] + J[\rho] + V[\rho] + E_{XC}[\rho]$$

where T is the non-interacting electron kinetic energy, J is the Coulomb energy, and V is the energy due to the external field generated by the nuclei. The first three terms can be computed exactly, while the exact E_{XC} functional form is not yet known except that for a uniform electron gas, and only approximate forms can be used. In the way for approximating the exact XC term, an increasing number of functionals, each one with its strength and limitations was implemented.

The simplest approximation of the XC term is the local density approximation[65] (LDA) where the energy is typically separated into an exchange and in a correlation part. While LDA has been widely used for studying bulk properties in solid-state physics, it is not appropriate to study surfaces or molecules, since it overestimates the bond energies and produces too short bond lengths.

A more sophisticated approximation, making use of both the spin densities and their gradients is GGA, generalized gradient approximation, whose parameters are obtained either by a fitting to some data sets, as in the B86 approach,[66] or derived using theoretical conditions, as in the PBE approach.[67] A broadly used variant of the GGA, largely applied to the study of the structure and properties of CDs, is constituted by the hybrid-GGA methods as the popular B3LYP, developed by Stephens[68] and co-workers.

The most used functionals in chemistry and material science are those based on the B3LYP and PBE functionals,[69] respectively. However, there are several limitations in using these functionals, such as the reproduction of dispersion

forces and the incorrect behavior of the XC functional at long-range, which have a relevant impact on the charge-transfer excitation. A promising approach is represented by hybrids functionals such as CAM-B3LYP and ωB97XD in which the XC functional is divided into short-range and long-range contributions.[70,71]

DFT methods provided information about the properties of the ground state but to give insight into excited state properties it is necessary to employ time-dependent methods. Time-dependent DFT (TD-DFT) is an increasingly popular method to treat the electronically excited states and study the optical properties of a variety of molecular and periodic systems solving numerically the time-dependent Schrödinger equation. Excitation energies, photoabsorption spectra, and frequency-dependent response properties can be calculated by analyzing the time response of the systems subject to an external time-dependent potential.[69,72]

As DFT, also TD-DFT is based on the idea of replacing the real interacting many-body electronic system with a noninteracting one having the same electron density. However, the construction of such a noninteracting system is much more complex for TD-DFT, mainly because the time-dependent effective potential at any given time depends on the value of the electronic density at all previous instances. TD-DFT is based on the theorem of Runge and Gross (RG)[73] and a time-dependent equivalent to that of Hohenberg–Kohn,[64] and for an initial electronic wave function ψ_0, it can be shown that there is a 1:1 correspondence between the time-dependent external potential $v(\mathbf{r},t)$ of a many-body system and its time-dependent density $\rho(\mathbf{r},t)$. Therefore, it is possible to write the external potential $v(\mathbf{r},t)$ as a functional of the density:

$$v(\mathbf{r},t) = v[\rho,\psi_0](\mathbf{r},t)$$

The RG theorem allows one to substitute the time-dependent many-body wave function with the corresponding time-dependent electron density. The main applications of TD-DFT are the calculations of excited states energies of isolated systems obtained under the assumption of a linear response of the electronic density, applying an external time-dependent potential.

Most investigations concerning the applications of DFT/TD-DFT methods in CD studies are focused on the simulation of CD structure and properties using small molecular models. Generally, the simulations make use of B3LYP functional and are carried out on popular easy-to-use software such as Gaussian. The target feature is in general the optical absorption since the computations of the emission properties are not always straightforward. Sometimes the density of states (DoS) or the vibrational spectra are also calculated.

Thus, the combined information from simulation and experiments is fundamental to reaching a better understanding of the CD properties, in particular when the topic is the doping/functionalization phenomenon.

2.3 Theoretical studies on doped and functionalized CDs

Given the great variety of CDs, it is difficult to choose the appropriate model for virtually mimicking their structure. Undoped CDs, whose chemical composition consists only of carbon and hydrogen (to passivate the surface), are usually employed as reference systems to rationalize the properties of more heterogeneous structures. These references can be ordered such as extended single or multiple layers of PAH or disordered as amorphous carbon structures.

It was proved that in most of these cases, the quantum conjugation effect plays a key role by inducing a redshift of the optical features as the extension of the sp^2 graphene domain increases.[23,74] Nevertheless, when considering the geometry of more disordered structures, an important role is played by the effects induced by changes in planarity, by the presence of stress, and by the changes in topology or the sp^2/sp^3 ratio.[74–78] All these studies address core and edge effects but also molecular and surface states need to be investigated in detail. The molecular model that considers molecules such as CZA, HPPT, and IPCA as possible PL centers of several bottom-up produced CDs, proves to be effective in reproducing both their absorption and emission properties.[22,54,79] But the location at the surface of the nanoparticle or within the inner structure has to be taken into account. Indeed, phenomena like aggregations are considered to affect the optical features and are recognized as possible sources of the excitation-dependent emission typically recorded.[43,44]

However, the most analyzed among the possible PL mechanisms is the surface state. The inclusion of different elements in CDs structure localized either in the core (dopants) and/or in the surface/edges (functional groups) highly influences the optical properties of these nanosized systems. The knowledge of how heteroatom positions affect optoelectronic activity would allow the design of a nanostructured material with band-gap size tailored to the specific application field. Thus, computational studies aim to overcome some limits of experimental techniques and give complementary information on the fundamental mechanisms responsible for this tailoring. An increasing number of studies were published on

this topic, combining experimental results with simulations, or performing pure theoretical calculations. In this section, literature on both GQD and CND models was included as both these systems were usually downsized to single or double graphene-like layers for model purposes. Commonly studied heteroatoms are oxygen, nitrogen, sulfur, and boron. Besides its presence in most non-doped CDs produced by bottom-up synthesis routes, oxygen can be counted among the heteroatoms in the form of carboxyl, carbonyl, hydroxyl, and epoxy groups. The synthetic route influences the type and amount of these groups on carbon structure from which not only emission properties but also solubility and biocompatibility depend on. On the other hand, nitrogen is well-known for affecting PL properties increasing the QY. Many works investigating GQD and CND properties focus on N-doping, trying to clarify the function of the incorporation of this element in the carbon network as graphitic, pyrrolic, and pyridinic nitrogen. Other dopants such as sulfur, boron, and phosphorous were also considered, including the possible co-doping with nitrogen and other elements.

The effect on optical absorption of oxygenated groups has been discussed in different papers.

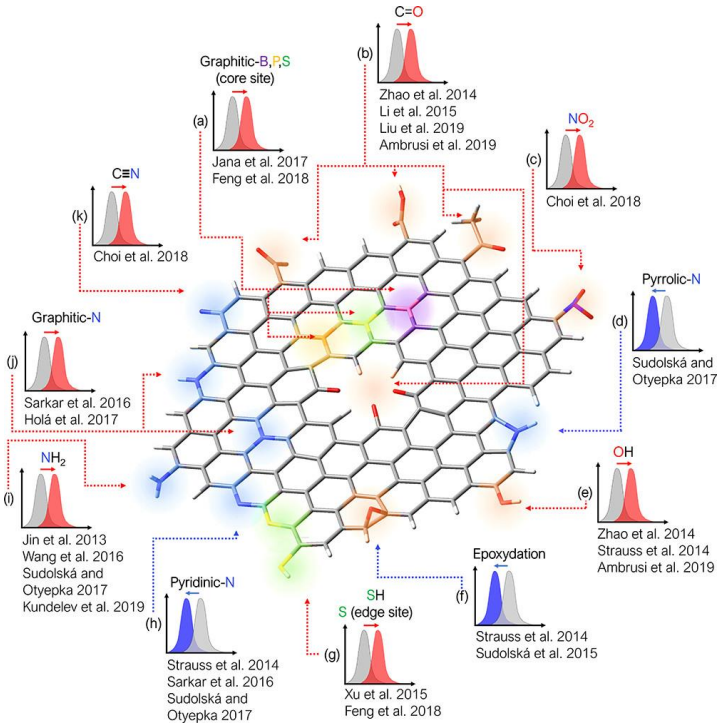

Figure 2.3.1. Computed effect on the absorption spectrum of different doping/functionalization of CNDs. CND is represented as a layer of graphene with doping heteroatoms or functional groups at the edge or within the carbon network. Original figure from our work.[50]

As reported in **Figure 2.3.1**, C=O-containing groups contribute to the shift of the absorption spectrum to longer wavelengths. Li et al.'s work,[78] exploited DFT and many-particle perturbation theories to understand the contribution to electronic and optical properties of GQDs from frontier orbital hybridization and charge transfer. The investigation shows that these two mechanisms can act both in collaboration or in opposition and the best choice for tuning these properties is the functionalization of GQDs with C=O functional groups that lead to small charge transfer and large hybridization. Supporting this point of view, Liu and co-workers[80] carried out a combined experimental and computational study on the variation of spectroscopic features due to the coupling of surface oxygenated groups and π-electron systems which produces opposite shifts of the experimental emission peaks. Indeed, as it was claimed by theoretical simulations the absorption peak was strongly blueshifted decreasing C=O content but this shift is effectively reduced increasing the C-C content and consequently, extending the delocalization of the π-electron system. Another paper supporting this thesis is the one of Ambrusi et al.[81] who focused on the interaction between CNDs, modeled as a few fused benzene rings, and silver nanoparticles. They performed a TD-DFT calculation showing that functionalizing models with -COOH and -OH brought a redshift of the optical absorption. Also, Zhao and coworkers[82] considered the contribution of COOH and OH groups on both absorption and PL spectra studying large PAH models of GQDs with different sizes and shapes. It was verified the redshift effect from COOH groups that increases with the number of groups and the same effect with OH, particularly when all the edge sites are substituted.

The presence of epoxy groups in the CND structure, instead, induces a blueshift. Sudolská et al.[45] performed a detailed TD-DFT investigation focusing on the role of oxygenated groups, stacking, and solvent interactions in the UV-Vis absorption spectrum using as models single and multilayer coronene and pyrene. This study underlines that the presence of epoxy groups on the surface of the model yields a large blueshift of the highest occupied molecular orbital-lowest unoccupied molecular orbital (HOMO-LUMO) peak. The same thesis is supported by Strauss and co-workers[75] modeling CNDs as functionalized graphene with different dimensions and number of layers. DFT and semi-empirical methods were employed to understand how structural characteristics influence optical properties. It was found that epoxidation along with the alteration of the sp^2 network causes a blueshift while hydroxylation is responsible for the redshift of both absorption and emission spectra.

For what concerns the effect of nitrogen on absorption features, in the work of Choi et al.[83] GQDs were modeled as circum-2-coronene, and it was demonstrated

that the increasing functionalization with electron-withdrawing groups such as -NO_2 and -CN provokes a redshift of the absorption spectrum.

Another important parameter that causes redshift with respect to the undoped model is the presence of graphitic nitrogen. Sarkar and co-workers[84] support this hypothesis by modeling CNDs as pyrene- and coronene-based structures and performed a TD-DFT study simulating HOMO and LUMO electronic levels and their electronic distribution from which they derived the absorption features. In this work also pyridinic, pyrrolic, and amino groups were analyzed finding no significant effect on optical properties except for a small blueshift due to pyridinic nitrogen. On the contrary, the already mentioned work of Strauss et al.[75] reports a high blueshift due to pyridinic nitrogen. Holá et al.,[85] instead, contribute to the explanation of the role of graphitic nitrogen via TD-DFT calculations. Indeed, graphitic nitrogen is supposed to reduce the HOMO-LUMO gap due to the excess of electrons injected in the unoccupied π^* orbitals of a conjugated system originating the redshift of the optical properties.

Amino group influence on optical absorption was studied by Jin and co-workers.[86] They merged experimental and computational results showing that the band gap reduces as the number of amino groups increases. The DFT simulations were performed modeling amino functionalized GQDs as 13-ring clusters with -NH_2 at the edges. Also, the work of Wang et al.[87] focused on the role of NH_2 functionalization finding the same redshift of absorption properties along with a large modification of the structure. Finally, Kundelev's work[88] reports that in addition to absorption redshift, amino groups do not affect the oscillator strength of the first radiative transition and consequently do not suppress the QY.

Absorption properties can be tailored also by S-doping and other chemical elements. Xu et al.[89] demonstrated that the presence of S, N, and S-N dangling bonds can be regarded as the origin of levels within the gap that favor charge transfer and charge recombination at the surface causing the redshift of the optical properties. Also, Feng et al.[90] work analyzes the doping of GQD by means of nitrogen and sulfur, adding to this investigation the possible contribution of boron and phosphorous using the TD-DFT method. Inner and edge doping were both considered for the calculation of absorption spectra. S and P in the inner positions lead to a clear redshift whilst just a slight blueshift is recorded with the presence of N and B. The opposite behavior was reported for edge doping being S and P responsible for the blueshift and N and B for the redshift. Finally, Jana and co-workers[91] aimed attention at the role of boron performing DFT and TD-DFT calculation on a functionalized PAH model with substitutional boron atoms or boron oxide molecules assessing that boron concentration shifts the absorption to

a longer wavelength range. The effect of heteroatoms on optical absorption properties is summed up in **Figure 2.3.1**.

The effect of doping and functional groups on emission properties has also been studied in many recent papers (**Figure 2.3.2**). The role of epoxy groups on the blueshift of the emission was confirmed by the already cited Strauss et al.[75]. The opposite outcome appears adding carboxyl groups to the model as illustrated by the already mentioned Li et al.'s[78] and Zhao et al.'s[82] works but also by Holà et al.[92] in which TD-DFT was performed on functionalized PAH models showing that a redshift of the emission maxima values are linked to the presence of carboxyl groups which move the charge towards the edges of the structure leading to a higher contribution in the optical properties.

Regarding N-doping, another paper by Sudolská and Otyepka[93] presents a TD-DFT series of calculations combined with Boltzmann averaging to study absorption and emission of CND models containing pyridinic, pyrrolic or amine nitrogen at the edge of pyrene models. It was observed that increasing the amount of nitrogen brought a larger redshift in amino models and a blueshift with pyridinic and pyrrolic functionalized models. The blueshift of the emission from pyridinic nitrogen was verified also by the previously cited Strauss et al.[75] who further reports that even epoxy groups cause a blueshift. Wang[87] and Kundelev[88] confirm the redshift caused by amino groups whilst Sarkar[84] and Holà[85] report the same effect from graphitic nitrogen. Feng[90] indeed assesses the role of different heteroatoms in the core as redshift origins whilst Chen and co-workers[94] in particular focused on the differences between the effect of ether groups in the core or in the edge displaying that only edge-oxidized models show an evident Stokes shift to longer wavelength.

To sum up, theoretical papers about the effect on the optical properties of CDs by heteroatom doping or functionalization by specific chemical groups were reported. The redshift of the HOMO-LUMO gap was ascribed to graphitic N[84,85] and edge amino groups.[86–88,93] On the contrary, pyridinic and pyrrolic N induce a blueshift of the absorption properties.[75,84,93] Regarding oxygen-related doping, carbonyl[78,80–82] and hydroxyl[75,81,82] groups are associated with a redshift while the epoxy group is reported to cause a blueshift.[45,75] Considering the influence of functionalization of the emission, it was found that the passivation with COOH groups[78,92] as well as doping with boron[90,91] or phosphor and sulfur[90] is strictly related to a redshift in emission. In the case of nitrogen, instead, a critical role is played by the exact position of the atom inside the system. While a clear redshift is reported when NH_2[87,88,93] and OH[75,82] groups are added to the system, evidence of a blueshift is presented in the case of pyridinic or pyrrolic nitrogen.[75,93]

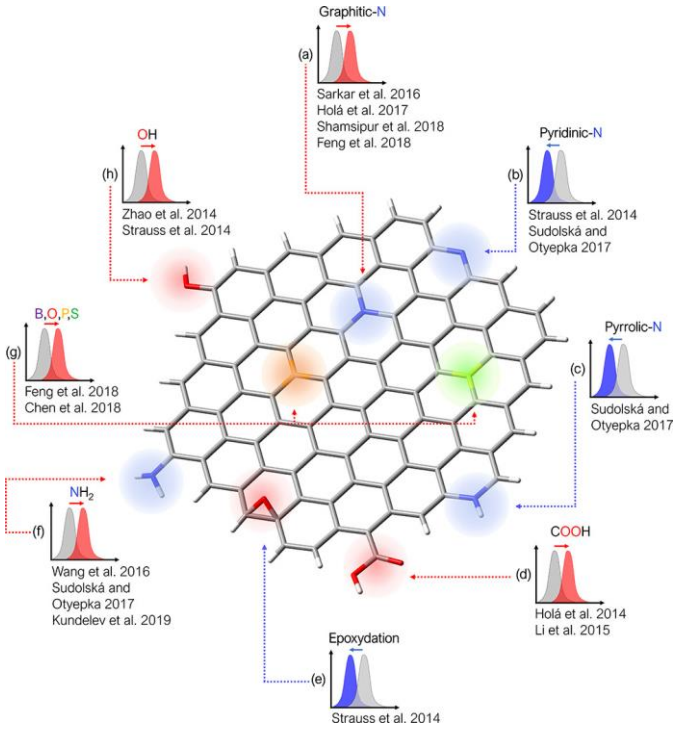

Figure 2.3.2. Computed effect on the emission spectrum of different doping/functionalization of CNDs. CND is represented as a layer of graphene with doping heteroatoms or functional groups at the edge or within the carbon network. Original figure from our work.[50]

2.4 Conclusions

The understanding of CD properties requires a comprehensive analysis performed at the levels of electrons, atoms, molecules, and nanostructures using modern computational modeling, which can be tightly correlated with experiments. Simulations can play a significant role in revealing the main features and properties of CDs, such as the aggregation of nanoparticles to tune optical properties or energy/charge transfer processes and non-radiative relaxation mechanisms. However, a clear and straightforward classification of CDs based on their core composition and structure is not yet available, which would serve as a framework for modeling investigations. At the same time, *in silico* studies can help to unravel the structural pathway during a specific synthesis and further define the boundaries of each category in the classification. It is important to note that more realistic CD models are needed, as current limitations in computing

power often lead to models for GQDs being adapted to other classes of CDs, ignoring the importance of the variable sp^2/sp^3 ratio for electronic properties.

When it comes to the photoluminescence mechanism, multireference calculations have been proposed to produce a benchmark for high computing cost systems, although a consistent and reliable method for calculating fluorescence spectra of large and complex systems like CDs has yet to be implemented. Therefore, a combination of computational and experimental methodologies is highly desirable, as it would allow for the explanation of PL mechanisms, surface functionalization, the interaction between the core and surface, and quantum confinement effects related to π-domains, all while exploring possible multipurpose applications.

Chapter 3

Analysis of Carbon Dots-silica hybrids for the tuning of optical properties

Olla, C.; Ricci, P.C.; Chiriu, D.; Fantauzzi, M.; Casula, M. F.; Mocci, F.: Cappai, A.; Porcu, S.; Stagi, L.; Carbonaro, C.M. **Selecting molecular or surface centers in Carbon Dots-silica hybrids to tune the optical emission: A photophysics study down to the atomistic level.** *Journal of Colloids and Interfaces Science* (**2022**), *634*, 402-417. https://doi.org/10.1016/j.jcis.2022.12.023

Carbonaro, C.M.; Thakkar, S. V.; Ludmerczki, R.; **Olla, C.**♦; Pinna, A.; Loche, D.; Malfatti, L.; Cesare Marincola, F.; Casula, M.F. **How porosity affects the emission of fluorescent carbon dot-silica porous composites.** *Microporous and Mesoporous Materials* (**2020**), *305*, 110302. https://doi.org/10.1016/j.micromeso.2020.110302

♦ Collaboration.

3.1 Introduction

The large panorama of possible emitting centers in CDs pinpoints the need to determine the connection between their structure and emission mechanism, also in view of proper exploitation of the resulting properties for the desired application.[95,96] To achieve this goal, a larger control on the obtained synthesis products, in terms of structure, composition, and morphology, possibly through a fast, easy, and green synthesis procedure, is required. Bottom-up routes represent an efficient method to obtain CDs in a cheaper way on large scale but make it difficult to achieve homogenous samples in size and distribution, thus requiring complex purification procedures. A valid approach consists in the production of CDs directly in porous solid-state matrices using them as nanoreactors to obtain size-selected nanoparticles.[97,98] Host matrices such as polymers,[99–102] zeolites,[103,104] MOFs,[105] silica gel,[106–109] and different mesoporous materials[110–112] provide multipotential support for the production of hybrid fluorescent materials for several purposes including room temperature phosphorescence and delayed fluorescence applications.[113–115]

Recently, we studied similar hybrid systems obtained by imbibition of mesoporous silica matrices with citrate-based CDs and focused on the optical emission change due to the interaction with the matrix.[116,117] The use of mesoporous silica as a suitable solid-state matrix for CDs is motivated, among others, by its well-known chemical inertness and high specific surface.[118,119] In this work, we investigate the properties of CDs synthesized within solid-state matrices of commercially available mesoporous silica employing a solvent-free synthesis in an open-air oven and comparing the photophysical properties of solid-state hybrids with those of reference CDs prepared without silica matrices and dispersed in water (CD-R). Using as precursors citric acid (CA) and urea, we synthesized CDs directly inside two types of mesoporous silica with different morphologies and pore sizes (commercial MCM-48, with 3 nm pore diameter, and SBA-15, with 8 nm pore diameter, S3, and S8 respectively in the following). The aim is to investigate a solvent-free solid-state synthesis,[120] exploiting silica matrices as nanoreactors to produce homogeneous CDs, avoiding complicated separation and purification procedures. Optical and structural properties of solid-state hybrids (S-CD) were measured and compared to the ones of CD-R by means of a multi-technique approach, encompassing irradiation-driven photophysics experiments and quantum chemistry simulations to verify which could be the possible emitting centers in the blue and green region and why the green ones are promoted when CDs are synthesized within silica matrix. Finally, we verified that

those optical properties tuned by the synthesis within mesoporous silica were also preserved once the CDs (CD-E) were extracted from the host matrices. Supplementary information is available in Appendix A.

3.2 Materials and Methods

3.2.1 Synthesis and Treatments

Reference nitrogen-doped CDs (CD-R) were synthesized via simple thermal decomposition of precursors in air and represent our reference sample. A 1:1 mol mixture of citric acid (1 g) and urea (0.285 g), all purchased from Sigma Aldrich, were dissolved in 10 mL of distilled water, and stirred in an ultrasonic bath for 15 minutes. Afterward, 2 mL of solution was transferred, put in a drying oven at 80 °C until the complete evaporation of water (in this sense the synthesis is defined as solvent-free), and heated in an open vessel at 180 °C for 3 hours. The upward ramp was set to 10 °C/min starting from room temperature (RT) and, at the end of the cycle, the sample was slowly cooled down since it reached RT again. Finally, we dissolved the produced powder in 40 mL of water and separated larger aggregates utilizing a centrifuge (30 min at 6000 rpm).

The synthesis of CDs directly in a matrix of mesoporous silica spheres (S-CD) was performed by drop casting the same aqueous solution of citric acid and urea upon mesoporous silica powders (MCM-48 and SBA-15, Sigma Aldrich) with different pore sizes (3 nm and 8 nm in diameter, as declared by the producer). Impregnated powders were left in a drying oven at 80 °C for about 45 minutes, allowing water to slowly evaporate (again solvent-free synthesis, water was exploited as a vector to introduce the precursors within the silica matrices), and finally put in the oven at 180 °C for 3 h, as previously described. After cooling down the hybrid samples, S3-CD and S8-CD were ready for measurements.

We also prepared silica samples soaked with the pre-formed reference CDs dispersed in water (I-CD) to compare the irradiation effects on different hybrid samples. Soaking was obtained by drop-casting 1 mL of CD water dispersion on 7 mg of bare silica powders.

To extract the CDs synthesized in silica matrices we performed a series of washing treatments in water, filtering the washed powders (filter pore size 0.22 μm) and collecting the water solution with the extracted CDs (CD-E, CD-3 and CD-8 as referred to the silica matrix exploited in the synthesis).

3.2.2 Measurements and Calculations

Structural, textural, and morphological characterization

Transmission electron microscopy (TEM) images were acquired with a Jeol JEM 1400 Plus microscope. Once dispersed in a tiny amount of n-octane the samples were dropcasted on a holey carbon-coated copper grid and let evaporate at RT.

Infrared spectra were collected by using a Bruker Vertex 70 spectrometer in the range 4000–400 cm^{-1} with a resolution of 4 cm^{-1} and 256 scans, using KBr pellets. Spectra were acquired in absorbance mode to measure the attenuated total reflection (ATR) of powders and dispersed samples.

XPS analysis was performed with a Theta Probe ARXPS spectrometer (Thermo Fischer Scientific) using the AlKα source at 70 W. The analyzer was operated in the fixed analyzer transmission mode. Three points with a spot size of 300 µm were analyzed on each sample. The residual pressure in the UHV chamber was always lower than 5×10^{-7} Pa. The binding energy scale was calibrated using the standard procedure. Sample charging was compensated by referring all binding energies to the C_{1s} signal at 285 eV. More details on experimental setup and data processing are provided by Fermo et al.[121]

N_2 physisorption experiments at 77 K were performed using a Sorptomatic 1990 System (Fisons Instrument). Prior to measurements, the samples were outgassed at room temperature for 24 hours.

Steady-state and Time-resolved optical spectroscopy

UV-Vis-NIR absorbance and reflectance spectra were collected by an Agilent Cary 5000 spectrophotometer with a spectral bandwidth of 2 nm in the 200-800 nm range. All the liquid samples were diluted with distilled water and put in quartz cuvettes with a 1 cm path length. Baseline corrections were performed on all spectra.

Three-dimensional fluorescence maps were performed using a spectrofluorometer Horiba Jobin Yvon Fluoromax-3 with a 450 W xenon lamp as the excitation source. The maps were collected with an excitation range of 300-600 nm and an emission range of 300-600 nm with a 2 nm spectral resolution for excitation and emission.

QY measurements for hybrid solid samples were carried out by comparing the light emitted by the samples to a reference dye excited at 350 nm, as described in ref [117,122], according to the following expression:

$$QY = QY_R \frac{I\ OD_R n^2}{I_R OD n_R^2}$$

where the subscript *R* refers to the reference (C120), *I* is the PL intensity of the sample, *OD* indicates the optical density evaluated at the excitation wavelength, and *n* refers to the refractive index of the relative solvent.

In the case of samples dispersed in water, QY measurements were performed by means of an integrating sphere paired with a Jasco FP-8550 spectrofluorometer at 350 and 440 nm excitation wavelengths.

As for time-resolved photoluminescence (TR-PL), the measurements were performed by exciting the samples with 200 fs long pulses delivered by an optical parametric amplifier (Light Conversion TOPAS-C) pumped by a regenerative Ti:Sapphire amplifier (Coherent Libra-HE). The repetition frequency was 1 kHz, and the PL signal was recovered by a streak camera (Hamamatsu C10910) equipped with a grating spectrometer (Princeton Instruments Acton SpectraPro SP-2300). All the TR-PL measurements were gathered by exciting the samples in the front-face mode to avoid the inner filter effect. In the case of CDs dispersed in water the solutions were placed in quartz cuvettes with a 1 cm path length. Solid hybrids were placed between transparent glass slides. Proper optical filters were applied when needed.

DFT and TD-DFT calculations

Quantum-chemistry calculations were performed using the Gaussian 16 suite of programs.[123] To model the silica matrix, we considered a cluster of 14 silicon atoms previously reported.[124,125] H or OH atoms terminated the dangling bonds of the surface Si atoms in the clusters. As for the representative emitting centers in CDs we considered different possible models: two selected molecules, the keto tautomer of CZA and HPPT molecules, which, from preliminary calculations, were more stable in water solution than the imine tautomer;[43,126] the OH and COOH functional groups at the edge of a pyrene structure (an archetypal PAH system to mimic carbon network of CDs[127]) and, finally, the presence of graphitic N within the same reference pyrene structure.

We performed a geometry optimization down to the self-consistent field (SCF) energy of each model system by means of DFT calculations carried out at the B3LYP/6-311++G(d,p) theory level.[128,129] Vibrational analysis on each optimized structure was performed to verify the absence of imaginary frequencies (the structures correspond to true local minima).

No solvent effect was accounted for since no water is supposed to be present within the silica mesoporous matrix after CD synthesis. However, to consider the possibility of some residual OH group at the silica surface some calculations were carried out by substituting the terminal H atoms of the silica cluster with 1 to 4 OH groups on the selected interaction sites with model structures. We also tested the system with full OH coverage.

To evaluate the silica-CD interaction we performed rigid scan calculations to probe the potential energy surface (PES) along a specific interaction coordinate and selected a few possible trajectories and interaction sites. Both the silica cluster model and the CD models were kept at frozen optimized positions during the scan (rigid scan procedure) to reduce the freedom degrees of the system. Once a minimum of energy in the PES was individuated, we performed TD-DFT/B3LYP/6-31G(d) and 6-311++G(d,p) calculations of that structure to calculate UV-VIS optical absorption. We also let the system relax from the fixed position minimum and re-calculated the UV-VIS features in the relaxed geometry at the same theory level.

3.3 Results and Discussion

3.3.1 Optical and structural characterization

The absorption spectrum (**Figure 3.3.1**a) of the reference CD dispersed in water (CD-R) and synthesized through the solvent-free approach here proposed reproduces the typical bands reported for citric-acid derived CDs, with a distinct contribution peaked at about 345 nm usually ascribed to n–π* transitions and a far UV band related to π–π* ones. Besides, a shoulder around 375 nm and a broad band at about 440 nm are also detected. When CD synthesis is performed within mesoporous silica and the solid-state samples are analyzed (S-CD), the relative contribution of the broad absorption band above 375 nm is largely increased compared to the main one at 350 nm recorded in CD-R dispersed in water. The gathered spectra suggest that the small shoulders peaked at about 375 and 440 nm observed in CDs in water keep their peak position and are largely increased in the hybrid samples. In addition, the S8-CD hybrid 350 nm absorption band is still resolved and larger than the broad shoulder in the blue range, whilst S3-CD near-UV band is not distinct anymore, its relative content being even lower than the blue one. These findings indicate that we should expect in hybrid samples an increase in the contribution of the emitting centers related to the absorption in the 375-450 nm range, in good agreement with our previous results.[117]

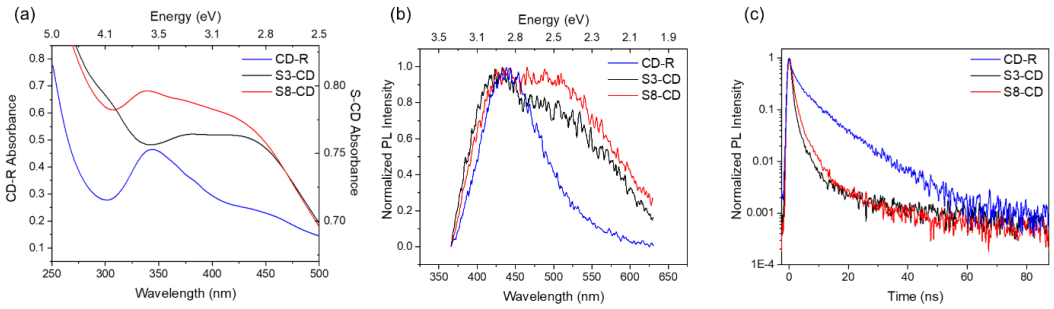

Figure 3.3.1. (a) Absorbance spectrum of CD-R and S-CD hybrids, (b) comparison of TR-PL spectra excited at 350 nm with an excitation power of 2.5 μW, (c) and the relative decay time plots in the 100 ns range. The decay time was recorded on the overall emission spectrum.

Comparing the emission features of hybrid samples to the ones of CD-R at 350 nm excitation wavelength and low laser power (2.5 μW), we indeed confirm a larger relative contribution of the green emission band (**Figure 3.3.1**b), paired with an overall reduced lifetime because of the interaction with the silica matrix and possible aggregation phenomena within the porous host (**Figure 3.3.1**c). The detailed analysis of time-resolved PL spectra (**Figure S.3.1** and **Table S.3.1**) clearly shows that, by means of deconvolution with two Gaussian bands (the fit is carried out in the energy space), a 10% larger contribution of the green band is gathered in the S8-CD hybrid as compared to the S3-CD one. The decay times display a non-single exponential profile due to a fast contribution shorter than 1 ns and a second decay in the 2-3 ns range for the S3-CD and S8-CD samples, with a further longer contribution due to the emission of the silica matrix matrix[130,131] (**Table S.3.2**, the other details are related to photo-physics experiments described in the next section). The plotted decay times refer to the whole emission recorded upon 350 nm excitation, since no significant differences within the experimental uncertainty (*vide infra*) were recorded by selecting specific emission ranges corresponding to the blue and green contributions. The overall faster decay time in hybrid samples as compared to CD-R dispersed in water causes a lower efficiency of the former (QY of about 1%), also due to the large scattering of the excitation by the hybrid powders, being the QY of CD-R of about 5%.

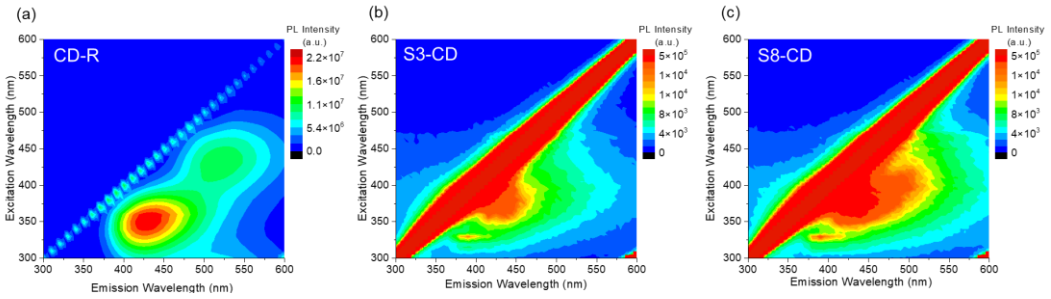

Figure 3.3.2. Excitation and Emission Maps (EEMs) of CD-R (a), S3-CD (b), and S8-CD (c).

The excitation-emission maps (EEMs) of CD-R dispersed in water and the two S-CD hybrids (**Figure 3.3.2**) confirm the scenario reported. Indeed, all the samples present two contributions, as expected from absorption measurements, but while in CDs in water those contributions are well separated and could be assigned to molecular-related centers,[22] the emission in the hybrid samples is less defined. A close inspection of the maps reveals that the common blue emission at 430 nm is mainly excited at 350 nm in water whereas in hybrids the excitation peak is shifted to 375 nm. Besides, the green emission is mainly excited at 430 nm and centered at 525 in water whilst it is excited at 400 nm and peaked at 510 nm in hybrids, particularly in the S8-CD sample which shows a larger contribution in this region. It is worth noting that the hybrid green band can be also excited in the near UV region, in opposition to CD-R dispersed in water, whose main green emission is excitable only above 410 nm. These findings suggest that the blue and green emitting centers observed in hybrids samples could be different from the ones displayed in CD-R dispersed in water. These differences can be related to the synthesis conditions (outside and inside silica), the different surrounding environments (water or silica), and the possible concentration effects realized in the hybrid samples. According to the literature,[50,132] the observed emission features could be related to intrinsic transitions, usually related to the carbogenic core, or extrinsic transitions due to the presence of dopants, surface centers, or molecular species, the latter being the most efficient ones.[101] The concentration effect is expected to be mainly relevant for the molecular emission centers, whilst less relevant for the core centers and the surface ones. Indeed, no emission could be collected from pure CD-R powders, supporting the hypothesis that concentration phenomena could be responsible for the emission quenching in silica, the interaction with the matrix allowing to observe, on the other hand, the less efficient emission transitions.

In the attempt to associate these optical differences with structural and morphological ones between our CD reference and the hybrid samples, we performed XPS and ATR measurements on CD-R and S-CD powders, along with TEM images of the samples. Once re-scaled for the contribution of silica, XPS measurements report a larger oxygen atomic content in the S3-CD hybrid (38%) at the expense of C and N content (52 and 10%, respectively), whilst the composition of the S8-CD hybrid is much alike the one of the CD reference sample (22, 64 and 14% for O, C and N respectively) with an increase of both absolute and relative to C concentration of N in the latter hybrid (**Table S.3.3**). Whilst the O_{1s} spectrum of both hybrids is due to the large contribution of silica (**Figure S.3.2**, **Table S.3.4**), C_{1s} and N_{1s} spectra allow discussing more in detail the composition in the two sets of samples (**Figure 3.3.3**).

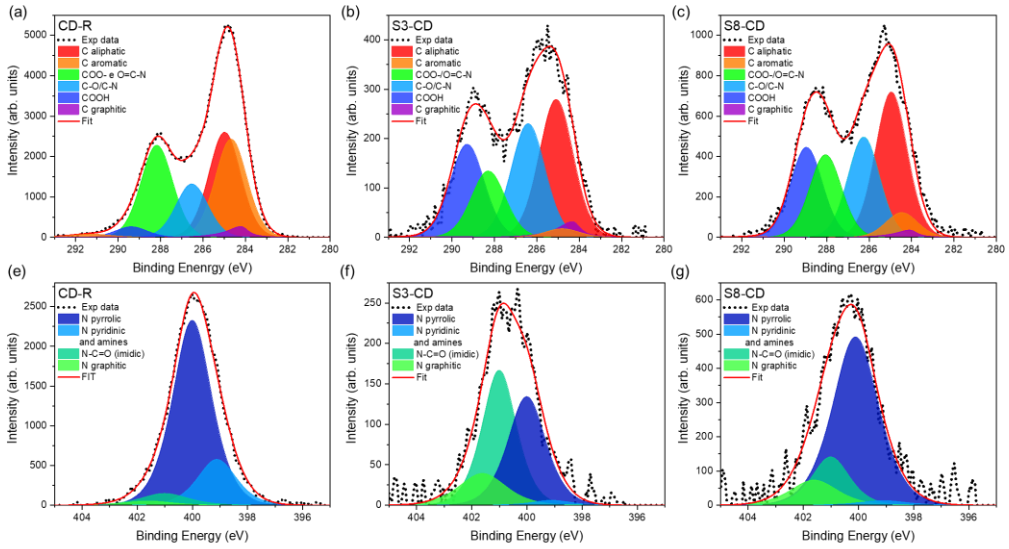

Figure 3.3.3. (top) C_{1s} and (down) N_{1s} XPS spectra. On the left of the CD reference sample, in the center of S3-CD, and on the right of S8-CD hybrid samples.

The relative content of organic carbon versus graphitic one is largely affected by the synthesis in the host matrix, being the percentage of graphitic one almost double in S3-CD than in the S8-CD hybrid, also higher than in the reference (**Table S.3.5**). These results support the idea that even matrix morphology plays an important role in the structuring of CD nanoparticles. Moreover, in contrast to the reference, silica hybrids have a larger contribution related to the presence of the carboxylic group (about 8 times) and an increase of the signal related to C-O/C-N bonds (about 1.5-2.0 times). The analysis of the N_{1s} spectrum (**Table S.3.6**) clarifies the N contribution, showing a very small content of pyridinic/aminic species in both hybrids as compared to the CD sample (1.8-1.9%

against 18.4%) and a larger content of graphitic N (14.4% and 10.8% in S3-CD and S8-CD versus 2% in CD). This is an indication that from one side no residues from urea pyrolysis are retrieved in the hybrids, from the other side those systems have a larger content of graphitic N and O-related species that calls for different CD structures compared to CD-R, where the contribution of N pyridinic molecules like CZA can be deduced. In addition, the larger content of imidic N gathered in S3-CD (44.4%) and S8-CD hybrid (16.6%) as compared to the reference, and the lower content of pyrrolic N in S3-CD than in S8-CD (39.5 and 70.7% respectively) calls for the presence of imidic HTTP-like centers and could indicate that a complete reaction toward the formation of nitrogen-incorporating emitting centers is not achieved in the former whilst is almost completed in the latter.

The effect of the nanometric size of the porous host exploited as a nano-reactor is also displayed by ATR measurements in the 1900-1500 cm^{-1} range, where the peak of C=O and C=N vibrations are recorded (**Figure S.3.3**a), whilst, excluding this range, the signal of silica matrices hid the expected contribution of other vibrations. The reported spectra display that the relative content of the broad band of the C=C bond in the reference sample (below 1600 cm^{-1}) is largely decreased in the hybrids, where two main contributions are detected at 1650 and 1725 cm^{-1}. The narrow 1725 cm^{-1} band calls for the presence of C=O stretching in aldehydes or esters, with no contribution from ketones or acids, as observed in the reference sample (the broad band with a peak at 1700 cm^{-1}). The large band at 1650 cm^{-1} is ascribed to C=N vibrations, whose relative contribution is larger in S3 hybrids than in S8 ones. These findings agree with the XPS data in suggesting that the silica nanoreactors modify the relative composition and bonding of the synthesized CDs. For the sake of completeness, **Figure S.3.3**b reports the ATR spectrum of CDs dispersed in water showing the fingerprints of the typically observed vibrations (OH, CH, CO, CN, and NH).[116]

As expected from the features of the commercial plain silica samples, TEM images (see **Figure S.3.4**) show the occurrence of mesoporous silicas with monodisperse pore size, with smaller pore size in the S3 sample as compared to the S8 sample. From TEM images of the hybrid samples (S3-CD and S8-CD, **Figure S.3.4**) it is not possible to distinctly assess the location of CDs due to the poor contrast ratio. In an attempt to image the CDs and further confirm their presence within silica matrices, we performed a washing procedure of the hybrid samples with water and collected the extracted nanoparticles. The TEM images of these CDs (CD-3 and CD-8) were compared to one of the reference CDs (that is the one synthesized without silica). As reported in **Figure 3.3.4** rounded CDs

were always observed with a size distribution affected by the interaction with the host matrix. Indeed, whilst reference CDs have a large distribution peaked at about 4.0 nm (SD = 1.1 nm), CD-3 and CD-8 samples have narrower distributions with mean diameters of 3.2 and 4.4 nm and SD = 0.7 and 0.6 nm respectively. These data confirm that the CD size distribution is affected by the features of the silica support.

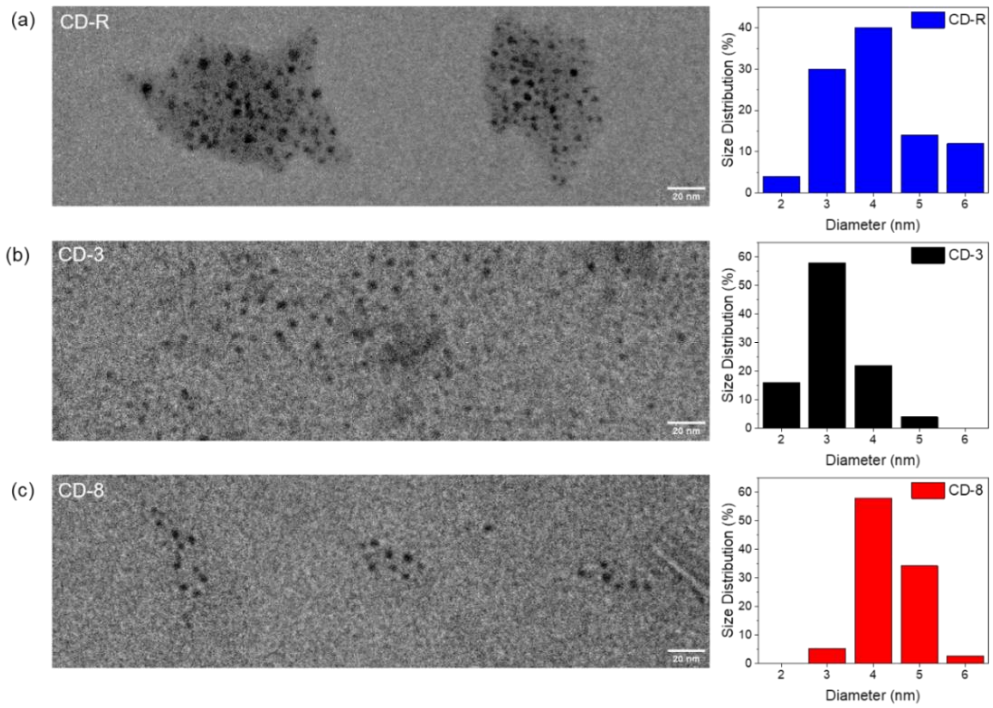

Figure 3.3.4. (left) TEM images of CD-R (a), CD-3 (b), and CD-8 (c) with their relative size distribution (right).

A textural investigation was also performed by N_2 physisorption measurements at 77 K, and the obtained isotherms for the S-CD samples (S3-CD and S8-CD) and the corresponding pure SiO_2 (S3, S8) are reported in **Figure S.3.5** and confirm the occurrence of mesoporous silicas with smaller pores in the S3-based samples as compared to S8-based samples. A significant decrease in surface area and pore volume is observed in the hybrid materials as compared to the plain silicas (see **Table S.3.7**). These findings could be due to the occurrence of CDs within the pores of the silica support.[133]

Finally, we also carried out the EEM measurements of the extracted CDs dispersed in water (**Figure 3.3.5**). The blue and the green emission centers are observed in both samples, with a larger contribution of the green emission with respect to the blue one, as compared to the reference CD samples (**Figure 3.3.2**a).

The green contribution is even larger in the CD-3 sample than in CD-8 one. The blue emission is peaked at about 450 nm with the main excitation at 365 nm in CD-3, and at 430 nm with excitation at 355 nm in CD-8. As for the green emission, it appears at 525 nm with the main excitation peak at 440 nm in both samples. Interestingly, the QY of these samples is comparable to the ones of the reference CDs, as reported in **Table S.3.8**. These data clearly show that, even though the hybrid samples have lower efficiency than the reference CD-R samples dispersed in water, the CD-E synthesized in silica display good emission properties once extracted from the host matrices, even restoring their emission efficiency when dispersed in water. Indeed, TR-PL measurements performed by exciting at 350 nm and 450 nm allow selecting a larger relative contribution of the blue and green bands, respectively, showing average lifetime comparable to the ones of the reference sample within the experimental uncertainty (see **Table S.3.9** and **Figure S.3.6**). Moreover, the estimated time constants suggest that the green emission is slightly faster than the blue one (4.9–5.6 ns vs 5.8–7.3 ns). As a further comparison, we also measured the decay time of the green emission of the hybrid samples by exciting at 410 nm, the estimated value being largely determined by the interaction with the silica matrix (**Figure S.3.7** and **Table S.3.10**). Two main considerations can be finally deduced from the above analysis: i) in the hybrid samples the decays excited at both 350 and 410 nm are always faster than the decays of the reference sample in water; ii) once the CDs are extracted from the silica matrix the estimated average lifetime is comparable to the one recorded for CD-R. Thus, the synthesis in silica allows tuning the size and the optical properties of the prepared CDs.

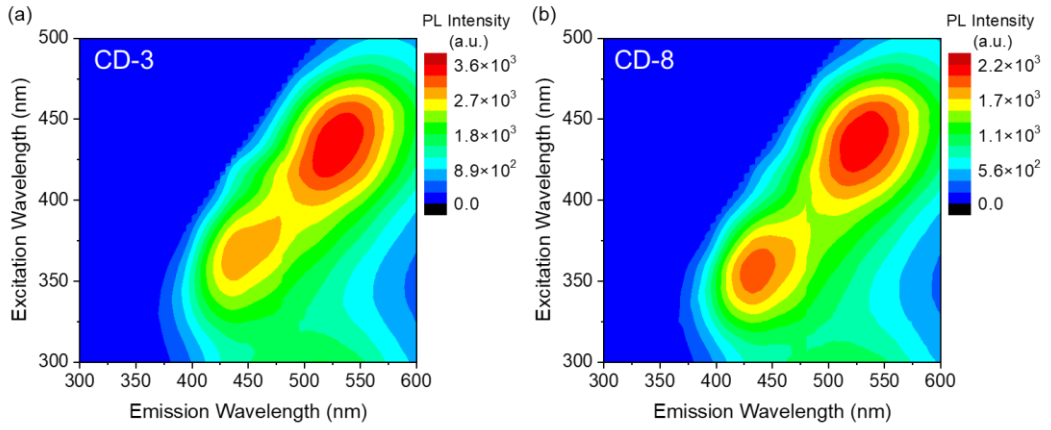

Figure 3.3.5. EEM plots of CD-3 (a) and CD-8 (b).

3.3.2 Photo-physics of CD-silica hybrids

To further discuss the emission features of CD hybrids, we carried out a series of photo-physics experiments by irradiating the samples with femtosecond pulsed and continuous wave (CW) laser light, changing both the excitation power and the irradiation time, and selecting the impinging light within the UV and blue absorption bands of the samples (at 350 nm in the pulsed case, at 405 nm for the CW one). The normalized PL spectra recorded at low and high excitation power (2.5 and 55 μW respectively, **Figure 3.3.6**) display that the relative contribution of the green band as compared to the blue one is larger for both the excitation power in S8-CD hybrids than in S3-CD hybrids.

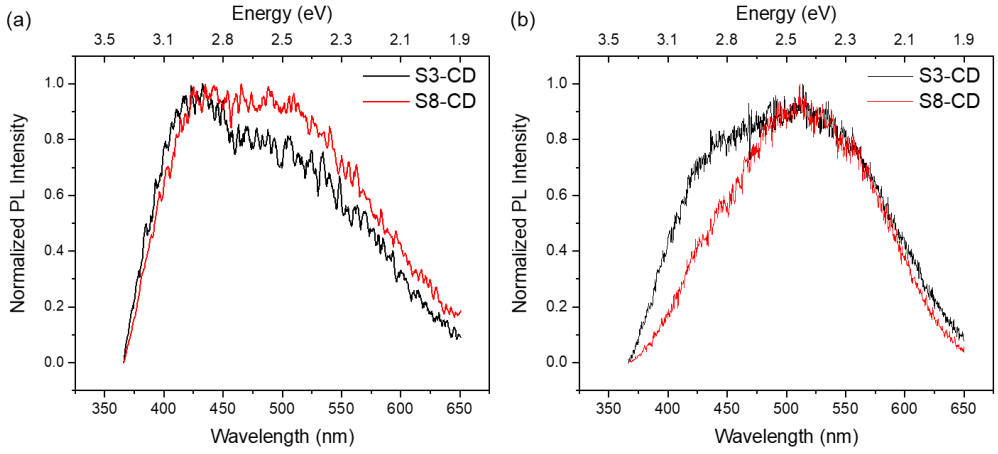

Figure 3.3.6. Normalized PL spectra of hybrid samples under 350 nm irradiation at 2.5 μW (a) and 55 μW excitation power (b).

As already anticipated, the fit of the spectra by two Gaussian bands (reported in **Figure S.3.1**) confirms the larger relative content of the green band (74% versus 64% at 2.5 μW and 66% versus 46% W at 55 μW in S8-CD and S3-CD hybrids respectively, see **Table S.3.1**). Those relative contents can be compared to the ones in the CD sample dispersed in water, where they are inverted (73% and 27% for the blue and green emission bands respectively, **Figure S.3.8**). Besides, as already noted before, the spectral features of the two bands excited at 350 nm are also quite different: the blue band is peaked at about 420 and 456 nm in the S-CD hybrids whilst at 440 nm in the CD-R in water, and the green band is centered in the 530-550 nm for the hybrids and at about 510 nm in the reference. The decay time plots (**Figures S.3.1** and **S.3.8)** confirm the interaction of CD with the silica matrix, with a net decrease of the lifetime at both low and high excitation power

as compared to CD-R dispersed in water (**Table S.3.2**). The average decay time (see **Appendix A** for details) was estimated through a non-single exponential decay fit, assuming three decays, with an experimental time resolution of about 0.8 ns over the investigated 100 ns time windows (evaluated using the signal 10%-90% rise time). The decrease in the average decay time from 7 ns to 2-3 ns in hybrid samples is due to the larger relative contribution of the fastest two decays.

The analysis of the spectrum as a function of the excitation power (**Figure 3.3.7**) indicates that the relative content of the blue band decreases as the excitation power increases suggesting some photo-activated process involving the blue and green emitting centers.

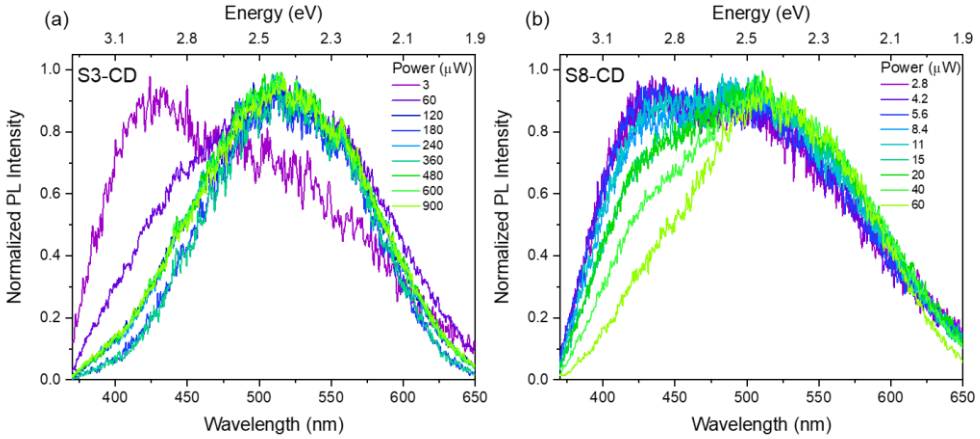

Figure 3.3.7. Effect of increasing excitation power on the PL spectra of S3-CD (a) and S8-CD (b) hybrids that underlines the reaching of the same spectral features under high power for S3-CD and low power for S8-CD.

It is interesting to note that the spectral variation is completed in the S8-CD hybrid when the irradiation power achieves 60 μW, whilst it keeps going on in the S3-CD sample up to about 200 μW. At the end of the process both the samples display an emission band peaked at about 520 nm with a reduced relative contribution in the blue range. To clarify the photo-activated process, we performed a photo-kinetic study of the hybrid samples. Indeed, the spectra in **Figure 3.3.7** were collected by shining the samples for the time required to achieve a good signal-to-noise ratio, thus representing a sort of averaged effect of excitation power and irradiation time. To follow the variation induced by the irradiation time at a fixed excitation power (2.5, 5, and 55 μW) we performed a series of acquisitions of 5 s over the irradiation time range of 500 s for the lower powers and 0.5 s over 50 s for the highest one. The spectra at the beginning of the

experiment and at the end of it are compared in **Figure 3.3.8,** showing the same trend reported as a function of the excitation power.

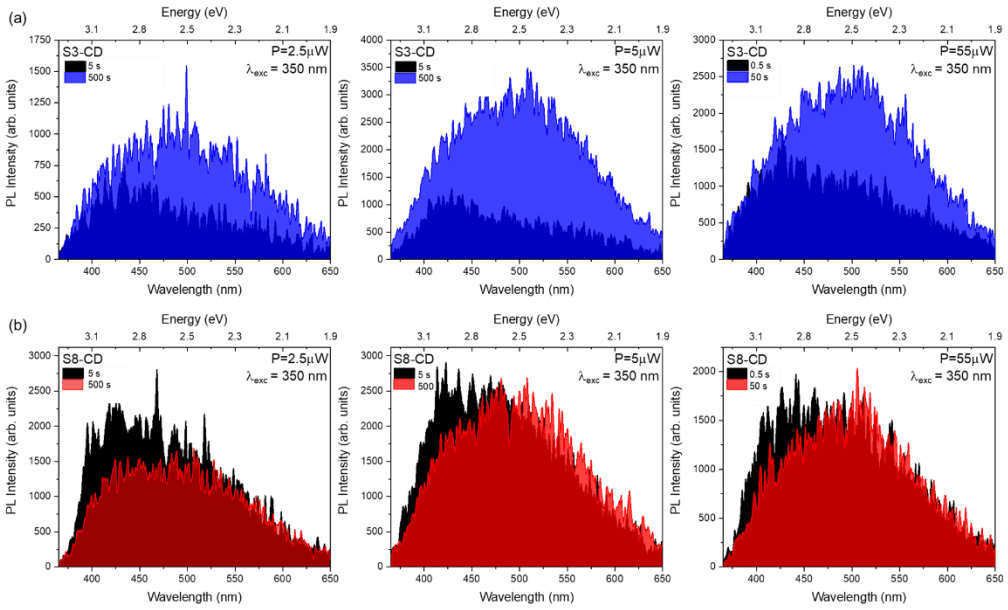

Figure 3.3.8. PL spectra of S3-CD and S8-CD hybrids obtained under varying excitation power levels (2.5, 5, and 55 μW). The spectra were collected at different time intervals, with the black spectrum obtained after 5 s at lower power values and 0.5 s at higher power, and the colored spectra recorded after 500 s or 50 s respectively (round focused spot laser was about 200 μm in diameter).

We see that the observed variation is mainly related to the increase of the green band in S3-CD hybrids whilst in the S8-CD samples the main process is the decrease of the blue band and a slight increase of the green one at the highest excitation power. The full sequence of the kinetics at 5 μW for the two hybrid samples is reported in **Figure 3.3.9**.

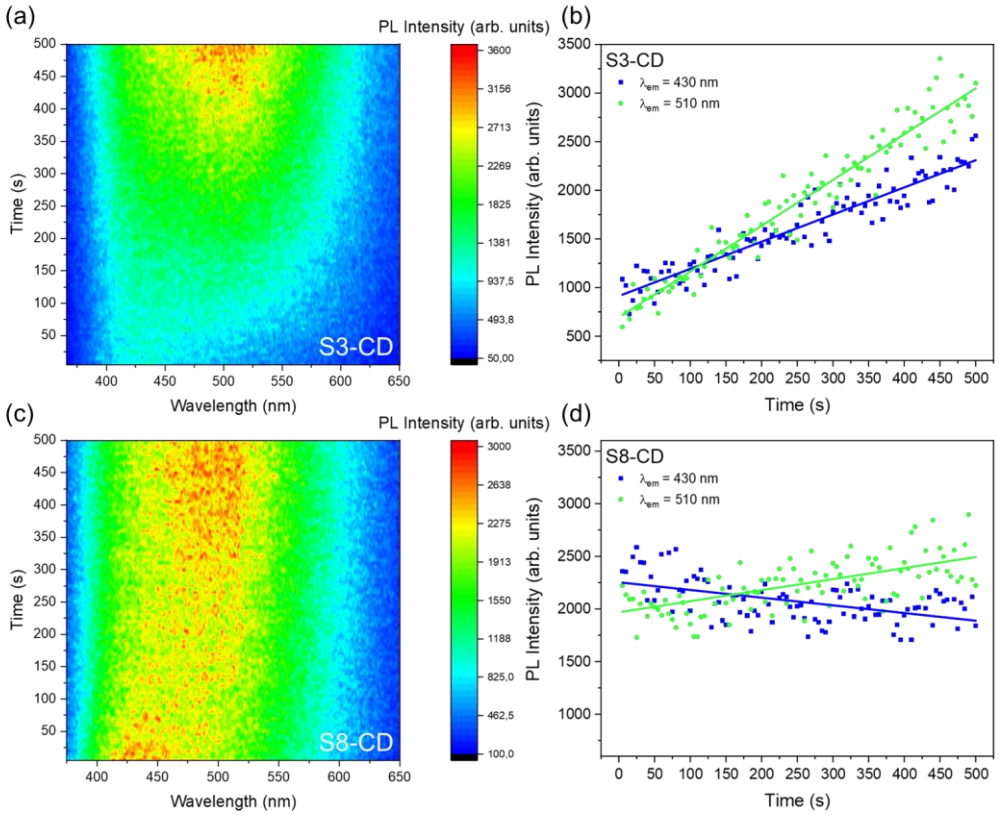

Figure 3.3.9. S3 (a) and S8 (c) CD kinetics recorded under 350 nm irradiation at 5 μW. The trend of the PL intensity VS time at selected emission wavelength for S3 (b) and S8 (d) CD samples.

The color maps display that in both cases the overall effect is a greener emission after the whole irradiation sequence coupled with an increase of the blue band in the case of the S3-CD hybrid and a decrease of the same emission in the S8-CD one. The trends are also highlighted by the plot of the PL intensity at 430 and 510 nm in both samples as a function of irradiation time. It is worth noting that all these trends are linear and in the latter case the two trends have equal but opposite slopes. We also observe that the increase rate of the green band in the case of the S3-CD hybrid is five times larger than in the case of the S8-CD one. These findings suggest that in the case of the S3-CD hybrid the irradiation promotes a larger increase of the emitting centers as compared to S8-CD samples, which could be related to the larger content of reaction intermediates observed in the former, as reported by XPS measurements. The effects of CW laser irradiation at 405 nm are also similar, as reported in **Figure S.3.9**, leading to a fast saturation effect on the S8-CD hybrids and a linear increase of the green band in S3-CD

samples. To address the origin of the photo-activated process we performed the photo-physics analysis also on the soaked samples (I-CDs). Indeed, as previously discussed, the CDs synthesized within the silica nanoreactors (S-CDs) have a different composition than the reference CDs (CD-R) synthesized without silica, and different main emitting centers were hypothesized in the two cases, calling for most molecular emitters in the latter and surface centers in the former. Thus, in the case of I-CD samples, we expect that the UV irradiation should affect the emitting molecular centers leading to photobleaching of the samples, as reported in the literature.[134]

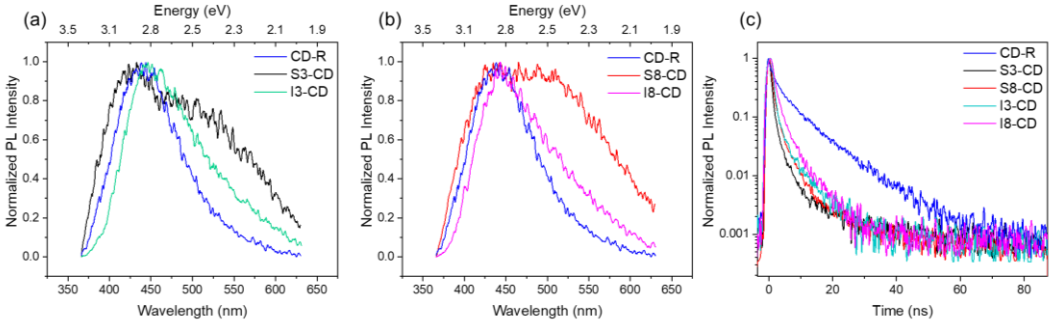

Figure 3.3.10. Comparison of PL spectra of reference CD-R dispersed in water, the S-CD hybrids, and the soaked I-CD samples in S3 (MCM-48) (a) and S8 (SBA-15) (b). Decay time plot of the samples excited at 350 nm with 2.5 μW excitation power (c). The decay time was recorded on the overall emission spectrum.

As reported in **Figure 3.3.10**, the spectral features of the emission in I3-CD and I8-CD hybrids excited at 350 nm are in between the ones of the S-CDs and the CD-R dispersed in water, showing a blue band at about 440 nm and an intermediate relative content of the green band peaked at about 510 nm. The decay time profiles are similar to the ones of S-CD hybrids, calling for the interaction with the porous matrix and concentration-related effects. The recorded kinetic map of I3-CD (**Figure 3.3.11**) displayed a large decrease in both the blue and green emissions during the first hundred seconds followed by an increase in the green emission and a constant blue contribution. In the case of I8-CD, we observed only the decrease of the two emission bands with no further modifications. Moreover, the irradiation with CW blue laser of impregnated samples causes the increase of the green band in I3-CD samples and almost no effects on the I8-CD ones (**Figure S.3.9**). The differences recorded in the two silica matrices for both the S-CD and I-CD hybrids could be related to the different content of OH groups in the two matrices, as discussed in the following Section (*vide infra*).

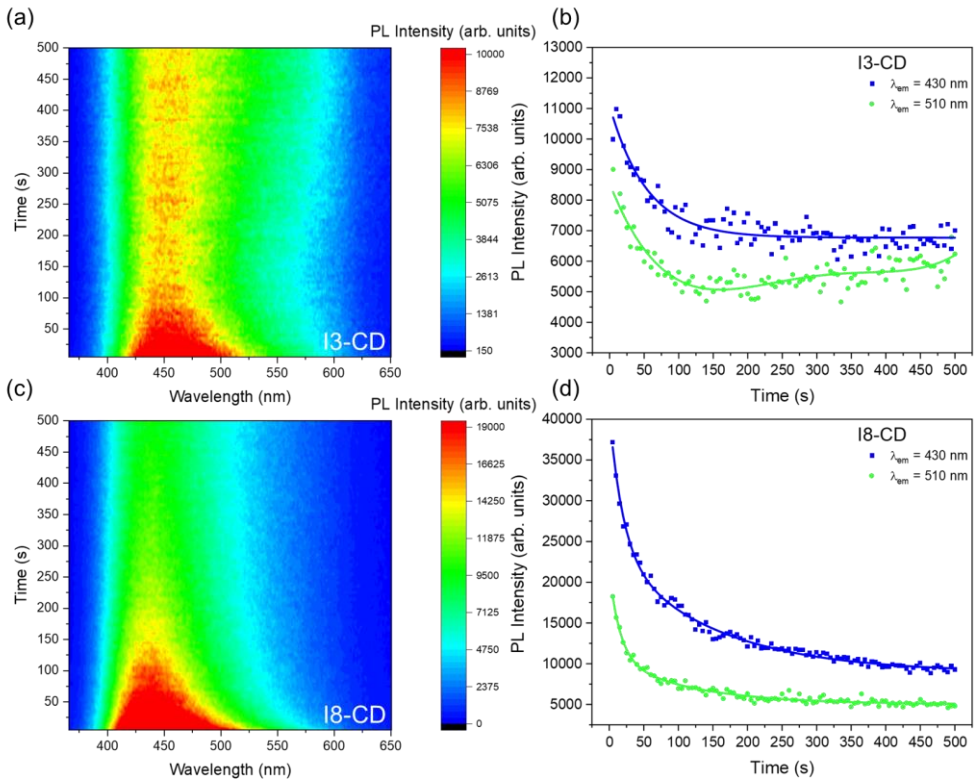

Figure 3.3.11. I3 (a) and I8 (c) CD kinetics recorded under 350 nm irradiation at 5 μW. The trend of the PL intensity vs time at selected emission wavelength for I3 (b) and I8 (d) CD samples.

To rationalize the data, we pinpoint that no variations were observed in the case of CD-R dispersed in water under different excitations powers of UV irradiation with the same experimental conditions applied for the hybrids (laser beam focused on the front face of the sample, cuvette of 1 cm for the dispersed samples). Indeed, UV photobleaching of CDs dispersed in water was reported when the whole sample was homogenously irradiated.[134] In the present case, the irradiated volume was very small, and the CDs dispersed in water could freely move around the whole cell, thus reducing the probability of being photobleached or modified by UV irradiation. The reported photo-physics effects are peculiar to the hybrid systems and the interaction of CDs with the silica host matrix. Indeed, not only did we observe a starting emission with a larger contribution in the green range as compared to the CDs in water in both the matrices, but also a larger surface photo-reactivity that further promoted the formation of green-emitting centers, eventually to the expense of the blue ones. The photo-activated process is mediated by the presence of the silica matrix, thus ascribing the recorded emission

features to surface centers interacting with the surrounding environment. The results gathered with impregnated hybrid samples further support this hypothesis, showing first a decrease in the molecular emission features and then an increase in the contribution of surface states, in agreement with previous results on CDs dispersed in water.[135] A few conclusions can be drawn from the overall reported experimental data, further considered to guide the computational work: the interaction of silica host with CDs produces a broader emission spectrum than for CDs dispersed in water, with a larger relative contribution of the green emission as compared to the blue one. The interaction with the matrix is demonstrated by the decrease of the average decay time of the emission because of non-radiative transitions mediated by the host also decreasing the overall emission efficiency. Aggregation phenomena of CDs within the silica may also decrease the global QY, in particular with reference to the molecular states. The emitting centers have different spectral features for hybrids and dispersed CDs, calling mostly for surface emitting centers in the first case and molecular centers in the second one. The structural analysis confirms this hypothesis since CDs in hybrid systems have a larger relative content of O and N as compared to CD sample in water. The larger content of O produces an increase in the OH and COOH groups, whilst the N relative increase is mainly related to a larger content of graphitic N. The comparison of the kinetics recorded under prolonged laser irradiation of S-CD and I-CD hybrids further confirms the proposed interpretation, showing that the photo-activated interaction with the silica matrix modifies the relative content of emitting surface centers in S-CD hybrids, leading to the increase of the emission in the green spectral range. In I-CD hybrids we mainly observe the photobleaching of the emitting molecular species, and eventually the increase of the surface ones.

3.3.3 DFT and TD-DFT calculations

To understand the interactions of CDs embedded in the hybrid systems, selected models of carbon dots within the silica host pores were studied by DFT and TD-DFT calculations. We considered a 14 Si atoms model of silica, already reported for simulating defects in silica,[116,124] and a set of possible CD-related systems, including OH and COOH edge functional groups on a pyrene model structure (PYR-OH, PYR-COOH, and PYR respectively), a graphitic N inside the pyrene model structure (PYR-NGRAPH) and two selected molecules, CZA and the HPPT, which could be formed during the citric acid synthesis and represent the prototype of pyridinic and imidic molecular centers (**Figure 3.3.12**). It is

known, indeed, that OH and COOH functional groups allow redshifting of the optical properties of CDs,[50,136] thus potentially contributing to the emission in the blue-green spectral range. In addition, the insertion of N in the PAH network in the form of graphitic N produces a large redshift of the pristine PAH model,[85,137] giving rise to emission in the green spectral range. For these reasons, and accounting for the experimental findings, we considered the pyrene structure as a reference PAH model and modified the system by adding an OH or COOH functional group on the edge of the pristine pyrene structure. Similarly, we inserted a graphitic N in the structure to test the formation of CDs with larger content of N within the C network. Besides, as discussed in the introduction, we considered CZA and HPPT molecules whose formation could be expected in the present synthesis, as suggested by the recorded absorption and emission features (**Figure 3.3.1** and **Figure 3.3.2**). Concerning the silica models here considered, with full H, full OH, and partial OH (1 and 4 OH) termination, the four models produced similar UV optical absorption peaked around 170 nm (**Figure S.3.3.10**). It is worth underlining that we do not consider any solvent effect in the reported calculations, since the synthesis was performed under solvent-free conditions.

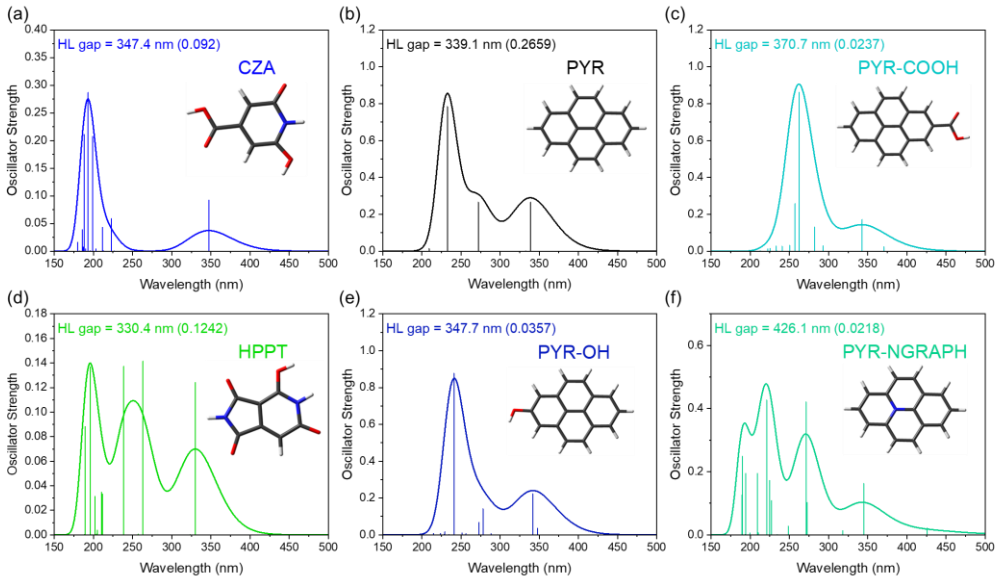

Figure 3.3.12. Calculated optical absorption features of isolated emitting center models (simplified stick representation: white stick = H atom, dark grey stick = C atom, red stick = O atom, and blue stick = N atom).

As reported in **Figure 3.3.12**, the presence of OH and COOH functional groups at the edge of our pyrene reference model produces a redshift of the HOMO-LUMO (HL) gap, from 339 nm to 347 and 370 nm for the OH and COOH group

respectively, also largely reducing the oscillator strength of the transition in both cases. These findings are in good agreement with previous results and suggest that these surface emitting centers could be responsible for a blue emission (OH) and a cyan emission (COOH) respectively, whilst the carbogenic core could be responsible for near UV-blue contributions.[117,132] The model with graphitic N shows a larger redshift of the HL gap, moving the transition up to 426 nm, thus fully supporting the possible attribution of the green emission to the presence of graphitic N.[50] However, the oscillator strength is reduced also in this case by about one order of magnitude as compared to the pristine undoped model. Concerning the two molecules, the results on CZA agree with previously reported ones,[43,126] calling for the assignment of the blue emission to this molecule when a blue molecular center is observed. Surprisingly, the results on HPPT do show an absorption transition at 330 nm, quite far away from the expected absorption at about 400 nm experimentally reported[22] and recently calculated but to a lower theory level (B3LYP and 6-31G(d,p) basis set[138]) for the anionic form of HPPT. A theoretical in-depth analysis of these results is beyond the scope of the present research and will be discussed in further work. Interestingly, both molecular species, CZA and HPPT, have larger oscillator strength than the other models here considered, thus providing more efficient emissions in the blue (CZA) and the green (HPPT) spectral range.

To mimic the interaction with the silica surface, we hypothesized a simplified model where the emitting centers are placed at the surface of the CD, either that they were molecules, like CZA and HPPT, or surface functional groups, like OH and COOH, or graphitic N within pyrene structures. The model centers can face the silica surface in a parallel or orthogonal way, assuming the centers are positioned at the CD surface as orthogonal spikes or as surface planar structures, as previously proposed.[74,139] This is clearly a simplified scheme since all the possible interaction angles between the silica surface and the centers should be considered. In addition, there are also many possible sites at the silica surface where our models can express their interaction with the matrix, thus making the configurational space of the interacting systems very large. Besides, we are not considering, as stated before, any possible homo or hetero aggregation between emitting species, which could be even favored by the CD-supporting surface.[116,118,140] Starting from the simplified assumptions made, Potential Energy Surfaces (PESs) were calculated to explore the interaction between CDs and silica along selected trajectories to specific interaction silica sites and performing rigid scan calculations, not allowing the silica network nor the emitting species to modify their structure during the scan. Finally, no PES were calculated for the

pyrene system, since the carbogenic core is expected to be not affected by the interaction with the surrounding media. As illustrated in **Figure 3.3.13** for the representative case of CZA, an energy minimum was obtained for the whole set of selected trajectories for the orthogonal relative position of the considered emitting center model with respect to the silica surface. In the case of CZA and HPPT also parallel orientation gave a minimum in the computed PES. We also calculated the relaxed geometries starting from the minima of the rigid scan PES calculations and letting the full system relax. The whole set of model systems did relax in a normal or slightly oblique position with respect to the silica surface, also the CZA and HPPT molecules when starting from the parallel one. Thus, for the configurations in the total energy minima of fixed and relaxed geometries, we calculated the absorption spectrum of the system, and the oscillator strength of the HL gap and compared the data to the results for the isolated model structures. The optical features recorded for the fixed and relaxed configurations were very similar for both the HL gap position and its oscillator strength.

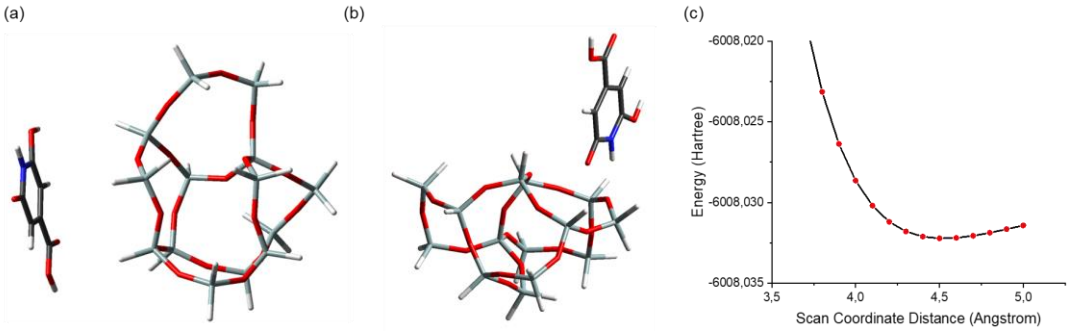

Figure 3.3.13. Schematic representation of CZA-silica relative position and PES trajectory for the parallel (a) and orthogonal (b) case. The calculated PES for the orthogonal case is reported in (c). Simplified stick representation: white stick = H atom, dark grey stick = C atom, light grey stick = Si atom, red stick = O atom, and blue stick = N atom.

The comparison of the HL gap of isolated and interacting with silica model structures, considering both fully H and OH terminated silica, shows interesting results (**Figure 3.3.14**): in general, the gap position is slightly affected by the interaction with the silica matrix but for the HPPT case, where a large redshift up to about 400 nm is recorded. Besides redshifting, the oscillator strength of HPPT interacting with silica (fully H terminated model) is slightly increased (+1.4%), like the one of graphitic N system (+1.4%). The COOH model also experiences an increase in the transition efficiency, of about +8.4%, whilst the OH model system

and CZA undergo a decrease in their oscillator strength (-25.3% and -4.5% respectively). Thus, the overall effect is an increase in the efficiency of the cyan and green emitting centers as compared to the blue ones, for both surface state and molecular state models, in very good agreement with the experimental findings. Similar results also hold for the fully OH terminated silica but for a large increase of the oscillator strength of the OH model system (+59.9%) and a decrease of the COOH system one (-8.9%) suggesting that the presence of water at the silica surface would blueshift the overall emission of CDs, as for the CDs dispersed in water.

Finally, we considered the possible presence of a few OH groups at the silica surface (1 and 4) and calculated the optical features of the system when the molecules interact with the silica surface in the nearby hydroxyl groups. The HL gap did not change so much for the OH, COOH, and graphitic N model systems, whilst a larger blueshift as compared to the full H or OH silica coverage was recorded for the CZA and HPPT molecules (**Figure S.3.11**). Besides, the oscillator strength changed a lot, in particular for the PYR-OH model system, suggesting that the interaction largely depends on the selected sites and on the eventual presence of OH groups which could promote, once again, the blue emission.

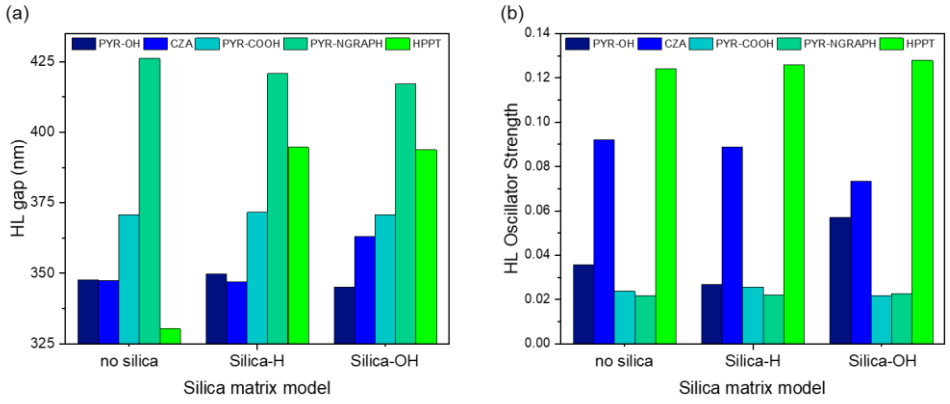

Figure 3.3.14. HL gap (left) and oscillator strength (right) for the different model structures without silica, or in presence of fully H-terminated or fully OH-terminated silica models.

To sum up all the simulations, the formation of graphitic N systems or HPPT molecules (here considered as a prototype of imidic molecular centers) can explain the observed green emission for the silica-CD hybrids, the interaction with the silica surface promoting the redshift of the HPPT HL gap, and the increase of the oscillator strength of both models. The other models here considered, OH and

COOH pyrene structures and CZA molecule, have optical features that could explain the observed blue emission (OH system and CZA) or cyan emission (COOH system) contributing to the overall emission spectrum of the hybrid systems with lower efficiency than in outside silica CDs. Despite the necessary simplifications in the studied models compared to the experimental samples, the reported computational results do explain the experimental data of CD samples in silica, where the interaction with the host matrix promotes the emission in the green range with respect to the blue one, in particular for the S8 silica. However, the presence of OH groups on the silica surface can largely affect the relative content of blue and green emissions, as gathered from the simulated interactions with silica fully or partially covered with OH groups. Indeed, the models associated with the blue emission displayed, on average, larger oscillator strength when OH groups are at the silica surface, also depending on the selected interaction site. The larger values of oscillator strength calculated for those model systems can explain the differences recorded between the two hybrid structures since a larger content of OH groups could be expected in the mesoporous matrix with lower pore volume (0.5 cm^3/g and 1.0 cm^3/g in S3 and S8 respectively) and larger specific surface area (1500 m^2/g and 500 m^2/g for S3 and S8 respectively).[141] These differences could explain from one side the different atomic content and chemical bonding observed in the two hybrids, on the other side could be also relevant for the photo-induced effects observed in the photo-physic experiments. Indeed, the hybrid samples were prepared with a solvent-free synthesis, and we should expect that no water could remain within the pores. However, some OH groups could cover the inner surface of the pores (with a larger concentration in smaller pore matrices, as explained above), thus influencing the interaction of CDs with the silica surface. According to the results of the simulations, on average, the presence of OH groups on the silica surface favors the blue-emitting model systems. Upon laser irradiation those OH groups on the silica surface could be removed, thus reducing the blue emission contributions, and promoting the luminescence of the green emitting model systems, the effect being more important in the silica matrices with larger content of OH groups at the surface.

A final comment regards the contribution of molecular and surface centers. The molecular contribution is largely quenched in silica hybrids because of aggregation phenomena. Indeed, once the CDs are extracted from the host matrices (CD-E) and dispersed in water their QY is restored, and a large green emission probably due to some imidic molecular center is observed. However, we have shown that the computed interaction with the silica matrix promotes the

green emitting centers when the content of hydroxyl groups on the silica surface is reduced and the blue emitting ones when the latter is increased. This observation holds for both the molecular and surface-emitting centers suggesting that if one could reduce the aggregation phenomena within the porous host, also the molecular centers could provide their contribution to the overall emission.[142] As a consequence, an increase in the QY of the hybrid systems could be expected because of their larger oscillator strength as compared to the surface centers. This indication agrees with the results reported to mitigate the concentration phenomena for dyes in solid-state applications[143] prompting the research on solid CDs towards an efficient mechanism of nanoparticle separation able to preserve the beneficial interaction with the supporting media.

3.4 Conclusions

The production of CDs-silica hybrids in silica matrices with different pore sizes and textures allowed discussing the formation of blue and green emitting CDs, by means of a multi-technique approach combined with quantum chemistry computations. We first assessed the possibility of producing the nanoparticles with a solvent-free synthesis, with spectral features in agreement with the ones of other solvent-mediated methods. As compared to nanoparticles dispersed in water, the hybrids show a larger relative content of the green emission which undergoes an increase under UV or blue irradiation, in particular for the matrix with smaller pores and larger interconnection. Higher content of graphitic N, O-related species, and imidic groups and a lower content of pyridinic one was measured in both hybrids as compared to reference CDs, suggesting that the nano-reactors favor the inclusion of N atoms within the C network of the nanoparticles and change the relative content of molecular centers. The reported analysis calls for a different distribution of emitting states in the hybrid samples as compared to the CDs dispersed in water, also related to the environment surrounding the nanoparticles: in the first ones we mostly observe the emission from surface centers, and in the second ones mostly from molecular centers. Indeed, the concentration effect of nanoparticles within the host matrix further reduces the contribution from molecular centers in the hybrid samples. This hypothesis is confirmed by the investigation of the hybrids prepared by imbibition of reference CDs into the silica matrices, the photo-physics experiments displaying a large decrease of the overall molecular emission followed by the increase of the surface center contribution. The larger efficiency of the green emitting centers in silica as

compared to the blue emitting ones was explained by performing quantum chemistry calculations on the interaction between silica surface and possible models of fluorescent centers, like OH and COOH surface groups, graphitic N, and citric acid-based prototype molecules, namely CZA and HPPT. The analysis of the computed optical features of the interacting systems confirmed that the host-guest interaction can affect both the spectral features and the efficiency of their transition. Indeed, the HL gap of HPPT is redshifted because of the interaction with the silica surface, and the oscillator strength of the cyan (COOH) and green emitting centers (graphitic N and HPPT) is increased, whilst the efficiency of the transitions of the blue emitting centers (OH and CZA) is decreased. Thus, the overall effect is promoting green emission, as experimentally observed. Computational results also indicate that the presence of OH groups on the silica surface can modify this overall effect, boosting the efficiency of blue emitting centers and further confirming the active role of the silica surface in tuning the optical properties of embedded CDs. Finally, the CD extracted from the silica matrices and dispersed in water restored their quantum yield and displayed a larger molecular-like green contribution. The simulations also indicate that if proper strategies to overcome aggregation phenomena are applied, the interaction with the silica matrix would be advantageous also for the more efficient molecular centers. Despite the low efficiency of the synthesized hybrid systems, mainly due to aggregation phenomena, we have shown that the mesoporous silicas are useful as nanoreactors and active support to host CD nanoparticles, exploitable as a lever for tuning the size and optical properties of CDs for both in solution and solid-state applications.

Chapter 4

Insights into Bare and N-doped Carbon Dots from citric acid

Olla, C.; Ricci, P.C.; Chiriu, D.; Fantauzzi, M.; Casula, M. F.; Mocci, F.: Cappai, A.; Porcu, S.; Stagi, L.; Carbonaro, C.M **Exploring the impact of nitrogen doping on the optical properties of Carbon Dots synthesized via citric acid pyrolysis** (submitted to *Nanomaterials*)

4.1 Introduction

Nowadays, a common methodology for the production of CDs involves the thermal degradation of citric acid and nitrogen sources. The reconstruction of the reaction involving only citric acid is challenging as it was demonstrated to form few fluorescent intermediates by itself which can be responsible for the luminescence properties of citrate-based CDs.[51] Highly efficient blue-emitting CDs can be obtained from the synthetic route of citric acid and different nitrogen sources such as ethylenediamine (EDA) and urea, whose reactions are assessed to produce fluorescent 5-Oxo-1,2,3,5-tetrahydroimidazo-[1,2-α]-pyridine-7-carboxylic acid (IPCA) and citrazinic acid (CZA, 2,6-dihydroxyisonicotinic acid),

respectively.[54,144] The reaction of a mixture of citric acid and urea could be considered even more complicated as it is known for producing according to their molar ratio not only CZA but also green emitting 4-hydroxy-1H-pyrrolo[3,4-c]pyridine-1,3,6(2H,5H)-trione (HPPT).[22] However, nitrogen can enter in CD structure in different ways. Indeed, N-doped CDs can contain embedded moieties, surface functional groups (amines and amides), and heteroaromatic rings (pyridinic, pyrrolic, and graphitic nitrogen) deeply changing the original citrate-based structure.

In this work, we will provide a detailed study of the similarities and differences recorded between CDB (bare CDs) obtained from the use of only citric acid and CDN (N-doped CDs) synthesized from a 1:1 molar ratio mixture of citric acid and urea. The employment of different techniques, from structural to spectroscopic ones, accompanied by simulations based on the experimental results, can help to understand the deep structural differences and the consequent different PL mechanisms that are involved in those cases. Supplementary information is available in Appendix B.

4.2 Materials and Methods

4.2.1 Synthesis and Treatments

Bare CDs (CDB) and nitrogen-doped CDs (CDN) were synthesized via thermal decomposition of precursors in the air. Only citric acid (1.000 g) for CDB and a 1:1 molar ratio of citric acid and urea (0.285 g) for CDN, all purchased from Sigma Aldrich, were dissolved in 10 mL of distilled water and stirred in an ultrasonic bath for 15 minutes. Subsequently, 2 mL of each solution was transferred and put in a drying oven at 80 °C until the complete evaporation of water. Each sample was heated in an open vessel at 180 °C at different times (1, 2, 3, 5, and 10 hours) to study the ideal time range for this synthesis temperature. The upward ramp was set to 10 °C/min starting from room temperature (RT) and, at the end of the cycle, the samples were slowly cooled down since they reached RT again. Finally, we dissolved each sample in 40 mL of water and separated larger aggregates using a centrifuge (30 min at 6000 rpm).

4.2.2 Structural and morphological characterization

The morphostructural features were assessed by X-ray diffraction (XRD) measurements by means of a Panalytical Empyrean diffractometer equipped with an X'Celerator linear detector. The scans were collected within the range of 7−40° (2θ) using Cu Kα radiation.

Surface Enhanced Raman Spectroscopy (SERS) measurements were performed in backscattering geometry with a confocal micro-Raman system (SOL Confotec MR750) equipped with a Nikon Eclipse Ni microscope. Samples were excited with a 532 nm laser diode (IO Match-Box series) and the spectral resolution was 0.6 cm^{-1}. SERS supports were ITO glasses coated with silver nanoparticles (S-Silver SERS substrates, Sersitive, Warsaw Poland).

Transmission electron microscopy (TEM) in both conventional and high-resolution mode was performed on a Jeol JEM 1400 Plus and Jeol JEM 2010 microscope, respectively. Once dispersed in a tiny amount of n-octane the samples were drop casted on a holey carbon-coated copper grid and let evaporate at RT.

XPS analysis was performed using a Theta Probe ARXPS spectrometer (Thermo Fischer Scientific) with the AlKα source at 70 W. The analyzer was operated in the fixed analyzer transmission mode. Three points with a spot size of 300 μm were analyzed on each sample and the residual pressure in the UHV chamber was always lower than 5×10^{-7} Pa. The binding energy scale was calibrated using the standard procedure. Sample charging was compensated by referring all binding energies to the C1s signal at 285 eV. More details on experimental setup and data processing are provided in Fermo et al.[121]

Infrared spectra were collected by using a Bruker Vertex 70 spectrometer in the range 4000–400 cm^{-1} with a resolution of 4 cm^{-1} and 256 scans, using KBr pellets. Spectra were acquired in absorbance mode to measure the attenuated total reflection (ATR) of dispersed samples.

4.2.3 Optical characterization

UV-Vis-NIR absorbance and transmittance spectra were collected by an Agilent Cary 5000 spectrophotometer with a spectral bandwidth of 2 nm in the 200-800 nm range. All the liquid samples were diluted with distilled water and put in quartz cuvettes with a 1 cm path length. Baseline corrections were performed on all spectra.

QY measurements were performed by means of an integrating sphere paired with a Jasco FP-8550 spectrofluorometer at 350 nm excitation wavelength.

Three-dimensional fluorescence maps of CDs dispersed in water were performed using a spectrofluorometer Horiba Jobin Yvon Fluoromax-3 with a 450 W xenon lamp as the excitation source. The maps were collected with an excitation range of 225-600 nm and an emission range of 225-600 nm with a 2 nm spectral bandwidth for excitation and emission.

As for time-resolved photoluminescence (TR-PL), the measurements were performed by exciting the samples with 200 fs long pulses delivered by an optical parametric amplifier (Light Conversion TOPAS-C) pumped by a regenerative Ti:Sapphire amplifier (Coherent Libra-HE). The repetition frequency was 1 kHz, and the PL signal was recovered by a streak camera (Hamamatsu C10910) equipped with a grating spectrometer (Princeton Instruments Acton SpectraPro SP-2300). The solutions were placed in quartz cuvettes with a 1 cm path length. Proper optical filters were applied when needed.

A pump and probe system (Ultrafast Systems HELIOS-80000-UV-VIS-NIR coupled with a CCD camera) was exploited for transient absorption measurements. A train of laser pulses obtained by a regenerative Ti:Sapphire amplifier Coherent Libra-F-1K-HE-230 to produce 200 fs pulses at 800 nm with a kHz-repetition rate. From the train of laser pulses, the pump and probe beams were generated, the former in the 300-800 nm range by means of an optical parametric amplifier (TOPAS-800-fs-UV-1), the latter as a white super-continuum pulse by means of a sapphire plate. The two pulses, properly delayed in time, were focused on a 1 mm quartz cuvette containing a dispersion of CDs with OD <0.5. All measurements were carried out at room temperature and no pump-intensity-dependent dynamics were observed at the selected excitation wavelength (in the 0.1-0.6 mJ/cm^2 range).

4.2.4 DFT and TD-DFT calculations

Quantum-chemistry calculations were performed using the Gaussian 16 suite of programs.[123] We performed a geometry optimization down to the self-consistent field (SCF) energy of each model system by means of DFT calculations carried out at the B3LYP/6-311++G(d,p) theory level.[128,129] Vibrational analysis on each optimized structure was performed to verify the absence of imaginary frequencies (the structures correspond to true local minima). To account for the interaction of simulated structures with water, the self-consistent reaction field model was considered to include the solvation effects. The dielectric solvent was simulated

through the polarizable continuum model calculation within the integral equation formalism (IEFPCM).[145] No imaginary frequencies were calculated for all the optimized ground state structures in the vibrational spectra, thus assuring that the simulated structures were real energy minima. TD-DFT calculations at the same level of theory (B3LYP/6-311++G(d,p)) were carried out on the optimized groud-state structures to evaluate the UV-Vis optical absorption.

4.3 Results and Discussion

The absorption spectra and the integrated emission intensity at two different excitation wavelengths were considered to assess the most luminescent materials among a set of bare carbon dots (CDB) and N-doped ones (CDN) obtained by changing the synthesis time (**Figure 4.3.1**). The typical absorption pattern of citric acid-based carbon dots is displayed for all samples, with the π–π* transition band at about 235 nm and the n–π* one at about 350 nm. Besides these contributions, a further shoulder is recorded in the 400-500 nm range in CDN samples which is not clearly observed in the CDB ones. Exciting the samples in the main absorption regions (350 nm and 410 nm), PL spectra were recorded for all samples (details in the following paragraphs). The inset shows that the maximum of the integrated emission is recorded for both sets after 2-3 hours of pyrolysis. This is in good agreement with the previous results of Ehrat et al.[146] so that, in the following, we consider only the samples prepared with 2 or 3 hours of thermal treatment, for the CDB and CDN samples respectively.

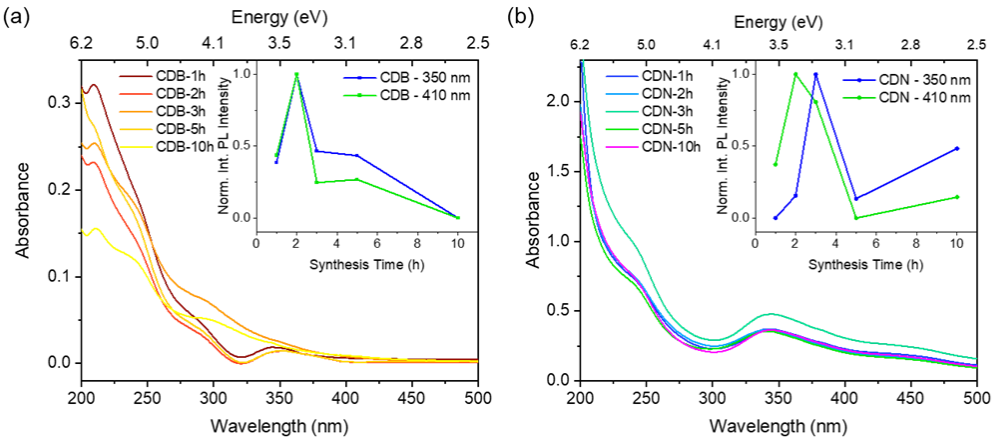

Figure 4.3.1. Optical absorption spectra of CDB and CDN samples obtained at different synthesis times. Inset: normalized integrated photoluminescence of CDB and CDN samples excited at 350 and 410 nm.

Structural analysis of the samples was performed by employing a multi-technique approach. The XRD patterns of bare and N-doped CDs are reported in **Figure 4.3.2**. The two broad 2θ peaks at about 17° and 26°, corresponding to 5.5 and 3.5 Å, indicate the highly disordered structure of the samples, with spacing similar to the ones of graphite with stacking faults (turbostratic carbons).[147,148] It is noted that the contribution at about 26° can be separated only in the CDN samples, suggesting an even larger disorder possibly induced by the presence of N. This is also confirmed by Raman spectra in the 1000-2000 cm^{-1} region. The spectra were collected by the SERS technique, allowing the detection of the vibrations up above the fluorescence signal. The two main bands for both CDB and CDN are the well-known D and G bands peaked at about 1350 and 1600 cm^{-1} and are generally ascribed to sp^3 and sp^2 hybridized C-structures.[149,150] The D band is associated with disordered graphite or glassy carbon whilst the G band corresponds to the E_{2g} mode of graphite, thus being associated with crystalline structures. The ratio between the intensities of the two bands is exploited to evaluate the disorder/crystalline ratio in the samples (I_D/I_G). The reported data indicate a larger degree of disorder in N-doped CDs ($I_D/I_G \approx 1$ in CDN and 0.6 in CDB), confirming the XRD results. We point out that the reported ratio in the case of CDN is in good agreement with previous results on microwave synthesized samples,[117] confirming that the applied solvent-free synthesis can produce nanoparticles with structural features similar to the ones in the literature. Besides the two D and G main bands, the spectra present several narrow peaks, mostly displayed in the CDB pattern. Comparing the spectra with the Raman of CA in an aqueous solution,[151] no fingerprints of pure CA have been identified pointing out the complete transformation of the precursor in some other molecular species. One of these expected species is CZA whose formation during the synthesis of CDN is suggested by vibrational modes at 934 and in the 1700-1750 cm^{-1} region.[43,126,137] Indeed, the large sensitivity of the SERS technique evidences a rich structured molecular-like spectrum over imposed upon the D and G bands in both CDB and CDN related to the presence of possible molecular fluorophores in the structure of both samples.

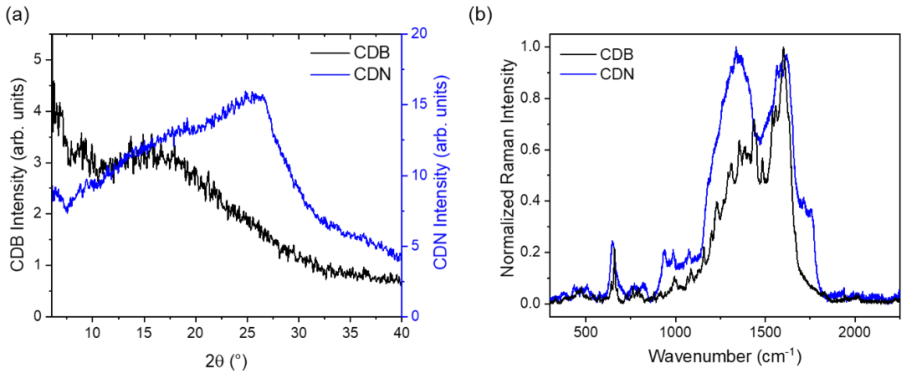

Figure 4.3.2. XRD patterns (a) and SERS spectra (b) of CDB and CDN samples.

TEM images (**Figure S.4.1**) report rounded nanoparticles for both samples with a mean diameter of 4.5 nm (SD = 1.4 nm) for CDB and 3.6 nm (SD = 0.9 nm) for CDN. No clear crystalline planes were detected by HRTEM (not reported), even in the CDB samples that, according to Raman indications, should have a larger content of sp^2 C atoms.

As suggested by XRD and Raman results, a rich gallery of atomic species and structures is expected, as typically reported in bottom-up prepared CD systems.[152] XPS allowed for estimating the relative content of C, O, and N atomic and assessing their binding features. The elemental composition of our samples is mostly constituted by C atoms (74% for CDB and 67% for CDN) whilst the remaining is completely oxygen in CDB (26%) and mostly oxygen (21%) and partly nitrogen (12%) in CDN (**Table S.4.1**). The original atomic ratio of these elements in the reagents was calculated to be 0.8 for C/O and 3.4 for C/N but the higher experimental values in all cases suggest that part of the oxygen and nitrogen had been released during the pyrolysis. The analysis of C_{1s} signals (**Figure 4.3.3**a-b, **Table S.4.2**) provides a detailed overview of the carbon species displaying a relatively similar content of aromatic (31.2 and 27.4%, for CDB and CDN, respectively) and aliphatic carbon (30.6% for CDB and 28.2% for CDN) for the two samples but a much higher content of graphitic (7.5% against 2.8%) and COOH (15.2% against 2.8%) species in CDB. Indeed, the deconvolution of the spectra shows a generally higher amount of organic C species compared to graphitic one, with a C_{org}/C_{graph} ratio of 12.4 and 35.4 in CDB and CDN respectively, confirming the XRD and Raman structural indications that pointing at a larger disordered contribution for the latter sample. Distinguishing between C-bonds with O or N in CDN samples by accounting for only the C_{1s} signal is quite challenging since C-O binding energy falls in the same region as C-N and

the same happens for COO- and O=C-N. The investigation on the N_{1s} spectrum helps us clarify this point (**Figure 4.3.3c, Table S.4.3**). In fact, different kinds of N-bonding were retrieved at the peak at about 400 eV of N_{1s}, including pyrrolic (74%), pyridinic/aminic (18.4%), graphitic, and imidic (2.0% and 5.7% respectively). Concerning O_{1s} spectra at about 532 eV (**Figure 4.3.3**d-e, **Table S.4.4**), besides a detected 10% due to the presence of water, a similar contribution for C=O/O-C=O (46.2%) and C-O-H/C-O-C (43.7%) bands were observed in CDB. The same contributions in CDN are generally decreased (37.8% for C=O/O-C=O and 20.3% for C-O-H/C-O-C) in favor of amidic and imidic oxygen species (41.8%).

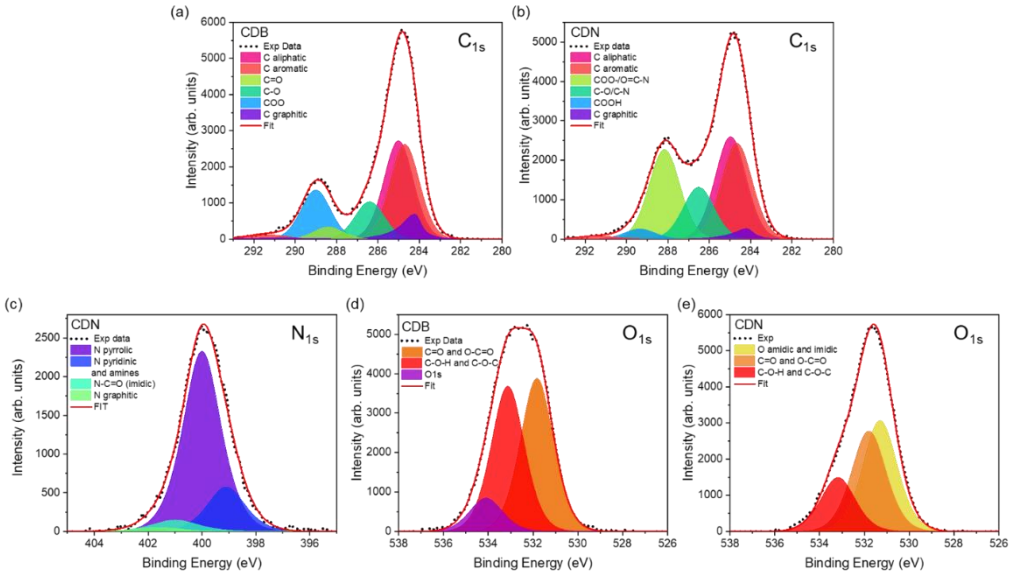

Figure 4.3.3. (top) C_{1s} and (down) N_{1s} and O_{1s} XPS spectra of CDB and CDN samples.

To get some additional hints on the functional groups, Fourier-Transform Infrared measurements in the attenuated total reflection (ATR) mode were carried out, and the expected -OH, C=O, C-N, -NH, and -CH groups were identified (**Figure 4.3.4**). We can observe that both the samples present a structured and broad absorption band in the 2000-3500 cm^{-1}, due to OH and NH stretching vibrations, at 3400 and 3200 cm^{-1} in CDNs, and to CH ones at 2935 and 2655 cm^{-1} in CDBs, also coupled with the sp^3 and sp^2 bending at 1413 and 918 cm^{-1} respectively. The fingerprinting region is in the 1800-900 cm^{-1} range and displays different relative contributions of the identified groups in the two samples. It should be noted that all the gathered peaks are in general quite broad, probably due to significant H-bonding between functional groups or molecules.[38] In particular, in the 1800-1700 cm^{-1} range, where C=O vibrations are identified, three

peaks at about 1760, 1725 and 1700 cm^{-1} can be ascribed to C=O stretching in ketones (1760 cm^{-1}), aldehydes, and esters (1725 cm^{-1}) or acids (1700 cm^{-1}), the relative contribution of the former two being larger in CDB samples. On the other hand, the presence of N-related vibrations, C=N and C-N in aromatic amine, at 1650 cm^{-1} and in the 1450-1350 cm^{-1} range, is observed only in the CDNs. Interestingly, the relative content of the C=C stretching mode, referred to as the 1700 cm^{-1} vibration, is larger in CDN than in CDB samples, confirming the XPS results on the C organic versus C graphitic ratio. Finally, the peaks in the 1300-1100 cm^{-1} are assigned to C-O alkoxy or phenyl vibrations.

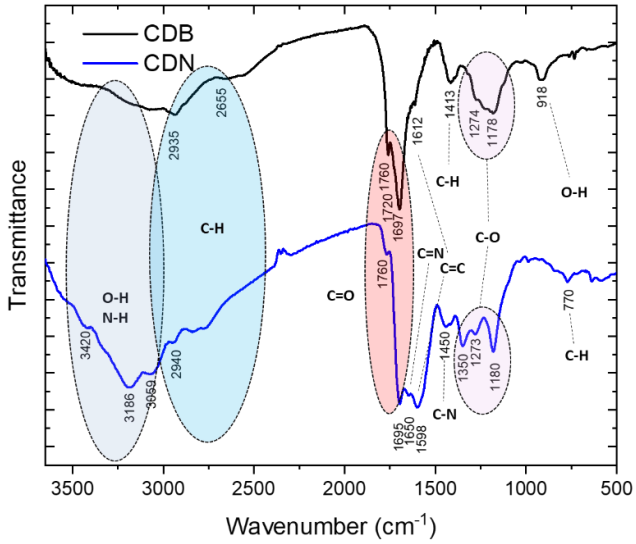

Figure 4.3.4. ATR spectra (transmittance mode) of CDB and CDN samples.

Both XPS and FTIR measurements point to a large decrease in C=O contributions in N-doped CDs as compared to bare ones. The O_{1s} spectra show the expected contribution of the N-related groups in CDNs (amidic and imidic), and the vibrational spectra display a large decrease in the relative content of aldehydes and esters. Thus, the introduction of N allows the reduction of O-containing functional groups at the surface of CDs and the formation of pyrrolic and pyridinic species, besides graphitic N in the carbon network.[146,153]

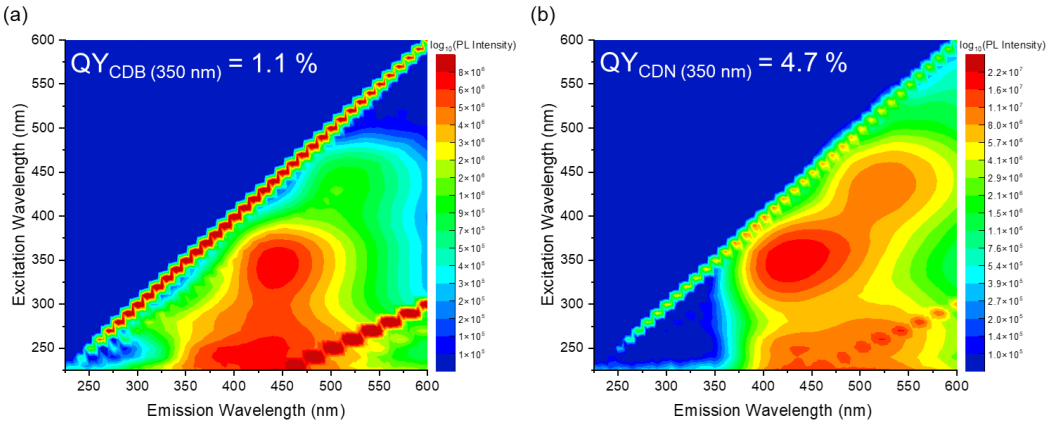

Figure 4.3.5. Excitation emission map of CDB (a) and CDN samples (b).

The excitation/emission maps (EEM) of CDB and CDN samples are reported in **Figure 4.3.5**, along with their QY values which result to be 1.1% and 4.7% for CDB and CDN, respectively. The maps show in both cases the presence of two emitting centers, one in the blue and the other in the green spectral range. In CDB, the blue contribution peaked at 445 nm can be excited both in the far (245 nm) and in the near (345 nm) UV region whilst under blue excitation wavelength (440 nm) a green luminescence (520 nm) is observed. Similar findings are reported for the CDN sample where the blue band peaked at about 430 nm is mainly excited by UV excitation at 350 nm with an excitation shoulder at 250 nm. The green band is centered at about 520 nm and is mainly excited at 430 nm, with another smaller excitation band in the same UV range as the blue one. Due to the combined spectroscopic features of these centers, both samples are characterized by the typical excitation-dependent emission with the PL peak redshifting as the excitation wavelength increases.

To delve into the nature of these centers, synchronous fluorescence (SF) spectra were extracted from EEM maps. This method is used for the identification of multiple emitting centers in the sample as it shrinks the bands by keeping a constant difference ($\Delta\lambda$) between the excitation and the emission wavelength. An example of the peculiar PL spectra obtained with this procedure is shown in **Figure 4.3.6a** for CDB (inset) and CDN where each point represents the emission (λ_{em}) intensity obtained by exciting the sample at an excitation wavelength equal to λ_{em}–$\Delta\lambda$. Several spectra were collected by changing $\Delta\lambda$ and from each of them, we recorded the positions of the main peaks and plotted them as a function of the relative offset as reported in **Figure 4.3.6b-f**.

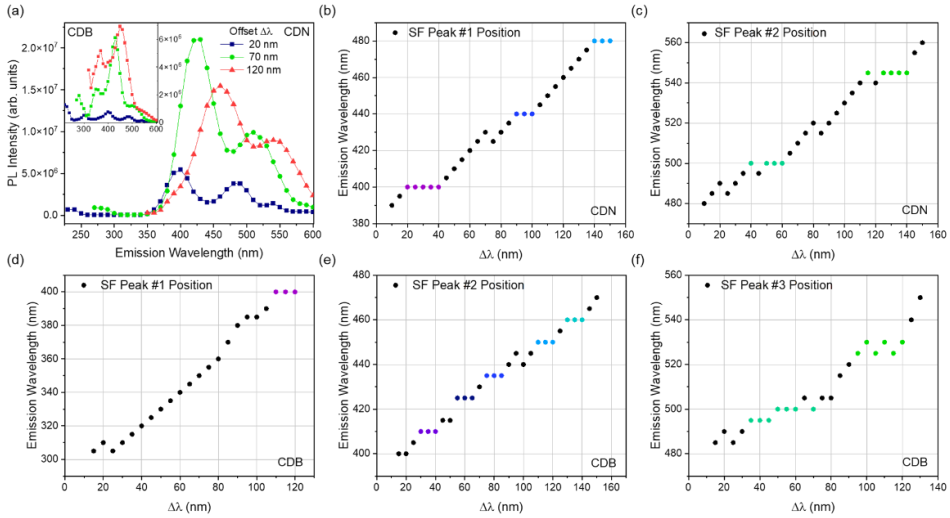

Figure 4.3.6. (a) SF emission plots at different offsets for CDB (inset) and CDN. (b-f) Emission wavelength of the peak as a function of the offset.

In CDN (**Figure 4.3.6a**) are always present two main large synchronous PL bands in the blue and green ranges, whose peak emission wavelength can be plotted as a function of the synchronous offset (**Figure 4.3.6b-c**). A third peak was also observed but it disappears for $\Delta\lambda > 30$ nm (see data represented by blue points) and was not considered in the following analysis. The plateaux in the above plots indicate the position and width of the excitation channels of specific emission peaks in a defined wavelength range (the blue and green ones). The trend of these graphs clearly suggests that for particular emission wavelengths the position of the peak is constant, targeting a fixed emission center for that specific excitation range. In CDN the peak position of the first band, the one at higher energy, identifies three violet/blue centers located at 400, 440, and 480 nm with excitation channels at 360-380 nm for the 400 nm peak, 340-350 nm for both the 440 and 480 nm. The second synchronous peak at lower energy identifies two cyan/green centers at 500 and 545 nm, with excitation channels at 440-460 nm and 405-430 nm respectively. The same analysis performed on CDB data furnishes more complex results. By tracking the position of the first SF peak it was possible to detect only one excitation plateau, corresponding to the emission at 400 nm with an excitation channel at 280-290 nm. The second plot identifies five narrow emissions at 410, 425, 435, 450, and 460 nm, with blueshifting excitation channels from 370-380 nm to 320-330 nm as the emission peak redshifts. The third SF band shows two emission peaks at 495-500 and 525-530 nm, with large excitation channels at 430-465 and 400-430 nm respectively. Once

obtained these particular emission values we extracted the PLE plots from the EEM maps as reported in **Figure 4.3.7a-6d**. PLE plots for both CDB and CDN samples are characterized by the same two main large excitation bands at about 350 nm and 440 nm. A third excitation region at higher excitation wavelengths was also recorded. The PLE plot allows for confirming and interpreting the data extracted from the SF analysis. For the CDB sample, a continuum of emission contributions excited in the near UV was detected, along with two emission bands at lower energy (500 and 530 nm) that can be excited both in the near UV and at 440 nm. In the CDN sample, the same excitation bands are observed with the difference that for lower energetic emissions the intensity of the 440 nm excitation channel is increased compared to the 350 nm one. Considering these two main excitation channels, PL spectra for both samples were extracted and deconvolute with gaussian bands without constraints except for the ground value. The best deconvolution fit of the emission spectrum of CDB excited at 350 nm (**Figure 4.3.7b**) results in two main bands, one in the blue region at about 450 nm and the other in the green one at almost 535 nm. The analysis from one side confirms the presence of a green-emitting center that can be excited in the near UV, from the other is not able to distinguish among the multiple narrow blue-emitting centers separated by the SF investigation and returns an overall large blue band. CDB PL spectrum excited at 440 nm (**Figure 4.3.7c**) allows a better identification of the green band showing one contribution peaked at about 505 nm and the other one at about 535 nm, in very good agreement with the SF results.

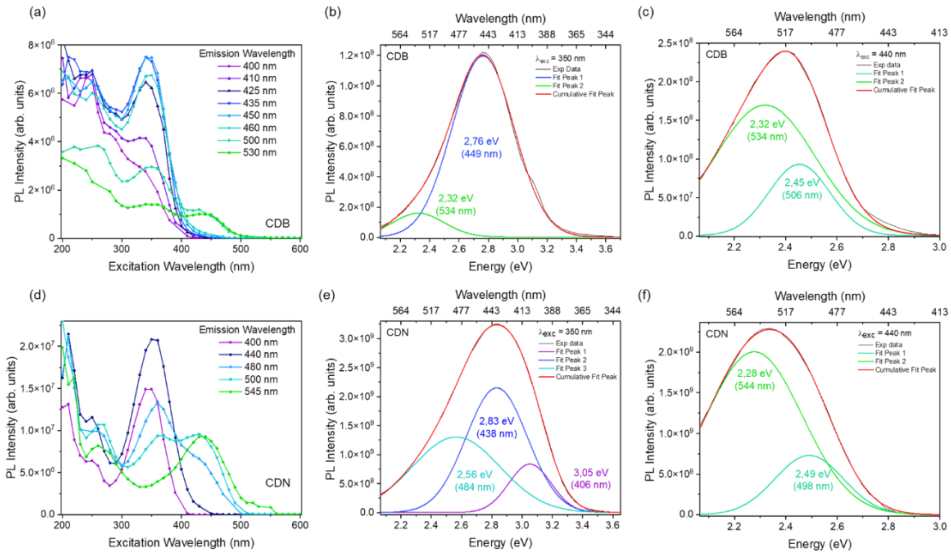

Figure 4.3.7. (top) PLE (a) and PL spectra at 350 (b) and 440 nm (c) of CDB sample. (down) PLE (d) and PL spectra at 350 (e) and 440 nm (f) of the CDN sample.

The same procedure was followed in the analysis of the PL spectra of CDN. The emission spectrum excited at 350 nm (**Figure 4.3.7e**) was fitted with three gaussian bands peaked at 405, 440, and 485 nm whilst the spectrum excited at 440 nm (**Figure 4.3.7f**) with two bands at around 500 and 545 nm, in agreement to the SF results. The above analysis suggests a different nature of the extracted emitting centers: whereas in CDB the blue emission can be constituted by a continuum of different luminescent contributions peaked in the same region, in CDN it is possible to distinguish three principal channels whose overlap represents the main input to emission pattern excited at 350 nm. Even the green emission cannot be an expression of the same phenomenon as suggested by PLE spectra. Indeed, despite the similarity of the peak positions of the green bands, in CDB the main excitation channel of these emissions is always centered at 350 nm with the 440 nm excitation as a minor shoulder. In CDN, instead, the increase in the intensity of the less energetic excitation channel (at 440 nm) is followed by a decrease in the higher one (at 350 nm). This observation leads us to hypothesize that in this case, the two excitation channels refer to two different emitting centers.

The presence of multiple emitting centers was furtherly confirmed by the decay times recorded upon excitation at 350, 410, and 450 nm (*vide infra*) which are non-single exponential decays, with a mean lifetime of about 4 and 7 ns at 350/410 nm and 3 and 5 at 450 nm for CDB and CDN, respectively (**Table S.4.5**). Thus, the different peak positions of the emissions, the width of the bands, and the non-single exponential trend of the decay time plots suggest the presence of more than a single emitting center for both the blue and green emissions. Two different fluorophores were already reported to have emissions at 450 nm, depending on the synthesis of the CDs, and identified as PAHs or fluorescent molecules.[146] Indeed, if the emission features in CDN samples are related to the presence of N, which could allow the formation of molecular species, like CZA, citrazinic amide, or HPPT, and their aggregates,[22,54,79,154] in the CDB ones the recorded optical properties should be related to emitting centers without N, eventually like PAHs, graphitic core regions or surface centers. In that sense, the emission properties of CDBs can be regarded as the intrinsic features whilst the ones of CDNs as the extrinsic ones due to the presence of N doping.[117]

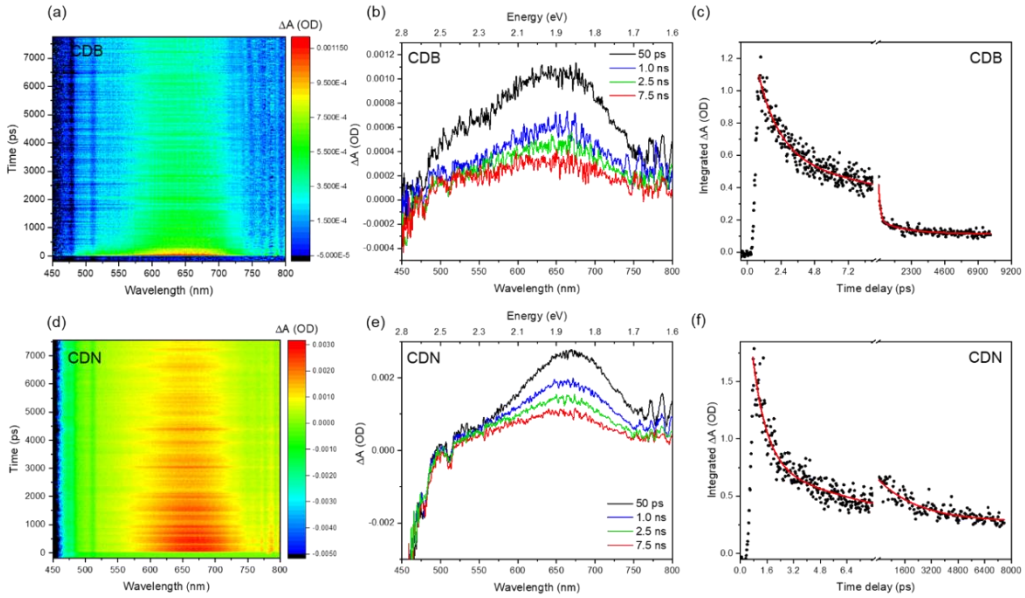

Figure 4.3.8. Time-wavelength TA plot of CDB (top) and CDN (bottom) samples in water solution in the ns range (a,d), TA signals at selected delay times (b,e), spectrally integrated TA signal decays in the ns and ps time range (c,f).

To understand the higher quantum-yield typically observed in N-doped CDs, we analyzed the transient absorption (TA) signals of CDN samples as compared to CDB ones in the ps to ns time regime, pumping the samples with a 360 nm excitation and probing them with a supercontinuum white light in the 400-800 nm range. We recorded a large and composite excited state absorption (ESA) feature showing both a short and a long decay (**Figure 4.3.8**). No ground state bleaching (GSA) or stimulated emission (SE) signals were recorded, whilst an expected intense spontaneous emission was recorded in the blue range. The ESA spectrum is due to the superimposition of 2 or 3 large Gaussian bands peaked at about 680, 580, and 520 nm whose spectral characteristics were gathered by analyzing the spectra in the energy space (**Figure S.4.2**). These transitions are ascribed to electronic transfer to edge functional groups or trapping levels, affecting the quantum efficiency of the emission.[49,155,156] Interestingly, the TA spectrum of CDN in the ns time scale displays only 2 Gaussian bands, 680 and 580 nm, whilst the third one at 520 nm is still recorded only in the ps spectrum. On the contrary, in the CDB samples, the relative contribution of the 520 nm ESA signal is twice the one in CDNs in the ps time scale and is still present in the ns regime. We assign the lower efficiency of CDB samples to the presence of this further excited absorption state up to the ns time scale. Indeed, whilst in CDN samples the integrated ESA signal decays as a single exponential of about 2.5 ns, in CDB ones we have two exponential decay times of 125 ps and 1.8 ns (**Figure 4.3.8**c and

Figure S.4.2c). These findings correlate well with the XPS and FTIR data reporting a lower content of C=O-related edge functional groups in CDNs because of the formation of N-related species. The TR-PL measurements confirmed the presence of de-activation channels of the blue and green bands in both samples, since the non-single exponential decays show a very fast contribution, typically below 1 ns and within the resolution of the experiment, affecting the whole spectrum. Concerning the decay times, the average decay time was estimated through a non-single exponential decay fit (**Figure 4.3.9**), assuming three decays (two exponential fit was considered only for CDN excited at 450 nm), with a time resolution of about 0.8 ns over the investigated 100 ns time windows (evaluated through the signal 10%-90% rise time). As also evidenced by the reported plots, the CDB samples are characterized by a faster average decay time due to the larger relative contribution of the sub-nanosecond fast decay as compared to the CDN samples. When the excitation is set at 350 nm the average decay time of CDB and CDN samples were 4.1 and 7.3 ns respectively (**Table S.4.5**). By increasing the excitation wavelength, the average decay time decreases, showing that the emission at larger wavelengths is characterized by faster decay, as already reported.[79,117]

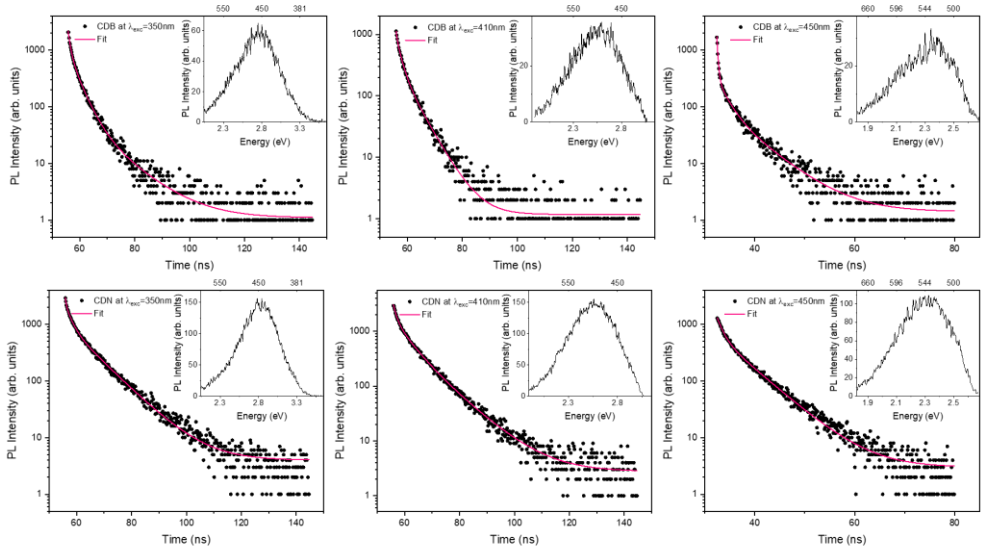

Figure 4.3.9. TR-PL spectra (inset) and decays of CDB (top) and CDN (bottom) excited at 350 nm, 410 nm, and 450 nm.

Finally, in order to give more insight into the formation of CDB and CDN systems, computational calculations were performed. To mimic the formation of

different emitting sites within the carbogenic core and/or at the surface of the synthesized CDs we considered two raw basic models, namely Pyrene (4 benzenic rings) and Perylene (5 benzenic rings), and some possible functionalization atom (pyridinic N), groups (COOH, $CONH_2$, and NH_2) or compounds (pyrrole and imide) according to XPS insights.

Table 4.3.1. Computational results relative to Pyrene and Perylene models with different doping/functional groups: HOMO-LUMO gap, the oscillator strength, and the differences between these calculated for the raw model and the other models.

	PYRENE				PERYLENE			
Model	**H-L gap (nm)**	***f***	**Δλ (nm)**	f_{RAW}/f	**H-L gap (nm)**	***f***	**Δλ (nm)**	f_{RAW}/f
RAW	344.55	0.3838	0	1	457.05	0.4354	0	1
COOH	376.88	0.0389	32.33	0.10	473.03	0.3658	15.98	0.84
$CONH_2$	356.51	0.0291	11.96	0.08	460.69	0.3939	3,64	0.91
NH_2	373.56	0.0459	29.01	0.12	470.58	0.3704	13.53	0.85
PYRIDINIC N	342.67	0.3753	-1.88	0.98	452.99	0.4388	-4.06	1.01
PYRROLIC RING	362.89	0.0334	18.34	0.09	466.90	0.4321	9.85	0.99
IMIDIC RING	498.42	0.0950	153.87	0.25	559.56	0.3038	102.51	0.70

Table 4.3.1 reports the calculated HOMO-LUMO gap (H-L gap) and the oscillator strength (*f*) for all the systems. To enlighten the effect of the functionalization both the produced wavelength shift and the relative change of the H-L transition were calculated. We can see that the functionalization produces comparable effects on both the raw structures. Except for pyridinic N, which causes a very small blueshift and no variation on the oscillator strength, all the other systems here considered move the H-L transition to larger wavelengths, thus producing a general redshift in the optical features of the simulated CDs. As for the oscillator strengths, larger reductions are in general estimated for the pyrene model (of about 1 order of magnitude for pyridinic N and imidic ring) as compared to the perylene one, where the efficiency is just slightly decreased. Among the groups and compounds, the imidic ring causes, in both pyrene and perylene cases, a very large redshift, of about 150 and 100 nm respectively, pushing the absorption and, consequently, emission properties of the starting raw models into the green-red region of the visible range. Thus, whilst the other functionalizations can be responsible for the optical properties of centers in the

blue or cyan range, green or even red features could be ascribed to imide compounds in CDs doped with N atoms, in very good agreement with the experimental XPS and PL results. Finally, it is interesting to note that even the two raw models can contribute to explaining the reported tuning of the optical properties in CDs, since the computed H-L gap shifts from the near UV to the blue range from pyrene to perylene systems, thus supporting the idea that even a proper combination of polyaromatic hydrocarbons (PAHs) can be involved in the observed optical features of CDs.[25]

4.4 Conclusions

In conclusion, the structural analysis highlighted the fundamentally different nature of CDs obtained by citric acid only and the ones produced by adding urea for N-doping purposes. It was underlined the higher degree of order in the CDB structure compared to the CDN one as well as the co-presence in both of a carbon-core system and molecular features. These nanoparticles with diameter in the 3-5 nm range showed indeed a higher presence of graphitic C and COOH functional groups in CDB whilst in CDN the presence of N-species mostly in pyrrolic and pyridinic form enhanced the disorder of the structure. Optical measurements displayed that both samples have emitting centers in the blue and green range, apparently sharing quite similar spectroscopic features. However, a deeper analysis demonstrated that a continuum of blue luminescent contributions could be identified in CDB whilst CDN fluorescence in the same region revealed three main channels at 400, 440, and 480 nm. The same study performed on the green bands unveiled two main bands, one at 500 nm for both samples and a band peaked at 535 nm and 545 nm for CDB and CDN, respectively. Whilst the cyan band at 500 nm band could be related to the same emitting centers in both samples because of the similar excitation pattern, the 535 and 545 nm emissions show different excitation spectra, thus calling for different emitting centers. These data suggest that the presence of N atoms modifies the intrinsic centers produced in the bare CDB samples leading to O- or N-related extrinsic centers. In addition, the configuration of excited state levels is modified reducing the de-activation channels and increasing the emission efficiency. For these reasons, although one should expect the presence of both intrinsic and extrinsic centers in the CDN samples, the lower quantum yield of intrinsic centers as compared to extrinsic ones and the close spectroscopic similarities makes it hard to isolate intrinsic from extrinsic contributions. Computational findings suggest that many intrinsic centers

can be responsible for the blue emission in CDB, since even the raw model plays a key role in the gap position, thus assessing it to a combination of PAHs forming the core state. The green emission at 535 nm could be instead due to the COOH functional groups present in large sp^2 carbon regions constituting CD surface. For what concerns CDN, simulations highlighted the great reduction in the HOMO-LUMO bandgap due to imidic species suggesting their attribution as green-emitting centers. Cyan broad emission could be related to extrinsic O/N-related functional groups whilst the violet one is possibly linked to core-state emission. The blue band at 440 nm is instead ascribed with enough certainty to CZA molecules, whose presence in this synthetic reaction has already been assessed.

Chapter 5

Systematic NMR/Optical analysis of Carbon Dots from Citric Acid and Urea

Olla, C.; Fusaro, L.; Porcu, S.; Ricci, P.C.; Carbonaro, C.M. **Exploring the complex structure and luminescent properties of N-doped Carbon Dots via Optical and Nuclear Magnetic Resonance spectroscopies** (work in preparation)

Mocci, F.; **Olla, C.**♦; Cappai, A.; Corpino, R.; Ricci, P. C.; Chiriu, D.; Salis, M.; Carbonaro, C. M. **Formation of citrazinic acid ions and their contribution to optical and magnetic features of carbon nanodots: A combined experimental and computational approach.** *Materials* (**2021**), *14*(4), 1–16. https://doi.org/10.3390/ma14040770

♦ Collaboration.

5.1 Introduction

The identification of emitting centers in CDs requires the study of the complex chemical reactions involved. A possible strategy is to compare the properties of CDs to those of the precursors and target molecules.

This procedure is based on the CD molecular state model, which has been largely confirmed in previous works through both experimental and computational approaches.[22,157–159]

In particular, recent studies on highly efficient blue-emitting CDs obtained from the thermal decomposition of citric acid and nitrogen sources have claimed the presence of fluorescent citrazinic acid (CZA) and its derivatives as green emitting HPPT.[54,146,152,159,160]

CZA is an organic fluorophore that consists of a 2,6-dihydroxypyridine ring with a carboxylic group in position 4. Its applications range from producing photosensitizers to synthesizing new microporous materials.[161–163] Its optical characteristics depend on both the aggregation states and chemical environment. CZA has the tendency to form dimers at high concentrations and tautomeric forms based on the solution pH.[164,165] Despite its potential role in CD emission properties, only a few research groups have investigated its physico-chemical features in detail. In one of our works,[126] we performed a systematic computational study of all the CZA tautomeric forms present in aqueous solutions, calculated their formation energy and compared the simulated vibrational and magnetic features of the formed species to the experimental Raman and NMR spectra of CZA, confirming that the CZA molecule can participate in the optical and magnetic properties of citric acid-related CDs synthesized at low temperatures and with short reaction time.

NMR is a powerful tool for identifying the chemical surroundings of selected atoms and tracing the molecular structure, including chemical bonding characteristics, in both organic and inorganic compounds. This spectroscopic technique investigates the atomic nuclei and their surroundings by exploiting the physical phenomenon in which nuclei in a strong constant magnetic field can be perturbed by a radio frequency pulse, responding with an electromagnetic signal with a frequency characteristic of the magnetic field at the nuclei. Recently, the application of NMR to investigating CDs has increased for detecting target molecules[166] as well as discovering new molecular fluorophores related to CD bottom-up synthesis, such as IPCA and HPPT.[22,54]

In this work, optical spectroscopy was combined with liquid and solid-state NMR for a detailed investigation of the reaction forming CDs from citric acid and

urea. NMR measurements were performed as part of a 6-month traineeship period at the University of Namur (Namur, Belgium) under the supervision of Dr. Luca Fusaro. Supplementary information is available in Appendix C.

5.2 Materials and Methods

5.2.1 Synthesis and Treatments

Nitrogen-doped CDs were synthesized via thermal decomposition of precursors in air. Citric acid (CA, 0.200 g) was combined with urea in a 1:1 molar ratio (0.077 g) for CD 1:1 and in a 1:10 molar ratio (0.774 g) for CD 1:10. Each sample was obtained starting from the same quantity in weight of reagents in an open vessel thermal reaction at 180 °C at different reaction time ranging from 30 s to 3 h.

5.2.2 Experimental characterization

UV-Vis absorbance spectra were collected (applying baseline corrections) by Jasco V-750 spectrophotometer with a spectral bandwidth of 0.2 nm in the 200-800 nm range.

As for time-resolved photoluminescence (TR-PL), the measurements were performed by exciting the samples with 200 fs long pulses delivered by an optical parametric amplifier (Light Conversion TOPAS-C) pumped by a regenerative Ti:Sapphire amplifier (Coherent Libra-HE). The repetition frequency was 1 kHz, and the PL signal was recovered by a streak camera (Hamamatsu C10910) equipped with a grating spectrometer (Princeton Instruments Acton SpectraPro SP-2300). The solutions were placed in quartz cuvettes with a 1 cm path length. Proper optical filters were applied when needed.

Solid state Magic Angle Spinning (MAS) Nuclear Magnetic Resonance (NMR) measurements of ^{13}C were recorded on a Jeol spectrometer operating at 14.1 T (600 MHz for ^{1}H). The samples were packed in 3.2 mm zirconia rotors and spun at 10000 Hz. The ^{13}C NMR spectra of CD 1:1 sequence, were recorded on a Varian spectrometer operating at 9.4 T, using 4 mm rotors and spinning at 8000 Hz. Liquid-state NMR measurements of samples dissolved in D_2O solutions were collected with the same Varian spectrometer, using a 5 mm broadband probe and temperature regulation.

5.3 Results and Discussion

The evolution of the synthesis of carbon dots from citric acid and urea in molar ratios of 1:1 (CD 1:1) and 1:10 (CD 1:10) pyrolyzed at 180 °C in an open vessel was investigated in a time ranging from 30 seconds to 3 hours. The obtained powder samples as well as their dispersion in water were analyzed with different spectroscopic techniques (see **Figure S.5.1** and **S.5.2**).

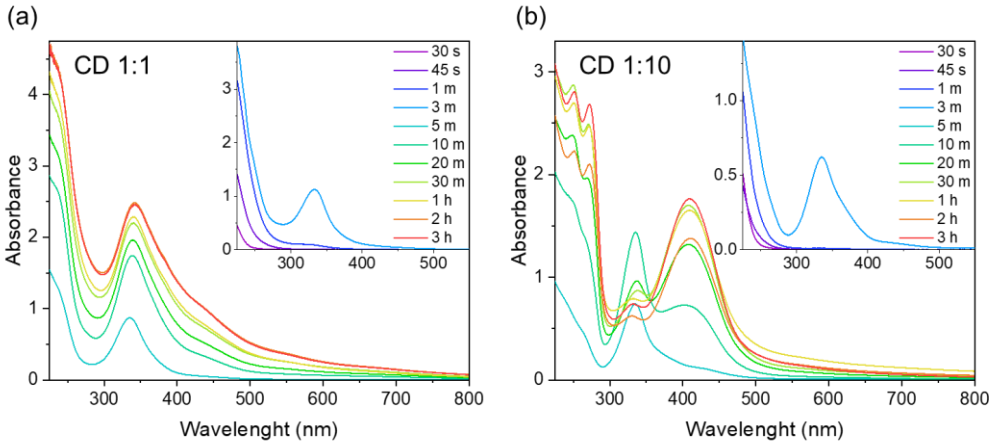

Figure 5.3.1. Absorption spectra of (a) CD 1:1 and (b) CD 1:10 series in solution. In the insets are reported the early stages of the reaction (30 s to 3 min) with a concentration in weight four times higher than the other samples.

UV-Vis absorption measurements of the CD 1:1 sequence in water underline a linear correlation trend between synthesis time and the increase of the overall absorption signal (**Figure 5.3.1**a). Since the very early stages of the thermal treatment, a high absorption contribution was recorded in the UV region at 225-275 nm due to the aromatic carbons provided by the precursors with their related electronic π–π* transition that can be considered the carbon core absorption centers. After a few minutes, a distinct and quite symmetrical band peaked at 335 nm arose and slightly redshifted to 345 nm over time. This band perfectly matches with citrazinic acid (CZA) optical absorption in water as reported in many experimental and computational works.[43,126,164,165] At longer times, few shoulders appeared at about 380, 440, and 540 nm, enlightening the growth of multiple absorbing species possibly related to the formation of surface/molecular states as the reaction carries on. A different pathway can be retrieved in CD 1:10 samples. Up to 10 minutes, along with the far UV absorption region and the same peak at 335 nm as in the other set of samples, the occurrence of two shoulders at 370 and 420 nm was observed. At increasing times, besides the far UV contribution that

became more definite with the appearance of two peaks at 250 and 270 nm, the band at 335 nm kept its position while the shoulders are replaced by a broad contribution peaked at 410 nm. As in CD 1:1, the UV absorption could be considered related to the carbon core centers and the 335 nm peak to CZA. The peak at 410 nm was recently assigned to the imide form of CZA named HPPT. It is very interesting to note that in a period ranging from 10 to 20 minutes the main contribution to absorption given by CZA seems to be overcome by the HPPT one, being this molecule formed at the expense of the other one as proposed in the literature.[22]

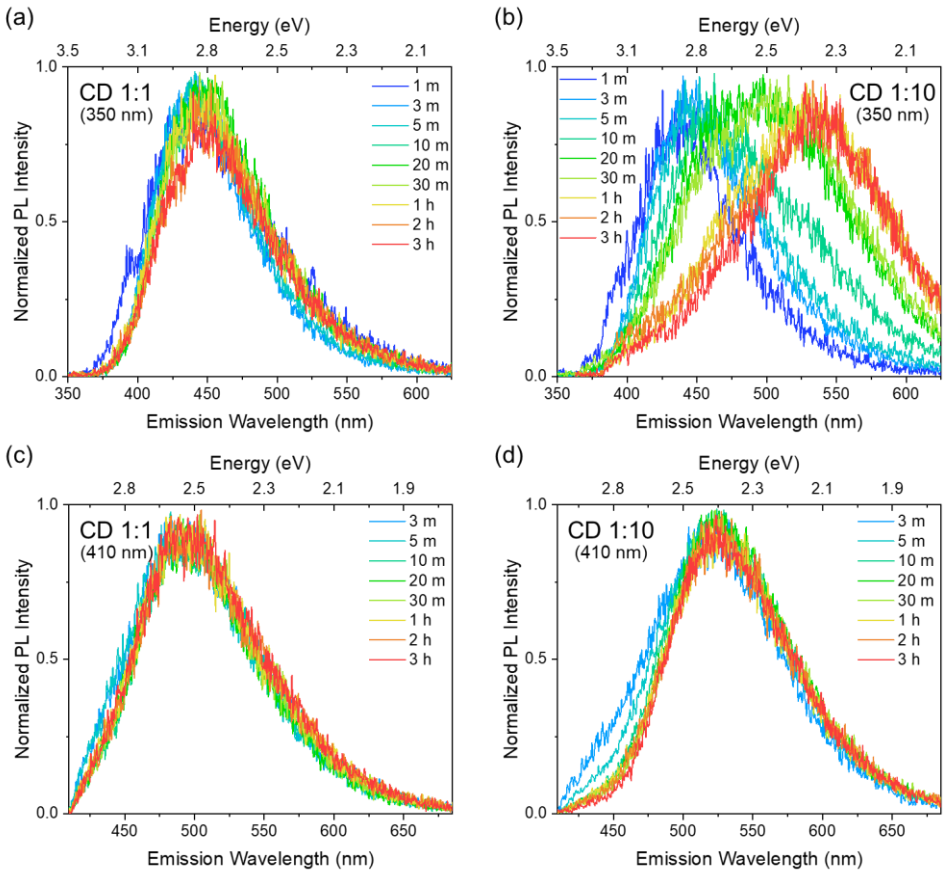

Figure 5.3.2. Normalized PL spectra of (a-c) CD 1:1 and (b-d) CD 1:10 series in solution excited at 350 nm (a-b) and 410 nm (c-d).

TR-PL measurements at two different excitation wavelengths were carried out to study the two main absorption contributions (**Figure 5.3.2**). All PL spectra of CD 1:1 sequence excited at 350 nm show a blue broad band peaked at about 440 nm with a little peak in the near UV region visible only in the 1-minute reaction sample. (**Figure 5.3.2**a**)**. Since part of these sets of measurements were performed

with the same experimental conditions, it was possible to take into account the intensity of the spectra that in this case display a decreasing trend as the reaction takes place (**Figure S.5.3**a). A completely different pathway is followed by CD 1:10 series at the same excitation wavelength. The initial blue emission peaked at about 440 nm is gradually redshifted to the green region as the synthetic treatment proceeds, stabilizing from one hour at 540 nm (**Figure 5.3.2**b**)**. However, the intensity of the samples from 5 minutes onward is not significantly affected by this redshift phenomenon (**Figure S.5.3**b). The measurements performed at 410 nm excitation wavelength were used to investigate the secondary absorption shoulders in CD 1:1 and the main band in CD 1:10 that overcome the one at 350 nm. In both sequences, the emission of the 1-minute samples was too low to be recorded, as the centers absorbing at 410 nm had not been produced yet. CD 1:1 sequence showed the same spectral shape at every step of the reaction with just a small decrease of the luminescence whose emission peak was recorded at 495 nm. (**Figure 5.3.2**c, **Figure S.5.3**c) In opposition, CD 1:10 increased the luminescent contribution peaked at 525 nm as the time ran along with a gradual decrease of the shoulder in the blue region (**Figure 5.3.2**d, **Figure S.5.3**d). Decay time plots recorded in all the emissive region (**Figure 5.3.3**) reported a single exponential decay for what concern the first stages of CD 1:1 at 350 nm (9.2 ns from 3 to 20 minutes, the 1-minute sample is multi-exponential with time values of 1 and 8.5 ns) and multi-exponential pattern as the reaction carries on (1.4 and 9.5 ns). This was quite interesting because single exponential decays are typical of molecular systems which seem to be the principal emitting centers in the first 20 minutes of reaction whilst after this time other emitting centers in the same region with shorter decay times are produced. When the same samples were excited at 410 nm multiple contributions were displayed with the overall time decay that slightly shortened as a function of time (1.5 and 8.0 ns at 3 m, 1.1 and 7.0 ns at 3 h), indicating a small variation in the relative contribution of the same emissive centers that does not change the spectral shape. Different conclusions can be drawn considering the multiple exponential decays in CD 1:10 at 350 nm where the emissive redshift over the reaction is accompanied by a change in the decay time (1.3 and 9 ns at 3 m, 3.8 and 9.5 ns at 3 h) possibly highlighting the different products obtained as the reaction keep going (**Figure 5.3.2**b). Under 410 nm excitation, the decay pattern changes from 10 minutes onward (3.2 and 6.7 ns, before 1.5 and 6.6 at 1 m and 2.7 and 6.8 ns at 3 m) showing the coexistence of two distinct emitting channels.

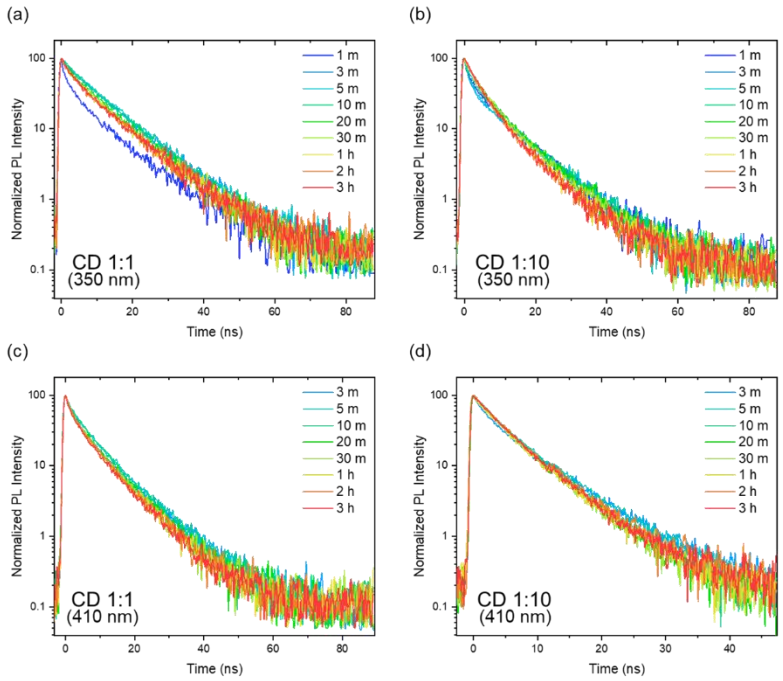

Figure 5.3.3. Decay time plots of (a-c) CD 1:1 and (b-d) CD 1:10 series in solution excited at 350 nm (a-b) and 410 nm (c-d).

To sum up, optical spectroscopy measurements helped to show the presence of multiple emitting centers in both the reactions studied. For what concern CD 1:1, UV-Vis measurements highlighted the formation of the main peak at about 340 nm that can be ascribed to CZA with various secondary absorption shoulders in the lower energy regions. When the samples are excited in their main absorbing peak at 350 nm the spectral shape is the same over time with just a small redshift of the peak that reflects the absorption findings. Nevertheless, the overall luminescence gradually decreased, and the decay time plots underlined some differences possibly linked to the initial formation of CZA followed by the formation of other emitting centers in the same region over 20 minutes. The same samples excited at 410 nm in a secondary absorption region showed a broad band peaked at 500 nm whose intensity is not substantially affected by the reaction time. The broadness of the band and the multi-exponential decay plots conceivably indicate the presence of multiple emitting centers whose relative contribution slightly changes over time. Finally, the CD 1:10 series showed a clear absorption/emission trend as a function of the synthesis time. The first absorbing species formed is the one peaked at 335 nm which is still attributed to the CZA molecule. However, a contribution at longer wavelengths surpassed the near-UV one in the 10–20-minute range. This band peaked at 410 nm was

recently ascribed to the HPPT molecule which is the imidic form of CZA from which is supposed to be derived. Indeed, emission results excited at 350 nm displayed the presence of many centers as evidenced by the multiple exponential decay times and by the overall luminescence gradually redshifted from 440 to 540 nm peak. The same measurements performed excited at 410 nm show the highest intensity reached in a time ranging from half to one hour with a spectral shape that is constant over time after 10 minutes, as a blue shoulder gradually disappeared before that time.

The above analysis clearly shows the optical properties of highly complex systems whose emission properties depend on reaction-time and excitation wavelength (see **Figure S.5.4**). These properties were measured in an aqueous solution as CDs are usually studied in this environment for their well-known solubility/dispersibility properties in it. Nevertheless, the obtained sequences of samples were highly interesting in their solid-state form (see **Figure S.5.5**). Indeed, in the initial step of the reaction the obtained products of both series are highly luminescent under UV-light changing from blue to green over a few minutes and their luminescence is resisting to photobleaching even after months. The issue that we are experiencing for further optical characterization concern the post-synthesis environmental conditions. These samples were synthesized in a dry and cold environment which kept them in a powdered phase that seems to be difficult to preserve under normal conditions. One of the future aims of the study is the measurements of these products' optical properties that could be very important for the development of solid-state luminescent devices and to investigate the non-molecular contribution to luminescence. Indeed, in our previous work described in **Chapter 3**, we assessed that in water the molecular contribution is predominant compared to the core/surface state one. If the luminescence of these samples is not photobleached by the solid-state phase, it could be due either to a molecular emission whose emission is preserved by the carbogenic network or to other surface emitting centers to be determined. For this reason, we applied, for the first time, liquid and solid-state NMR technique that can help us understand the differences between the two molecular and the surface/core state centers.

Solid-state NMR (ssNMR) provides broader signals compared to solution-state ones but can give remarkable information about the structure, the conformation, and the dynamics of solid-state materials. Nowadays, this technique is often combined with magic angle spinning (MAS) to reduce anisotropic interactions such as chemical shielding and dipolar coupling, enhancing the resolution and sensitivity. MAS spectra are obtained by rotating the samples at the magic angle

(54.74°) to the direction of the magnetic field. If the sample is not rotated at a rate higher than the largest component of the chemical shift anisotropy, the interaction with the magnetic field generates a set of sidebands centered at the isotropic chemical shift and separated from this frequency by a multiple of the spinning rate. If the nucleus under examination has a low gyromagnetic ratio (e.g., ^{13}C), which is directly proportional to the strength of the interaction with the external magnetic field and consequently on the intensity of the signal, cross-polarization (CP) allows the transfer of nuclear magnetization from abundant nuclei with a high gyromagnetic ratio such as ^{1}H, extremely improving the sensitivity of the measurement. In this methodology framework, further modifications of the radio frequency pulses allow the suppression of the sidebands (TOSS, Total Suppression of Spinning Sidebands) or the non-quaternary signals (NQS, Non-Quaternary Suppression).

In **Figure 5.3.4**, four different ^{13}C ssNMR spectra of CD 1:1 and CD 1:10 after 3 hours of thermal treatment are reported.

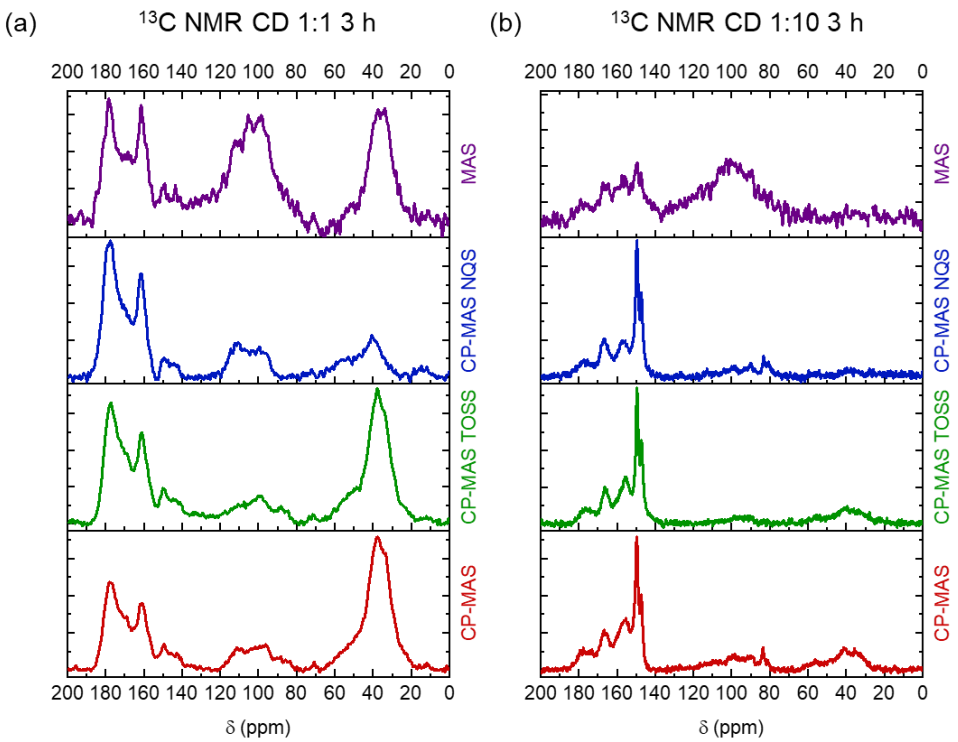

Figure 5.3.4. ^{13}C ssNMR spectra of (a) CD 1:1 and (b) CD 1:10 after 3 hours.

CD 1:1 after 3 hours presented many broad contributions with a very reduced presence of sidebands as evidenced by the TOSS spectrum. The first contribution in the 20-60 ppm chemical shift region was ascribed to C-C bonds in the form of

primary, secondary, tertiary, and quaternary carbons (aliphatic compounds). Indeed, this region was highly enhanced by CP measurements since the proximity with bonded hydrogen atoms helps the efficient transfer of their magnetization to the carbon atoms. Moreover, the NQS spectrum displayed a reduced but not totally suppressed contribution in this region, evidencing the presence of quaternary atoms that can be related to the small graphitic region in this type of CD. It must be taken into account also the presence of the superimposed 40-80 ppm shoulder related to C-O and C-N bonds which are usually recorded on CDs. At 80-120 ppm the signal of C=C in aromatic and heteroaromatics rings was displayed. In the same region, alkene signals could be found but the NQS pulse sequence would have suppressed them, thus ascribing the main contribution to aromatic structures. The presence of this signal is highly significant for the assessment of the formation of the carbon core in CDs. Finally, among 140-200 ppm the heteroatom region can be observed. In particular, the 140-160 ppm is related to the C=N bond and amide species whilst the 160-200 region is ascribed to C=O species like carboxylic acid. The overall set of measurements indicates the formation of a complex structure with a similar quantitative contribution of aliphatic, aromatic, and heteroatom carbon bonds as highlighted by the pure MAS measurement. A very different pattern was recorded for CD 1:10 sample at the same reaction time. Indeed, CP-MAS spectra evidenced a very low presence of aliphatic carbons compared to the dominant contribution in the heteroatom region with four distinct peaks related to carbon covalently bonded with oxygen and nitrogen atoms. Nevertheless, the MAS spectrum which is not influenced by the presence of hydrogen atoms underlined a similar contribution from carbon in aromatic or heteroaromatic rings, confirming once again the presence of sp^2 structures typical of CDs. Making a comparison among the obtained CDs, the precursors, and our CZA reference it is possible to understand the origin of our product peak positions (**Figure 5.3.5**). For instance, the C-C carbon region was clearly originated by CA that turned out in a vast family of C-C species in CD 1:1 while the contribution is almost negligible in CD 1:10 where the highest contribution is given by urea-derived composites. CZA signals lie in the same region of heteroatoms and aromatic regions, but it was not possible to assess its presence from these measurements. Indeed, the use of ssNMR allows the investigation of the whole sample which means in CD case the analysis of the carbon-core and surface state, being the possible aggregated molecules hidden by these dominant contributions.

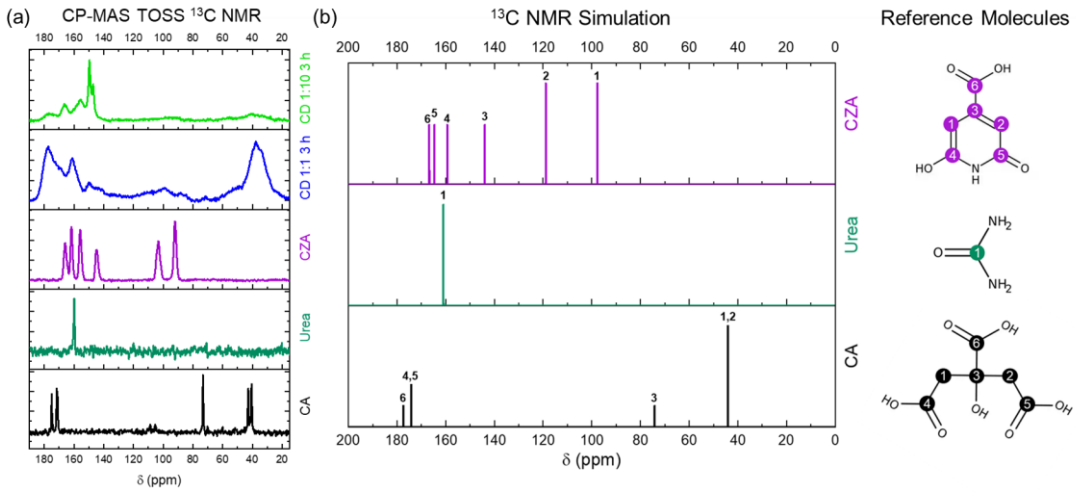

Figure 5.3.5. (a) From top to bottom TOSS CP-MAS ^{13}C ssNMR spectra of CD 1:10 3 h, CD 1:1 3h, commercial CZA, commercial urea, and commercial CA. (b) Simulation of NMR spectra of CZA, urea, and CA.

To give insight into these kinds of reactions, we focused on the CD 1:1 sequence performing a series of CP-MAS measurements following the structural changes as a function of the synthesis time (**Figure 5.3.6**). These results show that the reaction since the very first minutes modified the chemical structure increasing the family of aliphatic and heteroatom carbons. Even an aromatic network is formed but it is better observed in MAS measurements than CP-MAS ones as explained above. There are also two evident trends, the decrease as a function of the reaction time of the signal related to the carbons at the center of the CA structure being a proof of the process of aromatization of the system, and the increase of the C-N structures related to the incorporation of nitrogen from urea in the system.

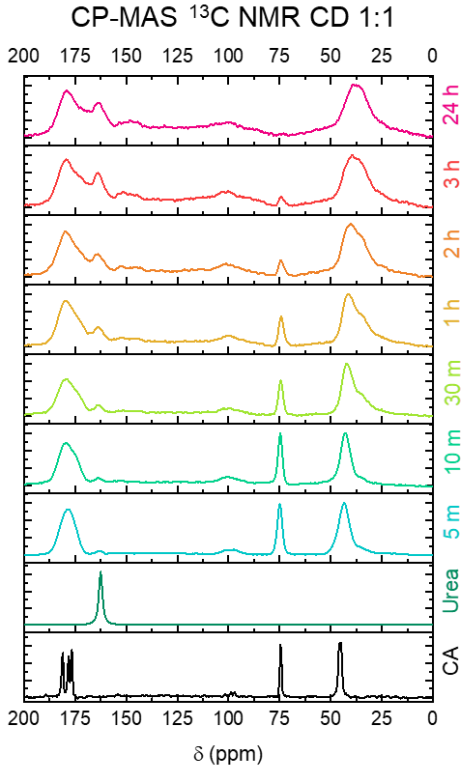

Figure 5.3.6. ^{13}C ssNMR spectra CD 1:1 as a function of time compared to their precursors.

Along with ssNMR measurements, liquid-state NMR spectra were collected in order to understand the molecular state of the obtained samples. Indeed, liquid-state NMR is a powerful technique for the identification of small molecular systems and the study of the effect of the surrounding environment. Our systems are too extensive and complex for being analyzed in solution and collect information about the overall nanoparticle, but since they do show molecular features, these can be investigated through it. In **Figure 5.3.7** the liquid-state NMR ^{1}H, ^{13}C, and ^{14}N spectra of different sets of CD 1:1 samples are reported. ^{1}H spectra show numerous signals derived from CA since the very early stages of the reaction indicating the presence of many molecular/surface species. The last spectrum was recorded using a large number of transients to increase the signal-to-noise ratio of the observed signals. After a very long experimental time (24 h) several sharp peaks and also intense broad bands were observed, highlighting the presence of big molecules and/or aggregates. It is worth noting the presence of peaks at 6 ppm in the aromatic region that further assess the formation of sp^2 structures. The same information is collected through ^{13}C spectra at a few

minutes' reaction with the increase of the number of signals as a function of time, in particular the ones related to C=O/C=N bonds.

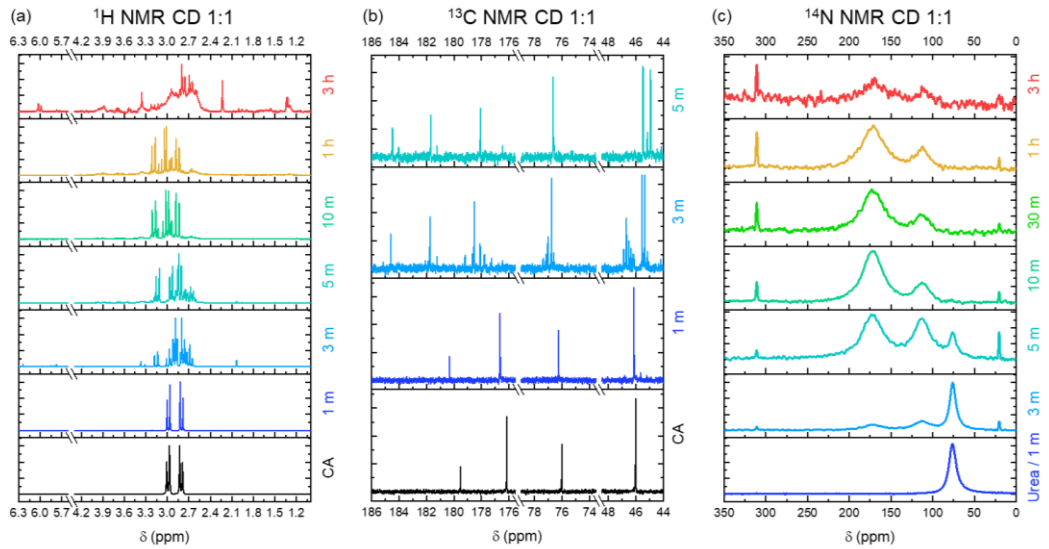

Figure 5.3.7. Liquid ^{1}H (a) ^{13}C (b) and ^{14}N (c) NMR spectra of CD 1:1 as a function of reaction time compared to their precursors.

More considerations can be done by analyzing the ^{14}N spectra. ^{14}N is a quadrupolar nucleus whose signals broaden with the increasing size of molecules or asymmetric environment. At first, the only recorded signal is trivially the one from urea at about 75 ppm but after just 3 minutes four more contributions arose. Two of them are narrow signals at 20 ppm and 311 ppm. The first one is ascribed to aliphatic amines and in particular, it can be ammonia or its ion, due to the reaction of dehydration of urea for the formation of CZA as reported in the literature.[22] The second narrow peak is linked to the formation of pyridinic structures which means that N is increasingly incorporated in the aromatic structure. The two broad regions are peaked at 112 and 172 ppm. The latter is typically ascribed to pyrrole-like N and imidic structures whilst at 112 ppm is the region of amide structures. Indeed, as the reaction carries on the amide contribution decreases in favor of imidic/pyrrolic structures.

In conclusion, both solid-state and liquid-state NMR measurements gave remarkable insights into the structure of CDs. In particular, different solid-state NMR techniques were employed for highlighting the nature of carbon atoms in the structure showing three main regions related to aliphatic, aromatic, and heteroatom-linked elements, being the latter dominant in CD 1:10 series as expected by the relatively high quantity of nitrogen source in the synthesis. The

evolution from precursors to the formation of CDs was followed by analyzing the CD 1:1 sequence from which it can be demonstrated that as the synthesis carries on a broad family of aliphatic and oxygen/nitrogen bonded carbons are formed along with the formation of a graphitic/aromatic network. These measurements evidenced the carbon core/surface structure of CDs, but the molecular state had to be addressed through liquid-state NMR which is sensitive to small molecules in solution. ^{1}H and ^{13}C show the fast transformation of the reagents in multiple products since the very first minutes of the reaction whilst ^{14}N evidenced the incorporation of nitrogen in the structure with the conversion of urea first in amide and then in imidic/pyrrolic structures with the release of ammonia.

5.4 Conclusions

In this ongoing work, a detailed analysis of the optical and structural properties of the thermal reaction from citric acid and urea in different molar ratios was provided. Both these spectroscopic approaches demonstrate the complexity of the CDs obtained and the differences introduced by changing the amount of dopant and by varying the reaction time. The investigation on CD 1:1 series supports the presence of multiple emitting centers, one of them particularly relevant for the optical properties is CZA whose absorption and emission band was recognized among the other emissive contributions. These molecular features match with the liquid-state NMR, in particular with ^{14}N measurements that evidence the presence of little molecules with increasing pyridinic and imidic features that are compatible with CZA and also HPPT structures. Moreover, solid-state NMR was essential for the investigation of the CD core/surface state features that are very important in the understanding of excitation-dependent emission. Indeed, NMR shows the presence of three main contributions that are aliphatic, aromatic, and heteroatom-linked carbon atoms, picturing an overall complex structure that as the reaction carries on tends to form cyclic structures with incorporated N. The analysis on CD 1:10 has not been completed yet since only optical measurements were performed on all the obtained samples for experimental issues concerning their tendency to absorb water that prevent them from being dry powders suitable for solid-state NMR measurements. Nevertheless, it was possible to examine CD 1:10 3h which displays a very different carbon structure in which the heteroatom contribution overcomes the aliphatic one for the dominant presence of urea-derived species. Also, optical properties highlight the change in the dominant emissive center as the reaction proceeds passing from a blue band identified as CZA to a green one ascribed to its imidic form HPPT.

In the future, research will be completed with further optical and NMR characterizations as well as with the employment of other structural techniques such as Raman, XPS, and TEM that can help clarify this complex scenario. It is important to underline that as far as our knowledge, there are no published studies about the systematic analysis of the formation of CDs from the very first minutes of reaction that can give significant results in the comprehension of CD's incredible properties.

Chapter 6

Investigation on N-doped Carbon Dots from hydrazines

Olla, C.; Porcu, S.; Secci, F.; Ricci, P.C.; Carbonaro, C.M. **Towards N–N-Doped Carbon Dots: A Combined Computational and Experimental Investigation**. *Materials* (**2022**), 15, 1468. https://doi.org/ 10.3390/ma15041468

6.1 Introduction

The role of nitrogen in the optical properties of CDs was widely studied both from an experimental and computational point of view.[84,85,167,168] Nevertheless, most of these studies are focused on N-doping from the most popular amine precursors and, consequently, investigate the carbon–nitrogen bond in the form of pyrrolic, pyridinic and graphitic nitrogen inside the carbon network. The nitrogen–nitrogen bond is not generally considered, and a few papers about this possible bonding are reported in the literature concerning the use of hydrazines as a CD precursor or, due to their high reduction power, for modifying the bonding type of N-atoms in formed CDs which enhance their QY.[169–174] Indeed, the simplest organic compounds that present this kind of bond are represented by

hydrazines, which are largely used in pharmaceutical and agrochemical industries.[175,176]

Hydrazine structures are characterized by a single covalent N–N bond which carries from one up to four alkyl or aryl substituents. Hydrazines are highly toxic for human health, and, among their wide range of applications, CDs have been adopted as a fluorescent sensor for this class of compounds.[177–184]

Despite its toxicity, hydrazine represents the simplest molecule that presents an N–N bond, and we exploited this as a proof of concept for the possible development of N–N doping in CDs. Inspired by these previous works[169–174] and by the results on the citric acid plus amines reaction,[37] we decided to study the possible formation of heterocyclic N–N-containing compounds as possible molecular seeds for the formation of CDs. For these reasons, a combined experimental and computational approach was adopted to investigate the optical features of hydrothermally produced citric acid and hydrazine-related CDs, showing that the formation of pyridinone structures could explain the excitation-dependent emission properties. As compared to a citric acid–urea CD reference sample, a larger relative contribution in the green region of the optical emission spectrum was obtained, suggesting promising application for these systems. Supplementary information is available in Appendix D.

6.2 Materials and Methods

6.2.1 Synthesis

N-doped CDs were synthesized via a simple single-step hydrothermal route using citric acid monohydrate as a precursor (CA), which was reacted with selected hydrazines as nitrogen sources: i) hydrazine hydrate (Hy), ii) phenylhydrazine (P-Hy), iii) N,N-dimethylhydrazine (DM-Hy). For each synthesis, 0.77 g CA (3.66 mmol) were combined with the nitrogen source in a 1:1 molar ratio (Hy, 120 μL; DM-Hy, 270 μL; P-Hy, 360 μL; urea, 0.22 g). The reagents were dissolved in 20 mL of distilled water and the obtained solutions were transferred into a Teflon-lined stainless-steel autoclave (volume 30 mL) and loaded in a hot air oven at 180 °C for 6 h. It was not possible to measure the actual pressure inside the reactor, but, since the typical range of hydrothermal synthesis is 0.3–4 MPa and the steam temperature of water at 180 °C is about 1 MPa, we estimated the pressure inside the autoclave to be about 1 MPa. Autoclaves were cooled to room temperature in order to collect the resulting solutions, which were

centrifugated at 4000 rpm and filtered using a 0.22 μm membrane to remove the larger aggregates from the final products. The synthesized samples are indicated, in the following, as CA-urea, CA-Hy, CA-DM-Hy and CA-P-Hy respectively.

6.2.2 Characterization

Surface Enhanced Raman spectroscopy (SERS) measurements were obtained in back scattering geometry with a micro-Raman scattering confocal system (SOL Confotec MR750) equipped with a Nikon Eclipse Ni microscope (Nikon Instruments Europe BV). The samples were excited at 532 nm (IO Match-Box series laser diode) and collected with a spectral resolution of 0.6 cm^{-1} (average acquisition time 50 s, average number of acquisitions 3, sensor temperature −23 °C, objective Olympus 100×, grating with 600 grooves/mm, power excitation 3 mW). SERS supports were ITO glasses coated with silver nanoparticles (S-Silver SERS substrates, Sersitive).

UV-Vis-NIR absorbance and transmittance spectra were collected by an Agilent Cary 5000 spectrophotometer (Agilent) with a spectral bandwidth of 2 nm in the 200–800 nm range. All the samples were diluted with distilled water with a dilution factor of 10^{-4} (%v/v) to avoid reabsorption effects and put in quartz cuvettes with a 1 cm path length. Baseline corrections were performed on all spectra.

Three-dimensional fluorescence mapping of samples was performed using a spectrofluorometer, the Fluoromax-4 by Horiba Jobin Yvon, with a 150 W Xenon lamp as the excitation source. The maps were collected with an excitation range of 250–500 nm and an emission range of 350–600 nm with a 1 nm spectral bandwidth for excitation and emission.

Time-resolved photoluminescence (TR-PL) measurements were performed by exciting the samples with 200 fs long pulses delivered by an optical parametric amplifier (Light Conversion TOPAS-C) pumped by a regenerative Ti:Sapphire amplifier (Coherent Libra-HE). The repetition frequency was 1 kHz and the PL signal was recovered by a streak camera (Hamamatsu C10910) equipped with a grating spectrometer (Princeton Instruments Acton SpectraPro SP-2300). Samples were excited in the front face mode and proper optical filters were applied when needed.Transmission Electron Microscopy (TEM) Images were collected by a Jeol JEM 1400 Plus.

6.2.3 Calculations

All the quantum-chemistry calculations were performed by using the Gaussian 16 suite of programs.[123] For all the structures simulated, we performed a geometry optimization down to the self-consistent field (SCF) energy of each system by means of DFT calculations carried out at a B3LYP/6-311G(d,p)[128,129] level of theory. To account for the interaction of simulated structures with water, exploited both as solvent in the synthesis and dispersion medium for the analysis (*vide infra*), the self-consistent reaction field model was considered to include the solvation effects. The dielectric solvent was simulated through the polarizable continuum model calculation within the integral equation formalism (IEFPCM).[145] No imaginary frequencies were calculated for all the optimized ground state structures in the vibrational spectra, thus assuring that the simulated structures were real energy minima.

Optical absorption transitions in the UV-visible spectral range were simulated by TD-DFT calculations at the same level of theory. Vertical energy transitions from the ground state configuration were calculated with the solvent environment (water) fixed as in the ground state.

6.3 Results and Discussion

6.3.1 Experimental Results

In order to verify the formation of CD-like structures, from hydrothermal treatment of citric acid and hydrazine compounds, detailed optical analysis was performed. Comparing the absorption spectrum of the hydrazine precursors and the obtained products, the observation of new and different bands indicates the formation of new compounds (**Figure S.6.1**).

Whilst the precursors have absorption in the far UV always below 300 nm, the formation of the band at about 330–350 nm is a distinctive signal of the possible formation of CDs. Indeed, in **Figure 6.3.1**, the absorption spectra of all samples present a shoulder in the UV region at 225–250 nm, which is generally ascribed to the π–π* transition of aromatic carbon that is supposed to be present in the CD core structure. An absorption peak at around 330 nm can be observed in all samples, except for CA-Hy, whose peak is at about 310 nm. This peak in the near UV region is typically attributed to the n–π* transition of N or O-containing structures. These assignments are well confirmed by the computational results here reported (see computational results). The intensity of the 350 nm peak is

higher in urea-sample than in hydrazine ones, suggesting the formation of a larger set of absorbing centers and possibly higher emission performances while, among the others, the sample derived from hydrazine hydrate shows the more intense peak (all the spectra were acquired considering the same amount of product dispersed in water).

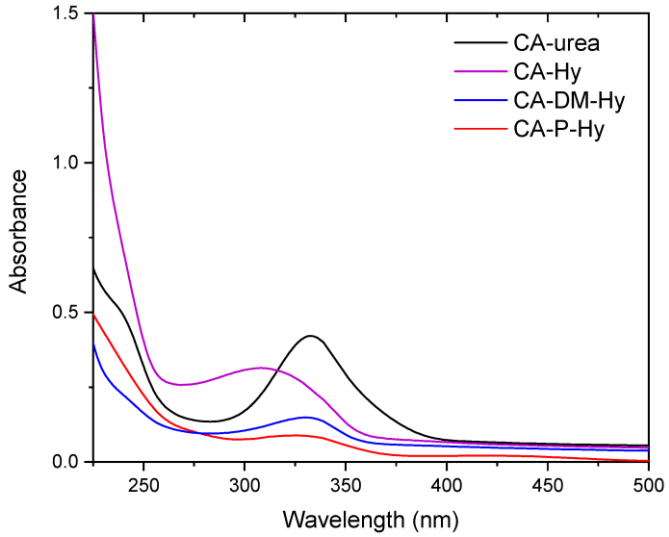

Figure 6.3.1. Absorption spectra of the hydrazine-based compounds compared to urea-derived carbon dots (CDs).

PL measurements of precursors were also gathered to further clarify the effective formation of the products. The signal collected from precursors was weak, peaking in the near UV spectral range and several orders of magnitude lower than the respective CA and nitrogen sources products, thus confirming that PL properties are ascribed only to the formation of new luminescent products. A complete overview of the photoluminescence properties of the samples can be obtained through excitation-emission maps in which is possible to analyze the intensity of the emission at different excitation wavelengths (**Figure 6.3.2**).

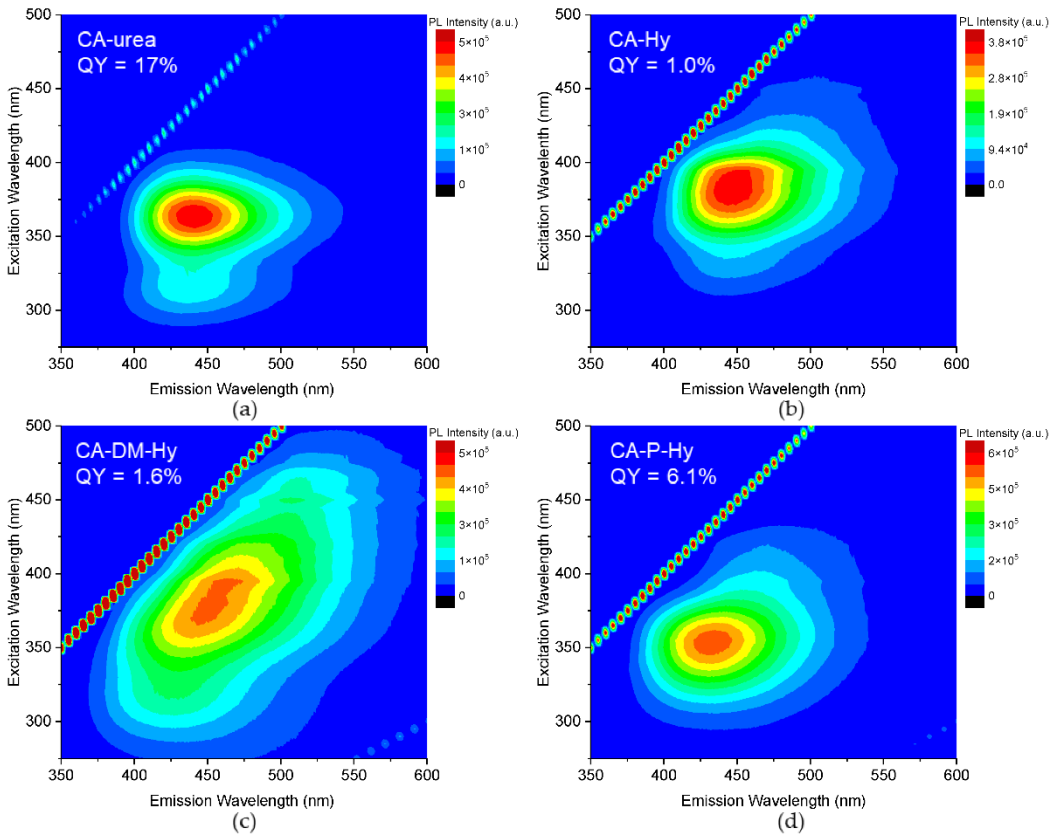

Figure 6.3.2. Excitation–emission maps of our reference CA-urea (a) compared to CA-Hy (b), CA-DM-Hy (c) and CA-P-Hy (d).

Despite the low QY, estimated using as reference an ethanol solution of Coumarin 120 (C120) with spectral features close to our investigated samples (absorption peak at 350 nm, emission at 430 nm, QY = 0.56),[185] PL emission of all products is characterized by an excitation-dependent behavior, which is typical of CDs, indicating the formation of more than one excitation channel and not just a single molecule. Extracting the PL and excitation of PL (PLE) graphs (**Figure 6.3.3**), it is possible to notice that, despite the quite similar absorption spectra, the samples show many differences one to another.

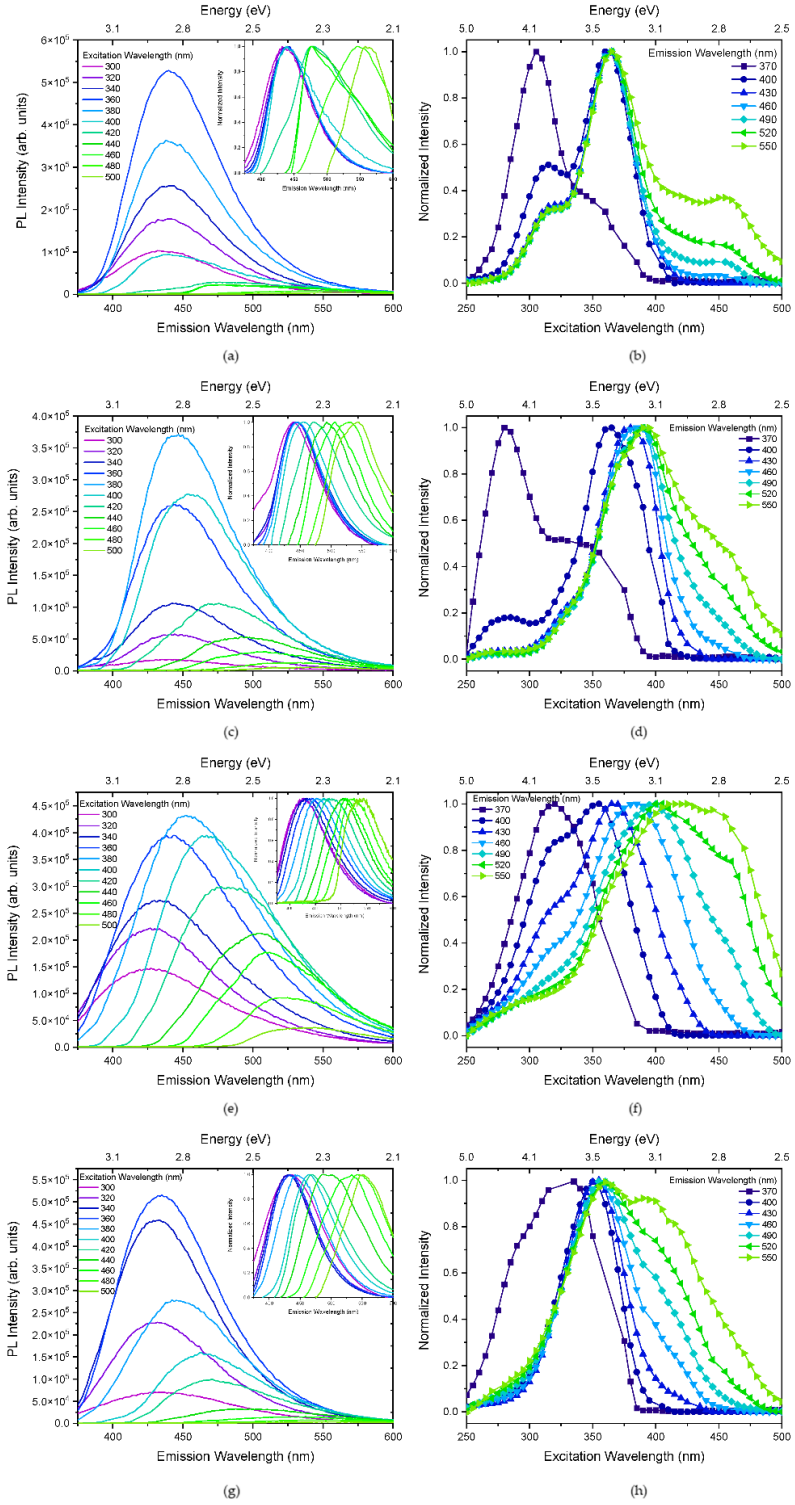

Figure 6.3.3. PL and normalized PL (inset) on the left column and normalized PL excitation (PLE) on the right one of CA-urea (a,b), CA-Hy (c,d), CA-DM-Hy (e,f) and CA-P-Hy (g,h).

The reference derived from urea (**Figure 6.3.3**a–b) has the highest QY (17%) and presents basically three excitation channels: those around 310 and 360 nm which both brought to the emission at 440 nm and another oat about 460 nm that led to a weak contribution in the green region. Previous studies attributed these optical features to the presence of citrazinic acid and citrazinic amide in the structure of CD.[22,120] CA-Hy (**Figure 6.3.3**c–d) has the highest luminescent emission at 450 nm, with the main excitation channel centered at about 380 nm. Even in this case we can distinguish two more excitation channels: one at 290 nm, responsible for the near UV emission, and another one that arises at above 490 nm, which brought a green contribution. Overall, even if the sample presents a low QY (1.0%), it does show a clear tunable emissive behavior. A clearer example of this peculiar characteristic is shown in CA-DM-Hy (**Figure 6.3.3**e–f), that not only presents an interesting broad emission centered around 455 nm under an excitation of 380 nm but also a great tunability under increasing excitation. Indeed, a slight change in the excitation results in an appreciable shift of emission, a property that makes this product potentially adaptable for a wide range of applications despite the low QY (1.6%). Finally, CA-P-Hy (**Figure 6.3.3**g–h) displays the highest QY among the hydrazine products (6.1%) and the main emission band centered at 440 nm, resulting from the 350 nm excitation, represents the main contribution, paired with a blue excitation above 410 nm accountable for the emission at longer wavelengths. In all these cases, the evident tunability of the optical properties let us to suppose that the formation of hydrazine related CDs was of a different nature as compared to CA-urea sample.

TR-PL measurements performed at 350 nm and 410 nm (**Figure 6.3.4**) confirm the presence of multiple emission channels.

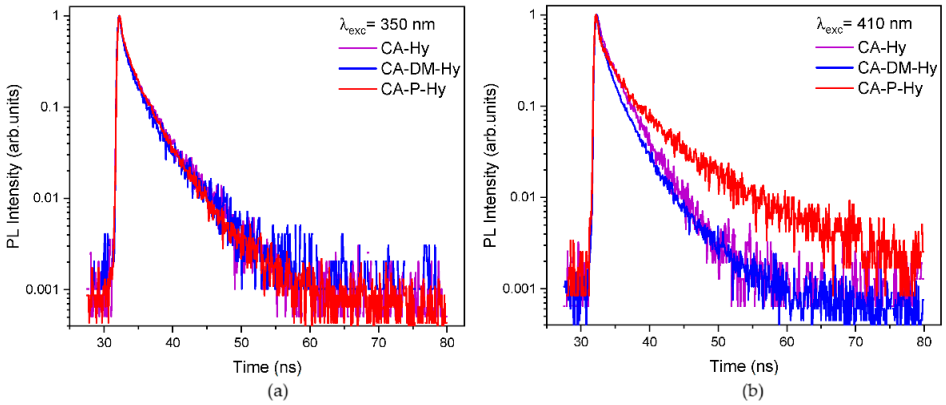

Figure 6.3.4. Decay time plots in the 50 ns range of the hydrazine-derived samples excited at 350 (a) and 410 nm (b). The decay time was recorded on the overall emission spectrum.

Indeed, this behavior is displayed by the non-single exponential profile of decay time investigated in the 50 ns time window (except for CA-urea which was measured in the 100 ns time window, **Figure S.6.2**).

The average decay times were estimated through a multi-exponential fit with two or three decays according to the sample under exam (**Figure S.6.2**, **Table S.6.1**). In all the cases, a sub-nanosecond decay time close to the time resolution of 0.4 ns (estimated by means of the signal from 10% to 90% rise time) has been reported. The average time was evaluated by calculating the fractional contribution of each fitted decay time.[122] All hydrazine composites excited in the 350 nm region show a decay time of about 2.6 ns. which let us imagine that the source of this emission could be the same in all samples. Instead, in the urea sample, the estimated lifetime is 5.6 ns, longer than in the other products, a value close to the one reported in the literature.[117,154,186] Exciting the samples at higher wavelength, the average lifetime is the same in CA-Hy and CA-DM-Hy, but it definitely increases in CA-P-Hy with the presence of a longer time of 8.8 ns and reaching an average lifetime of 5.1 ns, close to that of CA-urea of 4.6 ns.

Table 6.3.2. Fitting results of decay time data excited at 350 and 410 nm in the 50 ns window. A_i is the pre-exponential factor, τ_i is the lifetime, f_i is the fractional contribution and $\langle\tau\rangle$ is the average lifetime (calculated as in Table S.4.5).

Sample	λ_{exc}	A_1	τ_1 (ns)	A_2	τ_2 (ns)	A_3	τ_3 (ns)	f_1	f_2	f_3	$\langle\tau\rangle$ (ns)
CA-urea[1]	350	1141	0.7	1025	3.1	566	8.2	0.09	0.37	0.54	5.6
CA-Hy	350	1310	0.5	890	3.1	-	-	0.19	0.81	-	2.6
CA-DM-Hy	350	659	0.6	384	3.1	-	-	0.24	0.76	-	2.5
CA-P-Hy	350	1795	0.3	1890	1.4	1304	3.6	0.06	0.33	0.61	2.7
CA-urea	410	1578	0.4	1139	2.4	608	6.8	0.09	0.36	0.55	4.6
CA-Hy	410	795	0.8	836	3.0	-	-	0.20	0.80	-	2.6
CA-DM-Hy	410	3119	0.4	3267	1.7	950	4.2	0.13	0.51	0.37	2.5
CA-P-Hy	410	761	0.4	533	2.6	150	8.8	0.10	0.46	0.44	5.1

[1] Analyzed in the 100 ns time window with time resolution of 0.7 ns.

Moreover, Raman analysis suggests the formation of CD-like structures. Raman spectra were collected in the 600–1850 cm^{-1} region using SERS supports which allow the enhancement of the vibration signals, reducing the fluorescence of the samples (**Figure 6.3.5**).

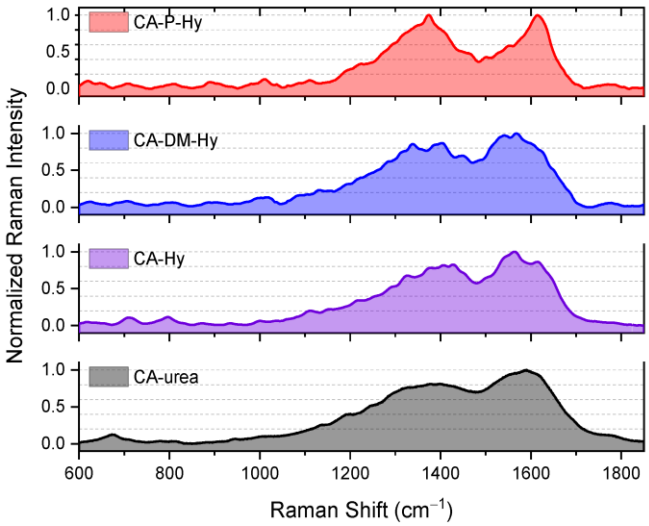

Figure 6.3.5. Raman spectra of the hydrazine-based compounds compared to urea-derived CDs.

All samples present two major peaks centered at about 1360 and 1580 cm^{-1}, which are generally ascribed to sp^3 and sp^2 hybridized carbon structures and are often reported in CD literature. [85,149,187,188] Indeed, the so-called D band at 1360 cm^{-1} is associated with disordered carbon systems, whilst the G band at 1580 cm^{-1} is typical of graphite and consequently is related to graphitic morphology. For evaluating the relative contribution to the structure of the graphitic core state and the disordered surface state, it is useful to calculate the ratio of these bands. Roughly considering the height of the peaks, the highest level of disorder was reported for the CA-P-Hy sample ($I_D/I_G \approx 1$), which suggests that it is a poor graphitic system. Slightly lower values are associated with the other hydrazine-based samples ($I_D/I_G \approx 0.8–0.9$) which present similar spectra, only with small differences in the D band multiple peaks due to the high sensitivity of SERS supports. Even the urea-derived reference sample shows an analogous disorder/order ratio value ($I_D/I_G \approx 0.8$) along with the most smoothed spectrum with little presence of defined peaks, which could be due to the completed formation of CDs. Smaller vibrational peaks gathered upon the larger signal of the two main bands are present and well above the sensitivity limit of the measurement. These vibrational findings have also been confirmed by simulated results (see computational results and **Figure S.6.3**).

TEM images of hydrazine-derived CDs are reported in **Figure S.6.4**. The images show that the performed synthesis produced rounded nanoparticles with a mean size of about 4–5 nm for the CA-Hy and CA-DM-Hy samples and about 10–13 nm for the CA-P-Hy ones.

6.3.2 Computational Results

The possible mechanism of reaction among the two precursors during hydrothermal synthesis is reported in the following scheme (**Scheme 6.1**), where citric acid and hydrazine react to produce a pyridinone molecule —by means of condensation and dehydration reactions—with different possible substituents depending on the starting hydrazine molecule precursor (**Scheme 6.1**, path a). Depending on R and R', we can obtain a simple 1-aminopyridin-2(1H)-one (Hy-CD), a mono-methyl 1-(methylamino)pyridin-2(1H)-one (MM-Hy-CD), a 1-(dimethylamino)pyridin-2(1H)-one (DM-Hy-CD) or a 1-(phenylamino)pyridin-2(1H)-one (P-Hy-CD). In the simulations, we also considered the formation of MM-Hy-CD for completeness' sake, even though it is not experimentally expected considering the exploited precursors. In the case of simple hydrazine, we can also hypothesize that the reaction might evolve through the dimerization (or oligomers formation) as described in the **Scheme 6.1** path b, once more by means of condensation and dehydration reactions, leading to di-pyridinone structures. The formation of the two different products, called Hy-2-CD and Hy-3-CD in the following, is represented in the **Scheme 6.1b**.

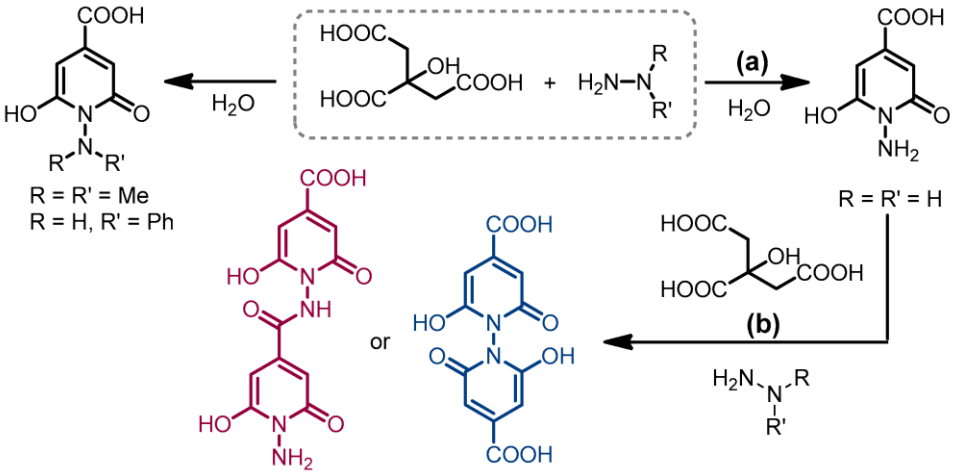

Scheme 6.1. Reaction scheme of citric acid and substituted hydrazine molecules. (a) In the case of hydrated hydrazine, the reaction can further proceed, leading to di-pyridinone structures (b).

We calculated the optimized ground state structures of the possible pyridinone and di-pyridinone molecules (Hy-CD, Hy-2-CD and Hy-3-CD) and simulated their optical absorption spectra in the UV-vis range. We also calculated the optical features of the substituted pyridinone structures (MM-Hy-CD, DM-Hy-CD and P-

Hy-CD). Finally, for all the structures, we calculated the vibrational spectra, both IR and Raman.

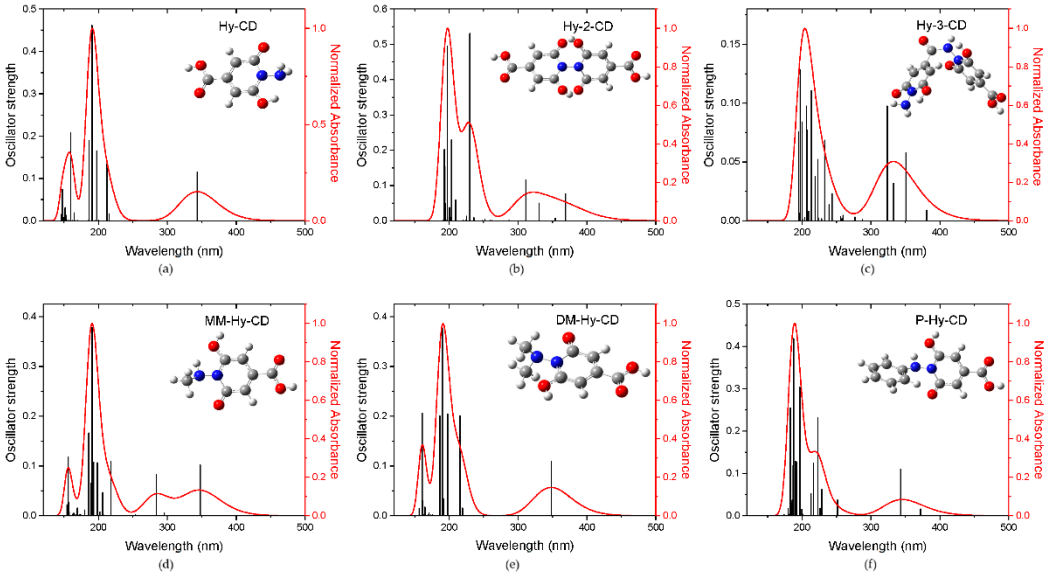

Figure 6.3.6. Simulated absorbance spectra and oscillator strength of pyridinone molecules. The insets report the ball-and-stick representation of the structures (H atom—white sphere, C atom—grey sphere, N atom—blue sphere, O atom—red sphere). (a) Hy-CD, (b) Hy-2-CD, (c) Hy-3-CD, (d) MM-Hy-CD, (e) DM-Hy-CD, (f) P-Hy-CD.

As reported in **Figure 6.3.6**a–c (top panel), all of the three molecules can provide transitions, accounting for an absorption band around 350 nm and a higher energy band in the 150–250 nm range. The normalized absorbance spectra (continuous red line in the figure) were simulated by assuming Gaussian bands of 0.33 eV half width at half height of the peaks centered at the transition energies of the first 20 calculated excited states (whose oscillator strength is reported as vertical black lines in the figure). The first absorbance band in the simplest Hy-CD mono-pyridinone structure is due to the single Highest Occupied Molecular Orbital (HOMO) to the Lowest Unoccupied Molecular Orbital (LUMO) transition, located at 344 nm. The di-pyridinone structures show a larger absorbance band around 350 nm with a redshifted HOMO–LUMO gap, at 369 and 381 nm for the Hy-2-CD and Hy-3-CD molecules, respectively. Concerning the substituted pyridinone structures, they also provide similar absorbance features (**Figure 6.3.6**d–f, bottom panel) with a HOMO–LUMO gap at 348 nm, 350, and 372 nm for MM-Hy-CD, DM-Hy-CD, and P-Hy-CD, respectively. We note that the MM-Hy-CD structure presents a second excitation band around 300 nm, not observed in the other structures, and the P-Hy-CD structure displays the

most redshifted optical transition among the substituted pyridinone structures. The computed vibrational features of the hydrazine precursors and those of the pyridinone structure are compared in **Figure S.6.5** in the 1250–1700 cm^{-1} band, where the G and D bands were experimentally observed. None of the precursor vibrational modes were present in both the 1350–1400 and 1550–1600 cm^{-1} regions, whilst the pyridinone structure shows two bands at 1400 and 1580 cm^{-1}.

To further explore the scenario, we considered for the Hy-CD case the formation of some typical aggregates already proposed for the CZA and IPCA systems[43,44,126,164,189], namely the parallel and anti-parallel stack dimers and the head-to-tail in the plane dimer. We calculated the absorption spectra for the aggregate systems at a fixed distance between the monomer units, namely at 0.366 nm for the stack dimers and at 0.288 for the heat-to-tail dimers, assuming the same geometries of the parent CZA system. We also let the dimers relax and calculate the absorption spectra in the optimized relaxed configurations. The spectra are reported in **Figure 6.3.7**: all the structures display a large absorption band in the 300–400 nm range, with HOMO–LUMO transition at 377 and 358 nm for the fixed and relaxed parallel stack dimers, at 389 and 394 nm for the fixed and relaxed anti-parallel stack dimers and at 354 and 356 nm for the fixed and relaxed head-to-tail dimer.

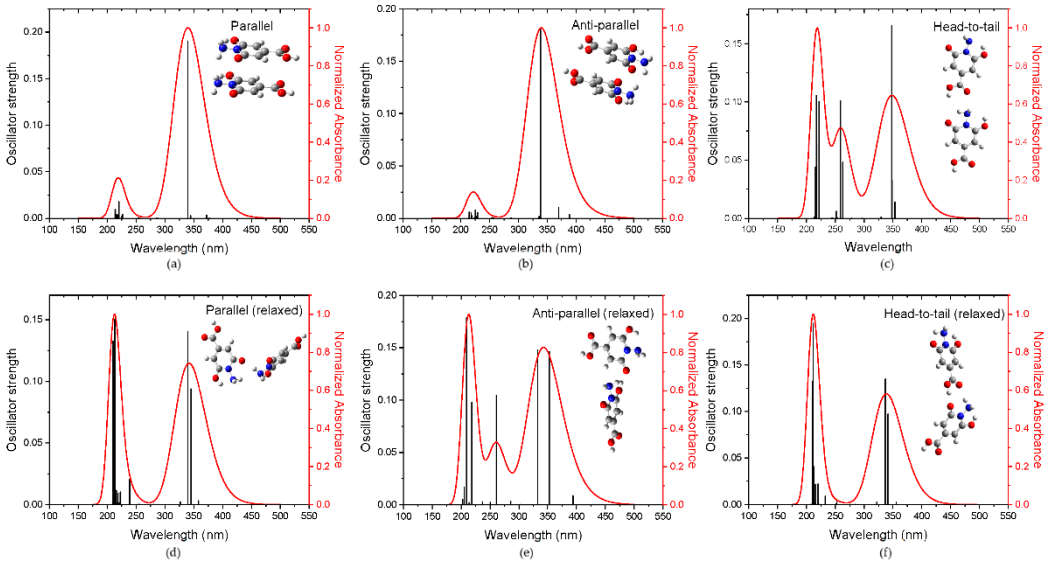

Figure 6.3.7. Simulated absorbance spectra and oscillator strength of parallel, anti-parallel and head-to-tail dimers for fixed geometries (a–c) and for the corresponding relaxed geometries (d–f). The insets report the ball-and-stick representation of the structures (H atom—white sphere, C atom—grey sphere, N atom—blue sphere, O atom—red sphere).

Finally, to look for larger redshifts, we considered the formation of some possible polymers. Indeed, one can hypothesize that, during the carbonatation process, some polymeric structure is formed, with the release of water. Among the possible choices, we calculated two potential polymer structures. For the simple Hy-CD system and the substituted di-methyl and phenyl systems we hypothesized the polymer chains that can be obtained when considering the reaction between the carboxyl group of one monomer and the hydroxyl group of another, as represented in **Scheme 6.2** for the case of the Hy-CD structure (this class of polymers will be indicated as O-Polymer in the following). We considered chains of two, three, and four units. A second possibility is to assume the formation of a peptide bond to form the polymer chain, thus considering the reaction of the carboxyl group of one monomer with the amide group of the other (A-Polymer). This bonding is the same that we have in the Hy-3-CD structure, which can be also considered as the first member of the A-Polymer family for the un-substituted hydrazine case (Hy-CD). The formation of the A-Polymer class was not considered for the substituted hydrazine precursors, since we expect that the steric volume of the substituents would reduce the probability of formation of A-Polymer in those cases. Although the reactivity of the amine group would favor the formation of A-Polymers, O-Polymers could also be expected, since the computed difference of formation energy among the two classes for the case of two units' chain was estimated as 4.83 kcal/mol (0.21 eV).

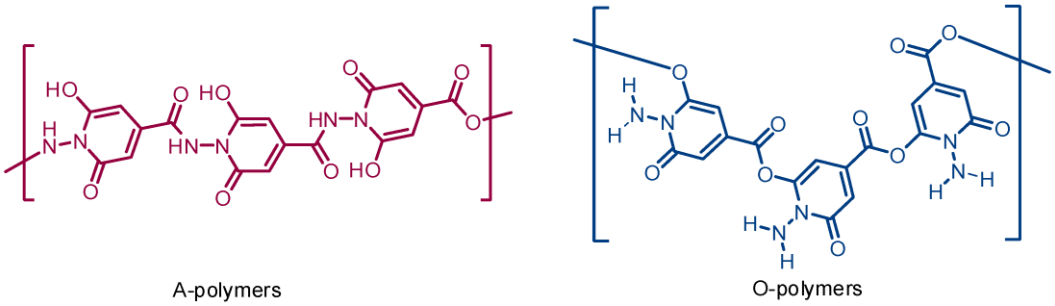

Scheme 6.2. Possible formation of polymeric chains for the Hy-CD case.

The calculated optimized ground state polymeric structures are reported in **Figure S.6.6**, together with the absorbance spectra of those structures.

To collect the general trend, in **Figure 6.3.8** we report the position of the HOMO–LUMO transition as a function of the number of monomer units for both the O-Polymer and A-Polymer classes. As we can see, the longer the chain the

larger the redshift, a sort of saturation effect in the redshifting being recorded for all the structures except the DM-Hy-CD ones.

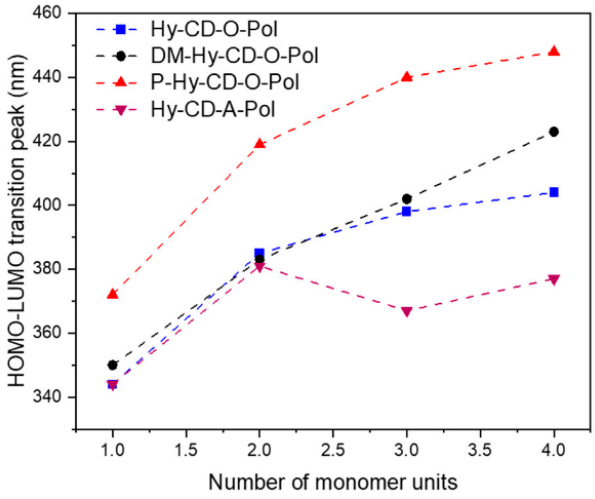

Figure 6.3.8. HOMO–LUMO transition wavelength as a function of the number of monomer units for the two classes of hypothesized polymers (lines are guides for the eyes).

Finally, we calculated the molecular orbitals (MOs) for the HOMO and LUMO states for all the simulated structures. In **Figure 6.3.9** we report, as an example, the MOs for the Hy-CD case and its O-polymer derivatives.

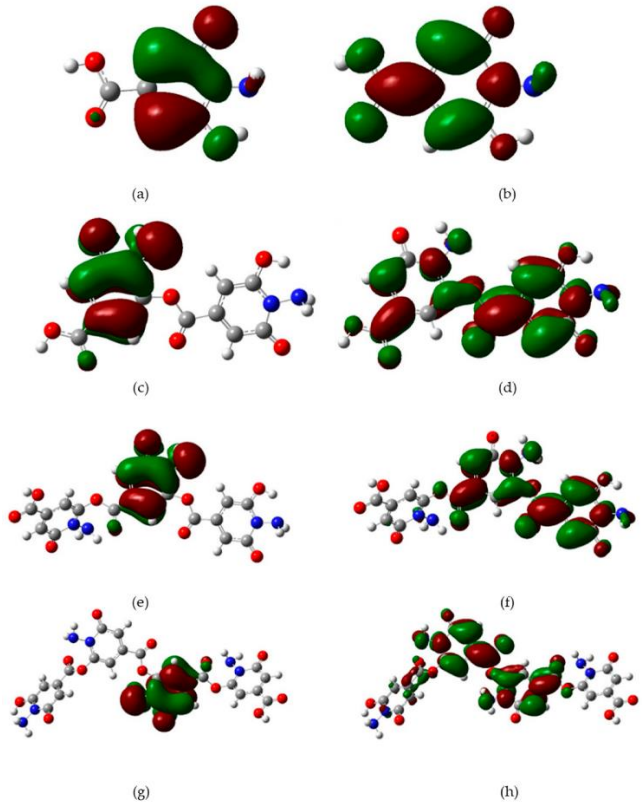

Figure 6.3.9. MOs of the HOMO–LUMO states (HOMO on the left and LUMO on the right) for the Hy-CD system (a,b) and its O-Polymer derived: Hy-CD-O-Pol-2 (c,d), Hy-CD-O-Pol-3 (e,f), Hy-CD-O-Pol-4 (g,h). The isocontour value is 0.02 au (H atom—white sphere, C atom—grey sphere, N atom—blue sphere, O atom—red sphere).

The reported data depict an n–π* transition for the whole set of structures, with the electronic charge distributed upon a single unit in the HOMO state and spread upon two units in the LUMO state, partially extending through the chain bonding for the cases with three and four units.

6.3.3 Discussion

The optical features of CDs are, in general, ascribed to three main mechanisms: the quantum confinement effects, related to the formation of graphitic core, the presence of molecular species, or the formation of surface centers related to the surface functionalization groups.[19,20] The formation of fluorescent molecules that can act as a seed for the CD enucleation or could be incorporated within the carbon network is the most accredited model in the case of bottom-up synthesis. The target of this study is the proof of concept of the formation of hydrazine-

related CDs. The whole set of experimentally observed features here reported calls for the formation of CDs: the rounded nanoparticle observed by means of TEM (mean size 5–12 nm), the measured D and G vibrational bands, the absorption band around 350 nm, the excitation dependent emission spectra and the non-single exponential decay times. As already proposed for parent CA-derived systems, those features are related to the formation of some specific molecule, as the IPCA and CZA molecules reported in those cases.[22,43,54,126] Starting from this consideration, we hypothesized that the pyridinone molecules produced during the synthesis of CA and hydrazine, their aggregated forms, or some polymeric structure derived by further reactions of the monomer units can be incorporated into the structure of the CDs and produce the optical features experimentally recorded. Indeed, if we consider the case of IPCA, a reaction of cyclization between CA and ethylene-diamine was hypothesized to produce the molecule that acts as a seed for the formation of the CDs and cause, with its aggregates, the excitation-dependent emission features recorded in those systems.[44,54,189] In a similar way, we recently studied the formation of CZA in the synthesis of CA and urea (the reference system in the present study) and we demonstrated that the formation of various ionic species and different aggregates can explain the optical features of citric acid derived CDs.[43,101,126,164] If we assumed the same reaction paths reported for CZA and IPCA, more than one product could be embedded during the CD formation. To also test this hypothesis in the present case, we calculated the vibrational and optical absorption spectra of different possible structures that we expect could be formed during the hydrothermal synthesis and compared the simulations to the experimental results. We first discuss Raman properties. Raman spectroscopy is largely applied to explore CD structures and in particular to evaluate the sp^2/sp^3 ratio, which is an important parameter also concerning the attribution of the emission properties, especially when applying the core-shell model.[117,190] We considered the computed vibrational features of the hydrazine precursors and compared them to the ones of the pyridinone structure. As reported in **Figure S.6.5**, the formation of these structures produces a few vibrational modes in the 1250–1700 cm^{-1} range, that of the experimentally observed D and G band (**Figure 6.3.5**, **Figure S.6.3**). Among the others, the two vibrational modes at 1400 and 1580 cm^{-1} are related to symmetric and asymmetric stretching vibrations of the atoms of the pyridinone ring. Similar results were obtained for all the simulated structures with the pyridinone ring. The precursors, on the contrary, did not show paired vibrations that could be referred to as the G and D bands. Moreover, the experimental Raman spectra are very similar to the reference CD sample. The presence of some overimposed fine

structures can be related to the presence of polyaromatic hydrocarbon structures, which could also give similar results.[191] These findings support, from one side, the hypothesis of the formation of the pyridinone structure, and from the other, the possible formation of CDs in the synthesis of CA and hydrazine compounds. Looking at the optical features, we considered both a single pyridinone molecule produced by the cyclization of citric acid and hydrazine (Hy-CD) and the formation of di-pyridinone structures obtained by the reaction of the first system with residual citric acid and hydrazine in the solution (Hy-2-CD and Hy-3-CD). The simulated spectra (**Figure 6.3.6**) display two bands in the near and far UV in good agreement with previously calculated results on parent structures (CZA and IPCA) and in good agreement with the reported experimental absorption measurements (**Figure 6.3.1**). Concerning the absorption band in the 300–350 nm range, typically ascribed to an n–π* transition in CDs, as also confirmed by our calculated MOs for all the considered structures (**Figure 6.3.9,** and **Figure S.6.7** and **S.6.8**), we note that the present experimental results and the ones reported in the literature on similar hydrazine-related CDs show a peak at about 330 nm, thus preferentially supporting the hypothesis of the single pyridinone molecule instead of the two redshifted di-pyridinone structures. However, the width of the band could indicate the presence of more than one pyridinone species, possibly including the di-pyridinone structures or other systems such as aggregates or polymer chains. Indeed, accounting for the larger sensitivity of the photoluminescence measurements, we should also consider that the excitation-emission maps here reported (**Figure 6.3.2**) display excitation transitions in the 330–450 nm range for the CA-Hy samples, in the 300–450 nm range for the CA-DM-Hy and in the 300–425 nm range for the CA-P-Hy. These data fully support the absorbance spectra of the simulated structures and even call for more complex structures to account for such a large excitation band, in particular for the CA-DM-Hy case. These results also highlight the optical difference between hydrothermally produced urea-derived CDs and these hydrazines compounds, showing that the latter are characterized by a higher tunability with a consequently larger contribution of the emission in the green region. In addition, the non-single exponential decays recorded for the different systems also require the formation of at least two or three different emitting centers. For these reasons, we first considered the formation of a few model aggregates, the parallel and anti-parallel stack dimers, obtained from the parallel or anti-parallel superimposition of two monomer units of Hy-CD, and the head-to-tail dimer, where the two monomer units lie on the same plane. Those aggregates were selected according to the results already reported for CZA and IPCA. Although the absorption spectra

simulated for all the dimers at a fixed distance or after relaxing the system are in the expected 300–400 nm range and could contribute to the experimentally observed absorption band in that range, we still needed to find some structure able to provide redder transitions. In addition, we noted that the relaxed geometries are quite far from those assumed by comparison with the CZA system. Thus, instead of collecting other aggregates' forms, as already proposed for the CZA case,[43] where the broadening of the absorption and excitation bands was smaller than in the present case, we considered the formation of small polymer chains of two, three and four units and the possibility of two different polymerization processes, depending on the chemical groups interested by the reaction. We considered up to four units because it should be noted that the longer the chain, the larger the distance between the two ends of the chain and the distortion of the optimized geometry; when four units are considered, a distance of about 2–3 nm is achieved in the simulated structures, in agreement with the typical average diameter of Carbon Dots. As reported in **Figure 6.3.8**, we calculated, in general, a redshift of the whole spectrum for all the simulated structures, with the HOMO–LUMO transition peak shifting up to 460 nm for the larger phenyl-hydrazine polymer considered. These findings support the hypothesis that besides the presence of more species, the formation of a small polymeric chain can explain the large excitation spectra observed in the experimental data and the possible formation of different emitting centers. We also note that whilst the redshift of the HOMO–LUMO peak seems to converge to a wavelength value in the blue range for the hydrazine and phenylhydrazine systems, this is not the case for the di-methyl one, where the redshift does not show, at least for the length of the chain investigated, the above-mentioned saturation effect. This consideration agrees well with the observed larger excitation band for these CDs and calls for the presence of even longer polymer chains or more complex structures.

6.4 Conclusions

The aim of this work was to investigate the formation of possible fluorescent N–N heterocyclic structures which could represent the seed for the synthesis of CDs and the origin of their emission properties by using, as precursors, N–N bonds containing hydrazines. The experimental results suggest the formation of compounds which present optical characteristics that could be compatible with such structures, as reported in similar synthetic treatment of CA and ammine sources, giving aromatic products such as IPCA and CZA. For instance, Raman and UV-Vis spectra assess the formation of aromatic products that are different

from the original, not cyclic, precursors. Moreover, excitation-emission maps underline that the obtained products show different degrees of emission tunability, in all cases with an emissive region larger than the urea-based CDs. These findings represent a sign of evident non-single-molecule nature that is also confirmed by multi-exponential decay spectra. Despite the low QY that could be increased by high standard sample purification, our products display undoubtedly interesting optical properties. The presence of multiple emission channels can be explained by the presence of different stages of the reaction leading to the formation of pyridinone-based structures. Indeed, since similar reactions were reported for parent fluorophores such as CZA and IPCA that have the tendency to form tautomers and can co-exist in different aggregation states, the same trend is expected to occur in the present case. In order to verify this hypothesis, we simulated the vibrational and optical absorption spectra of possible assembled structures, considering the formation of single and di-pyridinone compounds, also with different substituents depending on the hydrazine precursor. The computed Raman spectra confirmed the formation of the heterocycle structure, also supporting the observed D and G vibrational bands. Although those structures do show a HOMO–LUMO transition in the 300–400 nm range in good agreement with the experimental absorption spectra, we also considered more complicated structures to explain the large excitation band experimentally recorded. Besides some dimers, which provided a small broadening of the main absorption band, we considered the formation of short oligomers that made up to four monomer units. The HOMO–LUMO gap increases as the number of monomer units increases, showing a saturation effect for all the structures except the di-methyl one. Indeed, this system presents the broader excitation pattern, suggesting the formation of even larger polymers. This proof-of-concept work suggests that N–N-doped Carbon Dots could be produced, starting from the formation of hydrazine-derived heterocycle fluorophores. Along with TEM images, the assessed optical properties need to be further confirmed by advanced structural measurements such as XPS and NMR to definitely assess the formation of the pyridinone structures in this new family of CDs.

Chapter 7

Ongoing research: CDs from different precursors

Olla, C.; Rusta, N.; Porcu, S.; Ricci, P.C.; Carbonaro, C.M. **Carbon Dots from Citrazinic Acid: the role of synthetic procedure and the production of HPPT** (ongoing research)

Stagi, L.; **Olla, C.**♦; Carbonaro, C.M. **Phloroglucinol-derived Carbon Dots for LED applications** (ongoing research)

Olla, C.; Stagi, L; Porcu, S.; Hernandez Sanchez, E.; De Toro Sanchez, J.A.; Ricci, P.C.; Carbonaro, C.M. **Bi-functional citric-acid-derived luminescent and magnetic nanoparticles** (ongoing research)

Cappai, A.; Melis, C.; **Olla, C.**♦; Carbonaro, C.M. **Insights on the impact of synthetic conditions on early stages of formation of citric acid-based carbon dots by a molecular dynamics investigation.** (work in preparation)

♦ Collaboration.

7.1 Carbon Dots from CZA and Urea

The thermal reaction of citric acid (CA) and urea is well known to produce citrazinic acid (CZA), but the discovery of its green emitting imidic form known as HPPT, from the same precursors has led to further research into this complex synthetic mechanism. HPTT was discovered as a product of CA and urea mixed in a 1:10 molar ratio and according to the researchers who discovered it, the formation of HPPT requires the formation of CZA or its amide as the first step. It was also stated that HPPT can be formed directly from CZA, but only in non-aqueous conditions, however, no supporting data have been reported.[22] Hence, we attempted to produce HPPT directly from CZA (29 mg) mixed with urea (6, 11, and 60 mg for 1:0.5, 1:1, 1:5 molar ratios, respectively) through hydrothermal treatment (20 mL, 5 hours at 180 °C) and microwave-assisted pyrolysis synthesis (20 mL, 4 minutes at 350 W) (**Figure S.7.1**). The samples were compared to commercially available CZA and HPPT-containing CDs (M-CAMUR 1:10, 0.77 g of CA and 2.6 g of urea) synthesized in a microwave (20 mL, 4 minutes at 350 W). The synthesis conditions of the prepared samples are summarized in **Table 7.1.1**.

Table 7.1.1. List of analyzed samples and relative synthesis conditions.

Sample	Precursor	Synthesis	Temperature/ Power	Time
CZA	Citrazinic Acid	-	-	-
M-CAMUR 1:5	Citric Acid (77 mg), Urea (2.6 g)	Microwave (20 mL)	350 W	4 m
A-CZAUR 1:0.5	Citrazinic Acid (29 mg), Urea (6 mg)	Hydrothermal (20 mL)	180 °C	5 h
A-CZAUR 1:5	Citrazinic Acid (29 mg), Urea (60 mg)	Hydrothermal (20 mL)	180 °C	5 h
M-CZAUR 1:1	Citrazinic Acid (29 mg), Urea (11 mg)	Microwave (20 mL)	350 W	4 m
M-CZAUR 1:5	Citrazinic Acid (29 mg), Urea (60 mg)	Microwave (20 mL)	350 W	4 m

The collected materials were analyzed in water through optical absorption (Agilent Cary 5000 spectrophotometer with a spectral bandwidth of 2 nm in the

200-800 nm range), Surface Enhanced Raman Spectroscopy (S-Silver SERS substrates, SOL Confotec MR750 with 532 nm laser diode and spectral resolution 0.6 cm^{-1}) and TR-PL technique (200 fs long pulses Light Conversion TOPAS-C pumped by a regenerative Ti:Sapphire amplifier Coherent Libra-HE at 1 kHz repetition frequency). Supplementary information is available in Appendix E.

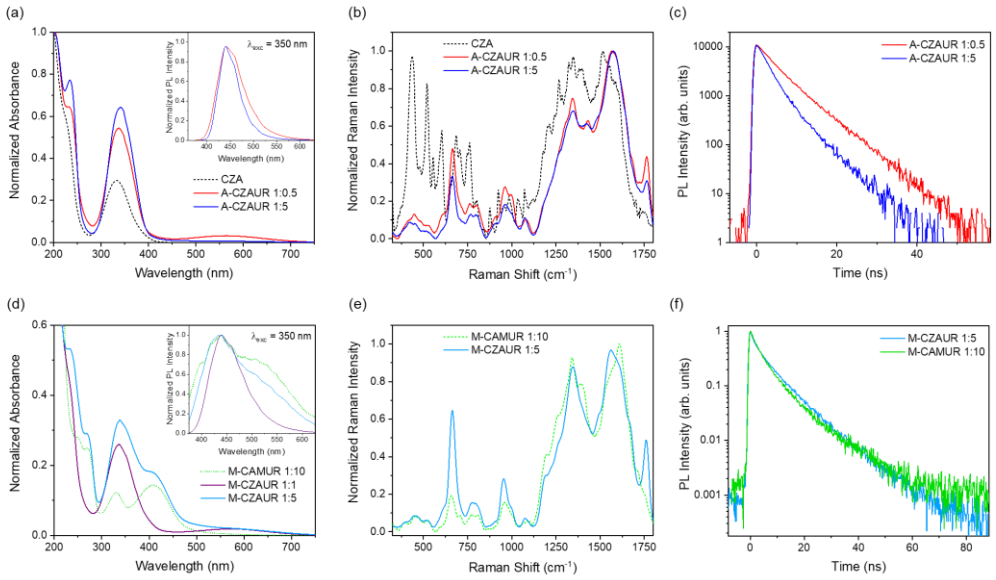

Figure 7.1.1. (a,d) UV-Vis measurements with PL spectra at 350 nm in the inset, (b,e) Raman spectra, and (c,f) decay time plots of the samples.

Our experimental findings on the samples obtained under the hydrothermal synthesis route, named A-CZAUR, show optical features that are similar to the CZA precursor (**Figure 7.1.1**a-c). Besides a slightly broad band in the yellow region in the A-CZAUR 1:0.5 sample, only a small redshift of the typical 335 nm peak and a more defined peak related to the π–π* transition was recorded. SERS spectra provided us with more detailed insights into their differences, showing similar spectra for the synthesized samples with distinct D and G bands that are attributed to sp^3 and sp^2 carbon structures, respectively. Despite similar D and G bands, the CZA Raman spectra present a more structured pattern with many intense peaks in the 400-800 cm^{-1} region, likely due to the aggregation phenomenon, revealing the molecular nature of the sample. Additionally, TR-PL measurements clearly show a shortening of the lifetime with increasing molar ratios of the reagents. The extracted lifetimes from the multi-exponential plots were indeed similar (4.1 and 7.5 ns in A-CZAUR 1:0.5 and 3.0 and 8.0 ns in A-CZAUR 1:5), but the resulting average decay was 5.6 ns and 3.5 ns for the 1:0.5

and 1:5 sample, respectively, displaying a significant variation in the relative contributions.

Regarding the samples produced via microwave-assisted pyrolysis (**Figure 7.1.1**d-f), the one obtained from a 1:1 molar mixture showed the characteristic CZA band, indicating the unsuccessful production of any green contribution. However, a more fruitful reaction was achieved in the synthesis of the M-CZAUR 1:5 sample, where two absorption contributions peaked at 340 and 410 nm, corresponding to the same peak positions recorded for our reference M-CAMUR 1:10, but with different intensity ratios. The emission at 350 nm excitation wavelength shows very broad bands for these two samples, with a significant increase in the green contribution in the 1:5 sample compared to the 1:1 sample, similar to the CAMUR sample. Furthermore, the SERS spectra and the decay time plots proved their similarity with the reference, showing similar Raman peaks and lifetimes (7.8 and 7.4 ns), respectively.

With these measurements, we have demonstrated that the optical features of HPPT can be reproduced starting from CZA and urea in a 1:5 molar ratio treated with microwave-assisted pyrolysis. Nevertheless, intrigued by the inhomogeneous appearance of this sample, we mechanically extracted two phases from the obtained powder, a blue (B) and a green one (G), and separately investigated their properties (**Figure S.7.2**). **Figure 7.1.2** indeed shows that during the synthesis, at least two contributions were formed with different emissive properties, one emitting in the blue region and the other in the green region, diverse Raman spectra with more intense peaks in the 500-1000 cm^{-1} and at 1750 cm^{-1} for the blue phase, and also various lifetimes, as it was 6.8 ns for the blue and averaged 5.8 ns for the green phase.

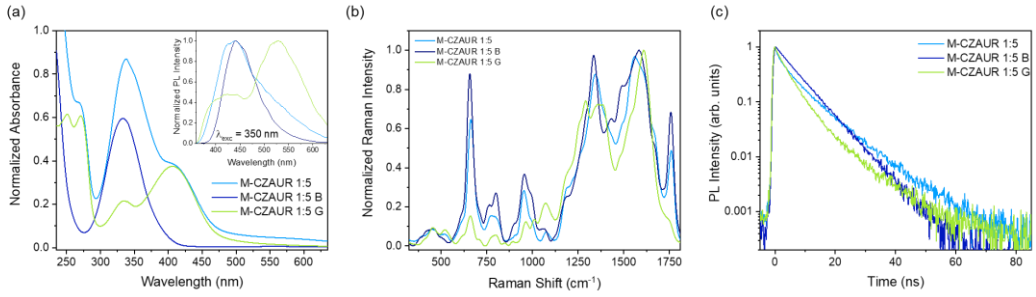

Figure 7.1.2. (a) UV-Vis measurements with PL spectra at 350 nm in the inset, (b) Raman spectra, and (c) decay time plots of the samples.

Indeed, it is clear that the blue-emitting powder has optical and structural features that are very akin to the samples obtained through the hydrothermal

synthesis, while the green phase has many similarities with the HPPT-containing reference as shown in **Figure 7.1.3**.

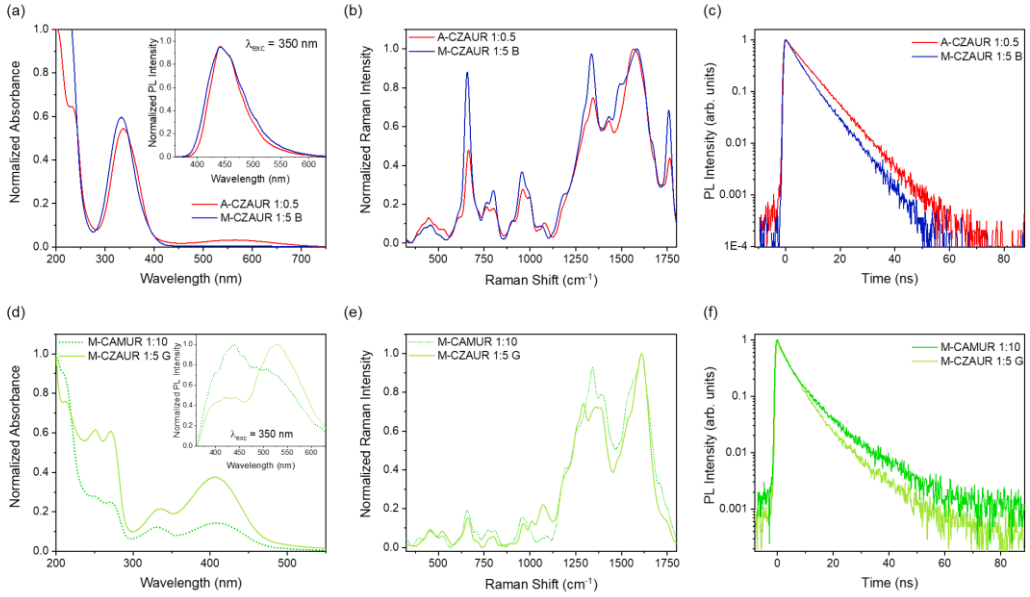

Figure 7.1.3. (a,d) UV-Vis measurements with PL spectra at 350 nm in the inset, (b,e) Raman spectra, and (c,f) decay time plots of the obtained samples.

This ongoing research experimentally demonstrates the production of potential CD structures starting from CZA, whose optical properties can be adjusted not only by changing the precursor molar ratio but also by varying the synthesis treatment. In the future, it will be completed by adding additional structural measurements to evaluate the formation of CDs and to deepen the the understanding of the formation mechanism involved.

7.2 Carbon Dots from Phloroglucinol

Phloroglucinol (FG) is a three-fold symmetrical molecule that is mainly used in the synthesis of pharmaceuticals and explosives. Recently, Yuan and coworkers[192] have successfully employed it in the hydrothermal synthesis of triangular CDs with high efficiency and narrow bandwidth for LED applications. Motivated by this work, we attempted to synthesize CDs from the same precursor using another synthetic route, which is pyrolysis in air atmosphere (A) and in vacuum (V, 1.5×10^{-4} mbar) at temperatures of 200 and 250 °C and reaction times of 5 and 10 hours. The conditions of the synthesized samples are summarized in **Table 7.2.1**.

Table 7.2.1. List of analyzed samples and relative synthetic conditions.

Sample	Precursor	Environment	Temperature	Time
P	Phloroglucinol	-	-	-
FG-A-200x5	Phloroglucinol	Air	200 °C	5 h
FG-V-200x5	Phloroglucinol	Vacuum	200 °C	5 h
FG-A-200x10	Phloroglucinol	Air	200 °C	10 h
FG-V-200x10	Phloroglucinol	Vacuum	200 °C	10 h
FG-A-250x5	Phloroglucinol	Air	250 °C	5 h
FG-V-250x5	Phloroglucinol	Vacuum	250 °C	5 h

Some of the early findings for what concern Raman (SOL Confotec MR750 with 532 nm laser diode and spectral resolution 0.6 $cm^{-}1$), optical absorption (Jasco V-750 spectrophotometer, spectral bandwidth of 0.2 nm in the 200-800 nm range) and steady-state PL properties (Jasco FP-8550 spectrofluorometer in the 250-550 nm excitation and 275-750 nm emission range, with spectral bandwidth of 5 and 1 nm) were reported in **Figure 7.2.1** (supplementary information in Appendix E).

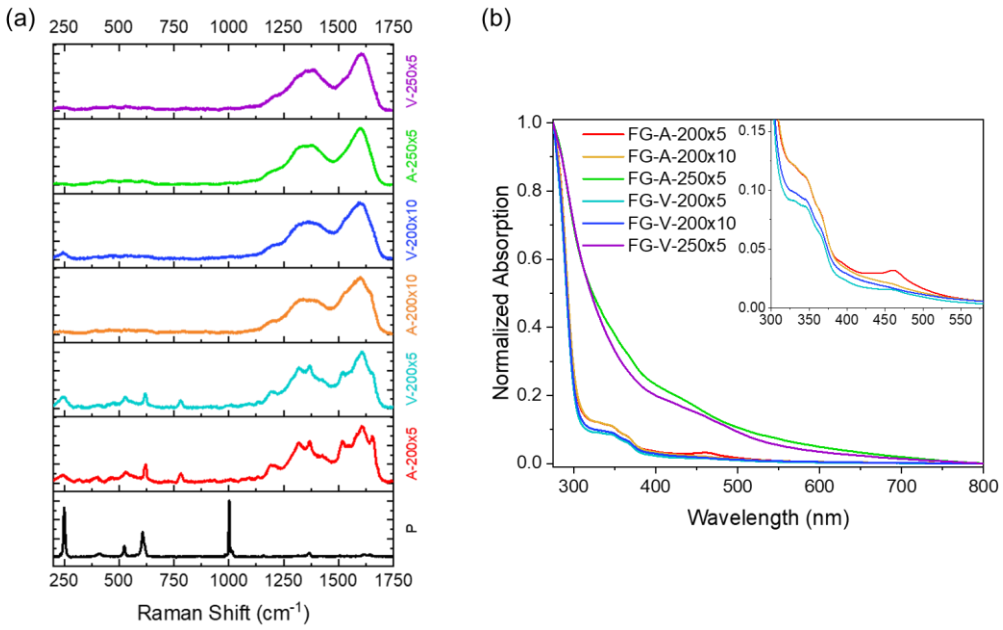

Figure 7.2.1. (a) Raman spectra and (b) UV-Vis absorption spectra with a zoom in the inset of the obtained samples.

The Raman spectra indicated the lack of molecular phloroglucinol peaks in the syntheses carried out at 250 °C for 5 hours or 200 °C for 10 hours. However, the thermal treatment performed at 200 °C for 5 hours displayed a more defined structure. In all cases the occurence of the D and G bands indicated the formation of a graphitic-like structure, as is typical in CD findings. The absorption measurements confirmed the formation of different products, as pure FG does not show any absorption contribution above 300 nm. The products obtained at 250 °C for 5 hours presented a very broad shoulder that extended up to 700 nm whilst all the samples produced at 200 °C showed more defined absorption contributions, with a shoulder peaked at 350 nm and a band at 460 nm. To study their emissive properties, EEMs were collected for each sample (**Figure 7.2.2**).

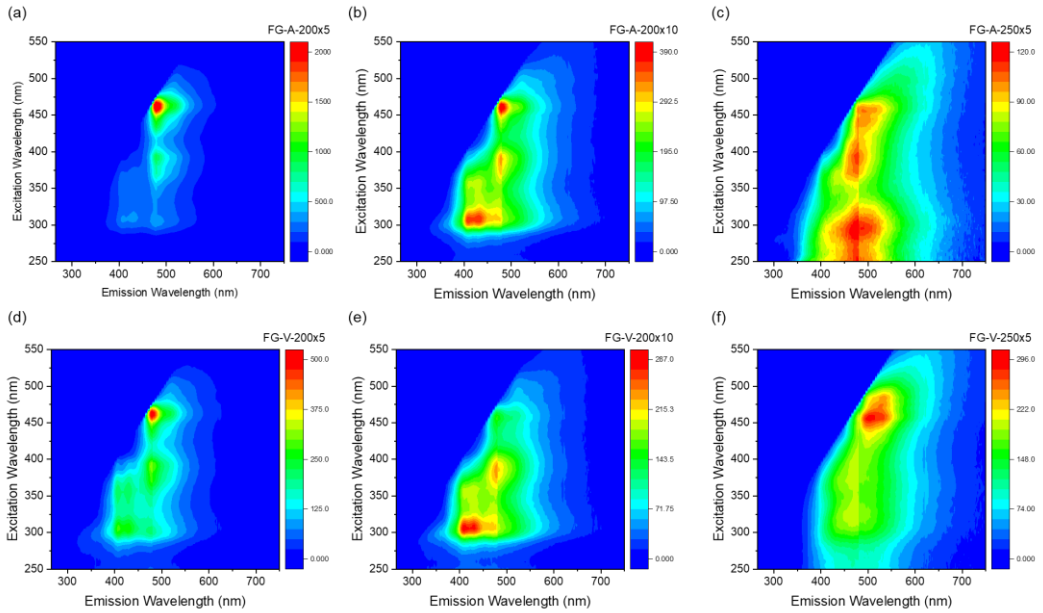

Figure 7.2.2. Excitation and Emission Maps (EEMs) of FG-A-200x5 (a), FG-A-200x10 (b), FG-A-250x5 (c), FG-V-200x5 (d), FG-V-200x10 (e), FG-V-250x5 (f).

These measurements revealed the presence of multiple emissive bands, whose widths broaden as the synthesis time increases (from 5 to 10 hours) and temperature increases (from 200 to 250 °C). Specifically, when focusing on the synthesis performed in air, the main emissive contribution at 200 °C for 5 hours was recorded at 480 nm when excited at 460 nm excitation wavelength, with minor emission bands excited at 390 and 310 nm. Other emissive contributions were detected in the blue range at 410 and 430 nm when excited at 310 nm and in the green range at 520 nm when excited at 460 nm. The PL intensity of these minor centers relatively increased as a function of time and temperature, but a

reduction in overall efficiency was also observed. Similar phenomena were observed in the synthesis performed in vacuum, with the notable difference that at longer times, the main emissive center became the blue one at 410-430 nm when excited in the UV region, while enhancing the temperature, the main contribution remained at 480 nm when excited at 460 nm but with broadening features. This work could not only aid in the identification of the emitting centers produced from FG, whose simple structure can be used as a reference for other CDs obtained through bottom-up routes, but it could also make FG a promising precursor for the development of solid-state lasing devices that require narrowband emissions.

7.3 Magnetic Carbon Particles

This research aimed to combine the efficient fluorescence and biocompatibility of CDs with the magnetic properties of gadolinium composites, in order to create bio-functional CDs as contrast agents for both medical magnetic resonance and fluorescence imaging. After several attempts with different Gd-composites as precursors and varying synthetic methods, the most promising material was obtained using monohydrate citric acid (1.0 g), urea (0.286 g) and gadolinium nitrate (0.2 g) dispersed in 20 mL of water in a stainless-steel autoclave and heated at 200 °C for 5 hours (A-GdCAUr sample). The solution was centrifuged at 10 kHz rotation frequency, and both the supernatant and precipitate were studied separately. Magnetic measurements (Quantum Design MPMS-XL system) on the precipitate confirmed the paramagnetic properties of the sample, due to the presence of gadolinium (Langevin paramagnetism), as shown in **Figure S.7.3** (supplementary information is available in Appendix E). Nevertheless, SEM-EDX measurements (Zeiss GeminiSEM 500) reported quite large spherical particles composed of carbon (50.1 %), oxygen (38.5 %), gadolinium (10.6 %) and nitrogen (0.9 %) (**Figure S.7.4**). Indeed, TEM images (Jeol JEM 1400 Plus) displayed possibly porous spheres with a diameter size of 400-500 nm, much larger than typical CDs (**Figure 7.3.1**).

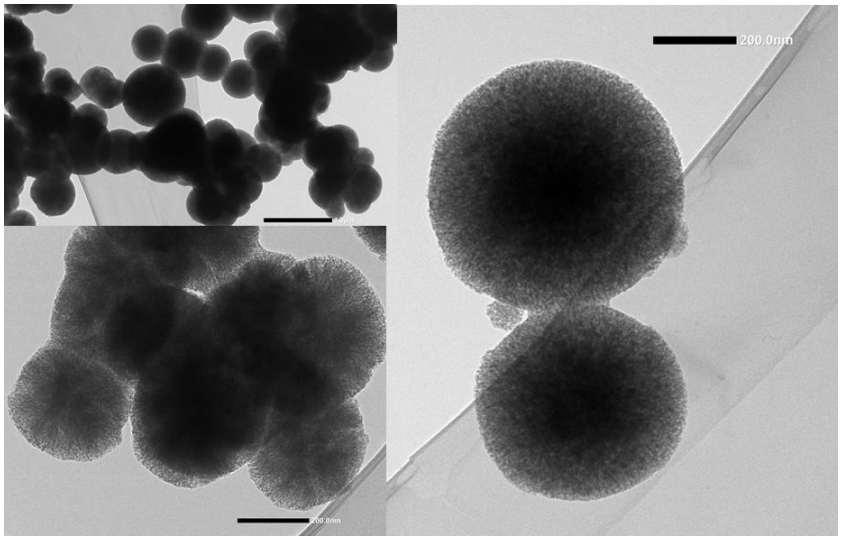

Figure 7.3.1. TEM pictures of the obtained A-GdCAUr product.

TR-PL measurements (200 fs long pulses Light Conversion TOPAS-C pumped by a regenerative Ti:Sapphire amplifier Coherent Libra-HE at 1 kHz repetition frequency) performed under 350 nm excitation wavelength show the typical CA-derived CD blue band peaked at 440 nm for both supernatant and precipitate but different lifetimes (2.5 and 10.2 ns for the supernatant, and 0.6, 4.1 and 11.1 ns for the precipitate).

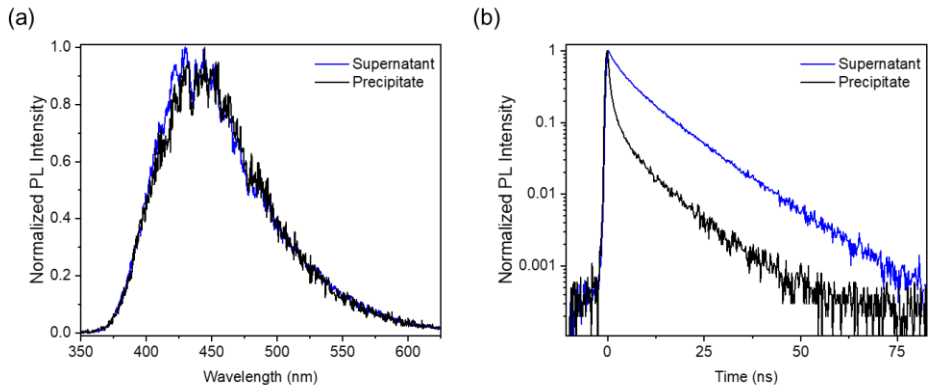

Figure 7.3.2. (a) TR-PL spectra and (b) decay time plot of the supernatant and precipitate of the obtained samples.

In an effort to gain a deeper understanding of the material's structure, we attempted to conduct Raman measurements on the precipitate sample. However, the high level of luminescence unexpectedly prevented the detection of weaker Raman signals. Indeed, under continuous wave (CW) laser excitation at 410 nm, the PL peak was centered at 530 nm, and under 530 nm CW excitation, it was

peaked at 620 nm (**Figure 7.3.3**). This excitation-wavelength dependence was not recorded with TR-PL instruments, most likely due to the differences in the time scales analyzed.

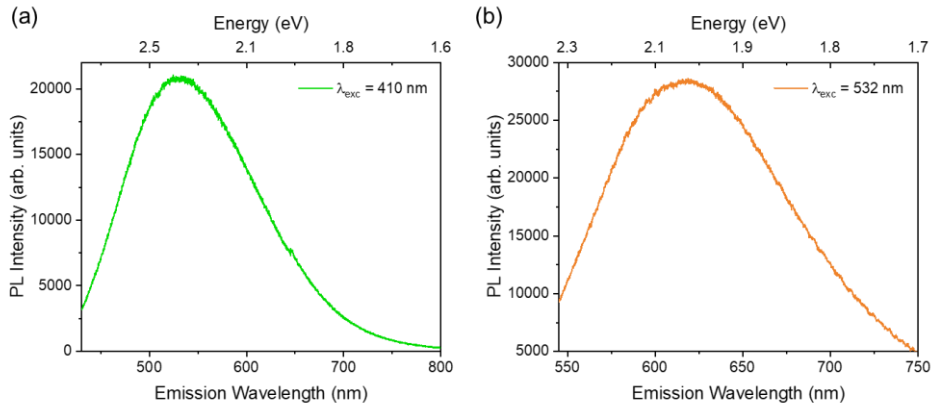

Figure 7.3.3. PL spectra of A-GdCAUr powder under CW laser light at 410 nm (a) and 532 nm (b).

Despite the fact that this material does not display typical CD characteristics, this research could still be valuable for the development of a material with both luminescent and magnetic properties that could be useful for both biomedical and optoelectronic applications.

7.4 Carbon Dots from CA and EDA

As previously stated in **Chapter 2**, computational simulations are an essential tool for the investigation of CD properties and formation. Unfortunately, a full ab-initio dynamical description of CD structure and reaction mechanism involving organic molecules is currently not feasible due to their high complexity. To address this challenge, a hybrid computational approach was employed in this study to investigate the early stages of IPCA production from CA and EDA via the hydrothermal synthesis route. This approach combined DFT to describe the bond thermodynamics and MD to simulate the overall kinematics of the reaction. Four potential reactions were analyzed and the activation energies were determined from Gibbs free energy variations (**Figure 7.4.1**).

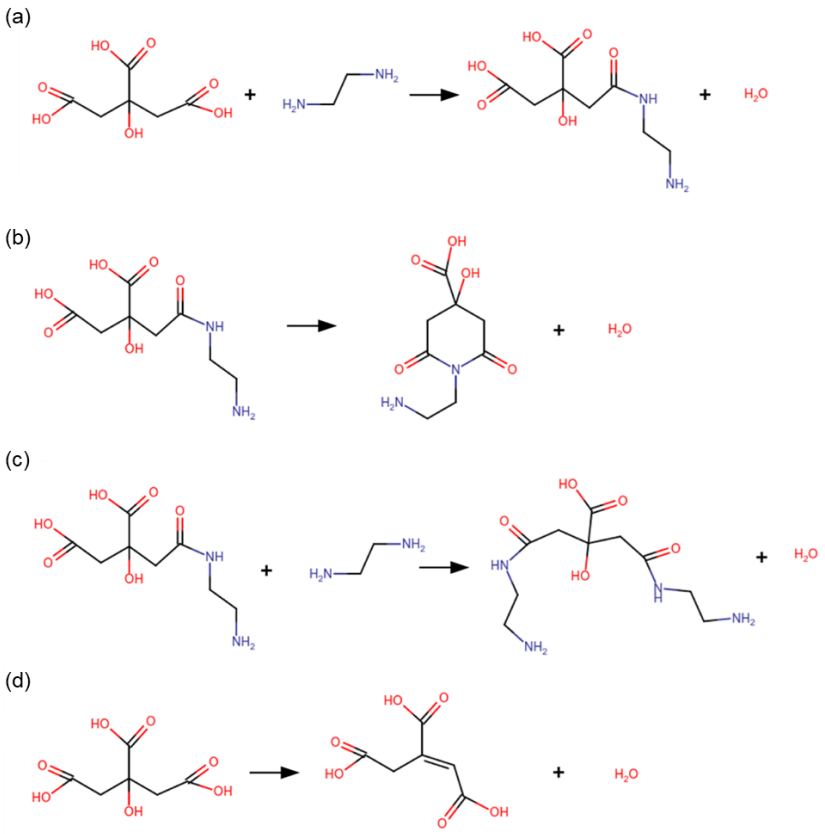

Figure 7.4.1. Reaction schemes analyzed in this work: (i) condensation of citric acid and ethylenediamine (dimer formation); (ii) cyclization; (iii) condensation of the dimer with an ethylenediamine molecule; (iv) decomposition of citric acid to transaconitic acid.

After conducting benchmark calculations to validate the DFT and MD protocols, the energy profiles of each reaction were determined. The evolution of chemical bonds was then investigated through MD simulations, examining the progression of the reaction at different temperatures and pressures typical of a closed vessel hydrothermal synthesis. The results showed that fluorophore precursors were primarily formed at the lowest temperature of 413.15 K, while higher temperatures resulted in an increase in the formation of optical inactive byproducts.

Chapter 8

Conclusions

This thesis work was fully developed within the framework of the three-year CANDL[2] project, with the specific aim of understanding the correlation between structure and optical features in Carbon Dots through a combined computational and experimental approach for possible optoelectronic applications.

The importance of theoretical studies focused on this topic was first presented, with particular emphasis on the simulation of the optical properties of doped and functionalized CDs through density functional theory methods. In particular, computational works on nitrogen and oxygen doping were extensively reviewed, highlighting the correlation between the heteroatom position in the structure and its effect on the absorption and emission characteristics.

Our investigation on the interaction of N-doped CDs with silica matrices highlighted the differences among these surface/molecular emitting centers. The emissive contributions of CDs can be tuned either by the pyrolytic synthesis performed directly in silica, which favors the formation of green-emitting N species, or by irradiating the samples in different environments, which allows the observation of surface centers in silica and molecular ones in water.

The role of nitrogen in emission was further discussed by researching the differences between the emissive centers present in bare CDs produced from citric acid as the only reagent and those obtained by adding urea as a nitrogen source to the reaction mixture. Our findings suggested that the core-state centers predominate in the emissive properties of bare CDs, while the presence of

molecular fluorophores as CZA and imidic species are responsible for more efficient luminescence properties.

The formation of these latter species was the subject of a systematic analysis of the reaction pathway of this type of N-doped CDs through nuclear magnetic resonance technique and optical spectroscopy. In addition to the fundamental correlation between the relative amount of nitrogen sources in the synthesis and the redshift of the emission due to the formation of imidic species such as HPPT molecules from CZA, this study demonstrated the use of NMR for the specific investigation of core/surface properties of CDs in solid-state mode and molecular features in samples in solution.

Continuing the focus on the importance of nitrogen in CD optical features, the formation of possible fluorescent N–N heterocyclic systems was explored by studying the products obtained through the hydrothermal treatment of N–N bonds containing hydrazines. The results suggested the formation of such structures with typical optical and structural features of CDs and prompted further research into the involvement of other N-sources in the reaction, such as CZA and EDA.

Finally, ongoing studies have focused on the application of CDs for lighting, such as phloroglucinol-derived products, or for biomedical purposes, such as the magnetic carbon nanoparticles obtained by adding gadolinium nitrate to the reagents.

In conclusion, the presented work provides insight into this incredibly promising nanomaterial, with the hope that its remarkable luminescent properties will be employed in the future for the design of new, non-toxic, and cost-effective optoelectronic devices for everyone.

References

(1) Tomar, R.; Abdala, A. A.; Chaudhary, R. G.; Singh, N. B. Photocatalytic Degradation of Dyes by Nanomaterials. *Mater Today Proc* **2020**, *29*, 967–973. https://doi.org/10.1016/J.MATPR.2020.04.144.

(2) Roduner, E. Size Matters: Why Nanomaterials Are Different. *Chem Soc Rev* **2006**, *35* (7), 583–592. https://doi.org/10.1039/B502142C.

(3) Geoffrion, L. D.; Guisbiers, G. Quantum Confinement: Size on the Grill! *Journal of Physics and Chemistry of Solids* **2020**, *140*, 109320. https://doi.org/10.1016/J.JPCS.2019.109320.

(4) Krishnan, S. K.; Singh, E.; Singh, P.; Meyyappan, M.; Nalwa, H. S. A Review on Graphene-Based Nanocomposites for Electrochemical and Fluorescent Biosensors. *RSC Adv* **2019**, *9* (16), 8778–8881. https://doi.org/10.1039/C8RA09577A.

(5) Wu, Q.; Miao, W.; Zhang, Y.; Gao, H.; Hui, D. Mechanical Properties of Nanomaterials: A Review. *Nanotechnol Rev* **2020**, *9* (1), 259–273. https://doi.org/10.1515/ntrev-2020-0021.

(6) Baig, N.; Kammakakam, I.; Falath, W. Nanomaterials: A Review of Synthesis Methods, Properties, Recent Progress, and Challenges. *Mater Adv* **2021**, *2* (6), 1821–1871. https://doi.org/10.1039/D0MA00807A.

(7) Alivisatos, A. P. Semiconductor Clusters, Nanocrystals, and Quantum Dots. *Science (1979)* **1996**, *271* (5251), 933–937. https://doi.org/10.1126/SCIENCE.271.5251.933.

(8) Reimann, S. M.; Manninen, M. Electronic Structure of Quantum Dots. *Rev Mod Phys* **2002**, *74* (4), 1283. https://doi.org/10.1103/RevModPhys.74.1283.

(9) Sharon, M.; Mewada, A. *Carbon Dots as Theranostic Agents*; 2018. https://doi.org/10.1002/9781119460435.

(10) Xu, X.; Ray, R.; Gu, Y.; Ploehn, H. J.; Gearheart, L.; Raker, K.; Scrivens, W. A. Electrophoretic Analysis and Purification of Fluorescent Single-Walled Carbon Nanotube Fragments. *J Am Chem Soc* **2004**, *126* (40), 12736–12737. https://doi.org/10.1021/ja040082h.

(11) Li, S.; Li, L.; Tu, H.; Zhang, H.; Silvester, D. S.; Banks, C. E.; Zou, G.; Hou, H.; Ji, X. The Development of Carbon Dots: From the Perspective of Materials Chemistry. *Materials Today* **2021**, *51*, 188–207. https://doi.org/10.1016/J.MATTOD.2021.07.028.

(12) Zhu, S.; Song, Y.; Zhao, X.; Shao, J.; Zhang, J.; Yang, B. The Photoluminescence Mechanism in Carbon Dots (Graphene Quantum Dots, Carbon Nanodots, and Polymer Dots): Current State and Future Perspective. *Nano Res* **2015**, *8* (2), 355–381. https://doi.org/10.1007/s12274-014-0644-3.

(13) Facure, M. H. M.; Schneider, R.; Mercante, L. A.; Correa, D. S. A Review on Graphene Quantum Dots and Their Nanocomposites: From Laboratory Synthesis towards Agricultural and Environmental Applications. *Environ Sci Nano* **2020**, *7* (12), 3710–3734. https://doi.org/10.1039/D0EN00787K.

(14) Kundu, S.; Pillai, V. K. Synthesis and Characterization of Graphene Quantum Dots. *Physical Sciences Reviews* **2019**, *5* (4). https://doi.org/10.1515/psr-2019-0013.

(15) Yan, F.; Sun, Z.; Zhang, H.; Sun, X.; Jiang, Y.; Bai, Z. The Fluorescence Mechanism of Carbon Dots, and Methods for Tuning Their Emission Color: A Review. *Microchimica Acta* **2019**, *186* (8). https://doi.org/10.1007/s00604-019-3688-y.

(16) Mintz, K. J.; Zhou, Y.; Leblanc, R. M. Recent Development of Carbon Quantum Dots Regarding Their Optical Properties, Photoluminescence Mechanism, and Core Structure. *Nanoscale* **2019**, *11* (11), 4634–4652. https://doi.org/10.1039/C8NR10059D.

(17) Wu, C.; Chiu, D. T. Highly Fluorescent Semiconducting Polymer Dots for Biology and Medicine. *Angewandte Chemie - International Edition* **2013**, *52* (11), 3086–3109. https://doi.org/10.1002/ANIE.201205133.

(18) Tao, S.; Zhu, S.; Feng, T.; Xia, C.; Song, Y.; Yang, B. The Polymeric Characteristics and Photoluminescence Mechanism in Polymer Carbon Dots: A Review. *Mater Today Chem* **2017**, *6*, 13–25. https://doi.org/10.1016/J.MTCHEM.2017.09.001.

(19) Carbonaro; Corpino; Salis; Mocci; Thakkar; Olla; Ricci. On the Emission Properties of Carbon Dots: Reviewing Data and Discussing Models. *C — Journal of Carbon Research* **2019**, *5* (4), 60. https://doi.org/10.3390/c5040060.

(20) Yan, F.; Sun, Z.; Zhang, H.; Sun, X.; Jiang, Y.; Bai, Z. The Fluorescence Mechanism of Carbon Dots, and Methods for Tuning Their Emission Color: A Review. *Microchimica Acta* **2019**, *186* (8), 583. https://doi.org/10.1007/s00604-019-3688-y.

(21) Dong, Y.; Pang, H.; Yang, H. bin; Guo, C.; Shao, J.; Chi, Y.; Li, C. M.; Yu, T. Carbon-Based Dots Co-Doped with Nitrogen and Sulfur for High Quantum Yield and Excitation-Independent Emission. *Angewandte Chemie International Edition* **2013**, *52* (30), 7800–7804. https://doi.org/10.1002/ANIE.201301114.

(22) Kasprzyk, W.; Świergosz, T.; Bednarz, S.; Walas, K.; Bashmakova, N. v.; Bogdał, D. Luminescence Phenomena of Carbon Dots Derived from Citric Acid and Urea – a Molecular Insight. *Nanoscale* **2018**, *10* (29), 13889–13894. https://doi.org/10.1039/C8NR03602K.

(23) Sk, M. A.; Ananthanarayanan, A.; Huang, L.; Lim, K. H.; Chen, P. Revealing the Tunable Photoluminescence Properties of Graphene Quantum Dots. *J Mater Chem C Mater* **2014**, *2* (34), 6954–6960. https://doi.org/10.1039/C4TC01191K.

(24) Tian, P.; Tang, L.; Teng, K. S.; Lau, S. P. Graphene Quantum Dots from Chemistry to Applications. *Mater Today Chem* **2018**, *10*, 221–258. https://doi.org/10.1016/J.MTCHEM.2018.09.007.

(25) Fu, M.; Ehrat, F.; Wang, Y.; Milowska, K. Z.; Reckmeier, C.; Rogach, A. L.; Stolarczyk, J. K.; Urban, A. S.; Feldmann, J. Carbon Dots: A Unique Fluorescent Cocktail of Polycyclic Aromatic Hydrocarbons. *Nano Lett* **2015**, *15* (9), 6030–6035. https://doi.org/10.1021/acs.nanolett.5b02215.

(26) Tao, S.; Zhu, S.; Feng, T.; Zheng, C.; Yang, B. Crosslink-Enhanced Emission Effect on Luminescence in Polymers: Advances and Perspectives. *Angewandte Chemie - International Edition* **2020**, *59* (25), 9826–9840. https://doi.org/10.1002/ANIE.201916591.

(27) Zhu, S.; Wang, L.; Zhou, N.; Zhao, X.; Song, Y.; Maharjan, S.; Zhang, J.; Lu, L.; Wang, H.; Yang, B. The Crosslink Enhanced Emission (CEE) in Non-Conjugated Polymer Dots: From the Photoluminescence Mechanism to the Cellular Uptake Mechanism and Internalization. *Chemical Communications* **2014**, *50* (89), 13845–13848. https://doi.org/10.1039/C4CC05806B.

(28) Carbonaro, C. M.; de Villiers Engelbrecht, L.; Olla, C.; Cappai, A.; Casula, M. F.; Melis, C.; Stagi, L.; Laaksonen, A.; Mocci, F. Graphene Quantum Dots and Carbon Nanodots: Modelling of Zero-Dimensional Carbon Nanomaterials. In *Zero-Dimensional Carbon Nanomaterials*; Elsevier, 2022.

(29) Chua, C. K.; Sofer, Z.; Šimek, P.; Jankovský, O.; Klímová, K.; Bakardjieva, S.; Hrdličková Kučková, Š.; Pumera, M. Synthesis of Strongly Fluorescent Graphene Quantum Dots by Cage-Opening Buckminsterfullerene. *ACS Nano* **2015**, *9* (3), 2548–2555. https://doi.org/10.1021/NN505639Q.

(30) Zhou, J.; Yang, Y.; Zhang, C. Y. A Low-Temperature Solid-Phase Method to Synthesize Highly Fluorescent Carbon Nitride Dots with Tunable Emission. *Chemical Communications* **2013**, *49* (77), 8605–8607. https://doi.org/10.1039/C3CC42266F.

(31) Pan, D.; Zhang, J.; Li, Z.; Wu, M. Hydrothermal Route for Cutting Graphene Sheets into Blue-Luminescent Graphene Quantum Dots. *Advanced Materials* **2010**, *22* (6), 734–738. https://doi.org/10.1002/ADMA.200902825.

(32) Sun, D.; Ban, R.; Zhang, P. H.; Wu, G. H.; Zhang, J. R.; Zhu, J. J. Hair Fiber as a Precursor for Synthesizing of Sulfur- and Nitrogen-Co-Doped Carbon Dots with Tunable Luminescence Properties. *Carbon N Y* **2013**, *64*, 424–434. https://doi.org/10.1016/J.CARBON.2013.07.095.

(33) Liu, M.; Xu, Y.; Niu, F.; Gooding, J. J.; Liu, J. Carbon Quantum Dots Directly Generated from Electrochemical Oxidation of Graphite Electrodes in Alkaline Alcohols and the Applications for Specific Ferric Ion Detection and Cell Imaging. *Analyst* **2016**, *141* (9), 2657–2664. https://doi.org/10.1039/C5AN02231B.

(34) Khayal, A.; Dawane, V.; Amin, M. A.; Tirth, V.; Yadav, V. K.; Algahtani, A.; Khan, S. H.; Islam, S.; Yadav, K. K.; Jeon, B. H. Advances in the Methods for the Synthesis of Carbon Dots and Their Emerging Applications. *Polymers 2021, Vol. 13, Page 3190* **2021**, *13* (18), 3190. https://doi.org/10.3390/POLYM13183190.

(35) Ai, L.; Yang, Y.; Wang, B.; Chang, J.; Tang, Z.; Yang, B.; Lu, S. Insights into Photoluminescence Mechanisms of Carbon Dots: Advances and Perspectives. *Sci Bull (Beijing)* **2021**, *66* (8), 839–856. https://doi.org/10.1016/J.SCIB.2020.12.015.

(36) Sharma, A.; Das, J. Small Molecules Derived Carbon Dots: Synthesis and Applications in Sensing, Catalysis, Imaging, and Biomedicine. *Journal of Nanobiotechnology 2019 17:1* **2019**, *17* (1), 1–24. https://doi.org/10.1186/S12951-019-0525-8.

(37) Qu, D.; Sun, Z. The Formation Mechanism and Fluorophores of Carbon Dots Synthesized via a Bottom-up Route. *Mater Chem Front* **2020**, *4* (2), 400–420. https://doi.org/10.1039/C9QM00552H.

(38) Vallan, L.; Urriolabeitia, E. P.; Ruipérez, F.; Matxain, J. M.; Canton-Vitoria, R.; Tagmatarchis, N.; Benito, A. M.; Maser, W. K. Supramolecular-Enhanced Charge Transfer within Entangled Polyamide Chains as the Origin of the Universal Blue Fluorescence of Polymer Carbon Dots. *J Am Chem Soc* **2018**, *140* (40), 12862–12869. https://doi.org/10.1021/JACS.8B06051.

(39) Zhu, S.; Meng, Q.; Wang, L.; Zhang, J.; Song, Y.; Jin, H.; Zhang, K.; Sun, H.; Wang, H.; Yang, B. Highly Photoluminescent Carbon Dots for Multicolor Patterning, Sensors, and Bioimaging. *Angewandte Chemie* **2013**, *125* (14), 4045–4049. https://doi.org/10.1002/ANGE.201300519.

(40) Hu, Y.; Yang, J.; Tian, J.; Yu, J. S. How Do Nitrogen-Doped Carbon Dots Generate from Molecular Precursors? An Investigation of the Formation

Mechanism and a Solution-Based Large-Scale Synthesis. *J Mater Chem B* **2015**, *3* (27), 5608–5614. https://doi.org/10.1039/C5TB01005E.

(41) Tao, S.; Feng, T.; Zheng, C.; Zhu, S.; Yang, B. Carbonized Polymer Dots: A Brand New Perspective to Recognize Luminescent Carbon-Based Nanomaterials. *Journal of Physical Chemistry Letters* **2019**, 5182–5188. https://doi.org/10.1021/ACS.JPCLETT.9B01384.

(42) Otyepka, M.; Langer, M.; Paloncýová, M.; Medved', M. Molecular Fluorophores Self-Organize into c-Dot Seeds and Incorporate into c-Dot Structures. *Journal of Physical Chemistry Letters* **2020**, *11* (19), 8252–8258. https://doi.org/10.1021/ACS.JPCLETT.0C01873.

(43) Cappai, A.; Melis, C.; Stagi, L.; Ricci, P. C.; Mocci, F.; Carbonaro, C. M. Insight into the Molecular Model in Carbon Dots through Experimental and Theoretical Analysis of Citrazinic Acid in Aqueous Solution. *Journal of Physical Chemistry C* **2021**, *125* (8), 4836–4845. https://doi.org/10.1021/acs.jpcc.0c10916.

(44) Siddique, F.; Langer, M.; Paloncýová, M.; Medved', M.; Otyepka, M.; Nachtigallová, D.; Lischka, H.; Aquino, A. J. A. Conformational Behavior and Optical Properties of a Fluorophore Dimer as a Model of Luminescent Centers in Carbon Dots. *Journal of Physical Chemistry C* **2020**, *124* (26), 14327–14337. https://doi.org/10.1021/acs.jpcc.0c02175.

(45) Sudolská, M.; Dubecký, M.; Sarkar, S.; Reckmeier, C. J.; Zbořil, R.; Rogach, A. L.; Otyepka, M. Nature of Absorption Bands in Oxygen-Functionalized Graphitic Carbon Dots. *Journal of Physical Chemistry C* **2015**, *119* (23), 13369–13373. https://doi.org/10.1021/ACS.JPCC.5B04080.

(46) Ludmerczki, R.; Malfatti, L.; Stagi, L.; Meloni, M.; Carbonaro, C. M.; Casula, M. F.; Bogdán, D.; Mura, S.; Mándity, I. M.; Innocenzi, P. Polymerization-Driven Photoluminescence in Alkanolamine-Based C-Dots. *Chemistry - A European Journal* **2020**. https://doi.org/10.1002/chem.202004465.

(47) Sui, L.; Jin, W.; Li, S.; Liu, D.; Jiang, Y.; Chen, A.; Liu, H.; Shi, Y.; Ding, D.; Jin, M. Ultrafast Carrier Dynamics of Carbon Nanodots in Different PH

Environments. *Physical Chemistry Chemical Physics* **2016**, *18* (5), 3838–3845. https://doi.org/10.1039/C5CP07558K.

(48) Mondal, S.; Yucknovsky, A.; Akulov, K.; Ghorai, N.; Schwartz, T.; Ghosh, H. N.; Amdursky, N. Efficient Photosensitizing Capabilities and Ultrafast Carrier Dynamics of Doped Carbon Dots. *J Am Chem Soc* **2019**, *141* (38), 15413–15422. https://doi.org/10.1021/JACS.9B08071.

(49) Sciortino, A.; Gazzetto, M.; Soriano, M. L.; Cannas, M.; Cárdenas, S.; Cannizzo, A.; Messina, F. Ultrafast Spectroscopic Investigation on Fluorescent Carbon Nanodots: The Role of Passivation. *Physical Chemistry Chemical Physics* **2019**, *21* (30), 16459–16467. https://doi.org/10.1039/C9CP03063H.

(50) Mocci, F.; Engelbrecht, L. D. V.; Olla, C.; Cappai, A.; Casula, M. F.; Melis, C.; Stagi, L.; Laaksonen, A.; Carbonaro, C. M. Carbon Nanodots from an In Silico Perspective. *Chemical Reviews*. American Chemical Society August 24, 2022, pp 13709–13799. https://doi.org/10.1021/acs.chemrev.1c00864.

(51) Ludmerczki, R.; Mura, S.; Carbonaro, C. M.; Mandity, I. M.; Carraro, M.; Senes, N.; Garroni, S.; Granozzi, G.; Calvillo, L.; Marras, S.; Malfatti, L.; Innocenzi, P. Carbon Dots from Citric Acid and Its Intermediates Formed by Thermal Decomposition. *Chemistry - A European Journal* **2019**, *25* (51), 11963–11974. https://doi.org/10.1002/chem.201902497.

(52) Loche, D.; Malfatti, L.; Carboni, D.; Alzari, V.; Mariani, A.; Casula, M. F. Incorporation of Graphene into Silica-Based Aerogels and Application for Water Remediation. *RSC Adv* **2016**, *6* (71), 66516–66523. https://doi.org/10.1039/C6RA09618B.

(53) Ferrari, A. C.; Basko, D. M. Raman Spectroscopy as a Versatile Tool for Studying the Properties of Graphene. *Nature Nanotechnology 2013 8:4* **2013**, *8* (4), 235–246. https://doi.org/10.1038/nnano.2013.46.

(54) Song, Y.; Zhu, S.; Zhang, S.; Fu, Y.; Wang, L.; Zhao, X.; Yang, B. Investigation from Chemical Structure to Photoluminescent Mechanism: A Type of Carbon Dots from the Pyrolysis of Citric Acid and an Amine. *J Mater Chem C Mater* **2015**, *3* (23), 5976–5984. https://doi.org/10.1039/C5TC00813A.

(55) Ghosal, K.; Ghosh, A. Carbon Dots: The next Generation Platform for Biomedical Applications. *Materials Science and Engineering: C* **2019**, *96*, 887–903. https://doi.org/10.1016/J.MSEC.2018.11.060.

(56) Roy, P.; Chen, P. C.; Periasamy, A. P.; Chen, Y. N.; Chang, H. T. Photoluminescent Carbon Nanodots: Synthesis, Physicochemical Properties and Analytical Applications. *Materials Today* **2015**, *18* (8), 447–458. https://doi.org/10.1016/J.MATTOD.2015.04.005.

(57) Guo, L.; Ge, J.; Wang, P. Polymer Dots as Effective Phototheranostic Agents. *Photochem Photobiol* **2018**, *94* (5), 916–934. https://doi.org/10.1111/PHP.12956.

(58) Choi, Y.; Choi, Y.; Kwon, O. H.; Kim, B. S. Carbon Dots: Bottom-Up Syntheses, Properties, and Light-Harvesting Applications. *Chem Asian J* **2018**, *13* (6), 586–598. https://doi.org/10.1002/ASIA.201701736.

(59) Yuan, F.; Li, S.; Fan, Z.; Meng, X.; Fan, L.; Yang, S. Shining Carbon Dots: Synthesis and Biomedical and Optoelectronic Applications. *Nano Today* **2016**, *11* (5), 565–586. https://doi.org/10.1016/J.NANTOD.2016.08.006.

(60) Chakraborty, P.; Ma, T.; Zahiri, A. H.; Cao, L.; Wang, Y. Carbon-Based Materials for Thermoelectrics. *Advances in Condensed Matter Physics* **2018**, *2018*. https://doi.org/10.1155/2018/3898479.

(61) Yuan, T.; Meng, T.; He, P.; Shi, Y.; Li, Y.; Li, X.; Fan, L.; Yang, S. Carbon Quantum Dots: An Emerging Material for Optoelectronic Applications. *J Mater Chem C Mater* **2019**, *7* (23), 6820–6835. https://doi.org/10.1039/C9TC01730E.

(62) Semeniuk, M.; Yi, Z.; Poursorkhabi, V.; Tjong, J.; Jaffer, S.; Lu, Z. H.; Sain, M. Future Perspectives and Review on Organic Carbon Dots in Electronic Applications. *ACS Nano* **2019**, *13* (6), 6224–6255. https://doi.org/10.1021/ACSNANO.9B00688.

(63) Yuan, F.; Xi, Z.; Shi, X.; Li, Y.; Li, X.; Wang, Z.; Fan, L.; Yang, S. Ultrastable and Low-Threshold Random Lasing from Narrow-Bandwidth-Emission Triangular Carbon Quantum Dots. *Adv Opt Mater* **2019**, *7* (2), 1–6. https://doi.org/10.1002/adom.201801202.

(64) Hohenberg, P.; Kohn, W. Inhomogeneous Electron Gas. *Physical Review* **1964**, *136* (3B), B864. https://doi.org/10.1103/PHYSREV.136.B864.

(65) Kohn, W.; Sham, L. J. Self-Consistent Equations Including Exchange and Correlation Effects. *Physical Review* **1965**, *140* (4A), A1133. https://doi.org/10.1103/PHYSREV.140.A1133.

(66) Becke, A. D. Density Functional Calculations of Molecular Bond Energies. *J Chem Phys* **1998**, *84* (8), 4524. https://doi.org/10.1063/1.450025.

(67) Perdew, J. P.; Burke, K.; Ernzerhof, M. Generalized Gradient Approximation Made Simple. *Phys Rev Lett* **1996**, *77* (18), 3865. https://doi.org/10.1103/PhysRevLett.77.3865.

(68) Stephens, P. J.; Devlin, F. J.; Chabalowski, C. F.; Frisch, M. J. Ab Initio Calculation of Vibrational Absorption and Circular Dichroism Spectra Using Density Functional Force Fields. *Journal of Physical Chemistry®* **1994**, *98* (45), 11623–11627. https://doi.org/10.1021/J100096A001.

(69) Burke, K. Perspective on Density Functional Theory. *J Chem Phys* **2012**, *136* (15), 150901. https://doi.org/10.1063/1.4704546.

(70) Toulouse, J.; Colonna, F.; Savin, A. Long-Range - Short-Range Separation of the Electron-Electron Interaction in Density-Functional Theory. *Phys Rev A* **2004**, *70* (6), 062505. https://doi.org/10.1103/PHYSREVA.70.062505.

(71) Gerber, I. C.; Ángyán, J. G. Hybrid Functional with Separated Range. *Chem Phys Lett* **2005**, *415* (1–3), 100–105. https://doi.org/10.1016/J.CPLETT.2005.08.060.

(72) Casida, M. E. Time-Dependent Density-Functional Theory for Molecules and Molecular Solids. *Journal of Molecular Structure: THEOCHEM* **2009**, *914* (1–3), 3–18. https://doi.org/10.1016/J.THEOCHEM.2009.08.018.

(73) Runge, E.; Gross, E. K. U. Density-Functional Theory for Time-Dependent Systems. *Phys Rev Lett* **1984**, *52* (12), 997. https://doi.org/10.1103/PhysRevLett.52.997.

(74) Tepliakov, N. v.; Kundelev, E. v.; Khavlyuk, P. D.; Xiong, Y.; Leonov, M. Y.; Zhu, W.; Baranov, A. v.; Fedorov, A. v.; Rogach, A. L.; Rukhlenko, I.

D. Sp2-Sp3-Hybridized Atomic Domains Determine Optical Features of Carbon Dots. *ACS Nano* **2019**, *13* (9), 10737–10744. https://doi.org/10.1021/acsnano.9b05444.

(75) Strauss, V.; Margraf, J. T.; Dolle, C.; Butz, B.; Nacken, T. J.; Walter, J.; Bauer, W.; Peukert, W.; Spiecker, E.; Clark, T.; Guldi, D. M. Carbon Nanodots: Toward a Comprehensive Understanding of Their Photoluminescence. *J Am Chem Soc* **2014**, *136* (49), 17308–17316. https://doi.org/10.1021/JA510183C.

(76) Stephan, U.; Frauenheim, T.; Blaudeck, P.; Jungnickel, G. π Bonding versus Electronic-Defect Generation: An Examination of Band-Gap Properties in Amorphous Carbon. *Phys Rev B* **1994**, *50* (3), 1489. https://doi.org/10.1103/PhysRevB.50.1489.

(77) Zhu, B.; Sun, S.; Wang, Y.; Deng, S.; Qian, G.; Wang, M.; Hu, A. Preparation of Carbon Nanodots from Single Chain Polymeric Nanoparticles and Theoretical Investigation of the Photoluminescence Mechanism. *J Mater Chem C Mater* **2013**, *1* (3), 580–586. https://doi.org/10.1039/c2tc00140c.

(78) Li, Y.; Shu, H.; Niu, X.; Wang, J. Electronic and Optical Properties of Edge-Functionalized Graphene Quantum Dots and the Underlying Mechanism. *Journal of Physical Chemistry C* **2015**, *119* (44), 24950–24957. https://doi.org/10.1021/ACS.JPCC.5B05935.

(79) Reckmeier, C. J.; Schneider, J.; Xiong, Y.; Häusler, J.; Kasák, P.; Schnick, W.; Rogach, A. L. Aggregated Molecular Fluorophores in the Ammonothermal Synthesis of Carbon Dots. *Chemistry of Materials* **2017**, *29* (24), 10352–10361. https://doi.org/10.1021/acs.chemmater.7b03344.

(80) Liu, C.; Bao, L.; Yang, M.; Zhang, S.; Zhou, M.; Tang, B.; Wang, B.; Liu, Y.; Zhang, Z. L.; Zhang, B.; Pang, D. W. Surface Sensitive Photoluminescence of Carbon Nanodots: Coupling between the Carbonyl Group and π-Electron System. *Journal of Physical Chemistry Letters* **2019**, *10* (13), 3621–3629. https://doi.org/10.1021/ACS.JPCLETT.9B01339.

(81) Ambrusi, R. E.; Arroyave, J. M.; Centurión, M. E.; di Nezio, M. S.; Pistonesi, M. F.; Juan, A.; Pronsato, M. E. Density Functional Theory Model for Carbon Dot Surfaces and Their Interaction with Silver

Nanoparticles. *Physica E Low Dimens Syst Nanostruct* **2019**, *114*, 113640. https://doi.org/10.1016/J.PHYSE.2019.113640.

(82) Zhao, M.; Yang, F.; Xue, Y.; Xiao, D.; Guo, Y. A Time-Dependent DFT Study of the Absorption and Fluorescence Properties of Graphene Quantum Dots. *ChemPhysChem* **2014**, *15* (5), 950–957. https://doi.org/10.1002/CPHC.201301137.

(83) Choi, J.; Kim, N.; Oh, J. W.; Kim, F. S. Bandgap Engineering of Nanosized Carbon Dots through Electron-Accepting Functionalization. *Journal of Industrial and Engineering Chemistry* **2018**, *65*, 104–111. https://doi.org/10.1016/J.JIEC.2018.04.018.

(84) Sarkar, S.; Sudolská, M.; Dubecký, M.; Reckmeier, C. J.; Rogach, A. L.; Zbořil, R.; Otyepka, M. Graphitic Nitrogen Doping in Carbon Dots Causes Red-Shifted Absorption. *Journal of Physical Chemistry C* **2016**, *120* (2), 1303–1308. https://doi.org/10.1021/acs.jpcc.5b10186.

(85) Holá, K.; Sudolská, M.; Kalytchuk, S.; Nachtigallová, D.; Rogach, A. L.; Otyepka, M.; Zbořil, R. Graphitic Nitrogen Triggers Red Fluorescence in Carbon Dots. *ACS Nano* **2017**, *11* (12), 12402–12410. https://doi.org/10.1021/ACSNANO.7B06399.

(86) Jin, S. H.; Kim, D. H.; Jun, G. H.; Hong, S. H.; Jeon, S. Tuning the Photoluminescence of Graphene Quantum Dots through the Charge Transfer Effect of Functional Groups. *ACS Nano* **2013**, *7* (2), 1239–1245. https://doi.org/10.1021/NN304675G.

(87) Wang, J.; Cao, S.; Ding, Y.; Ma, F.; Lu, W.; Sun, M. Theoretical Investigations of Optical Origins of Fluorescent Graphene Quantum Dots. *Scientific Reports 2016 6:1* **2016**, *6* (1), 1–5. https://doi.org/10.1038/srep24850.

(88) Kundelev, E. v.; Tepliakov, N. v.; Leonov, M. Y.; Maslov, V. G.; Baranov, A. v.; Fedorov, A. v.; Rukhlenko, I. D.; Rogach, A. L. Amino Functionalization of Carbon Dots Leads to Red Emission Enhancement. *Journal of Physical Chemistry Letters* **2019**, *10* (17), 5111–5116. https://doi.org/10.1021/ACS.JPCLETT.9B01724.

(89) Xu, Q.; Liu, Y.; Gao, C.; Wei, J.; Zhou, H.; Chen, Y.; Dong, C.; Sreeprasad, T. S.; Li, N.; Xia, Z. Synthesis, Mechanistic Investigation, and Application of Photoluminescent Sulfur and Nitrogen Co-Doped Carbon Dots. *J Mater Chem C Mater* **2015**, *3* (38), 9885–9893. https://doi.org/10.1039/C5TC01912E.

(90) Feng, J.; Dong, H.; Pang, B.; Shao, F.; Zhang, C.; Yu, L.; Dong, L. Theoretical Study on the Optical and Electronic Properties of Graphene Quantum Dots Doped with Heteroatoms. *Physical Chemistry Chemical Physics* **2018**, *20* (22), 15244–15252. https://doi.org/10.1039/C8CP01403E.

(91) Jana, J.; Ganguly, M.; Chandrakumar, K. R. S.; Rao, G. M.; Pal, T. Boron Precursor-Dependent Evolution of Differently Emitting Carbon Dots. *Langmuir* **2017**, *33* (2), 573–584. https://doi.org/10.1021/ACS.LANGMUIR.6B04100.

(92) Hola, K.; Bourlinos, A. B.; Kozak, O.; Berka, K.; Siskova, K. M.; Havrdova, M.; Tucek, J.; Safarova, K.; Otyepka, M.; Giannelis, E. P.; Zboril, R. Photoluminescence Effects of Graphitic Core Size and Surface Functional Groups in Carbon Dots: COO− Induced Red-Shift Emission. *Carbon N Y* **2014**, *70*, 279–286. https://doi.org/10.1016/J.CARBON.2014.01.008.

(93) Sudolská, M.; Otyepka, M. Exact Roles of Individual Chemical Forms of Nitrogen in the Photoluminescent Properties of Nitrogen-Doped Carbon Dots. *Appl Mater Today* **2017**, *7*, 190–200. https://doi.org/10.1016/J.APMT.2017.03.004.

(94) Chen, S.; Ullah, N.; Zhang, R. Exciton Self-Trapping in Sp2 Carbon Nanostructures Induced by Edge Ether Groups. *Journal of Physical Chemistry Letters* **2018**, *9* (17), 4857–4864. https://doi.org/10.1021/ACS.JPCLETT.8B01972.

(95) Kalytchuk, S.; Zdražil, L.; Bad'ura, Z.; Medved', M.; Langer, M.; Paloncýová, M.; Zoppellaro, G.; Kershaw, S. v.; Rogach, A. L.; Otyepka, M.; Zbořil, R. Carbon Dots Detect Water-to-Ice Phase Transition and Act as Alcohol Sensors via Fluorescence Turn-Off/On Mechanism. *ACS Nano* **2021**, *15* (4), 6582–6593. https://doi.org/10.1021/ACSNANO.0C09781.

(96) Gazzetto, M.; Sciortino, A.; Nazari, M.; Rohwer, E.; Giammona, G.; Mauro, N.; Feurer, T.; Messina, F.; Cannizzo, A. Photocycle of Excitons in Nitrogen-Rich Carbon Nanodots: Implications for Photocatalysis and Photovoltaics. *ACS Appl Nano Mater* **2020**, *3* (7), 6925–6934. https://doi.org/10.1021/ACSANM.0C01259.

(97) Chen, H.; Wang, G. D.; Sun, X.; Todd, T.; Zhang, F.; Xie, J.; Shen, B. Mesoporous Silica as Nanoreactors to Prepare Gd-Encapsulated Carbon Dots of Controllable Sizes and Magnetic Properties. *Adv Funct Mater* **2016**, *26* (22), 3973–3982. https://doi.org/10.1002/adfm.201504177.

(98) Zong, J.; Zhu, Y.; Yang, X.; Shen, J.; Li, C. Synthesis of Photoluminescent Carbogenic Dots Using Mesoporous Silica Spheres as Nanoreactors. *Chemical Communications* **2011**, *47* (2), 764–766. https://doi.org/10.1039/c0cc03092a.

(99) Suzuki, K.; Malfatti, L.; Takahashi, M.; Carboni, D.; Messina, F.; Tokudome, Y.; Takemoto, M.; Innocenzi, P. Design of Carbon Dots Photoluminescence through Organo-Functional Silane Grafting for Solid-State Emitting Devices. *Sci Rep* **2017**, *7* (1), 1–11. https://doi.org/10.1038/s41598-017-05540-5.

(100) Fernandes, D.; Heslop, K. A.; Kelarakis, A.; Krysmann, M. J.; Estevez, L. In Situ Generation of Carbon Dots within a Polymer Matrix. *Polymer (Guildf)* **2020**, *188*, 122159. https://doi.org/10.1016/j.polymer.2020.122159.

(101) Mura, S.; Ludmerczki, R.; Stagi, L.; Garroni, S.; Carbonaro, C. M.; Ricci, P. C.; Casula, M. F.; Malfatti, L.; Innocenzi, P. Integrating Sol-Gel and Carbon Dots Chemistry for the Fabrication of Fluorescent Hybrid Organic-Inorganic Films. *Sci Rep* **2020**, *10* (1), 4770. https://doi.org/10.1038/s41598-020-61517-x.

(102) Madonia, A.; Martin-Sabi, M.; Sciortino, A.; Agnello, S.; Cannas, M.; Ammar, S.; Messina, F.; Schaming, D. Highly Efficient Electron Transfer in a Carbon Dot–Polyoxometalate Nanohybrid. *J Phys Chem Lett* **2020**, *11* (11), 4379–4384. https://doi.org/10.1021/ACS.JPCLETT.0C01078.

(103) Liu, J.; Wang, N.; Yu, Y.; Yan, Y.; Zhang, H.; Li, J.; Yu, J. Carbon Dots in Zeolites: A New Class of Thermally Activated Delayed Fluorescence

Materials with Ultralong Lifetimes. *Sci Adv* **2017**, *3* (5), e1603171. https://doi.org/10.1126/sciadv.1603171.

(104) Liu, J.; Zhang, H.; Wang, N.; Yu, Y.; Cui, Y.; Li, J.; Yu, J. Template-Modulated Afterglow of Carbon Dots in Zeolites: Room-Temperature Phosphorescence and Thermally Activated Delayed Fluorescence. *ACS Mater Lett* **2019**, *1* (1), 58–63. https://doi.org/10.1021/acsmaterialslett.9b00073.

(105) Ma, Y.; Zhang, X.; Bai, J.; Huang, K.; Ren, L. Facile, Controllable Tune of Blue Shift or Red Shift of the Fluorescence Emission of Solid-State Carbon Dots. *Chemical Engineering Journal* **2019**, *374* (June), 787–792. https://doi.org/10.1016/j.cej.2019.06.016.

(106) Joseph, J.; Anappara, A. A. Cool White, Persistent Room-Temperature Phosphorescence in Carbon Dots Embedded in a Silica Gel Matrix. *Physical Chemistry Chemical Physics* **2017**, *19* (23), 15137–15144. https://doi.org/10.1039/c7cp02731a.

(107) Vassilakopoulou, A.; Georgakilas, V.; Vainos, N.; Koutselas, I. Successful Entrapment of Carbon Dots within Flexible Free-Standing Transparent Mesoporous Organic-Inorganic Silica Hybrid Films for Photonic Applications. *Journal of Physics and Chemistry of Solids* **2017**, *103* (November 2016), 190–196. https://doi.org/10.1016/j.jpcs.2016.12.027.

(108) Guo, Z.; Zhu, Z.; Zhang, X.; Chen, Y. Facile Synthesis of Blue-Emitting Carbon Dots@mesoporous Silica Composite Spheres. *Solid State Sci* **2018**, *76*, 100–104. https://doi.org/10.1016/j.solidstatesciences.2017.12.011.

(109) Sciortino, L.; Messina, F.; Buscarino, G.; Agnello, S.; Cannas, M.; Gelardi, F. M. Nitrogen-Doped Carbon Dots Embedded in a SiO2 Monolith for Solid-State Fluorescent Detection of Cu2+ Ions. *Journal of Nanoparticle Research 2017 19:6* **2017**, *19* (6), 1–11. https://doi.org/10.1007/S11051-017-3915-6.

(110) Liu, Y.; Liu, C. Y.; Zhang, Z. Y.; Yang, W. D.; Nie, S. D. Plasmon-Enhanced Photoluminescence of Carbon Dots-Silica Hybrid Mesoporous Spheres. *J Mater Chem C Mater* **2015**, *3* (12), 2881–2885. https://doi.org/10.1039/c4tc02599g.

(111) Sarkar, T.; Rawat, K.; Solanki, P. R.; Bohidar, H. B. Carbon Dots-Embedded Fluorescent Silica Xerogel. *Colloids Surf A Physicochem Eng Asp* **2019**, *583* (June), 123844. https://doi.org/10.1016/j.colsurfa.2019.123844.

(112) Babusenan, A.; Pandey, B.; Roy, S. C.; Bhattacharyya, J. Charge Transfer Mediated Photoluminescence Enhancement in Carbon Dots Embedded in TiO2 Nanotube Matrix. *Carbon N Y* **2020**, *161*, 535–541. https://doi.org/10.1016/j.carbon.2020.01.097.

(113) Li, J.; Wang, B.; Zhang, H.; Yu, J. Carbon Dots-in-Matrix Boosting Intriguing Luminescence Properties and Applications. *Small* **2019**, *15* (32), 1–16. https://doi.org/10.1002/smll.201805504.

(114) Sun, Y.; Liu, J.; Pang, X.; Zhang, X.; Zhuang, J.; Zhang, H.; Hu, C.; Zheng, M.; Lei, B.; Liu, Y. Temperature-Responsive Conversion of Thermally Activated Delayed Fluorescence and Room-Temperature Phosphorescence of Carbon Dots in Silica. *J Mater Chem C Mater* **2020**, *8* (17), 5744–5751. https://doi.org/10.1039/d0tc00507j.

(115) Sun, Y.; Liu, S.; Sun, L.; Wu, S.; Hu, G.; Pang, X.; Smith, A. T.; Hu, C.; Zeng, S.; Wang, W.; Liu, Y.; Zheng, M. Ultralong Lifetime and Efficient Room Temperature Phosphorescent Carbon Dots through Multi-Confinement Structure Design. *Nat Commun* **2020**, *11* (1), 1–11. https://doi.org/10.1038/s41467-020-19422-4.

(116) Carbonaro, C. M.; Thakkar, S. V.; Ludmerczki, R.; Olla, C.; Pinna, A.; Loche, D.; Malfatti, L.; Cesare Marincola, F.; Casula, M. F. How Porosity Affects the Emission of Fluorescent Carbon Dot-Silica Porous Composites. *Microporous and Mesoporous Materials* **2020**, *305* (May). https://doi.org/10.1016/j.micromeso.2020.110302.

(117) Carbonaro, C. M.; Chiriu, D.; Stagi, L.; Casula, M. F.; Thakkar, S. v.; Malfatti, L.; Suzuki, K.; Ricci, P. C.; Corpino, R. Carbon Dots in Water and Mesoporous Matrix: Chasing the Origin of Their Photoluminescence. *The Journal of Physical Chemistry C* **2018**, *122* (44), 25638–25650. https://doi.org/10.1021/acs.jpcc.8b08012.

(118) Carbonaro, C. M.; Ricci, P. C.; Grandi, S.; Marceddu, M.; Corpino, R.; Salis, M.; Anedda, A. On the Formation of Aggregates in Silica-

Rhodamine 6G Type II Hybrids. *RSC Adv* **2012**, *2* (5), 1905–1912. https://doi.org/10.1039/c2ra00830k.

(119) Carbonaro, C. M.; Meinardi, F.; Ricci, P. C.; Salis, M.; Anedda, A. Light Assisted Dimer to Monomer Transformation in Heavily Doped Rhodamine 6G-Porous Silica Hybrids. *Journal of Physical Chemistry B* **2009**, *113* (15), 5111–5116. https://doi.org/10.1021/jp810835j.

(120) Zholobak, N. M.; Popov, A. L.; Shcherbakov, A. B.; Popova, N. R.; Guzyk, M. M.; Antonovich, V. P.; Yegorova, A. v.; Scrypynets, Y. v.; Leonenko, I. I.; Baranchikov, A. Y.; Ivanov, V. K. Facile Fabrication of Luminescent Organic Dots by Thermolysis of Citric Acid in Urea Melt, and Their Use for Cell Staining and Polyelectrolyte Microcapsule Labelling. *Beilstein Journal of Nanotechnology* **2016**, *7* (1), 1905–1917. https://doi.org/10.3762/BJNANO.7.182.

(121) Fermo, P.; Andreoli, M.; Bonizzoni, L.; Fantauzzi, M.; Giubertoni, G.; Ludwig, N.; Rossi, A. Characterisation of Roman and Byzantine Glasses from the Surroundings of Thugga (Tunisia): Raw Materials and Colours. *Microchemical Journal* **2016**, *129*, 5–15. https://doi.org/10.1016/J.MICROC.2016.05.014.

(122) Lakowicz, J. R. *Principles of Fluorescence Spectroscopy*; Lakowicz, J. R., Ed.; Springer US: Boston, MA, 2006. https://doi.org/10.1007/978-0-387-46312-4.

(123) Frisch, M. J.; Trucks, G. W.; Schlegel, H. B.; Scuseria, G. E.; Robb, M. a.; Cheeseman, J. R.; Scalmani, G.; Barone, V.; Petersson, G. a.; Nakatsuji, H.; Li, X.; Caricato, M.; Marenich, a. v.; Bloino, J.; Janesko, B. G.; Gomperts, R.; Mennucci, B.; Hratchian, H. P.; Ortiz, J. v.; Izmaylov, a. F.; Sonnenberg, J. L.; Williams; Ding, F.; Lipparini, F.; Egidi, F.; Goings, J.; Peng, B.; Petrone, A.; Henderson, T.; Ranasinghe, D.; Zakrzewski, V. G.; Gao, J.; Rega, N.; Zheng, G.; Liang, W.; Hada, M.; Ehara, M.; Toyota, K.; Fukuda, R.; Hasegawa, J.; Ishida, M.; Nakajima, T.; Honda, Y.; Kitao, O.; Nakai, H.; Vreven, T.; Throssell, K.; Montgomery Jr., J. a.; Peralta, J. E.; Ogliaro, F.; Bearpark, M. J.; Heyd, J. J.; Brothers, E. N.; Kudin, K. N.; Staroverov, V. N.; Keith, T. a.; Kobayashi, R.; Normand, J.; Raghavachari, K.; Rendell, a. P.; Burant, J. C.; Iyengar, S. S.; Tomasi, J.; Cossi, M.; Millam, J. M.; Klene, M.; Adamo, C.; Cammi, R.; Ochterski, J. W.; Martin,

R. L.; Morokuma, K.; Farkas, O.; Foresman, J. B.; Fox, D. J. G16_C01. 2016, p Gaussian 16, Gaussian, Inc., Wallin.

(124) Atsuko Aboshi; Naoko Kurumoto, and; Yamada, T.; Uchino*, T. Influence of Thermal Treatments on the Photoluminescence Characteristics of Nanometer-Sized Amorphous Silica Particles. *Journal of Physical Chemistry C* **2007**, *111* (24), 8483–8488. https://doi.org/10.1021/JP0718505.

(125) Carbonaro, C. M.; Salis, M.; Corpino, R.; Chiriu, D.; Stagi, L.; Serra, G.; Bosin, A.; Ricci, P. C. Thermodynamic Models of the Adsorption and Desorption of Molecular Oxygen at the UV and Blue Emitting Centers in Mesoporous Silica under Variable Oxygen Pressure. *Microporous and Mesoporous Materials* **2017**, *239*, 371–380. https://doi.org/10.1016/j.micromeso.2016.10.037.

(126) Mocci, F.; Olla, C.; Cappai, A.; Corpino, R.; Ricci, P. C.; Chiriu, D.; Salis, M.; Carbonaro, C. M. Formation of Citrazinic Acid Ions and Their Contribution to Optical and Magnetic Features of Carbon Nanodots: A Combined Experimental and Computational Approach. *Materials* **2021**, *14* (4), 1–16. https://doi.org/10.3390/ma14040770.

(127) Shao, X.; Aquino, A. J. A.; Otyepka, M.; Nachtigallová, D.; Lischka, H. Tuning the UV Spectrum of PAHs by Means of Different N-Doping Types Taking Pyrene as Paradigmatic Example: Categorization: Via Valence Bond Theory and High-Level Computational Approaches. *Physical Chemistry Chemical Physics* **2020**, *22* (38), 22003–22015. https://doi.org/10.1039/d0cp02688c.

(128) Becke, A. D. Density-functional Thermochemistry. III. The Role of Exact Exchange. *J Chem Phys* **1993**, *98* (7), 5648–5652. https://doi.org/10.1063/1.464913.

(129) Tirado-Rives, J.; Jorgensen, W. L. Performance of B3LYP Density Functional Methods for a Large Set of Organic Molecules. *J Chem Theory Comput* **2008**, *4* (2), 297–306. https://doi.org/10.1021/CT700248K.

(130) Anedda, A.; Carbonaro, C. M.; Clemente, F.; Corpino, R.; Grandi, S. OH-Dependence of Ultraviolet Emission in Porous Silica. **2003**, *322*, 68–72. https://doi.org/10.1016/S0022-3093(03)00176-5.

(131) Anedda, A.; Carbonaro, C. M.; Clemente, F.; Corpino, R.; Raga, F.; Serpi, A. Ultraviolet Excitation of Photoluminescence of Porous Silica under Vacuum Conditions. *J Non Cryst Solids* **2003**, *322* (1–3), 95–99. https://doi.org/10.1016/S0022-3093(03)00184-4.

(132) Macairan, J.-R.; de Medeiros, T. v.; Gazzetto, M.; Yarur Villanueva, F.; Cannizzo, A.; Naccache, R. Elucidating the Mechanism of Dual-Fluorescence in Carbon Dots. *J Colloid Interface Sci* **2022**, *606*, 67–76. https://doi.org/10.1016/j.jcis.2021.07.156.

(133) He, Y.; He, J.; Wang, L.; Yu, Z.; Zhang, H.; Liu, Y.; Lei, B. Synthesis of Double Carbon Dots Co-Doped Mesoporous Al2O3 for Ratiometric Fluorescent Determination of Oxygen. *Sens Actuators B Chem* **2017**, *251*, 918–926. https://doi.org/10.1016/j.snb.2017.05.104.

(134) Terracina, A.; Armano, A.; Meloni, M.; Panniello, A.; Minervini, G.; Madonia, A.; Cannas, M.; Striccoli, M.; Malfatti, L.; Messina, F. Photobleaching and Recovery Kinetics of a Palette of Carbon Nanodots Probed by In Situ Optical Spectroscopy. *ACS Appl Mater Interfaces* **2022**. https://doi.org/10.1021/acsami.2c09496.

(135) Sun, M.; Liang, C.; Tian, Z.; Ushakova, E. v.; Li, D.; Xing, G.; Qu, S.; Rogach, A. L. Realization of the Photostable Intrinsic Core Emission from Carbon Dots through Surface Deoxidation by Ultraviolet Irradiation. *J Phys Chem Lett* **2019**, *10* (11), 3094–3100. https://doi.org/10.1021/acs.jpclett.9b00842.

(136) Minervini, G.; Panniello, A.; Madonia, A.; Carbonaro, C. M.; Mocci, F.; Sibillano, T.; Giannini, C.; Comparelli, R.; Ingrosso, C.; Depalo, N.; Fanizza, E.; Curri, M. L.; Striccoli, M. Photostable Carbon Dots with Intense Green Emission in an Open Reactor Synthesis. *Carbon N Y* **2022**, *198*, 230–243. https://doi.org/10.1016/j.carbon.2022.07.034.

(137) Sarkar, S.; Chowdhury, J.; Dutta, S.; Pal, T. A PH Dependent Raman and Surface Enhanced Raman Spectroscopic Studies of Citrazinic Acid Aided by Theoretical Calculations. *Spectrochim Acta A Mol Biomol Spectrosc* **2016**, *169*, 108–115. https://doi.org/10.1016/J.SAA.2016.06.023.

(138) Bashmakova, N. v.; Shaydyuk, Y. O.; Dmytruk, A. M.; Świergosz, T.; Kachkovsky, O. D.; Belfield, K. D.; Bondar, M. v.; Kasprzyk, W. Nature of

Linear Spectral Properties and Fast Electronic Relaxations in Green Fluorescent Pyrrolo[3,4-c]Pyridine Derivative. *Int J Mol Sci* **2021**, *22* (11). https://doi.org/10.3390/ijms22115592.

(139) Kundelev, E. v.; Tepliakov, N. v.; Leonov, M. Y.; Maslov, V. G.; Baranov, A. v.; Fedorov, A. v.; Rukhlenko, I. D.; Rogach, A. L. Toward Bright Red-Emissive Carbon Dots through Controlling Interaction among Surface Emission Centers. *Journal of Physical Chemistry Letters* **2020**, *11* (19), 8121–8127. https://doi.org/10.1021/acs.jpclett.0c02373.

(140) Carbonaro, C. M. Tuning the Formation of Aggregates in Silica–Rhodamine 6G Hybrids by Thermal Treatment. *J Photochem Photobiol A Chem* **2011**, *222* (1), 56–63. https://doi.org/10.1016/J.JPHOTOCHEM.2011.05.001.

(141) Anedda, A.; Carbonaro, C. M.; Clemente, F.; Corda, L.; Corpino, R.; Ricci, P. C. Surface Hydroxyls in Porous Silica: A Raman Spectroscopy Study. *Materials Science and Engineering: C* **2003**, *23* (6–8), 1069–1072. https://doi.org/10.1016/j.msec.2003.09.125.

(142) Wang, J.; Yang, Y.; Liu, X. Solid-State Fluorescent Carbon Dots: Quenching Resistance Strategies, High Quantum Efficiency Control, Multicolor Tuning, and Applications. *Mater Adv* **2020**, *1* (9), 3122–3142. https://doi.org/10.1039/D0MA00632G.

(143) Carbonaro, C. M.; Orrù, F.; Ricci, P. C.; Ardu, A.; Corpino, R.; Chiriu, D.; Angius, F.; Mura, A.; Cannas, C. High Efficient Fluorescent Stable Colloidal Sealed Dye-Doped Mesostructured Silica Nanoparticles. *Microporous and Mesoporous Materials* **2016**, *225*, 432–439. https://doi.org/10.1016/j.micromeso.2016.01.028.

(144) Duan, P.; Zhi, B.; Coburn, L.; Haynes, C. L.; Schmidt-Rohr, K. A Molecular Fluorophore in Citric Acid/Ethylenediamine Carbon Dots Identified and Quantified by Multinuclear Solid-State Nuclear Magnetic Resonance. *Magnetic Resonance in Chemistry* **2020**, *58* (11), 1130–1138. https://doi.org/10.1002/MRC.4985.

(145) Cancès, E.; Mennucci, B.; Tomasi, J. A New Integral Equation Formalism for the Polarizable Continuum Model: Theoretical Background and

Applications to Isotropic and Anisotropic Dielectrics. *J Chem Phys* **1998**, *107* (8), 3032. https://doi.org/10.1063/1.474659.

(146) Ehrat, F.; Bhattacharyya, S.; Schneider, J.; Löf, A.; Wyrwich, R.; Rogach, A. L.; Stolarczyk, J. K.; Urban, A. S.; Feldmann, J. Tracking the Source of Carbon Dot Photoluminescence: Aromatic Domains versus Molecular Fluorophores. *Nano Lett* **2017**, *17* (12), 7710–7716. https://doi.org/10.1021/ACS.NANOLETT.7B03863.

(147) Qu, S.; Wang, X.; Lu, Q.; Liu, X.; Wang, L. A Biocompatible Fluorescent Ink Based on Water-Soluble Luminescent Carbon Nanodots. *Angewandte Chemie International Edition* **2012**, *51* (49), 12215–12218. https://doi.org/10.1002/ANIE.201206791.

(148) Papaioannou, N.; Marinovic, A.; Yoshizawa, N.; Goode, A. E.; Fay, M.; Khlobystov, A.; Titirici, M. M.; Sapelkin, A. Structure and Solvents Effects on the Optical Properties of Sugar-Derived Carbon Nanodots. *Scientific Reports 2018 8:1* **2018**, *8* (1), 1–10. https://doi.org/10.1038/s41598-018-25012-8.

(149) Ferrari, A. C. Raman Spectroscopy of Graphene and Graphite: Disorder, Electron-Phonon Coupling, Doping and Nonadiabatic Effects. *Solid State Commun* **2007**, *143* (1–2), 47–57. https://doi.org/10.1016/j.ssc.2007.03.052.

(150) Matthews, M. J.; Pimenta, M. A.; Dresselhaus, G.; Dresselhaus, M. S.; Endo, M. Origin of Dispersive Effects of the Raman D Band in Carbon Materials. *Phys Rev B* **1999**, *59* (10), R6585. https://doi.org/10.1103/PhysRevB.59.R6585.

(151) Huang, Z.; Chen, X.; Li, Y.; Chen, J.; Lin, J.; Wang, J.; Lei, J.; Chen, R. Quantitative Determination of Citric Acid in Seminal Plasma by Using Raman Spectroscopy. *http://dx.doi.org/10.1366/12-06902* **2013**, *67* (7), 757–760. https://doi.org/10.1366/12-06902.

(152) Schneider, J.; Reckmeier, C. J.; Xiong, Y.; Seckendorff, M. von; Susha, A. S.; Kasák, P.; Rogach, A. L. Molecular Fluorescence in Citric Acid-Based Carbon Dots. *Journal of Physical Chemistry C* **2017**, *121* (3), 2014–2022. https://doi.org/10.1021/ACS.JPCC.6B12519.

(153) Hao, Y. N.; Guo, H. L.; Tian, L.; Kang, X. Enhanced Photoluminescence of Pyrrolic-Nitrogen Enriched Graphene Quantum Dots. *RSC Adv* **2015**, *5* (54), 43750–43755. https://doi.org/10.1039/C5RA07745A.

(154) Sharma, A.; Gadly, T.; Neogy, S.; Ghosh, S. K.; Kumbhakar, M. Molecular Origin and Self-Assembly of Fluorescent Carbon Nanodots in Polar Solvents. *Journal of Physical Chemistry Letters* **2017**, *8* (5), 1044–1052. https://doi.org/10.1021/acs.jpclett.7b00170.

(155) Wang, L.; Zhu, S. J.; Wang, H. Y.; Qu, S. N.; Zhang, Y. L.; Zhang, J. H.; Chen, Q. D.; Xu, H. L.; Han, W.; Yang, B.; Sun, H. B. Common Origin of Green Luminescence in Carbon Nanodots and Graphene Quantum Dots. *ACS Nano* **2014**, *8* (3), 2541–2547. https://doi.org/10.1021/NN500368M.

(156) Kwon, W.; Do, S.; Kim, J.-H.; Seok Jeong, M.; Rhee, S.-W. Control of Photoluminescence of Carbon Nanodots via Surface Functionalization Using Para-Substituted Anilines. *Scientific Reports 2015 5:1* **2015**, *5* (1), 1–10. https://doi.org/10.1038/srep12604.

(157) Righetto, M.; Privitera, A.; Fortunati, I.; Mosconi, D.; Zerbetto, M.; Curri, M. L.; Corricelli, M.; Moretto, A.; Agnoli, S.; Franco, L.; Bozio, R.; Ferrante, C. Spectroscopic Insights into Carbon Dot Systems. *Journal of Physical Chemistry Letters* **2017**, *8* (10), 2236–2242. https://doi.org/10.1021/ACS.JPCLETT.7B00794.

(158) Xiong, Y.; Schneider, J.; Ushakova, E. v.; Rogach, A. L. Influence of Molecular Fluorophores on the Research Field of Chemically Synthesized Carbon Dots. *Nano Today* **2018**, *23*, 124–139. https://doi.org/10.1016/j.nantod.2018.10.010.

(159) Wang, W.; Wang, B.; Embrechts, H.; Damm, C.; Cadranel, A.; Strauss, V.; Distaso, M.; Hinterberger, V.; Guldi, D. M.; Peukert, W. Shedding Light on the Effective Fluorophore Structure of High Fluorescence Quantum Yield Carbon Nanodots. *RSC Adv* **2017**, *7* (40), 24771–24780. https://doi.org/10.1039/C7RA04421F.

(160) Deeney, C.; Wang, S.; Belhout, S. A.; Gowen, A.; Rodriguez, B. J.; Redmond, G.; Quinn, S. J. Templated Microwave Synthesis of Luminescent Carbon Nanofibers. *RSC Adv* **2018**, *8* (23), 12907–12917. https://doi.org/10.1039/C7RA13383A.

(161) Chen, Y.; Zhao, Y.; Yu, B.; Wu, Y.; Yu, X.; Guo, S.; Han, B.; Liu, Z. Visible Light-Driven Photoreduction of CO2 to CH4 over TiO2 Using a Multiple-Site Ionic Liquid as an Absorbent and Photosensitizer. *ACS Sustain Chem Eng* **2020**, *8* (24), 9088–9094. https://doi.org/10.1021/acssuschemeng.0c02333.

(162) Youk, S.; Hofmann, J. P.; Badamdorj, B.; Völkel, A.; Antonietti, M.; Oschatz, M. Controlling Pore Size and Pore Functionality in Sp2-Conjugated Microporous Materials by Precursor Chemistry and Salt Templating. *J Mater Chem A Mater* **2020**, *8* (41), 21680–21689. https://doi.org/10.1039/d0ta05856d.

(163) Masoud, M. S.; Ibrahim, A. A.; Khalil, E. A.; El-Marghany, A. Spectral Properties of Some Metal Complexes Derived from Uracil-Thiouracil and Citrazinic Acid Compounds. *Spectrochim Acta A Mol Biomol Spectrosc* **2007**, *67* (3–4), 662–668. https://doi.org/10.1016/j.saa.2006.07.046.

(164) Mura, S.; Stagi, L.; Malfatti, L.; Carbonaro, C. M.; Ludmerczki, R.; Innocenzi, P. Modulating the Optical Properties of Citrazinic Acid through the Monomer-to-Dimer Transformation. *Journal of Physical Chemistry A* **2020**, *124* (1), 197–203. https://doi.org/10.1021/acs.jpca.9b10884.

(165) Stagi, L.; Mura, S.; Malfatti, L.; Carbonaro, C. M.; Ricci, P. C.; Porcu, S.; Secci, F.; Innocenzi, P. Anomalous Optical Properties of Citrazinic Acid under Extreme PH Conditions. *ACS Omega* **2020**, *5* (19), 10958–10964. https://doi.org/10.1021/acsomega.0c00775.

(166) Das, A.; Gude, V.; Roy, D.; Chatterjee, T.; De, C. K.; Mandal, P. K. On the Molecular Origin of Photoluminescence of Nonblinking Carbon Dot. *Journal of Physical Chemistry C* **2017**, *121* (17), 9634–9641. https://doi.org/10.1021/acs.jpcc.7b02433.

(167) Manioudakis, J.; Victoria, F.; Thompson, C. A.; Brown, L.; Movsum, M.; Lucifero, R.; Naccache, R. Effects of Nitrogen-Doping on the Photophysical Properties of Carbon Dots †. *J. Mater. Chem. C* **2019**, *7*, 853. https://doi.org/10.1039/c8tc04821e.

(168) Qu, D.; Zheng, M.; Zhang, L.; Zhao, H.; Xie, Z.; Jing, X.; Haddad, R. E.; Fan, H.; Sun, Z. Formation Mechanism and Optimization of Highly

Luminescent N-Doped Graphene Quantum Dots. *Scientific Reports 2014 4:1* **2014**, *4* (1), 1–11. https://doi.org/10.1038/srep05294.

(169) Dong, Y.; Dai, R.; Dong, T.; Chi, Y.; Chen, G. Photoluminescence, Chemiluminescence and Anodic Electrochemiluminescence of Hydrazide-Modified Graphene Quantum Dots. *Nanoscale* **2014**, *6* (19), 11240–11245. https://doi.org/10.1039/c4nr02539c.

(170) Feng, Y.; Zhao, J.; Yan, X.; Tang, F.; Xue, Q. Enhancement in the Fluorescence of Graphene Quantum Dots by Hydrazine Hydrate Reduction. *Carbon N Y* **2014**, *66*, 334–339. https://doi.org/10.1016/J.CARBON.2013.09.008.

(171) Fu, Y.; Zhao, S.; Wu, S.; Huang, L.; Xu, T.; Xing, X.; Lan, M.; Song, X. A Carbon Dots-Based Fluorescent Probe for Turn-on Sensing of Ampicillin. *Dyes and Pigments* **2020**, *172*, 107846. https://doi.org/10.1016/J.DYEPIG.2019.107846.

(172) Kim, S.; Shin, D. H.; Kim, C. O.; Kang, S. S.; Lee, K. W.; Kim, J.; Choi, S. H.; Hwang, S. W. Effect of Nitrogen Doping on the Structural and the Optical Variations of Graphene Quantum Dots by Using Hydrazine Treatment. *Journal of the Korean Physical Society* **2015**, *67* (4), 746–751. https://doi.org/10.3938/jkps.67.746.

(173) Shen, J.; Zhu, Y.; Chen, C.; Yang, X.; Li, C. Facile Preparation and Upconversion Luminescence of Graphene Quantum Dots. *Chemical Communications* **2011**, *47* (9), 2580–2582. https://doi.org/10.1039/c0cc04812g.

(174) Xu, X.; Zhang, K.; Zhao, L.; Li, C.; Bu, W.; Shen, Y.; Gu, Z.; Chang, B.; Zheng, C.; Lin, C.; Sun, H.; Yang, B. Aspirin-Based Carbon Dots, a Good Biocompatibility of Material Applied for Bioimaging and Anti-Inflammation. **2016**. https://doi.org/10.1021/acsami.6b12252.

(175) Elder, D. P.; Snodin, D.; Teasdale, A. Control and Analysis of Hydrazine, Hydrazides and Hydrazones—Genotoxic Impurities in Active Pharmaceutical Ingredients (APIs) and Drug Products. *J Pharm Biomed Anal* **2011**, *54* (5), 900–910. https://doi.org/10.1016/J.JPBA.2010.11.007.

(176) Serov, A.; Padilla, M.; Roy, A. J.; Atanassov, P.; Sakamoto, T.; Asazawa, K.; Tanaka, H. Anode Catalysts for Direct Hydrazine Fuel Cells: From Laboratory Test to an Electric Vehicle. *Angewandte Chemie International Edition* **2014**, *53* (39), 10336–10339. https://doi.org/10.1002/ANIE.201404734.

(177) An, Z.; Li, Z.; He, Y.; Shi, B.; Wei, L.; Yu, M. Ratiometric Luminescence Detection of Hydrazine with a Carbon Dots–Hemicyanine Nanohybrid System. *RSC Adv* **2017**, *7* (18), 10875–10880. https://doi.org/10.1039/C6RA27844B.

(178) Chen, W.; Wang, H.; Tang, H.; Yang, C.; Guan, X.; Li, Y. Amperometric Sensing of Hydrazine by Using Single Gold Nanopore Electrodes Filled with Prussian Blue and Coated with Polypyrrole and Carbon Dots. *Microchimica Acta* **2019**, *186* (6), 1–7. https://doi.org/10.1007/S00604-019-3486-6.

(179) Hiremath, S. D.; Priyadarshi, B.; Banerjee, M.; Chatterjee, A. Carbon Dots-MnO2 Based Turn-on Fluorescent Probe for Rapid and Sensitive Detection of Hydrazine in Water. *J Photochem Photobiol A Chem* **2020**, *389*, 112258. https://doi.org/10.1016/J.JPHOTOCHEM.2019.112258.

(180) Liu, W.; Jia, H.; Zhang, J.; Shao, L.; Wang, J.; Fang, D. A Novel Dual-Excitation and Dual-Emission Fluorescent Probe CDs–COO–F for Hydrazine Detection in Aqueous Solutions and Living Cells. *Dyes and Pigments* **2021**, *184*, 108831. https://doi.org/10.1016/J.DYEPIG.2020.108831.

(181) P Mason, R. Biotransformation of Hydrazine Dervatives in the Mechanism of Toxicity. *J Drug Metab Toxicol* **2014**, *05* (02). https://doi.org/10.4172/2157-7609.1000168.

(182) Sha, R.; Jones, S. S.; Vishnu, N.; Soundiraraju, B.; Badhulika, S. A Novel Biomass Derived Carbon Quantum Dots for Highly Sensitive and Selective Detection of Hydrazine. *Electroanalysis* **2018**, *30* (10), 2228–2232. https://doi.org/10.1002/elan.201800255.

(183) Wei, G.; Wang, L.; Huo, L.; Zhang, Y. Economical, Green and Rapid Synthesis of CDs-Cu2O/CuO Nanotube from the Biomass Waste Reed as Sensitive Sensing Platform for the Electrochemical Detection of Hydrazine.

Talanta **2020**, *209*, 120431. https://doi.org/10.1016/J.TALANTA.2019.120431.

(184) Xu, L.; Fan, H.; Huang, L.; Xia, J.; Huang, J.; Li, M.; Ding, H.; Huang, K.; Li, S. Eosinophilic Nitrogen-Doped Carbon Dots Derived from Tribute Chrysanthemum for Label-Free Detection of Fe3+ Ions and Hydrazine. *J Taiwan Inst Chem Eng* **2017**, *78*, 247–253. https://doi.org/10.1016/J.JTICE.2017.06.011.

(185) Pal, H.; Nad, S.; Kumbhakar, M. Photophysical Properties of Coumarin-120: Unusual Behavior in Nonpolar Solvents. *J Chem Phys* **2003**, *119* (1), 443. https://doi.org/10.1063/1.1578057.

(186) Stachowska, J. D.; Murphy, A.; Mellor, C.; Fernandes, D.; Gibbons, E. N.; Krysmann, M. J.; Kelarakis, A.; Burgaz, E.; Moore, J.; Yeates, S. G. A Rich Gallery of Carbon Dots Based Photoluminescent Suspensions and Powders Derived by Citric Acid/Urea. *Sci Rep* **2021**, *11* (1), 1–14. https://doi.org/10.1038/s41598-021-89984-w.

(187) Ding, H.; Yu, S. B.; Wei, J. S.; Xiong, H. M. Full-Color Light-Emitting Carbon Dots with a Surface-State-Controlled Luminescence Mechanism. *ACS Nano* **2016**, *10* (1), 484–491. https://doi.org/10.1021/acsnano.5b05406.

(188) Wang, Z.; Yuan, F.; Li, X.; Li, Y.; Zhong, H.; Fan, L.; Yang, S. 53% Efficient Red Emissive Carbon Quantum Dots for High Color Rendering and Stable Warm White-Light-Emitting Diodes. *Advanced Materials* **2017**, *29* (37), 1–7. https://doi.org/10.1002/adma.201702910.

(189) Langer, M.; Hrivnák, T.; Medved', M.; Otyepka, M. Contribution of the Molecular Fluorophore IPCA to Excitation-Independent Photoluminescence of Carbon Dots. *The Journal of Physical Chemistry C* **2021**, *125* (22), 12140–12148. https://doi.org/10.1021/acs.jpcc.1c02243.

(190) Tajik, S.; Dourandish, Z.; Zhang, K.; Beitollahi, H.; Le, Q. van; Jang, H. W.; Shokouhimehr, M. Carbon and Graphene Quantum Dots: A Review on Syntheses, Characterization, Biological and Sensing Applications for Neurotransmitter Determination. *RSC Adv* **2020**, *10* (26), 15406–15429. https://doi.org/10.1039/d0ra00799d.

(191) Castiglioni, C.; Mapelli, C.; Negri, F.; Zerbi, G. Origin of the D Line in the Raman Spectrum of Graphite: A Study Based on Raman Frequencies and Intensities of Polycyclic Aromatic Hydrocarbon Molecules. *Journal of Chemical Physics* **2001**, *114* (2), 963–974. https://doi.org/10.1063/1.1329670.

(192) Yuan, F.; Yuan, T.; Sui, L.; Wang, Z.; Xi, Z.; Li, Y.; Li, X.; Fan, L.; Tan, Z.; Chen, A.; Jin, M.; Yang, S. Engineering Triangular Carbon Quantum Dots with Unprecedented Narrow Bandwidth Emission for Multicolored LEDs. *Nat Commun* **2018**, *9* (1), 2249. https://doi.org/10.1038/s41467-018-04635-5.


Acknowledgments

My first acknowledgment is to my supervisor Prof. Carlo Maria Carbonaro, for his constant support, his contagious enthusiasm, and his limitless patience in transmitting to me his invaluable expertise during all my studies, making me wish to pursue this amazing job.

Also, in this three-year journey, I was lucky enough to belong to the most extraordinary research group of the Physics Department at the University of Cagliari: a big thank goes to all the Treetop Materials members, the current and the former ones, not only for their constant help in my research but also for their support and friendship.

All the publications presented in this work are the results of a strong collaboration among the CANDL^2 project partners who I sincerely acknowledge for this fruitful cooperation. In particular, I would like to express my gratitude to all the CANDL^2 members from the University of Cagliari who made our research a real pleasure to pursue.

A further thank goes to the CMA group of the University of Namur for hosting me during my 6-month period as a visiting Ph.D. student and the DESINe group of the University of Hasselt for our brand-new collaboration.

I gratefully acknowledge the Sardinian Regional Government for the financial support of my PhD scholarship (P.O.R. Sardegna F.S.E. - Operational Programme of the Autonomous Region of Sardinia, European Social Fund 2014-2020 - Axis III Education and training, Thematic goal 10, Investment Priority 10ii), Specific goal 10.5.

Un ultimo ringraziamento va a tutti i miei amici, vicini e lontani, vecchi e nuovi, per aver condiviso con me gioie e frustrazioni di questi tre anni da aspirante scienziata, e alla mia adorata famiglia, per essere sempre stata la mia forza e il mio paracadute in ogni istante della mia vita. Grazie, di cuore.

Appendix A: Supporting Information of Chapter 3

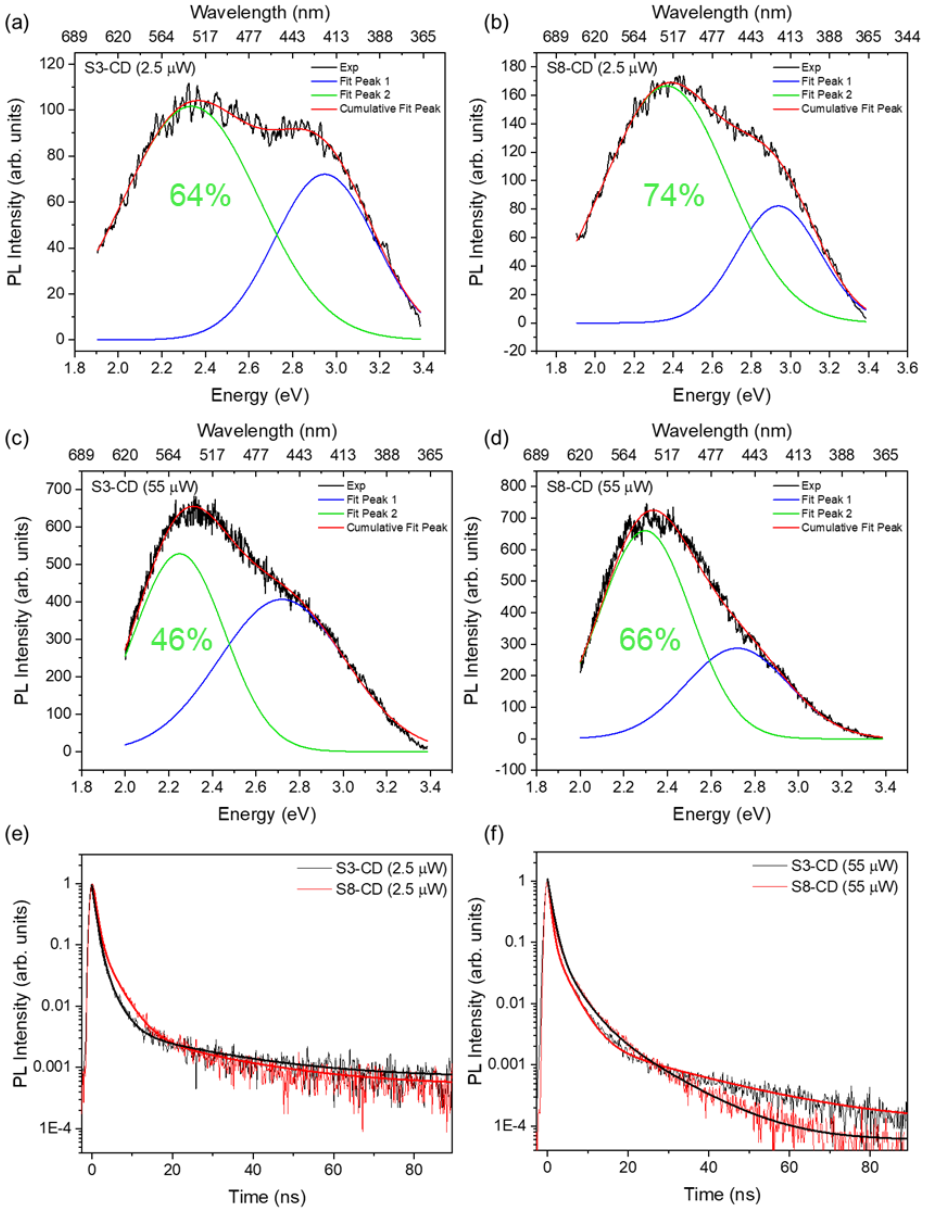

Figure S.3.1. Gaussian deconvolution of hybrid samples irradiated at 350 nm at low (2.5 µW) and high (55 µW) excitation power and corresponding decay time plots with relative fits (details in Table S.3.1 and S.3.2). Jacobian factor for the correction of the PL intensity was applied in all spectra. The decay time was recorded on the overall emission spectrum.

Table S.3.1: Gaussian band deconvolution data of S3-CD, S8-CD hybrids, and CD-R sample excited at 350 nm.

	Peak 1 (eV-nm)	FWHM (eV)	Relative Area (%)	Peak 2 (eV-nm)	FWHM (eV)	Relative Area (%)
S3-CD@350nm (2.5uW)	2.95 - 421	0.54	35.8	2.34 - 531	0.74	64.2
S3-CD@350nm (55uW)	2.72 - 456	0.68	54.4	2.25 - 551	0.49	45.6
S8-CD@350nm (2.5uW)	2.94 - 422	0.50	26.0	2.37 - 524	0.74	74.0
S8-CD@350nm (55uW)	2.72 - 456	0.55	34.5	2.30 - 539	0.49	65.5
CD-R@350nm (2.5-55 uW)	2.82 - 440	0.54	73.0	2.46 - 503	0.71	27.0

Table S.3.2: Exponential deconvolution of decay time data of S3-CD, S8-CD hybrids, and CD-R sample excited at 350 nm.

	A_1	τ_1 (ns)	A_2	τ_2 (ns)	A_3	τ_3 (ns)	τ_{mean}* (ns)
S3-CD@350nm (2.5uW)	119645	0.61	1620	2.81	37	21.66	0.95
S3-CD@350nm (55uW)	24350	0.56	5892	2.56	370	11.35	2.85
S8-CD@350nm (2.5uW)	13563	0.79	1747	3.25	59	16.93	2.52
S8-CD@350nm (55uW)	30310	0.69	6038	2.58	980	7.85	2.60
CD-R@350nm (2.5-55 uW)	1089	0.32	1411	2.08	982	9.21	7.26

*The average lifetime was calculated as the weighted mean of the retrieved values (J.R. Lakowicz, Principles of Fluorescence Spectroscopy, Springer US, Boston, MA, 2006):

$$\bar{\tau} = \sum_{i=1}^{n} \frac{\alpha_i \tau_i^2}{\alpha_i \tau_i}$$

Table S.3.3. Elemental composition in percentage (%) from XPS data (th = theoretical).

	C_{tot}	O_{tot}	N_{tot}	Tot	C/O (0.8 th.)	C/N (3.4 th.)
CD-R	67	21	12	100	3.2	5.6
S3-CD (w/o SiO_2)	52	38	10	100	1.4	5.2
S8-CD (w/o SiO_2)	64	22	14	100	2.9	4.6

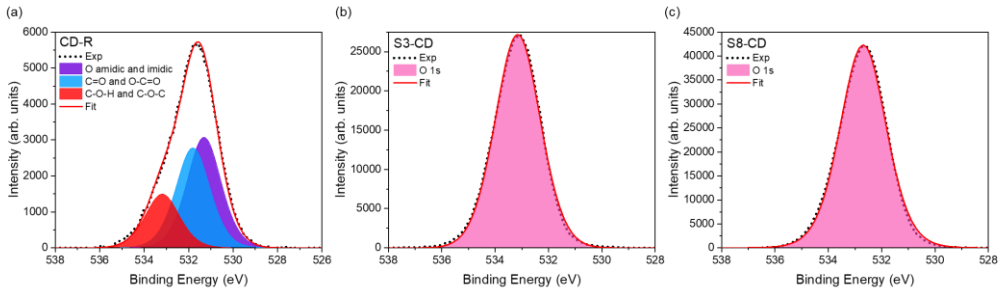

Figure S.3.2. O_{1s} XPS spectra of CD-R (a), S3-CD (b) and S8-CD (c).

Table S.3.4. Data in percentage (%) from XPS O_{1s} spectra.

	C=O O-C=O	C-O-H C-O-C	O_{1s}	$O_{amidic/imidic}$
CD-R	37.83	20.29	-	41.88
S3-CD (w/o SiO2)	-	-	100	-
S8-CD (w/o SiO2)	-	-	100	-

Table S.3.5. Data in percentage (%) from XPS C_{1s} spectra.

	$C_{graphitic}$	$C_{aromatic}$	$C_{aliphatic}$	C-O/C-N	COO-O=C-N	COOH	C_{org}/C_{graph}
CD-R	2.74	27.37	28.14	14.30	24.65	2.80	35.5
S3-CD (w/o SiO2)	3.41	2.05	31.74	26.15	15.25	21.41	28.3
S8-CD (w/o SiO2)	1.52	5.73	32.28	22.25	18.29	19.92	64.4

Table S.3.6 Data in percentage (%) from XPS N_{1s} spectra.

	$N_{pyridinic/amines}$	$N_{pyrrolic}$	$N_{graphitic}$	N-C=O (N_{imidic})
CD-R	18.36	73.98	1.99	5.67
S3-CD (w/o SiO_2)	1.75	39.48	14.37	44.40
S8-CD (w/o SiO_2)	1.89	70.72	10.82	16.57

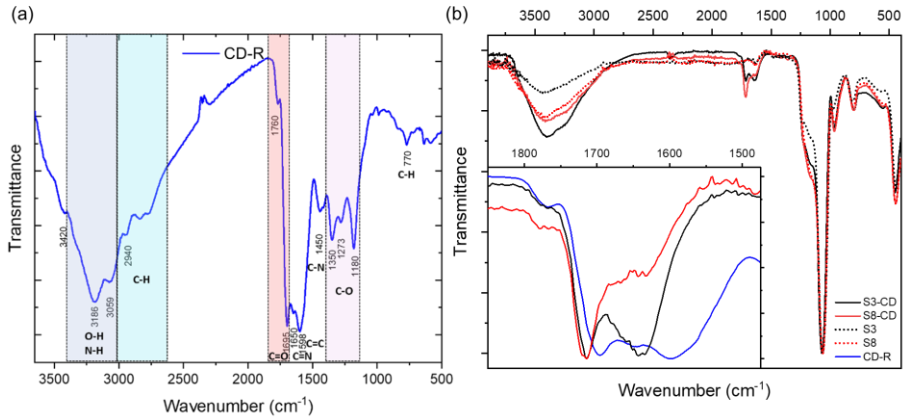

Figure S.3.3. ATR spectra of (a) CD-R reference and (b) silica and silica hybrids with a comparison with CD-R in the insight.

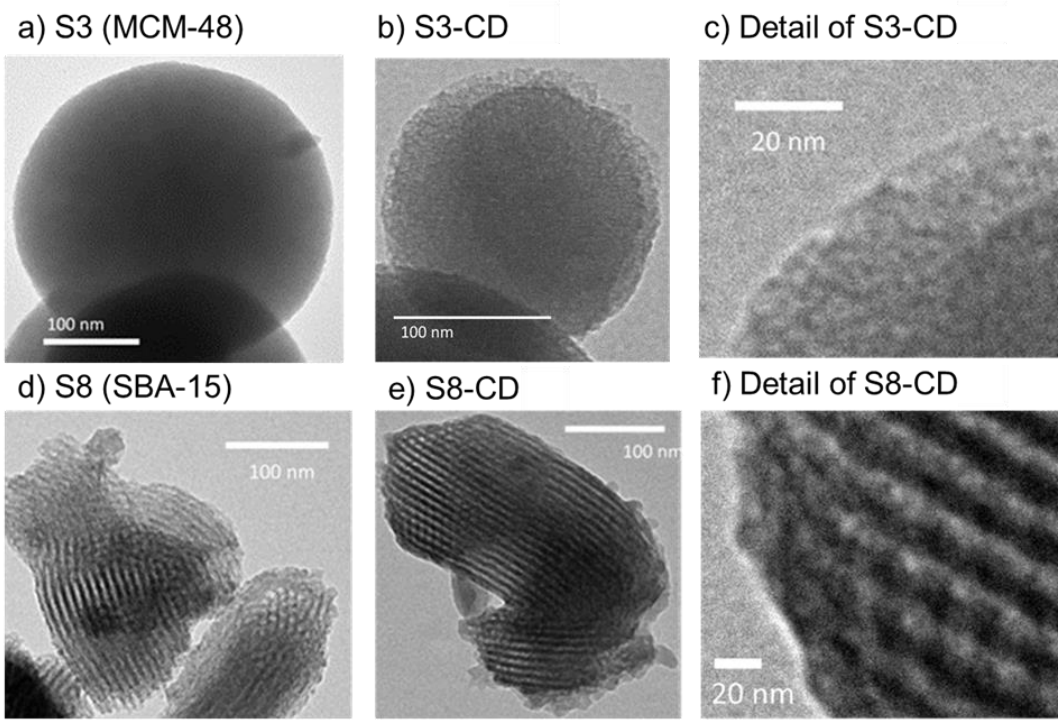

Figure S.3.4. TEM images of void silica matrices MCM-48 (a) and SBA-15 (d). Neither the images of the silica-CD hybrids (b,e) nor their zoom (c,f) show the presence of CDs clearly due to the poor contrast of the carbon particles.

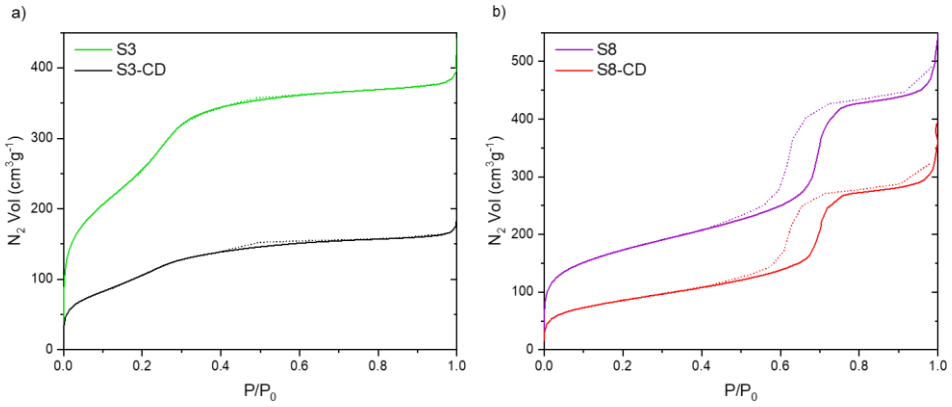

Figure S.3.5. N_2 adsorption–desorption curves (solid and dot, respectively) at 77 K of S3-CD (black line) and S3 (green line) samples (a), S8-CD (red line) and S8 (purple line) samples (b).

Table S.3.7. Surface area and pore volume of silica matrices and S-CD hybrids.

	S3	**S3-CD**	**S8**	**S8-CD**
S_{BET} ($m^2 \cdot g^{-1}$)	984	418	610	308
V_P ($cm^3 \cdot g^{-1}$)	0.59	0.27	0.81	0.54

Table S.3.8. QY of the reference sample and the CDs extracted from the hybrids.

	QY (λ_{exc} = 350 nm)	**QY (λ_{exc} = 440 nm)**
CD-R	4.7 %	6.5 %
CD-3	4.0 %	5.4 %
CD-8	4.4 %	5.2 %

Table S.3.9. Exponential deconvolution of decay time data of CD-3, CD-8 hybrids, and CD-R sample excited at 350 and 450 nm. The decay time was recorded on the overall emission spectrum.

	A_1	**τ_1 (ns)**	**A_2**	**τ_2 (ns)**	**A_3**	**τ_3 (ns)**	**τ_{mean} (ns)**
CD-R@350nm	982	9.2	1411	2.1	1089	0.3	7.3

(2.5-55 uW)							
CD-3@350nm (2.5-55 uW)	1326	9.1	3905	2.7	-	-	6.1
CD-8@350nm (2.5-55 uW)	1239	8.1	2831	2.4	-	-	5.8
CD-R@450nm (2.5-55 uW)	603	5.8	736	1.2	-	-	4.9
CD-3@450nm (2.5-55 uW)	1311	6.4	1257	1.7	-	-	5.5
CD-8@450nm (2.5-55 uW)	2076	6.5	2075	1.6	-	-	5.6

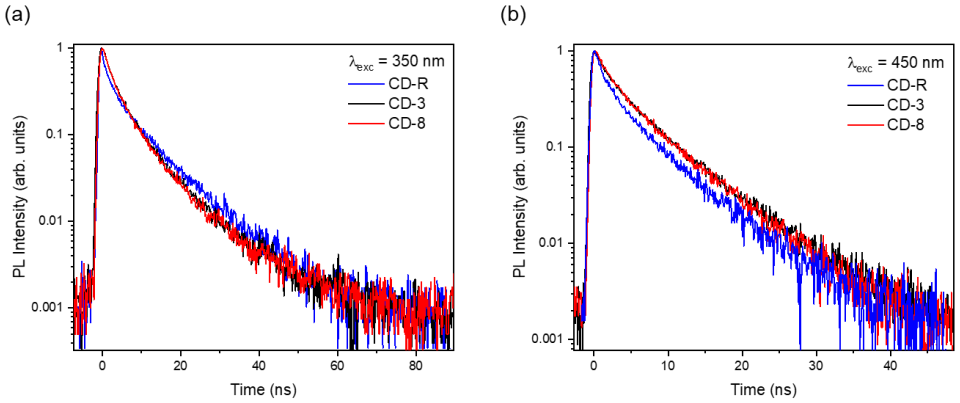

Figure S.3.6. Decay time plots in the 100 ns range of CD-R, CD-3 and CD-8 excited at 350 and 450 nm. The decay time was recorded on the overall emission spectrum.

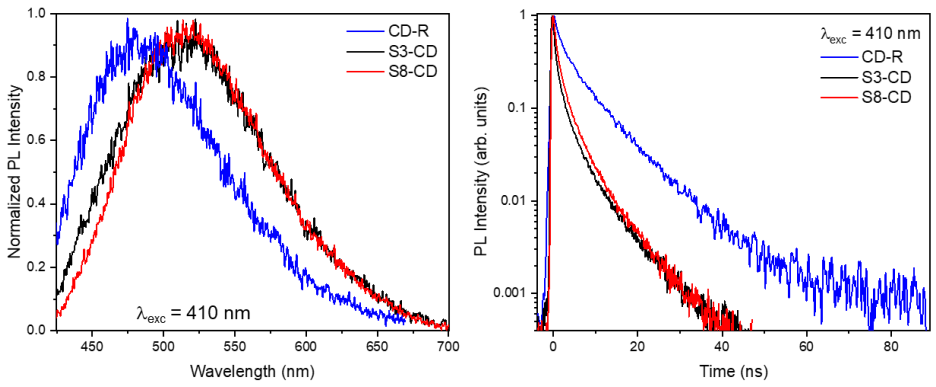

Figure S.3.7. Comparison of TR-PL spectra excited at 410 nm with an excitation power of 55 µW, and the relative decay time plots in the 100 ns range for CD-R and 50 ns range for the hybrids S3-CD and S8-CD. The decay time was recorded on the overall emission spectrum.

Table S.3.10. Exponential deconvolution of decay time data of S3-CD, S8-CD hybrids, and CD-R sample excited at 410 nm. The decay time was recorded on the overall emission spectrum.

	A_1	τ_1 (ns)	A_2	τ_2 (ns)	A_3	τ_3 (ns)	τ_{mean} (ns)
CD-R@410nm (2.5-55 uW)	1494	1.2	984	5.0	689	10	7.0
S3-CD@410nm(55uW)	13515	0.6	3379	3.0	443	9.2	2.2
S8-CD@410nm(55uW)	30310	0.7	6038	2.6	980	7.9	2.5

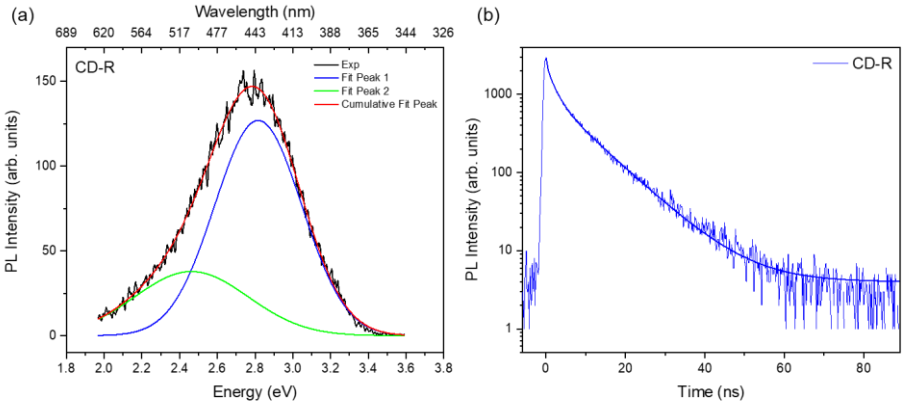

Figure S.3.8. Spectral deconvolution by gaussian bands of CD-R sample (a) and data fit of its decay time (b) excited at 350 nm. Details in Table S.4.1 and S.4.2. Details in Table S.3.1 and S.3.2. The decay time was recorded on the overall emission spectrum.

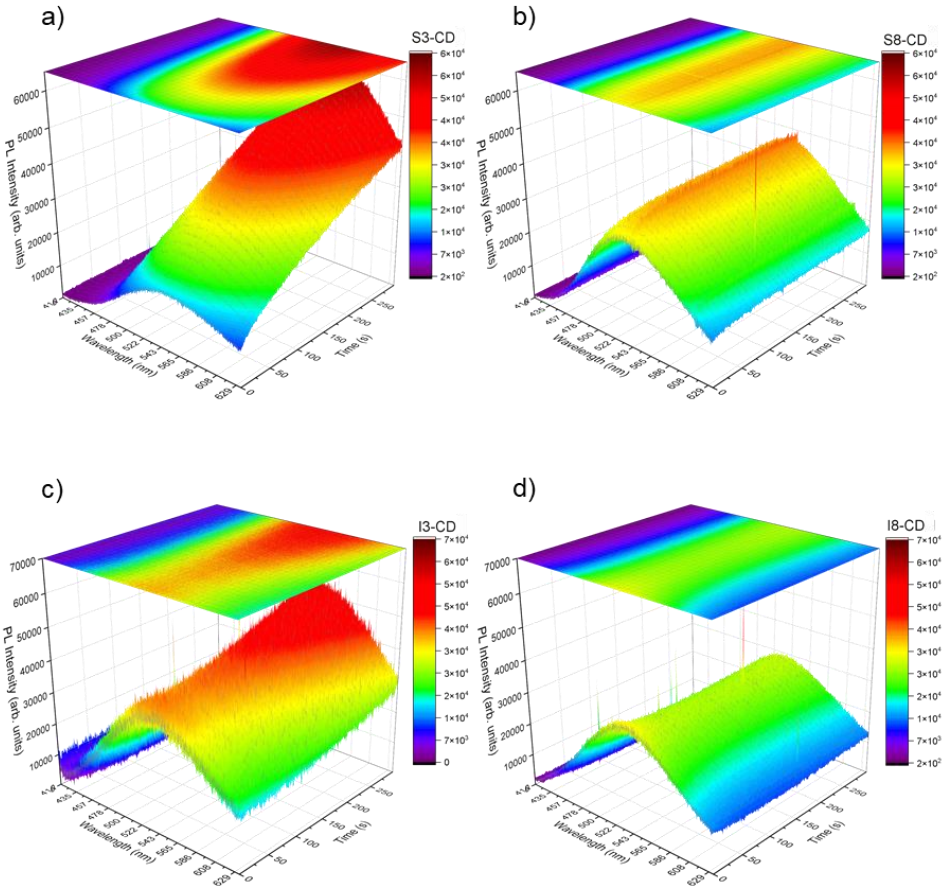

Figure S.3.9. 3D plots of irradiation effects on S3-CD (a) and S8-CD (b), I3-CD (c), I8-CD (d). Laser irradiation was performed with 405 nm CW light focused on the samples with a microscope objective (power 5 μW, spot diameter 6.4 μm).

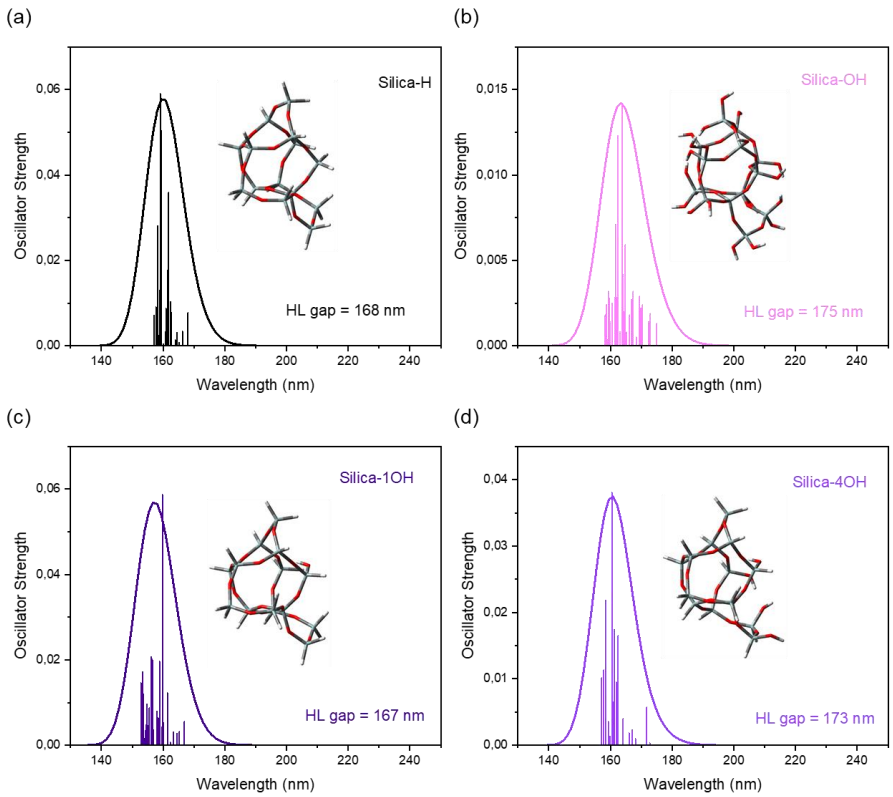

Figure S.3.10. Calculated optical absorption features of isolated emitting center models (simplified stick representation: white stick = H atom, grey stick = Si atom, red stick = O atom).

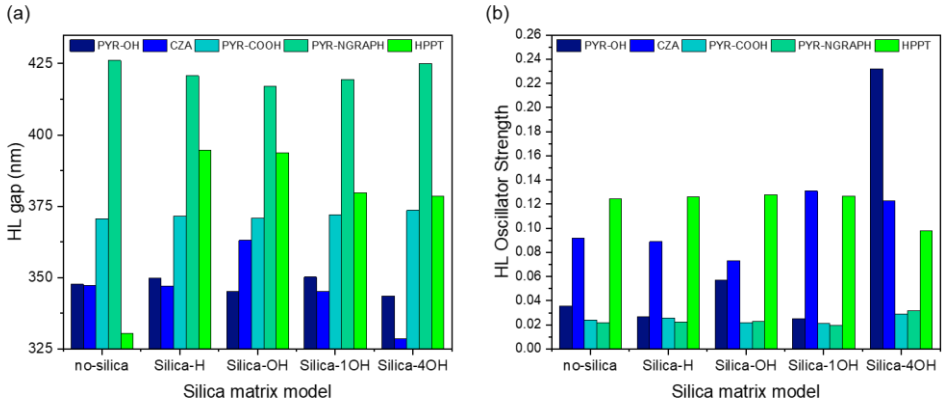

Figure S.3.11. HL gap (left) and oscillator strength (right) for the different model structures without silica, or in presence of fully H terminated, fully OH terminated silica, and partially OH terminated (1 OH or 4 OH) silica models.

Appendix B: Supporting Information of Chapter 4

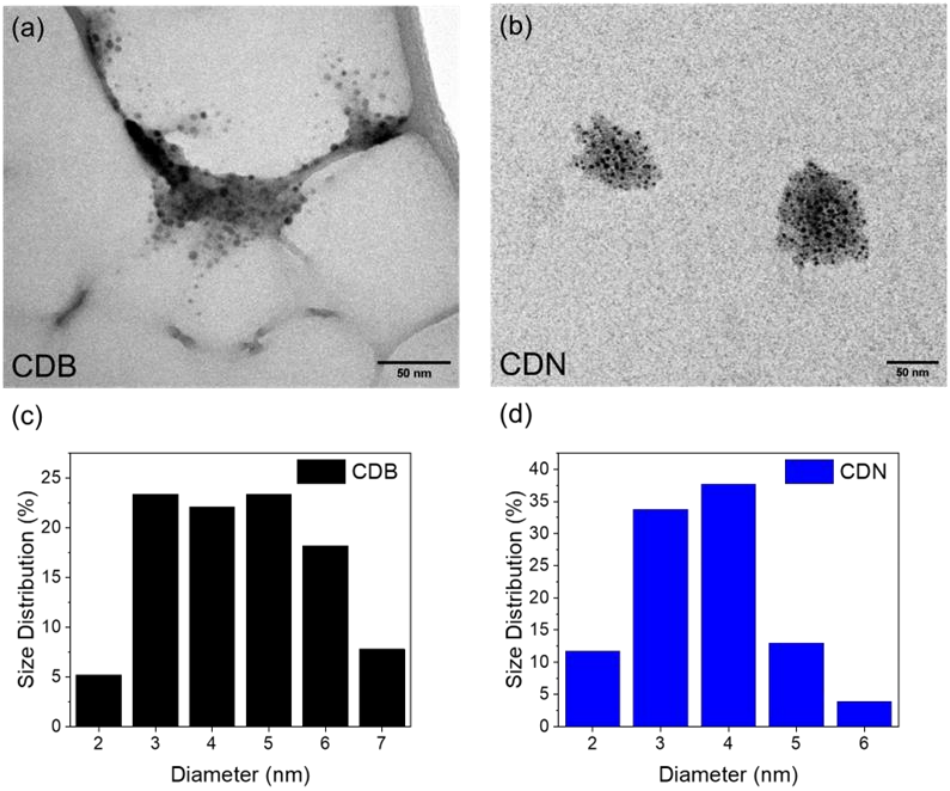

Figure S.4.1. TEM images of CDB (a) and CDN (b) samples with their relative particle size distribution plots (c,d).

Table S.4.1. Elemental composition in percentage (%) from XPS data.

	C_{tot}	O_{tot}	N_{tot}	Tot	C/O (0.8 th.)	C/N (3.4 th.)
CDB	74	26	-	100	2.8	-
CDN	67	21	12	100	3.2	5.6

Table S.4.2. Data in percentage (%) from XPS C_{1s} spectra.

C1s	$C_{graphitic}$	$C_{aromatic}$	$C_{aliphatic}$	C-O/C-N	C=O	O=C-O O=C-N	COOH	C_{org}/C_{graph}
CDB	7.48	31.23	30.61	11.63	3.80	-	15.24	12.4

CDN	2.75	27.42	28.17	14.29	-	24.59	2.79	35.4

Table S.4.3. Data in percentage (%) from XPS N_{1s} spectra.

N1s	**$N_{pyridinic/amines}$**	**$N_{pirrholic}$**	**$N_{graphitic}$**	**N-C=O (imidic)**
CDN	18.36	73.98	1.99	5.67

Table S.4.4. Data in percentage (%) from XPS O_{1s} spectra.

O1s	**C=O O-C=O**	**C-O-H C-O-C**	**O1s**	**$O_{amidic/imidic}$**
CDB	46.23	43.72	10.05	-
CDN	37.83	20.29	-	41.88

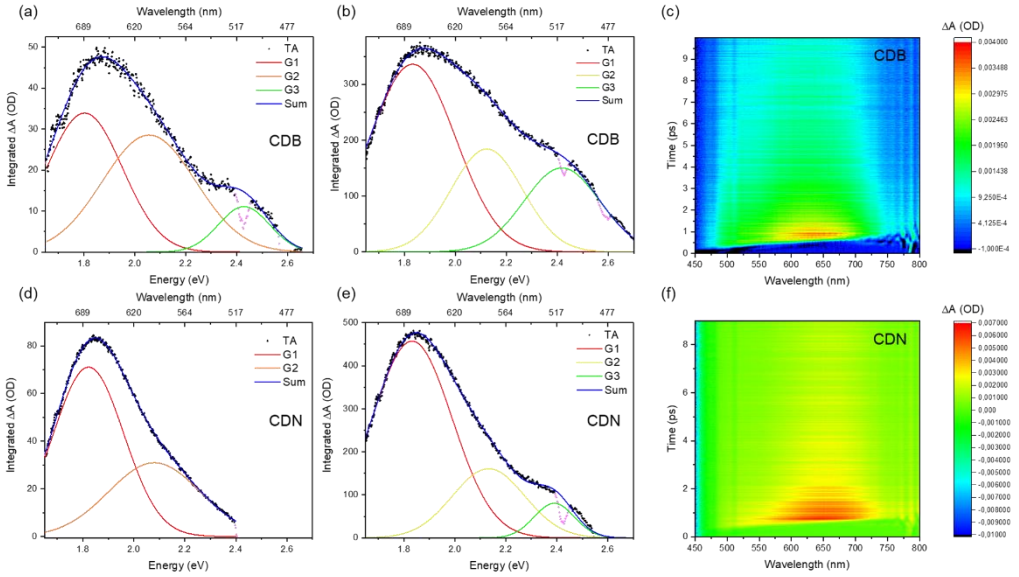

Figure S.4.2. Deconvolution of integrated TA spectra in the ns (a,d) and ps (b,e) domain for CDB (a,b) and CDN (d,e); TA plots of CDB (c) and CDN (f) in the ps domain.

Table S.4.5. Exponential deconvolution of time decay data of CDB and CDN samples excited at 350, 410 and 450 nm.

	A_1	τ_1 (ns)	A_2	τ_2 (ns)	A_3	τ_3 (ns)	τ_{mean} (ns)
CDB@350nm	1331	0.84	859	3.37	78	10.8	4.08
CDN@350nm	1089	0.32	1411	2.08	982	9.21	7.26
CDB@410nm	338	0.38	658	1.67	316	5.42	3.80
CDN@410nm	1494	1.17	985	4.95	690	10.1	7.10
CDB@450nm	1260	0.23	227	1.84	95	6.11	3.40
CDN@450nm	727	1.16	613	5.70	-	-	4.82

The average lifetime was calculated as the weighted mean of the retrieved values (J.R. Lakowicz, Principles of Fluorescence Spectroscopy, Springer US, Boston, MA, 2006):

$$\bar{\tau} = \sum_{i=1}^{n} \frac{\alpha_i \tau_i^2}{\alpha_i \tau_i}$$

Appendix C: Supporting Information of Chapter 5

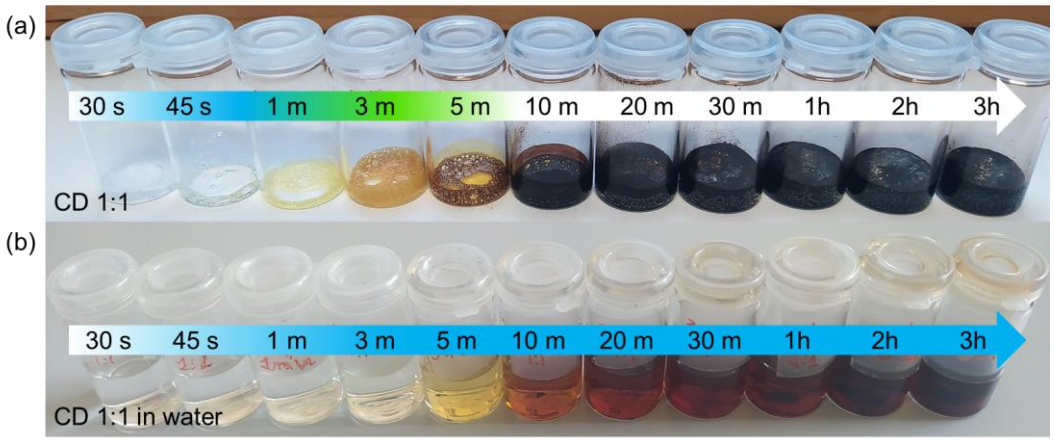

Figure S.5.1. CD 1:1 original powdered samples (a) and dispersed in water (b). The arrows indicate their solid-state (top) and in water (bottom) PL color under UV light at 395 nm (white color means no PL signal to the human eye).

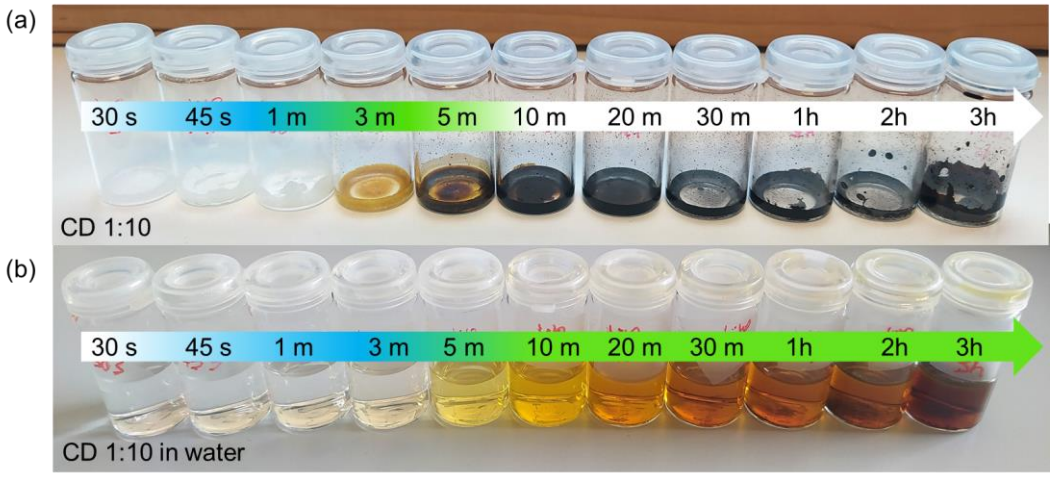

Figure S.5.2. CD 1:10 original powdered samples (a) and dispersed in water (b). The arrows indicate their solid-state (top) and in water (bottom) PL color under UV light at 395 nm (white color means no PL signal to the human eye).

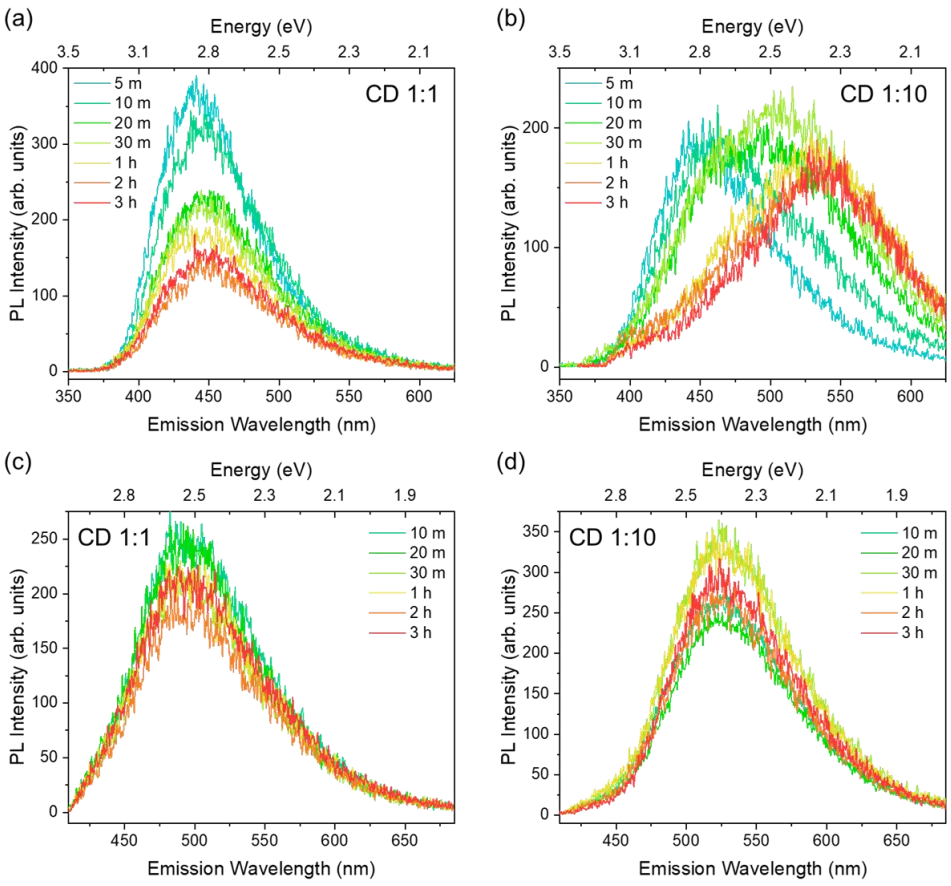

Figure S.5.3. PL spectra of (a-c) CD 1:1 and (b-d) CD 1:10 series in solution excited at 350 nm (a-b) and 410 nm (c-d). All the spectra relativly to each plot were obtained at the same experimental conditions.

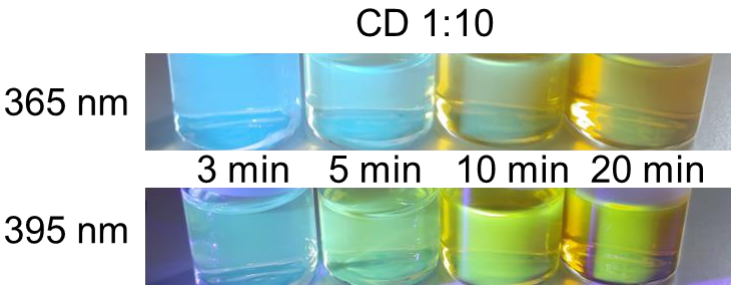

Figure S.5.4. Picture of CD 1:10 samples obtained after 3, 5, 10 and 20 minutes in water solution under 365 (top) and 395 (bottom) nm UV light.

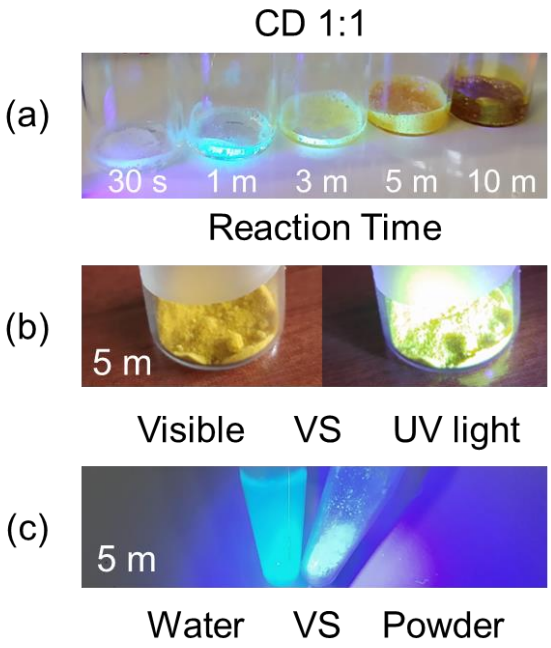

Figure S.5.5. Picture of CD 1:1 samples at different reaction time under UV-light (a), the difference of the 5-minute sample under visible and UV light (b) and the luminescence of the same compared to the one in water under UV light (c).

Appendix D: Supporting Information of Chapter 6

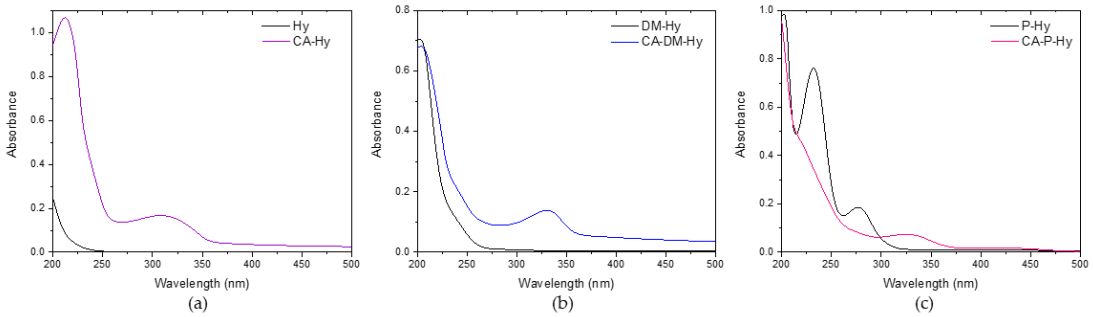

Figure S.6.1. Absorption spectra of hydrazine precursors compared to the corresponding product. (a) Hy and CA-Hy; (b) DM-Hy and CA-DM-Hy; (c) P-Hy and CA-P-Hy.

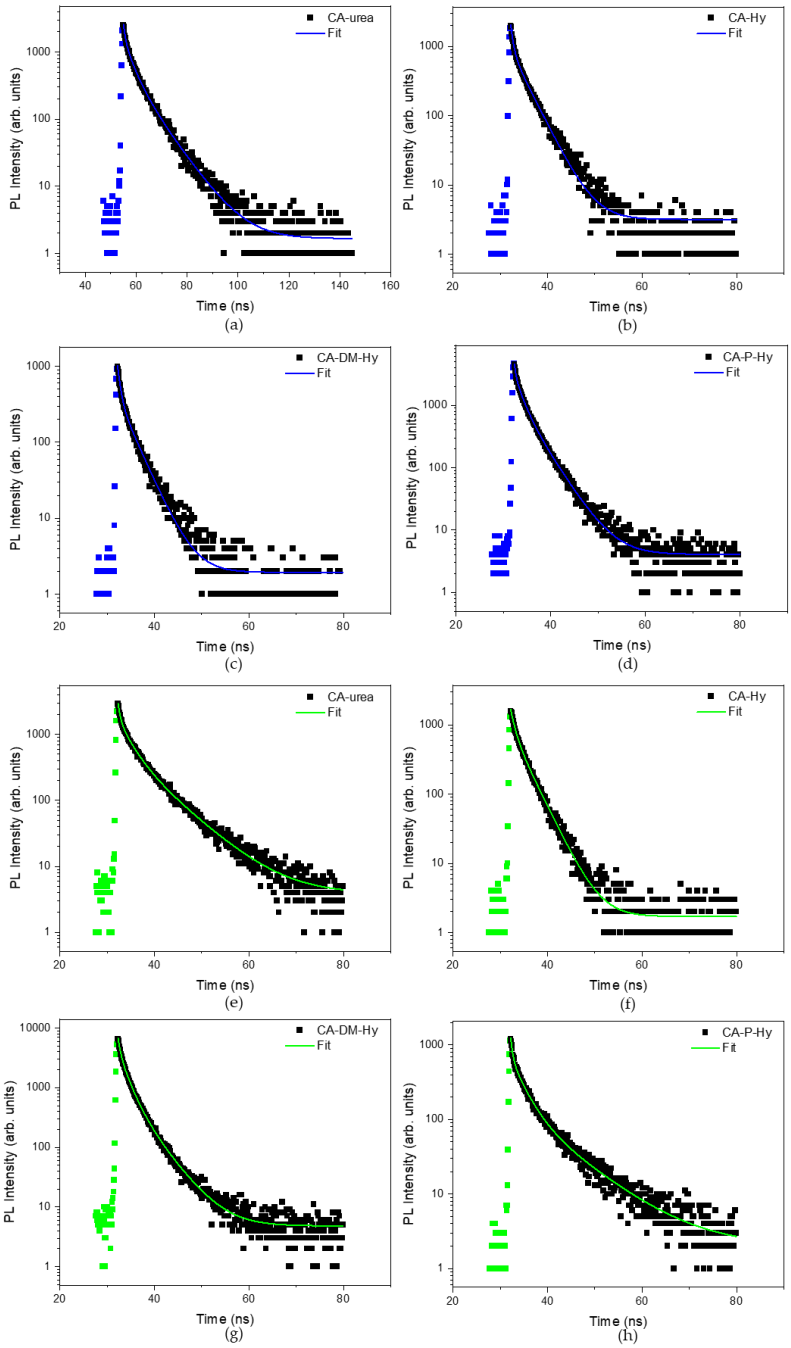

Figure S.6.2. Decay times recorded under 350 nm (blue) and 410 nm (green) excitation light. (Risetime 0.7 in 100 ns, 0.4 in 50ns.) (a) CA-urea excited at 350 nm in 100 ns; (b) CA-Hy excited at 350 nm in 50 ns; (c) CA-DM-Hy excited at 350 nm in 50 ns; (d) CA-P-Hy excited at 350 nm in 50 ns; (e) CA-urea excited at 410 nm in 50 ns; (f)

CA-Hy excited at 410 nm in 50 ns; (g) CA-DM-Hy excited at 410 nm in 50 ns; (h) CA-P-Hy excited at 410 nm in 50 ns.

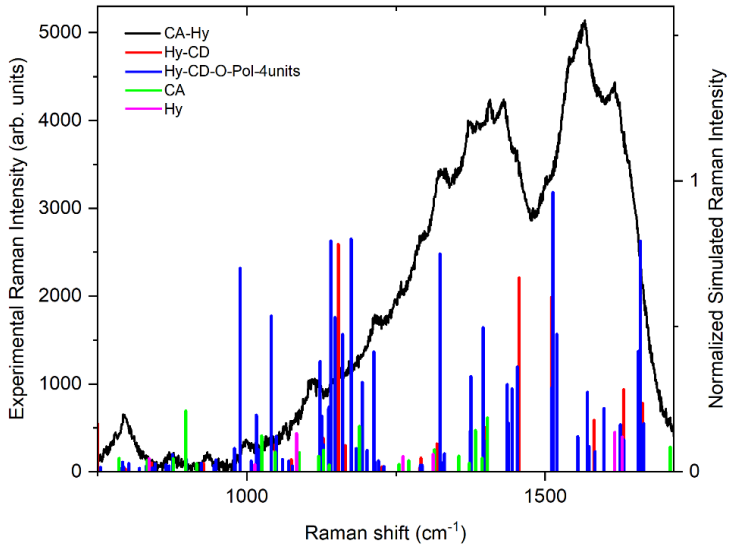

Figure S.6.3. Comparison of experimental Raman spectrum of CA-Hy and computed Raman vibrations for precursors (CA and Hy) and possible Hy-CD structures.

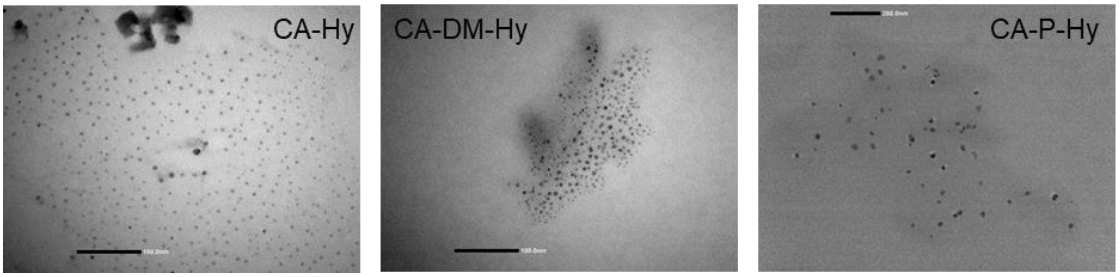

Figure S.6.4. Comparison of experimental Raman spectrum of CA-Hy and computed Raman vibrations for precursors (CA and Hy) and possible Hy-CD structures.

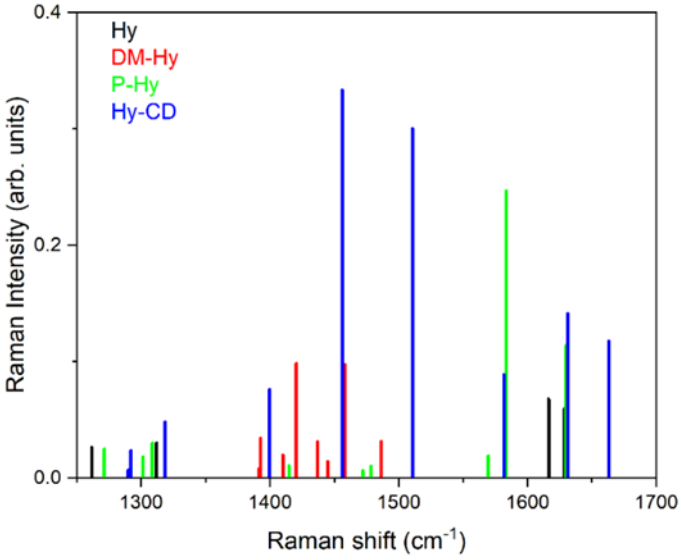

Figure S.6.5. Computed Raman vibrations for hydrazine precursors and Hy-CD structure.

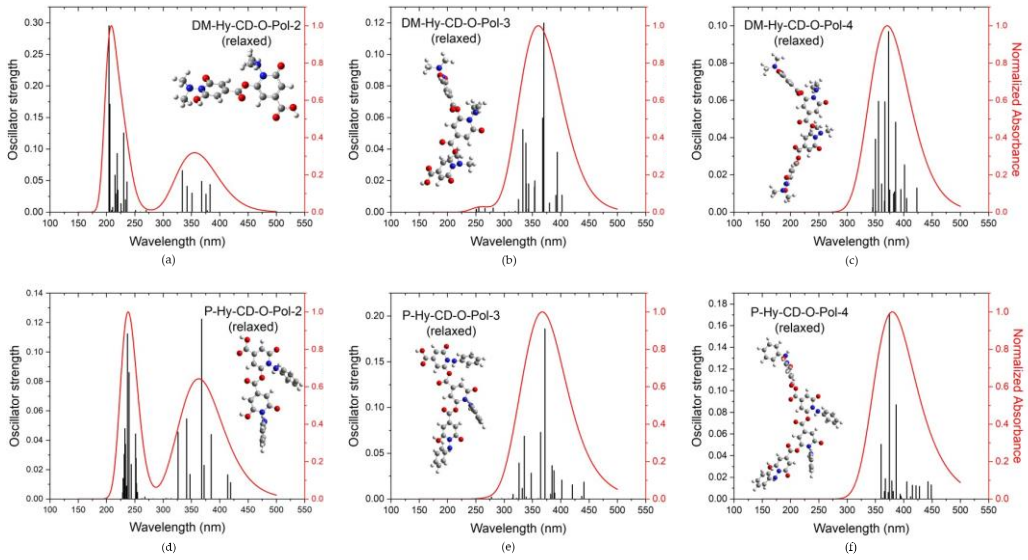

Figure S.6.6. Simulated absorbance spectra and oscillator strength of DM- and P-Hy-CD polymers. The insets report the ball-and-stick representation of the structures (H atom—white sphere, C atom—grey sphere, N atom—blue sphere, O atom—red sphere). (a) DM-Hy-CD-O-Pol-2; (b) DM-Hy-CD-O-Pol-3; (c) DM-Hy-CD-O-Pol-4; (d) P-Hy-CD-O-Pol-2; (e) P-Hy-CD-O-Pol-3; (f) P-Hy-CD-O-Pol-4.

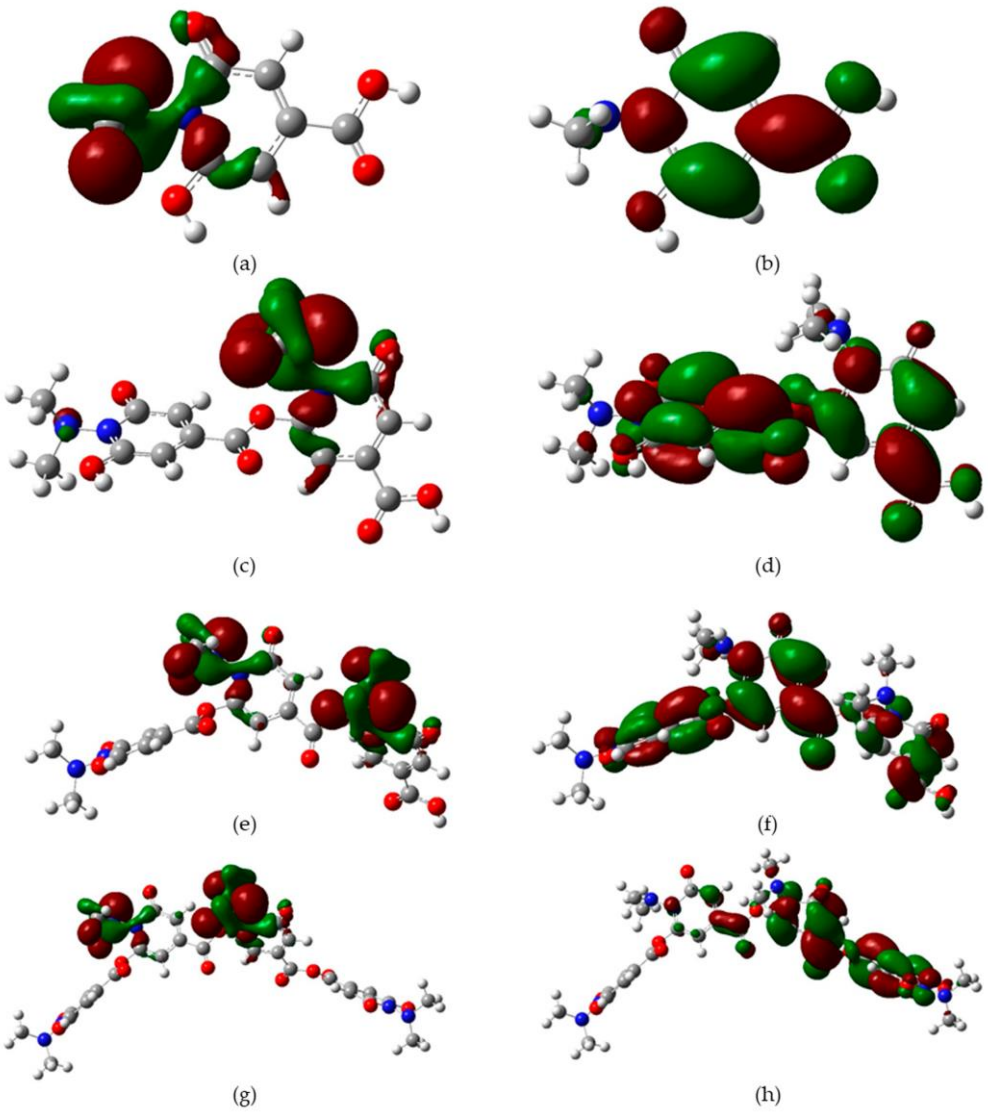

Figure S.6.7. MOs of the HOMO–LUMO states (HOMO on the left and LUMO on the right) for the DM-Hy-CD system (a,b) and its O-Polymer derived system: DM-Hy-CD-O-Pol-2 (c,d), DM-Hy-CDO-Pol-3 (e,f), DM-Hy-CD-O-Pol-4 (g,h). The isocontour value is 0.02 au (H atom—white sphere, C atom—grey sphere, N atom—blue sphere, O atom—red sphere).

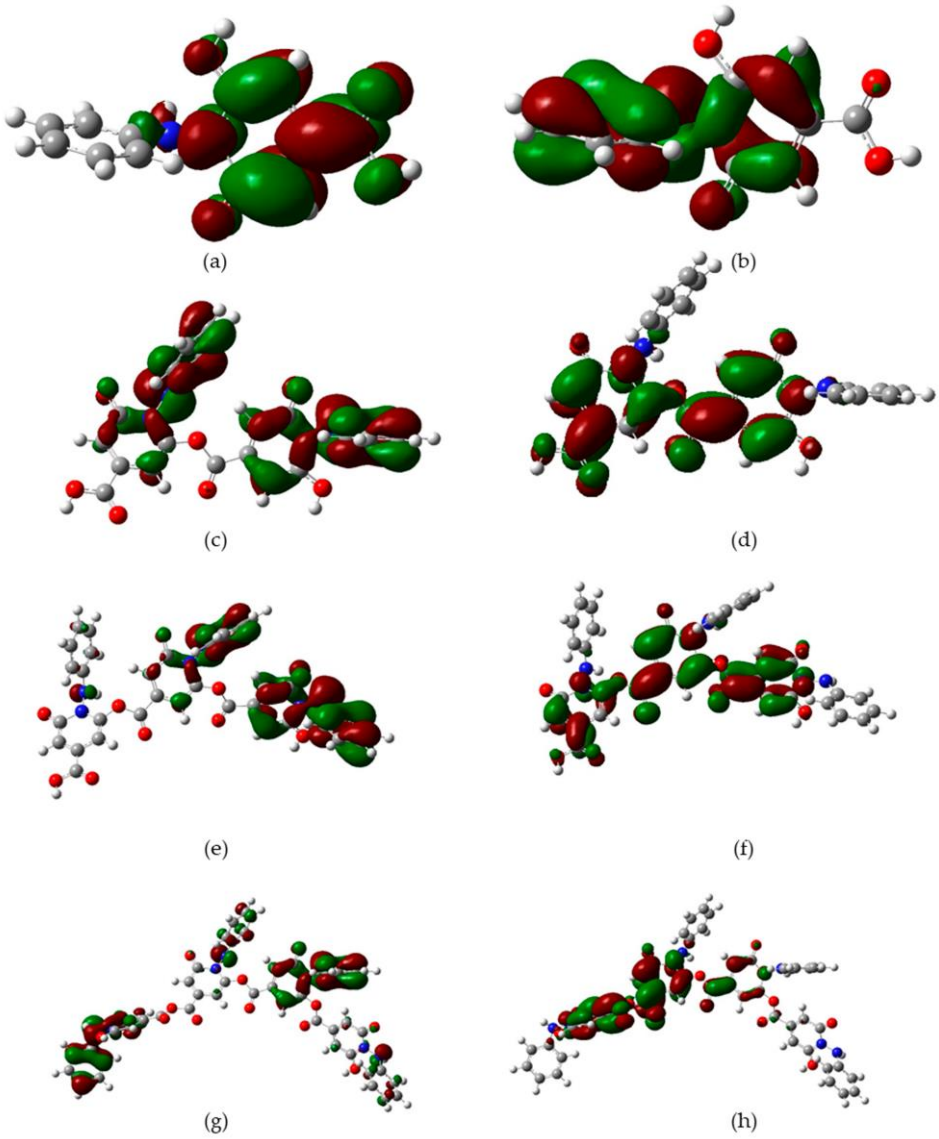

Figure S.6.8. MOs of the HOMO–LUMO states (HOMO on the left and LUMO on the right) for the PHy-CD system (**a,b**) and its O-Polymer derived system: P-Hy-CD-O-Pol-2 (**c,d**), P-Hy-CD-O-Pol-3 (**e,f**), P-Hy-CD-O-Pol-4 (**g,h**). The isocontour value is 0.02 au (H atom—white sphere, C atom—grey sphere, N atom—blue sphere, O atom—red sphere).

Appendix E: Supporting Information of Chapter 7

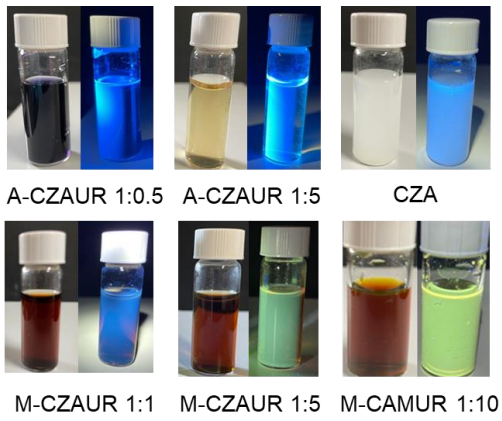

Figure S.7.1. Produced sample from the reaction of CZA and urea in different ratios and with different synthetic treatment (A stands for autoclave and M for microwave) compared to commercial CZA and HPPT-containing CDs from citric acid and urea under UV-light.

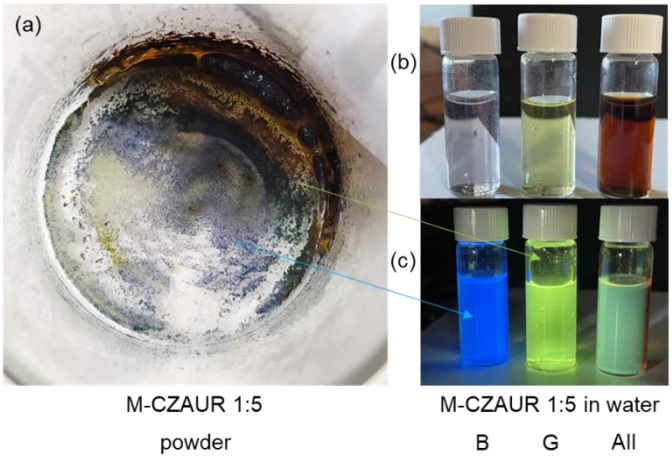

Figure S.7.2. Produced sample from the reaction of CZA and urea in 1:5 molar ratio as a powder (a) and in water under visible (b) and UV-light at 365 nm (c).

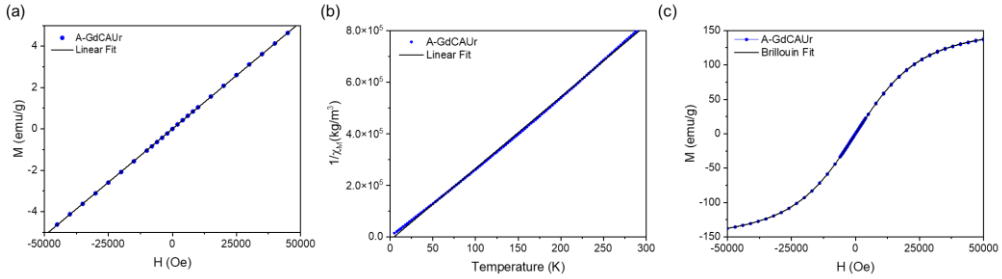

Figure S.7.3. Measurements of magnetization M as a function of the magnetic field (H) at 300 K (a), plot of the inverse of the magnetic susceptibility constant χ as a function of the temperature (b) and loop measurement of the magnetization M as a function of the magnetic field (H) at 5 K.

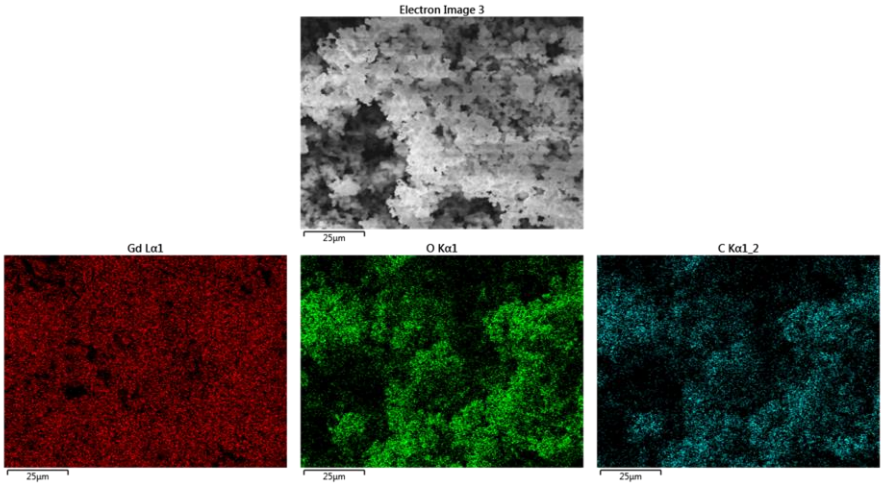

Figure S.7.4. SEM image of the A-GdCAUr precipitate sample (top) and EDX identification on the same image of Gd, O and C elements.

Summary of Ph.D. Activities

Publications on Carbon Dots:

Olla, C.; Ricci, P.C.; Chiriu, D.; Fantauzzi, M.; Casula, M. F.; Mocci, F.: Cappai, A.; Porcu, S.; Stagi, L.; Carbonaro, C.M **On the different nature of bare and N-doped Carbon Dots from citric acid** (submitted to *Nanomaterials*)

Olla, C.; Ricci, P.C.; Chiriu, D.; Fantauzzi, M.; Casula, M. F.; Mocci, F.: Cappai, A.; Porcu, S.; Stagi, L.; Carbonaro, C.M. **Selecting molecular or surface centers in Carbon Dots-silica hybrids to tune the optical emission: a photo-physics study down to the atomistic level.** *Journal of Colloids and Interfaces Science* (**2022**), *634*, 402-417. https://doi.org/10.1016/j.jcis.2022.12.023

Carbonaro, C.M.; de Villiers Engelbrecht, L.; **Olla, C.**; Cappai, A.; Casula, M. F.; Melis, C.; Stagi, L.; Laaksonen, A.; Mocci, F. **Graphene Quantum Dots and Carbon Nanodots: modelling of zero-dimensional carbon nanomaterials.** Chapter of the book "Zero-Dimensional Carbon Nanomaterials", edited by *Elsevier* (in printing, **2022**)

Mocci, F.; de Villiers Engelbrecht, L.; **Olla, C.**; Cappai, A.; Casula, M. F.; Melis, C.; Stagi, L.; Laaksonen, A.; Carbonaro, C. M. **Carbon Nanodots from an *In Silico* Perspective.** *Chemical Reviews* **2022**, *122* (16), 13709–13799. https://doi.org/10.1021/acs.chemrev.1c00864.

Olla, C.; Porcu, S.; Secci, F.; Ricci, P.C.; Carbonaro, C.M. **Towards N–N-Doped Carbon Dots: A Combined Computational and Experimental Investigation**. *Materials* (**2022**), 15, 1468. https://doi.org/ 10.3390/ma15041468

Mocci, F.; **Olla, C.**♦; Cappai, A.; Corpino, R.; Ricci, P. C.; Chiriu, D.; Salis, M.; Carbonaro, C. M. **Formation of citrazinic acid ions and their contribution to optical and magnetic features of carbon nanodots: A combined experimental and computational approach.** *Materials* (**2021**), *14*(4), 1–16. https://doi.org/10.3390/ma14040770

♦ Collaboration.

Carbonaro, C.M.; Thakkar, S. V.; Ludmerczki, R.; **Olla, C.**♦; Pinna, A.; Loche, D.; Malfatti, L.; Cesare Marincola, F.; Casula, M.F. **How porosity affects the emission of fluorescent carbon dot-silica porous composites.** *Microporous and Mesoporous Materials* (**2020**), *305*, 110302. https://doi.org/10.1016/j.micromeso.2020.110302

Other Publications:

Piras, A; **Olla, C.**♦; Reekmans, G.; Kelchtermans, A-S.; De Sloovere, D.; Elen, K.; Carbonaro, C.M.; Fusaro, L.; Adriaensens, P.; Hardy, A.; Aprile, C.; Van Bael, M.K. **Photocatalytic performances of undoped and Al-doped ZnO nanoparticles in the degradation of Rhodamine B under UV-visible light: the role of defects and morphology.** *International Journal of Molecular Sciences* (**2022**), *23*(*24*), 15459. https://doi.org/10.3390/ijms232415459

Thesis Co-Supervision:

Mattia Lizzano, Bachelor's Degree in Physics (September **2021**):
Sintesi e caratterizzazione ottica di Carbon Dots e studio dell'imbibizione in fibre fotoniche

Alessandro Mameli, Bachelor's Degree in Chemistry (December **2020**): **Synthesis and characterization of Carbon Dots from new N-precursors**

Conferences:

E-MRS Spring Meeting 2021 (May **2021**, online):

- Green luminescent carbon nanoparticles for lighting applications (**poster**)
- Carbon Dots in mesoporous silica matrices: high stability solid-state phosphors for lighting applications (**talk**)

13th International Symposium on SiO_2, Advanced Dielectrics and Related Devices (June **2021**, online):

- Carbon Dots in mesoporous silica matrices: high stability solid-state phosphors for lighting applications (**talk**)

♦ Collaboration.

Young Belgian Magnetic Resonance Scientist symposium (December **2021**, online)

International Experiences and Schools:

- FemtoUP 2020-21 International School (March **2021**, online)
- Experimental research at the NMR laboratory of the University of Namur under the supervision of Dr. Luca Fusaro (September **2021**-March **2022**, Namur, BE)
- 6th HRSMC/EPA Advanced Summer School on Photochemistry "Photochemistry: Fundamentals and Applications" (July **2022**, Noordwijk, NL)

Certifications:

- C1 Level English Course (March-October **2020**, UNICA)
- Radioprotection Course (March **2021**, UNICA)
- Basic Laboratory Safety (September **2021**, UNamur)